

DISSERTATION

# Simulation of High Electron Mobility Transistors

ausgeführt zum Zwecke der Erlangung des akademischen Grades  
eines Doktors der technischen Wissenschaften

eingereicht an der Technischen Universität Wien  
Fakultät für Elektrotechnik und Informationstechnik  
von

STANISLAV VITANOV



Wien, im Dezember 2010

---



*The open society, the unrestricted access to knowledge, the unplanned and uninhibited association of men for its furtherance – these are what may make a vast, complex, ever growing, ever changing, ever more specialized and expert technological world, nevertheless a world of human community.*

by J. Robert Oppenheimer

To my father

---

# Abstract

---

**H**IGH Electron Mobility Transistors (HEMTs) based on GaN are already established for high-power and high-frequency applications, such as mobile communications and radar. Discrete transistors and Monolithic Microwave Integrated Circuits (MMICs) are commercially available, however, emerging new technologies, such as ultra-broadband communication and hybrid vehicles, require further device optimization. On the other hand normally-off structures, while essential for some applications (both analog and digital), still suffer from several performance issues. In order to solve these problems and enable a cost and time effective optimization routine, device simulation tools are expedient.

This thesis discusses III-Nitride materials and material systems on which HEMTs are based. Own Monte Carlo simulations are supplemented by an extensive study of experimental and theoretical works available. Using the most recent findings for the band structure and accounting for all relevant scattering mechanisms the simulations show electron transport properties which are in agreement with those reported for GaN and AlN. For InN superior transport characteristics are predicted due to the lower band gap.

New transport models suitable for III-V materials are developed based on the extensive summary of available experimental and theoretical data and the own simulations results. They are subsequently implemented in the device simulator MINIMOS-NT. Established physical models for the lattice and thermal properties of the materials as well as models describing relevant effects are discussed with respect to HEMT specifics and material properties.

Several GaN-based device generations are simulated using the presented models and model parameters. A very good agreement with experimental data and excellent predictive results allow for extensive optimization studies of the gate geometry. Performance predictions for down-scaled devices in high-temperature operation are shown. Transconductance investigations are discussed with respect to the transport model used. InAlN/GaN structures are studied and their *RF* performance is analyzed accounting for improved material quality. At last two different approaches towards the realization of normally-off devices are examined: the recess gate technique and band structure engineering using an additional InGa<sub>N</sub> cap layer. Based on experimental *DC* data, the *RF* performance is predicted and compared.



---

# Kurzfassung

---

**H**IGH Electron Mobility Transistors (HEMTs) haben sich für Anwendungen, welche gutes Hochfrequenzverhalten sowie hohe Ausgangsleistung erfordern, z.B. mobile Kommunikation und Radartechnik, bereits etabliert. Diskrete Bauelemente sowie Monolithic Microwave Integrated Circuits (MMICs) von mehreren Herstellern sind verfügbar. Aufkommende technologische Neuentwicklungen, wie z.B. Breitband-Kommunikation und Hybrid-Fahrzeuge, erfordern aber weitere, gezielte Optimierung der Strukturen. Andererseits sind normally-off Transistoren, welche in mehreren digitalen sowie auch analogen Anwendungsfeldern vorteilhaft sind, immer noch von bestimmten Problemen geplagt. Um diese zu lösen und eine kostengünstige Optimierung zu ermöglichen, sind Bauelementensimulationen von entscheidender Bedeutung.

In der vorliegenden Dissertation werden die in HEMTs verwendeten III-V Halbleiter diskutiert. Eigene Monte Carlo-Simulationen werden durch eine umfassende Studie von vorhandenen experimentellen und theoretischen Werken ergänzt. Unter Berücksichtigung neuester Forschungsergebnisse über die Bandstruktur der Materialien und aller wichtigen Streuungs-Mechanismen werden Elektronen-Transporteigenschaften errechnet, welche für GaN und AlN in guter Übereinstimmung mit den vorhandenen Ergebnissen sind. Aufgrund der kleinen Bandlücke für InN, deuten die Simulationen auf ein besseres Transportverhalten als bisher angenommen.

Auf der Basis eigener Simulationsergebnisse sowie auch zusammengefasster experimenteller und theoretischer Daten, werden neue Transportmodelle, maßgeschneidert für III-V Materialien, entwickelt und anschließend in den generischen Bauelementsimulator MINIMOS-NT implementiert. Bestehende Modelle für die Gittereigenschaften und das Temperaturverhalten, sowie auch Modelle für wichtige Effekte, werden unter Berücksichtigung der HEMT-Besonderheiten und Materialeigenschaften diskutiert.

Eine Reihe HEMT Bauelemente aus verschiedenen Generationen wird modelliert. Dabei werden die beschriebenen Modelle und Materialparametersätze benutzt. Sehr gute Übereinstimmung mit experimentellen Messdaten und bemerkenswerte prädiktive Simulationsergebnisse ermöglichen eine Optimierungsstudie der Gate-Elektrodengeometrie. Ferner werden die Transistoreigenschaften bei höheren Temperaturen und kürzeren Gate-Längen untersucht. Transkonduktanzanalysen in Bezug auf die benutzten Transportmodelle werden durchgeführt. InAlN/GaN Transistoren werden simuliert und das *HF*-Verhalten für erhöhte Materialqualität wird erörtert. Als Abschluß werden zwei unterschiedliche Ansätze zum Erzielen des normally-off Verhaltens geprüft: Die Gate-Recess-Technik und das Band-Structure-Engineering mittels einer InGaN Schicht. Das *HF*-Verhalten wird verglichen und analysiert.





---

# Acknowledgment

---

**A**MONG the numerous people without who this work would have been impossible I would like to thank especially:

*Prof. Dr. Siegfried Selberherr* for giving me the opportunity to join the Institute for Microelectronics at Technische Universität Wien. As my advisor he was always available for discussion, and was also a constant source of encouragement and motivation (even when the deadlines seemed impossible to meet). He showed belief and patience throughout the whole course of work.

*Dr. Vassil Palankovski* for accepting me to the *Advanced Material and Device Analysis Group* and the financial support from his START project. I owe him my very special thanks for introducing me to device modeling and simulation software and guiding and advising my work through all the years. He was available seven days a week with great ideas and solutions and was the one from whose vast experience I learned the most.

*Dr. Rüdiger Quay*, Fraunhofer IAF, for the sustained collaboration, for providing experimental data, and for serving on my examination committee. I greatly benefitted from his extensive knowledge in the area of GaN-based HEMTs.

*Dipl.-Ing. Stephan Maroldt*, Fraunhofer IAF, for fruitful discussions and *RF* measurements.

*Prof. Dr. Dionyz Pogany*, *Dr. Jan Kuzmik*, and *Dr. Gianmauro Pozzovivo*, FKE, TU Wien, for the collaboration on InAlN/GaN structures.

*Dr. Johann Cervenka* for the programming support, for thorough proofreading, and for the head-to-head competition for the “most messy desk” award.

*Prof. Dr. Tibor Grasser* for his help on the simulation software. His laconic advices were always spot-on.

*Prof. Dr. Erasmus Langer* for providing me the opportunity to attend several workshops and courses.

*Dr. Martin Vasicek* for many discussions including but not limited to semiconductor physics.

Above all, I would like to thank my father. I am greatly indebted to him for the continuous support through all the years of my studies. Even when things were looking bad his belief kept me going. For the endless patience this work is dedicated to him.



---

# Contents

---

<b>Abstract</b>	<b>iii</b>
<b>Kurzfassung</b>	<b>v</b>
<b>Acknowledgment</b>	<b>vii</b>
<b>Contents</b>	<b>ix</b>
<b>List of Abbreviations and Acronyms</b>	<b>xiii</b>
<b>List of Symbols</b>	<b>xv</b>
Notation . . . . .	xv
Physical Quantities . . . . .	xvi
Fundamental Constants . . . . .	xvii
<b>List of Figures</b>	<b>xix</b>
<b>List of Tables</b>	<b>xxv</b>
<b>1 Introduction</b>	<b>1</b>
<b>2 State-of-the-Art</b>	<b>3</b>
2.1 History of HEMTs . . . . .	3
2.2 Applications for GaN HEMTs . . . . .	4
2.2.1 <i>RF</i> Applications: Broadband Communication . . . . .	4

## CONTENTS

---

2.2.2	<i>RF</i> Applications: Radar Components . . . . .	6
2.2.3	Automotive Applications . . . . .	6
2.2.4	Sensors . . . . .	6
2.3	Normally-Off HEMT . . . . .	6
2.3.1	Gate Recess and Surface Treatment . . . . .	7
2.3.2	Barrier and Capping Layers . . . . .	7
2.4	GaN-Based HEMTs . . . . .	9
2.4.1	Reports by Research Groups . . . . .	9
2.4.2	Commercially Available Products . . . . .	12
2.5	GaAs-Based HEMTs . . . . .	13
2.6	GaN-Based HBTs . . . . .	15
2.6.1	AlGaN/GaN HBTs . . . . .	15
2.6.2	InGaN/GaN HBTs . . . . .	16
2.7	Simulation Software . . . . .	17
2.7.1	Commercial Software . . . . .	17
2.7.2	Minimos-NT . . . . .	18
<b>3</b>	<b>Materials</b>	<b>19</b>
3.1	The Monte Carlo Method . . . . .	19
3.2	Gallium Nitride . . . . .	20
3.2.1	Material Properties . . . . .	20
3.2.2	Electron Transport . . . . .	20
3.2.3	Hole Transport . . . . .	23
3.3	Indium Nitride . . . . .	26
3.3.1	Material Properties . . . . .	26
3.3.2	Electron Transport . . . . .	28
3.3.3	Hole Transport . . . . .	33
3.4	Aluminum Nitride . . . . .	33
3.5	Ternary Alloys . . . . .	35
<b>4</b>	<b>Physical Models</b>	<b>37</b>
4.1	Semiconductor Equations . . . . .	37

4.1.1	Maxwell's Equations . . . . .	37
4.1.2	Poisson Equation . . . . .	38
4.1.3	Continuity Equations . . . . .	38
4.1.4	The Drift-Diffusion Transport Model . . . . .	39
4.1.5	The Hydrodynamic Transport Model . . . . .	39
4.1.6	The Lattice Heat Flow Equation . . . . .	40
4.1.7	Insulator Equations . . . . .	41
4.1.8	Boundary Conditions . . . . .	41
4.2	Lattice and Thermal Properties . . . . .	47
4.2.1	Permittivity . . . . .	47
4.2.2	Mass Density . . . . .	48
4.2.3	Thermal Conductivity . . . . .	48
4.2.4	Specific Heat . . . . .	50
4.3	Band Structure . . . . .	52
4.3.1	Band Gap Energy . . . . .	54
4.3.2	Band Gap Energy Offset . . . . .	55
4.4	Carrier Mobility . . . . .	56
4.4.1	Low-Field Mobility . . . . .	57
4.4.2	High-Field Mobility for DD Equations . . . . .	62
4.4.3	High-Field Mobility for HD Equations . . . . .	65
4.4.4	Energy Relaxation Times . . . . .	67
4.5	Spontaneous and Piezoelectric Polarization . . . . .	69
4.6	AC Simulation: Equivalent Circuits and Parameter Extraction . . . . .	71
<b>5</b>	<b>Simulation Studies</b>	<b>75</b>
5.1	Depletion-Mode HEMTs . . . . .	76
5.1.1	AlGaN/GaN Devices . . . . .	76
5.1.2	High Temperature Simulations . . . . .	84
5.1.3	Transconductance Study . . . . .	92
5.1.4	Optimization Techniques . . . . .	98
5.1.5	InAlN/GaN Devices . . . . .	104

## CONTENTS

---

5.2	Enhancement-Mode HEMTs . . . . .	105
5.2.1	Recessed Gate . . . . .	108
5.2.2	InGaN Cap . . . . .	111
5.2.3	Comparison Gate Recess versus InGaN Cap Layer . . . . .	116
<b>6</b>	<b>Conclusion and Outlook</b>	<b>121</b>
	<b>Bibliography</b>	<b>123</b>
	<b>Own Publications</b>	<b>153</b>
	<b>Curriculum Vitae</b>	<b>155</b>

---

# List of Abbreviations and Acronyms

---

BTE	...	<i>Boltzmann's</i> transport equation
CMOS	...	Complementary MOS
DD	...	Drift-Diffusion
ET	...	Energy-Transport
HD	...	Hydrodynamic
MC	...	Monte Carlo
TCAD	...	Technology Computer-Aided Design
HEMT	...	High Electron Mobility Transistor
DH-HEMT	...	Double Heterojunction HEMT
E-Mode	...	Enhancement-Mode
D-Mode	...	Depletion-Mode
2DEG	...	Two-Dimensional Electron Gas
HBT	...	Heterojunction Bipolar Transistor
AC	...	Alternating Current
DC	...	Direct Current
PA	...	Power Amplifier
RF	...	Radio Frequency
PAE	...	Power Added Efficiency
LED	...	Light Emitting Diode
MMIC	...	Monolithic Microwave Integrated Circuit
LTE	...	Long Term Evolution
3G	...	Third Generation Mobile Communications
WiMAX	...	Worldwide Interoperability for Microwave Access
FP	...	Field-Plate
SP	...	Shield-Plate
NDM	...	Negative Differential Mobility
SEM	...	Scanning Electron Microscopy





---

# List of Symbols

---

## Notation

$x$	Scalar
$\mathbf{x}$	Vector
$\mathbf{A}$	Matrix
$A_{ij}$	Elements of the matrix $\mathbf{A}$
$\partial_t(\cdot)$	Partial derivative with respect to $t$
$\nabla$	Nabla operator
$\nabla x$	Gradient of $x$
$\nabla \cdot \mathbf{x}$	Divergence of $\mathbf{x}$

## Physical Quantities

Symbol	Description
$\epsilon$	Dielectric permittivity
$\epsilon_s$	Relative low frequency dielectric permittivity
$\epsilon_\infty$	Relative high frequency dielectric permittivity
$\mathcal{E}$	Energy
$\mathcal{E}_0$	Reference energy
$\mathcal{E}_c$	Conduction band edge energy
$\Delta\mathcal{E}_c$	Conduction band edge energy difference
$\mathcal{E}_f$	<i>Fermi</i> energy
$\mathcal{E}_g$	Band gap energy
$\mathcal{E}_v$	Valence band edge energy
$\Delta\mathcal{E}_v$	Valence band edge energy difference
$\kappa$	Thermal conductivity
$\kappa_L$	Lattice contribution to thermal conductivity
$\kappa_n$	Electron contribution to thermal conductivity
$\kappa_p$	Hole contribution to thermal conductivity
$\mu_\nu$	Mobility of carrier type $\nu$
$\mu_n$	Electron mobility
$\mu_p$	Hole mobility
$\mu_\nu^L$	mobility due to lattice scattering
$\mu_\nu^{LI}$	mobility due to lattice and impurity scattering
$\mu_\nu^{LIF}$	mobility including lattice, impurity, and high field reduction
$\mu_\nu^{LIT}$	mobility including lattice, impurity, and high temperature reduction
$C_{\text{net}}$	Net concentration
$\sigma$	Electric conductivity
$\tau_{\epsilon,n}$	Electron energy relaxation time
$\tau_{\epsilon,p}$	Hole energy relaxation time
$\varphi$	Electrostatic potential
$\mathbf{B}$	Magnetic field vector
$c_L$	Lattice heat capacity
$c_n$	Heat capacity of the electron subsystem
$c_p$	Heat capacity of the hole subsystem
$\mathbf{F}$	Force vector
$G$	Carrier generation rate
$H$	Heat generation term
$\mathbf{J}$	Current density

---

$m^*$	Density of states effective mass
$M_{c,v}$	Valley multiplicity
$n$	Electron concentration
$n_i$	Intrinsic carrier concentration
$N_A$	Concentration of acceptors
$N_c$	Effective density of states in the conduction band
$N_D$	Concentration of donors
$N_{\text{tot}}$	Total dopant concentration
$N_v$	Effective density of states in the valence band
$p$	Hole concentration
$Q$	Heat flow
$R$	Carrier recombination rate
$R_{\text{th}}$	Thermal resistance
$t$	Time
$T_v$	Carrier temperature
$T_L$	Lattice temperature
$T_n$	Electron temperature
$T_p$	Hole temperature
$I$	Current
$V$	Voltage
$V_C$	Contact voltage
$v$	Velocity
$v_s$	Average sound velocity
$v_{\text{st}}$	Transversal sound velocity
$v_{\text{sl}}$	Longitudinal sound velocity

## Fundamental Constants

$h$	<i>Planck's constant</i>	$6.6260755 \times 10^{-34} \text{ J s}$
$\hbar$	Reduced <i>Planck's constant</i>	$h/(2\pi)$
$k_B$	<i>Boltzmann's constant</i>	$1.3806503 \times 10^{-23} \text{ JK}^{-1}$
$q$	Elementary charge	$1.6021892 \times 10^{-19} \text{ C}$
$m_0^*$	Electron rest mass	$9.1093897 \times 10^{-31} \text{ kg}$
$\epsilon_0$	Vacuum permittivity	$8.8541878 \times 10^{-12} \text{ Fm}^{-1}$



---

## List of Figures

---

2.1	Down link rate for mobile communication systems. . . . .	5
2.2	$g_m$ vs. $V_{th}$ of GaN HEMTs featuring different techniques. . . . .	8
2.3	Cut-off frequency of GaN HEMTs over time. . . . .	10
2.4	Cut-off frequency $\times$ gate length of GaN HEMTs. . . . .	10
2.5	Power density vs. frequency of GaN HEMTs. . . . .	11
2.6	Breakdown voltage $V_{BR}$ of GaN HEMTs over time. . . . .	11
2.7	Cut-off frequency $\times$ breakdown voltage of GaN HEMTs. . . . .	12
2.8	Cut-off frequency of GaAs mHEMTs over time. . . . .	14
2.9	Current gain (measured and simulated) of GaN HBTs over time. . . . .	16
3.1	Low-field electron mobility as a function of carrier concentration in GaN: Comparison of the MC simulation results and experimental data. . . . .	24
3.2	Low-field electron mobility as a function of lattice temperature in GaN at carrier concentration of $10^{17} \text{ cm}^{-3}$ . . . . .	24
3.3	Electron drift velocity versus electric field in wurtzite GaN: Comparison of MC simulation results and experimental data I. . . . .	25
3.4	Electron drift velocity versus electric field in wurtzite GaN: Comparison of MC simulation results and experimental data II. . . . .	25
3.5	Low-field hole mobility as a function of carrier concentration in GaN. . . . .	27
3.6	Low-field hole mobility as a function of lattice temperature. . . . .	27
3.7	Hole drift velocity versus electric field. . . . .	28
3.8	Low-field electron mobility as a function of carrier concentration in InN: Comparison of the MC simulation results and experimental data. . . . .	30

---

## LIST OF FIGURES

---

3.9	Illustration of the scattering rates in our simulation for wurtzite InN as a function of carrier concentration at 300 K. . . . .	31
3.10	Low-field electron mobility as a function of carrier concentration in InN: Comparison of the MC simulation results with different setups. . . . .	31
3.11	Drift velocity versus electric field in wurtzite InN: Comparison of MC simulation results. . . . .	32
3.12	Drift velocity versus electric field in wurtzite InN: MC simulation results with different parameter setups. . . . .	32
3.13	Illustration of the scattering rates in our simulation for wurtzite InN as a function of electric field. . . . .	33
3.14	Drift velocity versus electric field in wurtzite AlN: Comparison of MC simulation results. . . . .	35
4.1	GaN thermal conductivity as a function of temperature. . . . .	49
4.2	AlN thermal conductivity as a function of temperature. . . . .	49
4.3	AlGaIn thermal conductivity as a function of Al content. . . . .	51
4.4	InGaIn thermal conductivity as a function of In content. . . . .	51
4.5	InAlN thermal conductivity as a function of In content. . . . .	52
4.6	GaN specific heat as a function of lattice temperature. . . . .	53
4.7	InN specific heat as a function of lattice temperature. . . . .	53
4.8	Material composition dependence of the band gap of $\text{In}_x\text{Al}_{1-x}\text{N}$ . . . . .	55
4.9	Band alignment of InN, GaN, and AlN at room temperature. . . . .	56
4.10	Electron mobility versus concentration in GaN. . . . .	58
4.11	Electron mobility versus concentration in InN. . . . .	58
4.12	Electron mobility versus concentration in AlN. . . . .	59
4.13	Hole mobility versus concentration in GaN. . . . .	59
4.14	Electron mobility versus temperature in bulk GaN. . . . .	61
4.15	Electron mobility versus temperature in 2DEG GaN. . . . .	61
4.16	GaN electron drift velocity versus electric field: simulations with different mobility models compared to MC simulation results and experimental data. . . . .	63
4.17	AlN electron drift velocity versus electric field: simulations with different mobility models compared to MC simulation results. . . . .	63
4.18	InN electron drift velocity versus electric field: simulations with different mobility models compared to MC simulation results. . . . .	64

4.19	GaN valley occupancy as a function of the electric field. . . . .	68
4.20	Piezoelectric and spontaneous polarization-induced charge $\sigma/q(P_{SP} + P_{PE})$ . . . . .	70
4.21	Voltages and currents at a two-port network. . . . .	71
4.22	Incident and reflected waves at a two-port network. . . . .	72
4.23	Equivalent circuit for a HEMT. . . . .	73
4.24	Extrinsic parasitic elements. . . . .	73
5.1	SEM image of two HEMTs (IAF Freiburg). . . . .	76
5.2	Schematic layer structure. . . . .	78
5.3	Comparison of measured and simulated transfer characteristics (Device A). . . . .	80
5.4	Comparison of measured and simulated output characteristics (Device A). . . . .	80
5.5	Comparison of measured and simulated transfer characteristics (Device B). . . . .	81
5.6	Comparison of measured and simulated output characteristics (Device B). . . . .	81
5.7	Comparison of measured and simulated transfer characteristics (Device C). . . . .	82
5.8	Comparison of measured and simulated output characteristics (Device C). . . . .	82
5.9	Comparison of measured and simulated cut-off frequency (Device C). . . . .	83
5.10	Comparison of measured and simulated S-parameters (Device C). . . . .	83
5.11	Simulated electron temperature and velocity along the channel. . . . .	84
5.12	Calibrated transfer characteristics (lines) versus experimental data (symbols) for $L_g = 0.25 \mu\text{m}$ HEMT. . . . .	86
5.13	Calibrated output characteristics versus experimental (symbols) data for $L_g = 0.25 \mu\text{m}$ HEMT at 425 K. Dot-dashed lines - without self-heating, solid lines - with self-heating. . . . .	86
5.14	Lattice temperature in the calibration device, $V_{gs} = 2 \text{ V}$ , $V_{ds} = 20 \text{ V}$ . . . . .	87
5.15	Predicted transfer characteristics (lines) compared to measured data (symbols) for $L_g = 0.5 \mu\text{m}$ HEMT at different temperatures. . . . .	87
5.16	Predicted output characteristics versus experimental data for $L_g = 0.5 \mu\text{m}$ HEMT at 425 K. . . . .	88
5.17	Current gain $ h_{21} $ for $L_g = 0.25 \mu\text{m}$ HEMT, experimental data (solid lines) versus simulation (dashed lines). . . . .	88
5.18	Simulated cut-off frequency $f_t$ (lines) compared to measurements (symbols) for $L_g = 0.25 \mu\text{m}$ HEMT. . . . .	89
5.19	S-parameters for the $L_g = 0.25 \mu\text{m}$ device at 300 K. . . . .	90
5.20	S-parameters for the $L_g = 0.25 \mu\text{m}$ device at 425 K. . . . .	90

## LIST OF FIGURES

---

5.21	S-parameters for the $L_g = 0.5 \mu\text{m}$ device at 300 K. . . . .	91
5.22	S-parameters for the $L_g = 0.5 \mu\text{m}$ device at 425 K. . . . .	91
5.23	Simulated maximum $I_D$ ( $V_{ds} = 7 \text{ V}$ ) as a function of ambient temperature normalized to 300 K values. . . . .	92
5.24	Simulated maximum $f_t$ ( $V_{ds} = 7 \text{ V}$ ) as a function of ambient temperature normalized to 300 K values. . . . .	93
5.25	Drain current and transconductance at $V_{ds} = 7 \text{ V}$ : measured data compared to simulation. . . . .	94
5.26	Electron velocity along the channel [cm/s]. . . . .	94
5.27	Electric field along the channel [V/cm]. . . . .	95
5.28	$\Delta v_n$ (scaled) along the channel [ $\text{cm}^{-2}\text{s}^{-1}$ ]. . . . .	96
5.29	Transconductance $g_m$ versus gate voltage $V_{GS}$ for five devices with different source-gate length ( $V_{ds} = 7 \text{ V}$ ). . . . .	97
5.30	Change of electron velocity $\Delta v$ along the channel at $V_{gs} = -1 \text{ V}$ and $1 \text{ V}$ for two devices with different $L_{SG}$ . . . . .	97
5.31	A schematic layer structure of single heterojunction AlGaIn/GaN HEMTs with field plates. . . . .	99
5.32	Transfer characteristics for different polarization charge densities at the AlGaIn/GaN heterojunctions. . . . .	99
5.33	Comparison of measured (solid lines) and simulated (dashed lines) output characteristics of $L_g=L_{FP}=600 \text{ nm}$ HEMTs. . . . .	100
5.34	Comparison of measured (symbols) and simulated (lines) transfer characteristics of HEMTs with and without field plate. . . . .	100
5.35	Simulated electric field along the channel of $L_g = 600 \text{ nm}$ HEMTs with and without field plate for $V_{gs} = 0 \text{ V}$ and $V_{ds} = 7 \text{ V}$ . . . . .	101
5.36	Simulated electric field along the channel for various field plate lengths $L_{FP}$ ( $L_g = 600 \text{ nm}$ ). . . . .	102
5.37	Simulated electric field along the channel for various gate lengths ( $L_{FP}=L_g$ ). . . . .	102
5.38	Simulated electric field along the channel for various field plate lengths $L_{FP}$ ( $L_g = 300 \text{ nm}$ ). . . . .	103
5.39	Simulated electric field along the channel for various field plate lengths $L_{FP}$ ( $L_g = 150 \text{ nm}$ ). . . . .	103
5.40	Schematic layer structure of the investigated device. . . . .	104
5.41	Band alignment of the heterointerface. . . . .	105
5.42	Transfer characteristics for different values of the polarization charge density at the InAlN/GaN interface and $-10^{13} \text{ cm}^{-2}$ at the InAlN top surface ( $V_{ds} = 8 \text{ V}$ ). . . . .	106



5.43	Transfer characteristics for different values of the total charges (polarization and traps) at the InAlN top surface and $3.3 \times 10^{13} \text{ cm}^{-2}$ at the InAlN/GaN interface ( $V_{ds} = 8 \text{ V}$ ).	106
5.44	Comparison of simulated transfer characteristics for different values of the thermal resistance and experimental data ( $V_{ds} = 8 \text{ V}$ ).	107
5.45	Comparison of simulated output characteristics and experimental data.	107
5.46	Schematic layer structure of the recessed device.	108
5.47	Transfer characteristics at $V_{ds} = 7 \text{ V}$ : lines - simulation, symbols - experimental data.	109
5.48	Transconductance $g_m$ at $V_{ds} = 7 \text{ V}$ : lines - simulation, symbols - experimental data.	109
5.49	Comparison of DHEMT output characteristics, $V_{GS}$ stepping $0.5 \text{ V}$ .	110
5.50	Comparison of EHEMT output characteristics, $V_{GS}$ stepping $0.5 \text{ V}$ .	110
5.51	Comparison of the cut-off frequency $f_t$ : symbols - simulation, lines - experimental data.	111
5.52	Simulated transfer characteristics for devices with different barrier thickness $t_{bar}$ under the gate.	112
5.53	Simulated transconductance for devices with different barrier thickness $t_{bar}$ under the gate.	112
5.54	Simulated cut-off frequency for devices with different barrier thickness $t_{bar}$ under the gate.	113
5.55	Simulated gate-source capacitance for devices with different barrier thickness $t_{bar}$ under the gate.	113
5.56	Schematic layer structure of the three HEMTs under investigation.	114
5.57	Comparison of simulated and measured transfer characteristics for the three devices.	115
5.58	Energy band diagrams of a HEMT with (dot-dashed line) and without (solid line) InGaN layer.	116
5.59	Simulated $DC$ $g_m$ for the three devices.	117
5.60	Output characteristics of a HEMT with non-recessed InGaN cap layer.	117
5.61	Comparison of the measured (symbols) and simulated (lines) transfer characteristics at $V_{ds} = 5 \text{ V}$ .	118
5.62	Simulated transfer characteristics at $V_{ds} = 5 \text{ V}$ for HEMTs with different gate recess depths.	118
5.63	Comparison of the measured (symbols) and simulated (lines) $DC$ transconductance $g_m$ at $V_{ds} = 5 \text{ V}$ .	119



---

# List of Tables

---

2.1	Device/material features and merits of GaN HEMTs. . . . .	5
2.2	Comparison of different techniques for E-mode structures. . . . .	8
2.3	Companies offering substrates and GaN-based products. . . . .	13
3.1	Summary of material parameters of wurtzite GaN for Monte Carlo simulation. . . . .	21
3.2	Summary of elastic constants of GaN and the resulting longitudinal and transverse elastic constants and sound velocities. . . . .	22
3.3	Summary of piezoelectric coefficients of GaN for Monte Carlo simulation of piezoelectric scattering. . . . .	22
3.4	Summary of material parameters of wurtzite InN for MC simulation. . . . .	29
3.5	Summary of elastic constants of InN and the resulting longitudinal and transverse elastic constants and sound velocities. . . . .	29
3.6	Summary of piezoelectric coefficients of InN for MC simulation of piezoelectric scattering. . . . .	30
3.7	Summary of material parameters of wurtzite AlN for Monte Carlo simulation. . . . .	34
3.8	Summary of elastic constants of AlN and the resulting longitudinal and transverse elastic constants and sound velocities. . . . .	34
3.9	Summary of piezoelectric coefficients of AlN for Monte Carlo simulation of piezoelectric scattering. . . . .	35
4.1	Schottky barrier heights of common contacts. . . . .	45
4.2	Model parameters for the static permittivity. . . . .	47
4.3	Model parameters for the mass density [g/cm <sup>3</sup> ]. . . . .	48

## LIST OF TABLES

---

4.4	Model parameters for the thermal conductivity. . . . .	50
4.5	Parameter values for the specific heat model. . . . .	52
4.6	Summary of band structure model parameters. . . . .	54
4.7	Parameter values for the low-field mobility. . . . .	60
4.8	Parameters for DD high-field electron mobility Model A. . . . .	64
4.9	Parameters for DD high-field electron mobility Model B. . . . .	66
4.10	Parameters for HD high-field electron mobility Model A. . . . .	66
4.11	Parameters for the energy relaxation times for HD high-field electron mobility Model B [ps]. . . . .	68
4.12	Parameters for the energy relaxation time model [ps]. . . . .	68
4.13	Spontaneous polarization parameters [ $C/m^2$ ]. . . . .	69
4.14	Piezoelectric polarization parameters. . . . .	70
4.15	Applied parasitic elements for GaN HEMT simulation. . . . .	74
5.1	Charge density [ $cm^{-2}$ ] for three AlGaIn/GaN HEMTs. . . . .	77
5.2	Layer properties for three AlGaIn/GaN HEMTs. . . . .	79
5.3	Summary of values of interface charge density [ $cm^{-2}$ ] for the three structures. . .	115

# Chapter 1

---

## Introduction

---

SOME refer to the age we are living in, as the Information Age. It is the age of global information exchange and instant access to knowledge, the age of computers, mobile telephones, email, and on-line social networking services. The technological revolution has provided us with enough computational power to satisfy one's every day needs at acceptable costs. Even handheld devices are able to handle computationally intensive tasks, such as complex encoding algorithms, for instance.

However, one should evaluate technological evolution not only by the ability to process information, but also by the ability to transfer it. The progress in the latter has been also nothing short of impressive: while the first transatlantic telephone cable was able to carry only 36 telephone connections some 55 years ago, a single mobile telephone can achieve the hundred-fold bandwidth nowadays. Both the cable-bound and wireless telecommunications have experienced a rapid development. Due to the nature of the transport medium there are different hurdles which apply to the two techniques. For cable-bound communications one of the major obstacles is the lack of broadband cable networks (optical cables still are not an established replacement for classic telephone lines in the last-mile), while the technology has been available for some years already.

Wireless communications on the other hand face still some technology challenges, despite the steady development in the last decade. One of the key technologies, that made this evolution possible was the Gallium Nitride (GaN) based High Electron Mobility Transistor (HEMT). It offers a high current density at radio frequencies that, combined with its high breakdown voltage, makes it an excellent choice for high-power amplifiers. While this was the application, which granted the HEMT technology entry into the mass market, other emerging areas include automotive power inverters for hybrid vehicles, for instance. An overview of the different present and future application areas is included in Chapter 2. It is followed by a review of the current state-of-the-art and an overview of device simulation tools able to deal with the specifics of HEMTs.

A profound knowledge of the material system is a key requirement for proper device modeling. Chapter 3 summarizes some of the properties of the III-V materials used in HEMT structures, with focus on the carrier transport. It features an extensive study of available experimental and simulation data compared against own Monte Carlo simulations.

Chapter 4 introduces the basics of device simulation. Relevant models and model parameters are discussed, with focus on the carrier transport models. Subsequently, different simulation studies are presented in Chapter 5. These include optimization for various applications, high-temperature performance analysis, and transconductance collapse investigation of normally-on devices. Further, several techniques for normally-off devices are studied and compared.

The last chapter provides a short summary and points out several possible directions for future work.

## Chapter 2

---

# State-of-the-Art

---

FOLLOWING a brief review of the history of HEMTs different application areas are presented. Those are split in three major groups: *RF* communication systems, automotive electronics, and sensors. The advantages of complementary normally-off structures is discussed and several approaches to achieve such operation are described. Reports of different research groups during the last decade are summarized also in respect of currently available commercial products. HEMT structures based on other materials than GaN are shortly discussed followed by a brief summary of reports on GaN-based HBTs. The chapter ends with a review of various simulation software packages and an introduction of our device simulator MINIMOS-NT.

### 2.1 History of HEMTs

As many other discoveries, the idea for a HEMT structure was a product of a research with different purposes and there were several factors superimposed. The late 70s saw the evolution of the molecular beam epitaxy growth technique and modulation doping together with a vivid interest in the behavior of quantum well structures [1] (the latter peaking in the work of Klitzing, Laughlin, Stomer, and Tsui).

At this time T. Mimura and his colleagues at Fujitsu were working on GaAs MESFETs. Facing problems with a high-density of the surface states near the interface, they decided to use a modulation-doped heterojunction superlattice and were able to produce depletion type MOSFETs [2]. While those structures were still plagued by several issues, the idea to control the electrons in the superlattice occurred to him. He achieved this by introducing a *Schottky* gate contact over a single heterojunction. Thus, the AlGaAs/GaAs HEMT was born [3]. Subsequently the first HEMT based integrated circuit was reported [4]. Alongside Fujitsu a number of other research facilities joined on the further development of the new structures: Bell Labs, Thomson CSF, Honeywell, IBM [5]. In order to counter different problems, several designs were proposed: AlGaAs/GaAs HEMTs, AlGaAs/InGaAs pseudomorphic HEMTs (pHEMTs), AlInAs/ InGaAs/InP HEMTs (ordered by increasing  $f_t$ ) [6]. However, until the end of the decade HEMTs mainly found military and space applications [7]. Only in the 90s the technology entered the consumer market in satellite receivers and emerging mobile phone systems.

In the beginning of the last decade new methods for deposition of GaN on sapphire by MOCVD were developed. Thus, the production of AlGaIn/GaN-based HEMTs was possible [8]. GaN has a wide band gap which brings the advantages of higher breakdown voltages and higher operational temperature. Due to the large lattice mismatch between AlN and GaN a strain in the AlGaIn layer is induced, which generates a piezoelectric field. Together with the large conduction band offset and the spontaneous polarization this leads to very high values for the electron sheet charge density [9]. This large potential of AlGaIn/GaN structures (and the indirect advantage of excellent thermal conductivity of the sapphire substrates) was realized very soon and the research focus partially shifted from AlGaAs/GaAs to AlGaIn/GaN devices.

In the course of further development and optimization various techniques were adopted. An approach previously used in high-voltage p-n junctions [10], the field-plate electrode, significantly improved device performance by reducing the peak values of the electric field in the device. Thus, the breakdown voltage could be further increased. This technique was further refined to T-shaped [11] and subsequently Y-shaped gate electrodes [12]. Another step in optimization of the structure is the addition of a thin AlN barrier between the GaN channel and the AlGaIn layer. It increases the conduction band offset and the two-dimensional electron gas (2DEG) density and decreases the alloy disorder scattering, thereby increasing the mobility [13]. An additional option to enhance the electron gas transport properties is the double-heterojunction structure [14]. The InGaIn layer under the channel introduces a negative polarization charge at the interface, and thereby improves the carrier confinement in the channel.

While the depletion mode (D-mode) technology has been significantly improved, no comparable progress on the enhancement counterparts can be noted. However, such devices have advantages in certain applications and are therefore getting in the focus of research activities in the recent years. Several groups have proposed interesting approaches. Devices featuring very thin AlGaIn layers [15] and Fluoride-based plasma treatment [16] have been proposed, however certain stability concerns remain. A very promising method is the recess gate structure reported by Kumar *et al.* [17]. Also recently, excellent results have been achieved with InGaIn-cap devices [18].

## 2.2 Applications for GaN HEMTs

The material and device properties make AlGaIn/GaN HEMT structures suitable for a wide range of applications. In this section the major application areas are listed, without thoroughly exploring all possible options. A detailed discussion can be found in [19].

### 2.2.1 RF Applications: Broadband Communication

In the last two decades wireless mobile technologies have matured from enthusiast and business niche-market to a dynamical mass-market industry. Starting with the first analog networks in the 80s the first fourth generation networks are already available in 2010. Transmission speeds are rising accordingly (Fig. 2.1). The limiting factor for all systems is the microwave power amplifier (PA) performance. Both on subscriber and base station side it has an impact on power consumption, volume, and weight. While weight is not substantial in the base station design, low efficiency dramatically increases power consumption and thereby the complexity of the required cooling equipment. Thus development is focused on high efficiency. GaN power



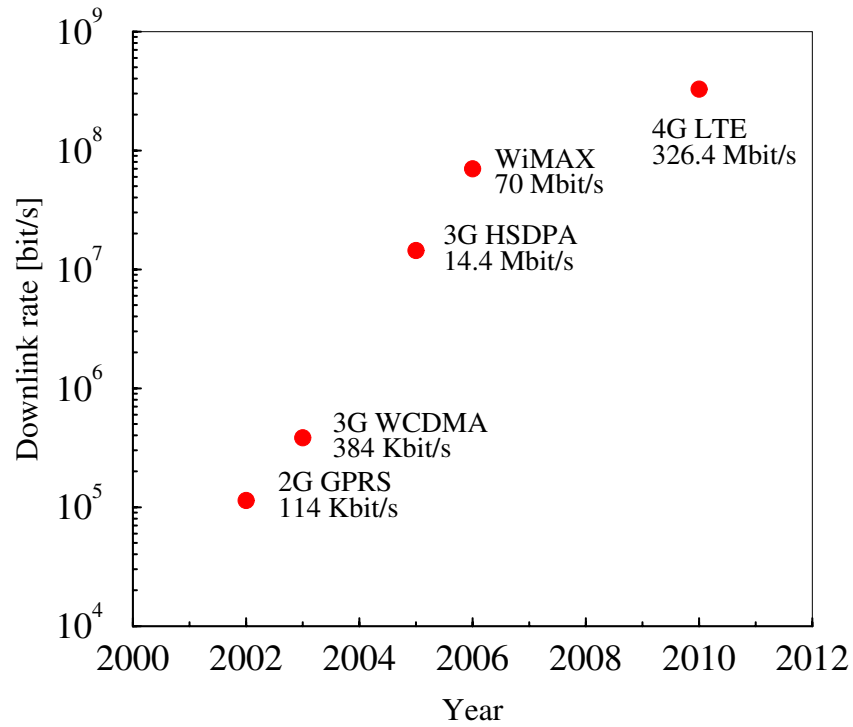


**Figure 2.1:** Down link rate for mobile communication systems.

amplifiers with characteristics surpassing those of GaAs have been demonstrated [20] and prove that the material system and the device structure are an excellent choice for *RF* PAs (Table 2.1). The frequency range of the reported amplifiers extends from the S-band [21], [22], [23] and C-band [24], [25] up to the Ka-band. Devices for the X-band [26] - Ka-band [27], [28] range have been demonstrated.

**Table 2.1:** Device/material features and merits of GaN HEMTs.

device/material features	merits for <i>RF</i> PA	merits for automotive applications
high breakdown	high efficiency	high efficiency
	high-voltage operation	high-voltage operation
wide band gap	high-temperature operation	high-temperature operation
high current density	high power density	high power density
high electron velocity	high frequency	
HEMT topology	high linearity	

### 2.2.2 *RF* Applications: Radar Components

**Military Applications** Based on the platform constraints three main application areas for GaN-based HEMTs are distinguished (depending on the application the available power and/or volume are limited) [29]: ground-based applications, airborne applications, and maritime applications. Phased array systems for these applications are characterized by their power-aperture product and high reliability. The frequency range includes the S-band, C-band, and X-band [30], with ultra-broadband applications reaching into the Ku-band [31].

**Space Applications** Phased array systems are also used for remote sensing and earth observation for civilian and scientific purposes. Several such programs have been started [32]. Due to the immense costs of delivering cargo in near-earth orbits, reduced volume and weight, as well as low power consumption are the main goals. The high radiation levels and extreme temperatures must also be considered.

### 2.2.3 Automotive Applications

Hybrid electric vehicles and fuel cell hybrid vehicles are entering the market in the last couple of years. Those need high electric power inverters [33]. In order to increase efficiency high voltage boosters are adopted. Therefore, high breakdown voltage as well as low resistance and high temperature operation are key requirements.

### 2.2.4 Sensors

Chemical sensors for liquids [34] and gases [35] were demonstrated recently. High temperature greatly widens the application field for gas sensors and also reduces the response times [36]. The temperature stability of GaN devices is therefore a distinguishable merit. Pressure sensors, sensitive to high and low pressures, require different techniques. For high pressure applications planar devices are used [37], while for low pressure applications membranes are required [38].

## 2.3 Normally-Off HEMT

The properties of GaN and AlN and their heterostructures have encouraged the research of AlGaIn/GaN based transistors for various applications in the last decade. Consequently, outstanding results have been reported for the depletion mode (D-mode) high electron mobility transistors. However, for several applications enhancement mode (E-mode) devices are essential.

In analog electronics E-mode devices supersede the negative voltage supply and also assure a safe state in case of power loss. In digital electronics, they allow complementary FET-based logic [39]. Normally-off operation is also a requirement for automotive applications (e.g. hybrid vehicles) [33]. Despite the interest in E-mode operation, the excellent results as in D-mode devices remain to be demonstrated.

### 2.3.1 Gate Recess and Surface Treatment

The first E-mode transistor, reported back in 1996 by Khan *et al.* [15], was achieved by using thin AlGa<sub>N</sub> barriers. Endoh *et al.* [40] relied on thin AlGa<sub>N</sub> layer too. However, the device worked only in a very narrow drain-source voltage  $V_{DS}$  region. Liu *et al.* [41] could overcome this issue by substituting AlGa<sub>N</sub> for AlInGa<sub>N</sub> and also reach higher threshold voltage  $V_{th}$ , however the maximum drain current  $I_D$  and transconductance  $g_m$  decreased.

A similar approach was adopted by other groups [42], [43], [17], [44], who introduced Induced Coupled Plasma Reactive Ion Etching (ICP-RIE) in order to etch the AlGa<sub>N</sub> barrier. This technique was also used by Okite *et al.* [45] and Lanford *et al.* [46]. However, dry etching has low selectivity and results in a high concentration of defects and thus a high gate-leakage. In order to cure the damage, thermal annealing is required. Some of the metal stacks used for the gate contacts are incompatible with the high annealing temperatures. Therefore, the annealing has to be performed before the gate deposition. As the resist layer has to be removed, self-centered gate metal deposition is not possible. A second annealing step is required after the gate metal deposition in order to improve the Schottky barrier [47]. Cai *et al.* [16] demonstrated fluoride-based plasma treatment, which introduces fluoride ions in the barrier. Those raise the potential of the AlGa<sub>N</sub> barrier and the 2DEG channel. As no recess is required, damage to the AlGa<sub>N</sub> layer is avoided. This approach was further applied to double hetero-junction HEMTs (DH-HEMTs) [48] and used in combination with the gate recess technique [49]. All those approaches offer an optimization of the parameters ( $V_{th}$  and  $g_m$ ) of selected devices on the same wafer.

Very thin AlGa<sub>N</sub> barrier layers have also been demonstrated to significantly rise the threshold voltage [50], [51]. Devices fabricated using this technique are particularly well-suited for high-voltage applications due to the demonstrated high breakdown voltage.

### 2.3.2 Barrier and Capping Layers

Several approaches, relying on additional layers introduced under the gate, have also been proposed. The first was by Hu *et al.* [54], who suggested a pn-junction under the gate. Mizutani *et al.* [18] proposed an InGa<sub>N</sub> capping (cap) layer in order to raise the conduction band under the gate. Also Higashiwaki *et al.* [53] reported an AlN/GaN structure with a thin AlN layer, with positive  $V_{th}$ .

Fig. 2.2 shows the correlation between  $V_{th}$  and  $g_m$  achieved with the different techniques. During the years an overall significant improvement can be noted. The last results show that for the AlGa<sub>N</sub>/GaN system there is a certain limit which, while allowing for trade-off between  $V_{th}$  and  $g_m$ , has to be overcome. Table 2.2 gives a summary of the advantages and the drawbacks of the different approaches.

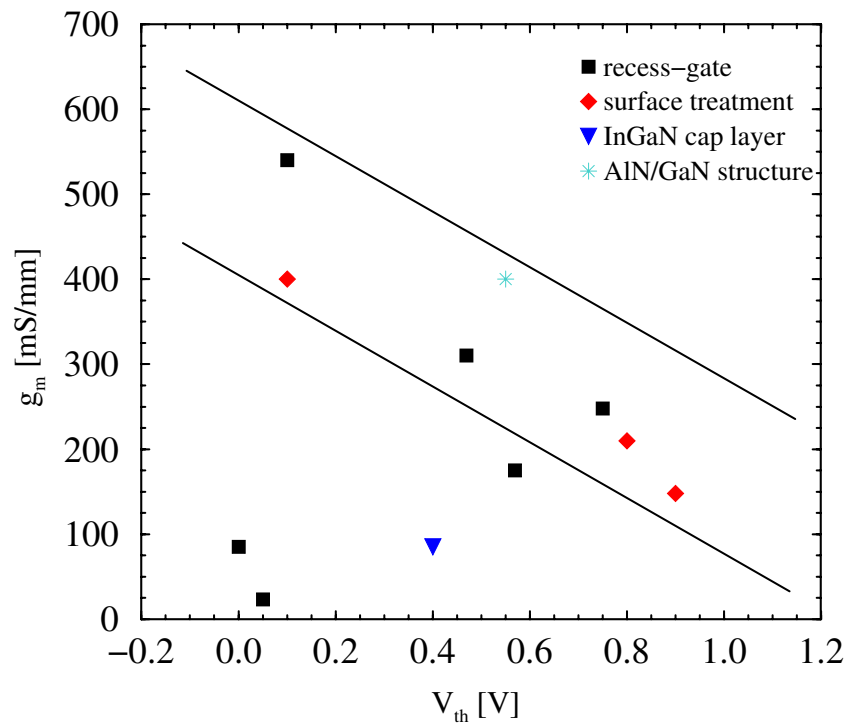


**Figure 2.2:**  $g_m$  vs.  $V_{th}$  of GaN HEMTs featuring different techniques.

**Table 2.2:** Comparison of different techniques for E-mode structures.

Technique	Advantages	Disadvantages	Reported by
gate recess	on-wafer	surface damage not self-centered	HRL [42], [43], UIUC [17], [46] Oki [45], UCSB [49]
surface treatment	low access resistance on-wafer	no 100% damage-recovery	HKU [16], [52], [48] UCSB [49]
InGaN cap	good $RF$ performance	low $g_m$ & $I_{dMAX}$	Univ. Nagoya [18]
AlN/GaN	good $DC$ performance	low 2DEG mobility	Fujitsu [53]
pn-junction gate	on-wafer (selective)	very low $I_D$ and $g_m$	USC [54]
thin barrier	low gate leakage	high $R_{on}$	Furukawa [50], Nichia [51]

## 2.4 GaN-Based HEMTs

### 2.4.1 Reports by Research Groups

The evolution of MBE growth technique and modulation doping together with a vivid interest in the behavior of quantum well structures in the late 70s made the demonstration of the first AlGaAs/GaAs HEMT by Mimura *et al.* [3] possible. The potential of the technology was quickly realized and several designs (AlGaAs/InGaAs PHEMT and AlInAs/InGaAs/InP HEMT) were proposed in order to counter various problems. The first AlGaN/GaN based HEMTs were demonstrated in the early 90s [8] after methods for deposition of GaN on sapphire by MOCVD were developed.

However, the main driving force for the continuous improvements in the material growth technology [55] were Nitride-based light-emitting diodes (LEDs). There is a strongly growing demand for the latter for home electronics but also lighting and back-lighting, where the market in 2010 amounts to over 10 billions USD. For comparison the market for GaN *RF* transistors in 2010 is only 100 millions USD.

The very high values for the electron sheet charge density were the reason for a shift of the research interest from AlGaAs/GaAs to AlGaN/GaN based devices. Consequently the characteristics of GaN based HEMTs have been improved steadily in the last decade. While the first HEMTs exhibited a cut-off frequency  $f_t$  and a maximum oscillation frequency  $f_{\max}$  of 11 GHz and 35 GHz ( $L_g=0.25 \mu\text{m}$ ) [56] later devices reached 50 GHz and 120 GHz, respectively, in 2002 [57]. Currently the highest reported  $f_t$  and  $f_{\max}$  values are 190 GHz and 240 GHz, respectively, for  $L_g = 60 \text{ nm}$  devices with high Al-composition and thin barrier layers [58]. Another notable achievement is reported by Shinohara *et al.*, who measured a cut-off frequency of 153 GHz of a DH-HEMT with  $L_g = 60 \text{ nm}$  [59], and also Chung *et al.*, who produced a device with the same gate length and a maximum frequency of 300 GHz [60]. However, such a performance is near the limit of the AlGaN/GaN technology, imposed by the limited polarization-induced electric fields and current collapse. Fig. 2.3 shows a steady increase of the measured  $f_t$  over the years, however such a illustration does not account only for the technology improvement, but also for the down-scaling of the gate lengths. This is avoided in Fig. 2.4, where the product  $f_t \times L_g$  is depicted. There is a clear limit of roughly  $20 \text{ GHz} \times \mu\text{m}$ , which was rarely exceeded. This value was also recently reached with AlGaN/GaN HEMTs [61]. First proposed by Kuzmik in 2001 [62], the InAlN/GaN interface possesses a higher polarization-induced sheet charge density as AlGaN/GaN. As the InAlN layer can be grown lattice-matched to GaN, possible strain relaxation problems are significantly reduced. Consequently, this potential was quickly realized and the focused research of such structures is yielding excellent results: e.g. cut-off frequencies of 144 GHz for a  $L_g = 100 \text{ nm}$  device [63].

Another optimization goal is the maximum power density (Fig. 2.5). The first HEMTs exhibited barely  $1.1 \text{ W/mm}$  at 2 GHz [64] (Fig. 2.5). Employing multiple field-plates the power density was raised up to  $40 \text{ W/mm}$  at 4 GHz [65]. By using internally matched amplifier technology the limits have been pushed up to  $550 \text{ W}$  at 3.5 GHz [66]. Because of the large band gap, GaN based HEMTs are also considered for high power operations.

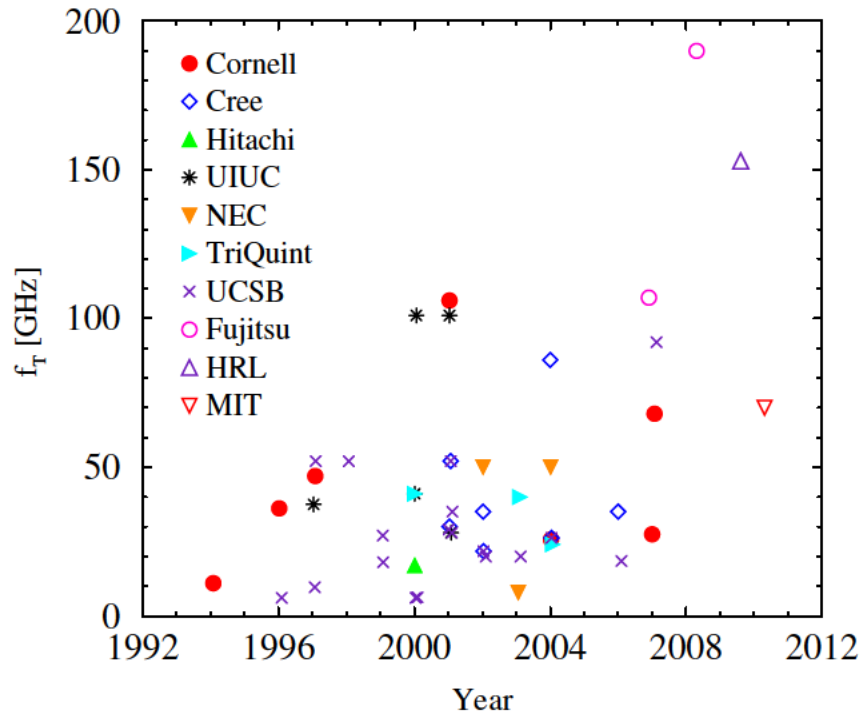


Figure 2.3: Cut-off frequency of GaN HEMTs over time.

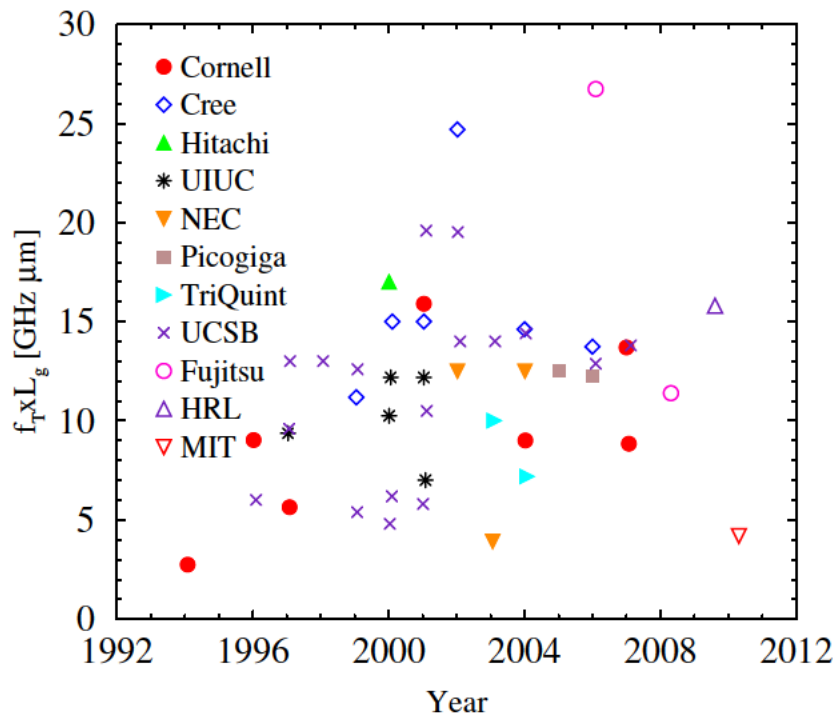


Figure 2.4: Cut-off frequency  $\times$  gate length of GaN HEMTs.

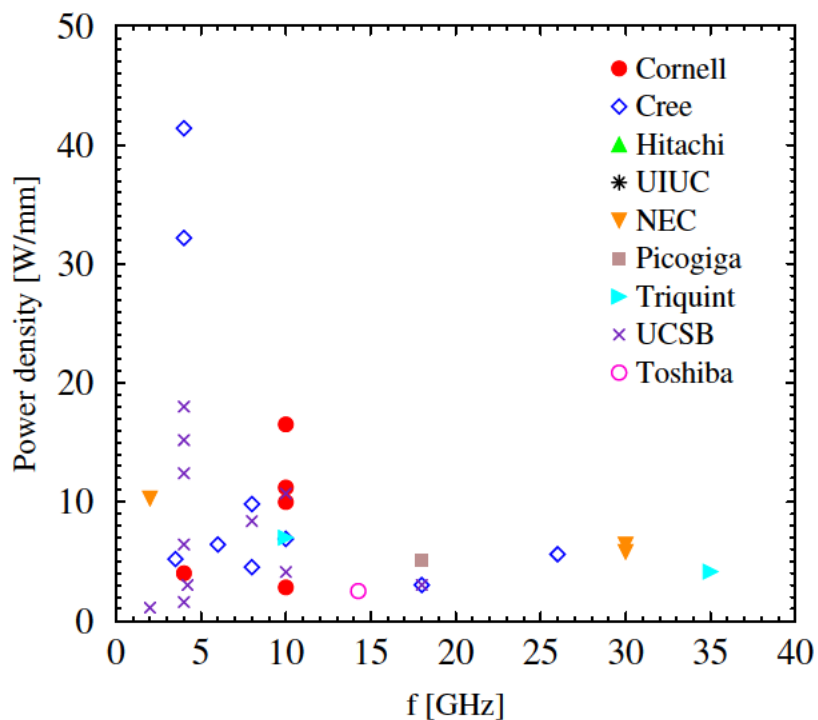
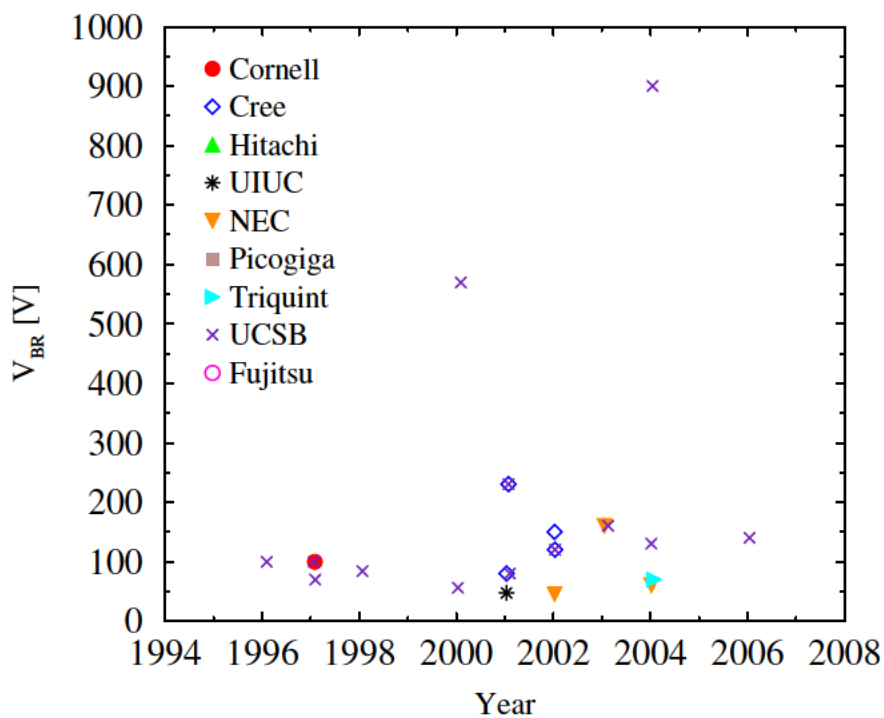
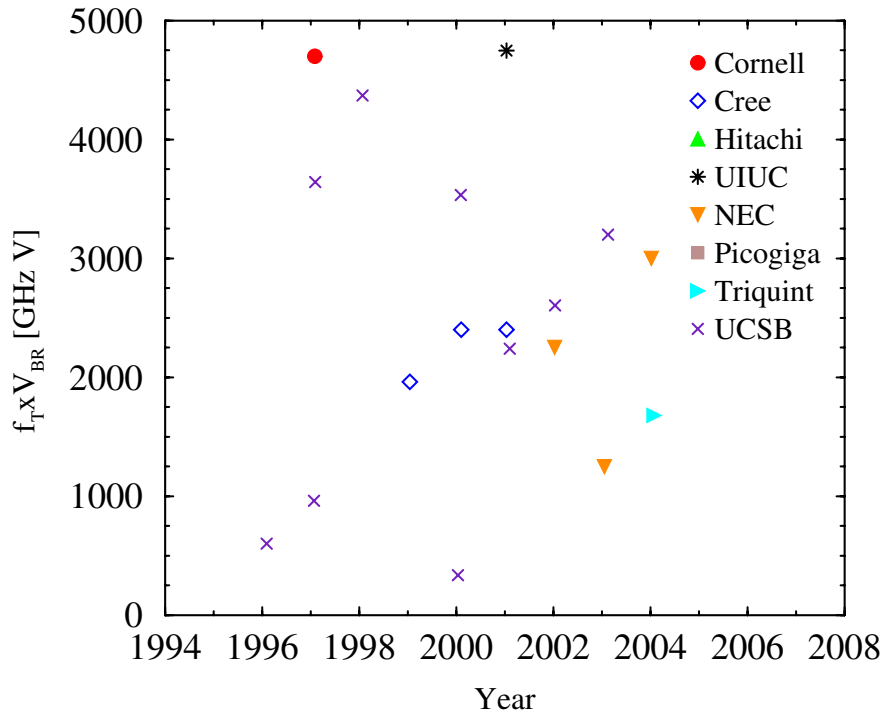


Figure 2.5: Power density vs. frequency of GaN HEMTs.

Figure 2.6: Breakdown voltage  $V_{BR}$  of GaN HEMTs over time.



**Figure 2.7:** Cut-off frequency  $\times$  breakdown voltage of GaN HEMTs.

Early samples demonstrated impressive breakdown voltages in the range of 230 V, but also poor subthreshold behavior [67]. Those issues were addressed and breakdown voltages  $V_{BR}=570$  V were reached by gate geometry optimization [68]. By using a “slant-field-plate” technology a  $V_{BR}=1900$  V could be achieved at the cost of drain current degradation [69]. Another way of increasing  $V_{BR}$  is by using a thick buffer layer, leading to a maximum value of  $V_{BR}>1800$  V [70]. While the breakdown voltage increases steadily over the years (Fig. 2.6), a more significant characteristic is the product  $f_t \times V_{BR}$ . Some of the achieved very high voltages are due to exceptionally large devices. The cut-off frequency of the latter is quite low, which translates in a low  $f_t \times V_{BR}$  (Fig. 2.7).

## 2.4.2 Commercially Available Products

The first commercially available GaN-based products were available in 2005/2006 by companies with a long experience with GaAs technology (e.g. Cree, Nitronex). In the following years several other companies also entered the market. Table 2.3 gives an overview of the major substrate suppliers and foundries. Most of the products are based on epitaxially grown material on SiC substrates, however, there are some on Silicon, which offers lower costs and good thermal conductivity. One of the companies, which developed a GaN on Si process technology, is Azzuro, however, the bulk of its production is targeted at LED applications. Only recently Azzuro started providing substrates for GaN power devices. Another company, offering GaN epitaxial layers grown on Si is Nitronex. It also produces *RF* power transistors. Only two companies offer MMICs based on GaN: one of them is Cree which has developed traveling wave amplifiers, two-



**Table 2.3:** Companies offering substrates and GaN-based products.

Company	Substrate	Device
Azzuro	GaN on Si	LEDs
Cree	GaN on SiC	220 W@4 GHz <i>RF</i> devices, MMICs
Eudyna	-	up to 3 GHz <i>RF</i> devices
Freescale	GaN on SiC	GaN-based HEMTs in research
Fujitsu	GaN on SiC	wireless equipment based on GaN HEMTs
Group4Labs	GaN on Diamond	-
IQE	GaN epiwafers	-
Nitronex	GaN on Si	up to 6 W@6 GHz <i>RF</i> devices
Picogiga	GaN on SiC	-
RFMD	-	up to 120 W power devices
Triquint	-	up to 25W power devices
Toshiba	-	65.4 W@14.5 GHz <i>RF</i> devices

stage amplifiers, and high efficiency, high gain devices for radio communications. It uses SiC substrates. The other company to offer power amplifiers is Toshiba. It introduced its first GaN-based amplifier in 2008. Nowadays amplifiers delivering 50 W in the Ku-band are commercially available.

One of the early players was Eudyna, which was a joint-venture of Fujitsu and Sumitomo Electric until 2009, before it was bought back by the latter. It offers both general purpose and high efficiency, high-gain devices for 3G/LTE applications with an operational voltage of 50 V.

Freescale produces GaN epi layers on SiC substrate and is currently researching HEMTs, however, no commercial products are available yet. Another company, which is driving the research in this field is Fujitsu. While it already offers GaN-based products, it also plans to deliver the first power supply products employing enhancement-mode GaN HEMTs in 2011.

Several companies focus solely on epi structure fabrication (Group4Labs, IQE, Picogiga). While most of them use a substrate SiC wafer, Group4Labs has developed a technology to attach GaN epi layers to diamond substrates and is researching HEMTs based on this approach.

## 2.5 GaAs-Based HEMTs

InP-based InGaAs/InAlAs pseudomorphic HEMTs (pHEMTs) were long considered to be the best devices for high-frequency communication applications because of their excellent *RF* and

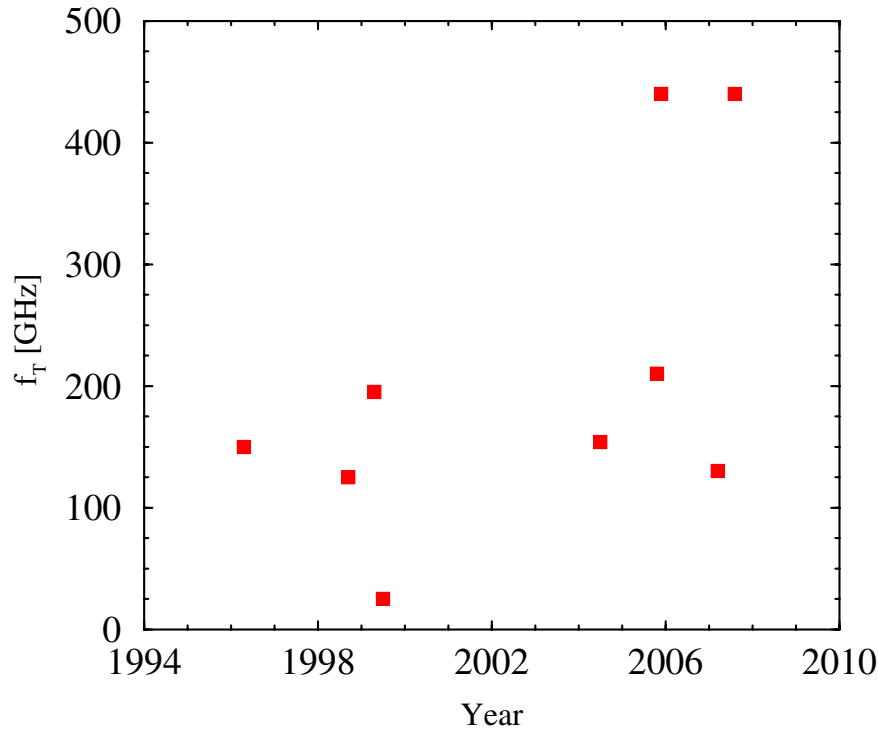


**Figure 2.8:** Cut-off frequency of GaAs mHEMTs over time.

low-noise performance: e.g. in the beginning of the decade structures with a gate length of 25 nm, 45 nm and a cut-off frequency of 526 GHz, 400 GHz, respectively, were reported [71], [72]. However, InP pHEMTs have some issues, including high cost of InP substrates, low mechanical stability, and last but not least poor breakdown performance due to the low band gap of the InGaAs channel. An alternative are GaAs pHEMTs with lower In content in the channel, and therefore superior breakdown performance but limited by the lower mobility and velocity saturation. The advantages of both technologies are combined in metamorphic HEMTs. Those use a strain-relaxed, compositionally-graded buffer to accommodate the lattice mismatch between the substrate and the top layer. The technology offers very good  $RF$  performance, the lowest noise figures, and high gain performance. Aggressive gate scaling and several optimization techniques such as zig-zag formed T-shaped gate electrodes helped to push the cut-off frequency to 440 GHz [73], [74] (see Fig. 2.8). Interest in these devices is still strong and numerous efforts are devoted to improve the performance. As an example, Su *et al.* suggest a dilute antimony channel in order to improve the interface quality and channel confinement [75]. Another focus point of research is the design of an enhancement mode device, which faces several issues. The narrow-gap channel enables high impact ionization rates, which combined with the high *Schottky* gate leakage current limit the input dynamic range and increase the noise figure. Therefore, attempts to restrain the gate leakage current in E-mode devices through MOS structures are ongoing [76]. An advantage of the MOS technique is the improved  $RF$  performance of the devices due to the lower gate-source and gate-drain capacitances [77].

## 2.6 GaN-Based HBTs

### 2.6.1 AlGaIn/GaN HBTs

In the end of the 1990s III-Nitride technology advanced rapidly. The interest was mainly driven by the progress in lasers and LEDs but also in HEMTs. The latter soon reached record microwave performance and thus prompted the development of heterojunction bipolar transistors (HBTs). They offer traditional advantages over field effect transistors, such as linearity, threshold uniformity, and current handling. One of the first working samples was demonstrated in [78], but was plagued by poor contacts and the quality of the material. Subsequently a current gain ( $\beta$ ) of only 3 was reached with a very high  $V_{CE}$  offset of 5 V. Other groups [79] faced similar problems. However, while the technology was still lacking, various theoretical studies pointed out the large potential of the devices. Using a two-dimensional model and based on material properties reported in literature, [80] predicted a maximum  $\beta$  of 1130, collector saturation current of 3.5 kA/cm<sup>2</sup>, breakdown voltage of 55 V, and  $f_t$  of 18 GHz. Even higher theoretical values (reaching  $\beta=2000$  and  $f_t=30$  GHz) were reported by employing compact models [81]. Other studies focused on a comparison between npn- and pnp-structures [82] and the worse high-frequency characteristics of the latter. Using models and material parameters verified by modeling experimental device characteristics, an optimization was performed in [83] and a theoretical  $f_t$  of 44 GHz was predicted. Based on improved fabrication processes developed previously for other compound systems, HBTs with a similar performance ( $\beta \approx 3$  at room temperature) were fabricated on MBE and MOCVD grown material [84]. The device performance was again limited by the base resistance. Better results were achieved in [85] by using MOCVD grown material, with  $\beta=80$ , but high forward resistance at the base-emitter junction due to possible diffusion of Magnesium into the emitter. The same group also introduced selective area growth resulting into high crystalline quality, but a still leaky base-emitter diode [86]. The same technique was used by McCarthy *et al.* [87], while they also employed emitter mesa regrowth to avoid etch damage, and material grown using lateral epitaxial overgrowth technique to achieve low dislocation density. Through optimization of the width and grading of the base, operation at 70 V with a  $\beta=6$  was possible.

In the following years work on AlGaIn/GaN based HBTs continued [88], [89], [90], [91], [92], [93], [94] (Fig. 2.9). A possible issue with the measured values of the extrinsic current gain, was however pointed out [92]. Due to the low quality ohmic contacts and the leaky base-collector junction, the anomalous current gain at low current levels can be erroneously attributed to the intrinsic device performance. This was also observed by Hsueh *et al.* [95], who proposed that a common-emitter I-V under high current bias is the best way to evaluate the transistor performance, instead of the Gummel plot. Some of the experimental studies focused on high-temperature performance [90], [96]. As the hole concentration increases by thermal activation, the current gain of pnp structures is enhanced [90]. Device operation at temperatures up to 400° C was demonstrated, although the device performance shows a degradation after prolonged operation at this temperature [96]. Despite the progress in the last years the technology faces still several major problems:

- low base conductivity,
- deep acceptor levels of Mg,
- and emitter-collector leakage currents.

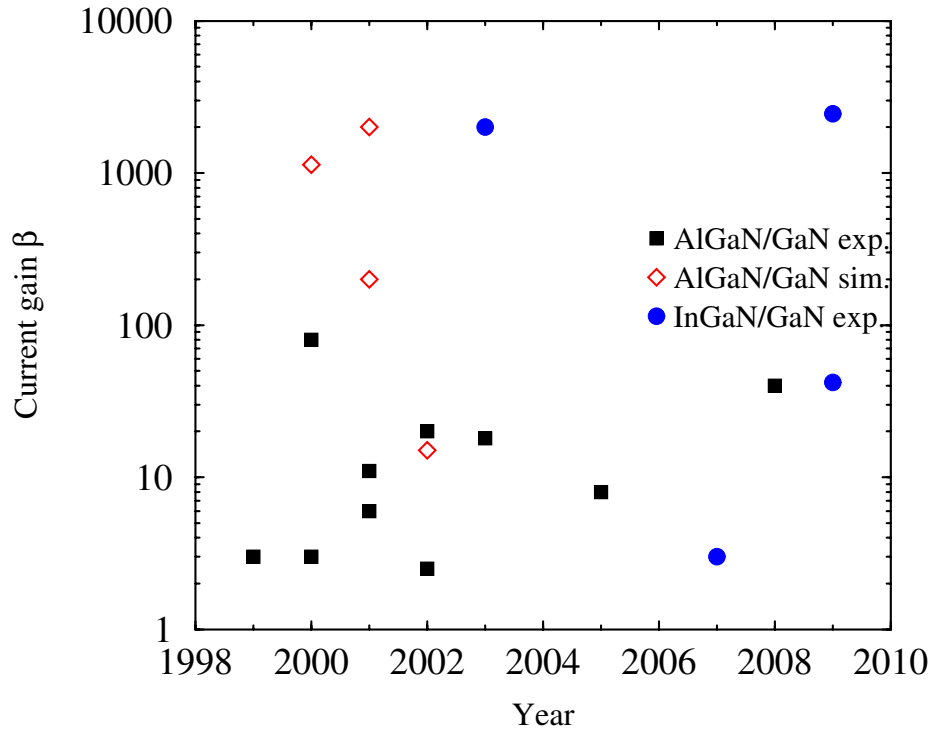


**Figure 2.9:** Current gain (measured and simulated) of GaN HBTs over time.

### 2.6.2 InGaIn/GaN HBTs

One of the suggested ways to counter the low base conductivity is to employ a lower gap material such as InGaIn. InGaIn is also more resistant against the damage introduced by the dry etching step used to expose the surface of the base layer [97]. Thus, the potential of an InGaIn/GaN HBT was quickly realized, first in theoretical studies [98], [79], [99] and subsequently in experiments [97]. The latter is the first reported InGaIn/GaN (D)HBT. It achieved a  $\beta$  of 20 but also a high offset voltage (5 V). Further studies reported breakdown voltages as high as 100 V, mainly due to the low damage of the InGaIn base layer [100]. Ongoing improvement of the base ohmic characteristics resulted in a decrease of the offset voltage (from 5 V down to 1 V) in addition to a record  $\beta=2000$  [101]. The same group reported a collector current density of  $6.7 \text{ kA/cm}^2$  corresponding to a power density of  $270 \text{ kW/cm}^2$  [102].

Several works employed a theoretical approach in exploring and optimizing the device performance. Ensemble Monte Carlo simulations were used to determine the temperature and doping concentration dependence of the low-field mobility [99]. Based on this calculations the temperature dependence of the cut-off frequency was studied. The impact of non-uniform base doping on  $\beta$  was studied in [103].

The implementation of a graded emitter layer was experimentally studied by Keogh *et al.* [104]. A low offset voltage (2-3 V) and  $\beta=27$  with breakdown voltage greater than 40 V was reported. The current gain decreased to 10 at  $300^\circ \text{C}$ , but no device degradation was observed. The same technique was used by other groups [105], [106]. A state-of-the-art device with  $\beta=42$ , a current

density of  $5.2 \text{ kA/cm}^2$ , and a breakdown voltage larger than  $75 \text{ V}$  was obtained in [106]. A record current gain of 2450 was reported in [107] at room temperature. At  $40 \text{ K}$  it reaches 5000 due to a reduction of the recombination current in the base layer. By introducing an AlGaIn collector Kumakura *et al.* [108] were able to achieve a breakdown voltage of  $190 \text{ V}$  albeit the current gain was only 3 due to the low quality AlGaIn.

## 2.7 Simulation Software

Modeling and simulating a wide band gap semiconductor such as GaN faces some physical effects not encountered in Si or GaAs. The main difference is that GaN crystallizes with a non-cubic symmetry, which results in an increased size and number of atoms per unit cell, thus in a more complex band structure [109]. Accounting for those new complexities Monte Carlo (MC) studies of the transport properties of wurtzite GaN have been conducted. The advantage of this approach is that it does not require extensive experimental input. Earlier works employed analytical two-band conduction band models [110]. Other groups use ensemble Monte Carlo simulation to calculate the transport properties [109] paying special attention to the band intersection points and their impact on impact ionization. Some studies focus exclusively on the high-field properties of GaN using a microscopic rigid-ion model and focus on the isotropy of the properties and the effects of non-equilibrium hot phonons [111].

However MC techniques can also be used to calculate GaN based device characteristics. GaN MESFETs with different phases were compared by such a method in [112]. Yamakawa *et al.* employed a cellular MC approach with quantum corrections [113], however, the overall current of the device remained nearly unchanged due to the dominant polarization charge. Several works focused on the proper modeling of the piezoelectric polarization effects by using a quasi-two-dimensional model based on a self-consistent charge control [114], [115]. Others studied deep levels at the AlGaIn surface and their impact on current-slump phenomena: it was found that surface trapping effects may play a major role [116]. A method, which combines MC electronic simulation with an analytical thermal resistance matrix method, was used to investigate the self-heating effects [117]. Accounting for self-heating effects too, the high-frequency noise at different temperatures was studied in [118]. The impact of threading dislocation on the velocity-field characteristics was shown to be small, due to the high carrier concentration screening effects [119].

### 2.7.1 Commercial Software

Parallel to the MC approach drift-diffusion (DD) and hydrodynamic (HD) multi-dimensional modeling approaches have been employed for studies of GaN based HEMTs. Some of them make use of commercial software while others rely on university-developed simulators. Some simulators are tailored for simulation of nitride-based optoelectronic devices such as TIBERCAD [120], [121], although it also features drift-diffusion and hydrodynamic transport and heat balance models. The device simulation tool TCAD STUDIO [122] developed by ESEMI has been used for the simulation of SiC based heterostructures [123], but no support for GaN based devices is available yet. A simulation tool which features models for Nitrides is APSYS by Crosslight [124]. The simulator focuses on compound semiconductors with silicon as a special case. Though the main

application area is the analysis of optoelectronic devices, the simulator has also been employed for studies of HEMT structures [125]. Another commercial device simulation tool is GENIUS by Cogenda [126]. While it features DD and HD transport models and also lattice heating, it does not offer built-in material models for Nitrides and consequently has yet to be applied for GaN based HEMTs.

A commercial device simulation tool which is widely used is the SENTAURUS device simulator by Synopsys. It is based on TAURUS MEDICI (which itself is derived from the PISCES software by the Stanford University) and the device simulator DESSIS by ISE. The latter has been employed in numerous theoretical studies of GaN-based HEMTs. Those include the breakdown characteristics dependent on surface defect charges [127], quantum and hot electron effects [128], and self-heating and current collapse effects [129].

Another commercial simulator based on the Stanford tools is ATLAS by Silvaco. It features HD and DD transport models and material models for Nitrides. It was used for field-plate optimization of HEMT structures [130] and drain-lag and gate-lag effects [131] (a DD transport model was considered in those works), but also for verification of analytical models [132].

### 2.7.2 Minimos-NT

MINIMOS-NT is a general-purpose semiconductor device simulator providing steady-state, transient, and small-signal analysis of arbitrary two- and three-dimensional device structures. The first approach to study a heterostructure device using MINIMOS-NT dates back to the 90s, when mobility models for GaAs and extended recombination/generation models were implemented [133]. Simultaneously interface models for heterojunctions (i.e. a thermionic field emission model) were developed [134]. Using the extended software tool a simulation setup for the optimization of GaAs-based HEMTs was established, which delivered results in good agreement with experimental data and allowed predictive device simulation [135]. Work on heterojunction devices continued in this decade: both HBT and HEMT structures were analyzed [136], [137]. A consistent set of model and model parameters was achieved, which best described the physical behavior of both III-V HEMTs and HBTs [138]. Work was focused on several pseudomorphic AlGaAs/InGaAs/GaAs and InAlAs/InGaAs HEMT technologies, while device optimization was conducted with respect to statistical process variations. Additionally, three-dimensional thermal simulations of III-V HEMTs were conducted in order to help thermal investigations. Accordingly, impact ionization and self-heating were included in the simulation. Additionally, small signal S-parameters were extracted from *AC* simulations. The first performed simulation of a GaN HEMT with MINIMOS-NT showed a good agreement with measurements [137].

## Chapter 3

---

# Materials

---

**T**HIS chapter focuses on the properties of the semiconductor materials relevant for Nitride-based devices: GaN, InN, and AlN, and their ternary alloys. The chapter starts with a brief introduction of the MC technique used to compute macroscopic parameters. Important material as well as the electron transport properties from other studies are summarized and compared. A short discussion of p-type conductivity is provided. The order in which the materials are presented corresponds to their importance from a device modeling point of view. GaN is discussed first as nearly all of the current HEMT designs rely on it as a channel material. Technology issues have hampered structures with an InN channel, however, its recently revised band structure suggests some excellent carrier transport properties. At last, there is AlN which due to its very large band gap and lack of experimental as well as simulation reports is only briefly discussed.

### 3.1 The Monte Carlo Method

The MC method is a powerful technique to establish a consistent link between theory and experiments. It helps to gain understanding of the transport properties and it provides macroscopic parameters which are necessary for the description of electronic devices. A single-particle MC technique is employed here to investigate stationary electron transport in GaN. The model includes the three lowest valleys of the conduction band. Several stochastic mechanisms such as acoustic phonon, polar optical phonon, inter-valley phonon, ionized impurity, and piezoelectric scattering are considered and their impact is assessed. The particular advantage of the MC method is that it provides a transport formulation on a microscopic level, limited only by the extent to which the underlying physics of the system is included. Since III-N material systems are yet not so well explored, several important input parameters are still missing or just inaccurately known. In an iterative approach the influence of the input parameters and their interdependence are assessed in order to get a set of parameters which are in agreement with experimental data available for different physical conditions (doping, temperature, field, etc.). Such a calibrated set of models and model parameters delivers valuable data for low-field mobility, velocity saturation, energy relaxation times, etc.

## 3.2 Gallium Nitride

### 3.2.1 Material Properties

The choice on the bandgap energies for GaN is based on a publication [139]. The particular setup for the masses has negligible impact within the available range, thus an average value [140] is chosen.

An interesting result of the literature search is the fact that in almost all MC simulations the piezoelectric scattering mechanisms were modeled assuming a cubic crystal structure. This is a correct approach to most of the technologically significant semiconductors, whereas for wurtzites the hexagonal structure has to be accounted for in the relevant piezoelectric scattering model.

The role of piezoelectric interaction in bulk wurtzite GaN has been analyzed by Kokolakis *et al.* [141]. In particular, the effect of acoustic piezoelectric scattering is taken in consideration, and the scattering rates have been calculated including the effect of screening. In accordance with their simulations, present results show that the piezoacoustic rates are higher in the wurtzite phase than in the cubic phase, and they are very sensitive to the background doping of the sample. Since nitrides exhibit the largest piezoelectric constants among all of the III-V semiconductors, an accurate modeling of piezoelectric scattering is especially important. In this work a piezoelectric scattering model similar to [142], [141] is used, assuming equipartition, valid at temperatures over one Kelvin and considering non-parabolicity and screening in terms of the Thomas-Fermi inverse length  $q_0$ .

Material parameters as used by different groups are given in Table 3.1, while Table 3.2 summarizes the experimental and theoretical values of the elastic constants  $c_{11}$ ,  $c_{12}$ , and  $c_{44}$ , available for wurtzite GaN in the literature. From these the corresponding values for  $c_L$ ,  $c_T$ ,  $v_{sl}$ , and  $v_{st}$  are calculated. The latest experimental values for GaN [143] are adopted in the MC simulation [144].

Table 3.3 summarizes the experimental and theoretical values of the piezoelectric coefficients  $e_{15}$ ,  $e_{31}$ , and  $e_{33}$ , available for GaN in the literature. In cases, where  $e_{15}$  is not available,  $e_{15} = e_{31}$  is assumed. From these, the corresponding  $\langle e_L^2 \rangle$  and  $\langle e_T^2 \rangle$  are calculated, which are necessary to obtain the coupling coefficient  $K_{av,WZ}$  taking into account the wurtzite structure [144].

### 3.2.2 Electron Transport

Using the established setup of models and model parameters, MC simulation results for different physical conditions are obtained (doping, temperature, field, etc.) for bulk GaN. Fig. 3.1 shows the low-field electron mobility in hexagonal GaN as a function of free carrier concentration. The mobility depends on the sound velocity via the piezoelectric and the acoustic deformation potential (ADP) scattering mechanism. A higher sound velocity reduces the ADP scattering rate, which results in an increased mobility.

The simulations show, that the piezoelectric scattering is the dominant mobility limitation factor at low concentrations even at room temperature, beside the commonly accepted importance at low temperatures.

The MC simulation is in fairly good agreement with experimental data from collections or single



**Table 3.1:** Summary of material parameters of wurtzite GaN for Monte Carlo simulation.

Bandgap energy			Electron mass			Non-parabolicity			Scattering models						Ref.
$\Gamma_1$	U	$\Gamma_3$	$m_{\Gamma_1}$	$m_U$	$m_{\Gamma_3}$	$\alpha_{\Gamma_1}$	$\alpha_U$	$\alpha_{\Gamma_3}$	ADP	$\hbar\omega_{ij}$	$\hbar\omega_{LO}$	$\rho$	$\epsilon_r$	$\epsilon_\infty$	Year
[eV]	[eV]	[eV]	[ $m_0$ ]	[ $m_0$ ]	[ $m_0$ ]	[1/eV]	[1/eV]	[1/eV]	[eV]	[meV]	[meV]	[g/cm <sup>3</sup> ]	[-]	[-]	
3.5	-	-	0.19	-	-	0.187	-	-	12.0	-	99.5	6.1	9.5	5.35	[145]
3.5	5.00	-	0.19	1.00	-	0.187	-	-	12.0	-	92.0	6.1	9.5	5.35	[146]
3.5	5.00	-	0.19	0.7	-	0.187	-	-	12.0	-	92.0	6.1	9.5	5.35	[147]
3.4	5.50	5.60	0.19	-	-	-	-	-	10.1	-	92.0	6.095	9.5	5.35	[148]
3.5	5.50	5.60	0.20	0.40	0.60	0.183	0.065	0.029	8.3	92.9	92.9	6.1	8.9	5.35	[149]
3.5	5.5	5.6	0.19	0.4	0.6	0.187	0.065	0.029	12.0	-	92.0	6.1	9.5	5.35	[150]
3.39	5.39	5.59	0.20	0.40	0.60	0.189	0.067	0.029	8.3	91.2	91.2	6.15	8.9	5.35	[151]
3.5	4.99	5.25	0.20	0.24	0.40	0.19	0.17	0	7.8	65.0	92.0	6.095	9.5	5.35	[110]
3.39	5.49	5.29	0.20	1.00	1.00	0.189	0	0	8.3	91.2	91.2	6.15	8.9	5.35	[152]
3.5	5.50	5.60	0.19	0.40	0.60	0.183	0.065	0.029	10.1	92.0	92.0	6.1	8.9	5.35	[153]
3.5	5.45	5.60	0.21	0.25	0.40	0.19	0.1	0	8.0	65.0	92.0	6.095	9.5	5.35	[140]
3.36	-	-	0.20	-	-	-	-	-	10.1	-	92.0	6.095	9.5	5.35	[154]
3.52	5.77	5.87	0.212	-	-	0.37	-	-	8.3	65.8	90.88	6.087	9.7	5.28	[155]
3.5	4.5	4.6	0.186	0.40	0.60	0.189	0.065	0.029	8.3	-	99.5	6.15	9.5	5.35	[116]
3.52	5.77	5.87	0.212	0.493	0.412	-	-	-	8.3	-	90.88	6.087	9.7	5.28	[156]
3.5	5.60	3.90	0.20	0.60	0.22	0.183	0.029	0.065	8.3	80.0	92.2	6.15	9.95	5.35	[157]
3.39	5.49	5.29	0.21	1.00	1.0	0.189	0	0	8.3	92.0	92.0	6.15	8.9	5.35	[139]
3.39	5.49	5.29	0.2	1.0	1.0	0.189	0	0	8.3	91.2	91.2	6.15	8.9	5.35	[158]
3.39	5.49	5.29	0.2	1.0	1.0	0.189	0	0	8.3	92.0	92.0	6.15	8.9	5.35	[159]
3.39	5.29	5.49	0.20	0.30	0.40	0.189	0	0	8.3	91.0	92.0	6.1	8.9	5.35	

**Table 3.2:** Summary of elastic constants of GaN and the resulting longitudinal and transverse elastic constants and sound velocities.

$c_{11}$	$c_{12}$	$c_{44}$	Data	Refs.	$c_L$	$c_T$	$v_{sl}$	$v_{st}$
[GPa]	[GPa]	[GPa]			[GPa]	[GPa]	[m/s]	[m/s]
296	120	24	exp.	[160]	245	50	6342	2855
374	106	101	exp.	[161]	348	114	7557	4331
390	145	105	exp.	[162]	376	112	7859	4290
377	160	81	exp.	[163]	355	92	7637	3888
365	135	109	exp.	[164]	360	111	7693	4278
370	145	90	exp.	[165]	364	108	7733	4212
373	141	94	exp.	[143]	355	103	7641	4110
369	94	118	calc.	[166]	353	126	7620	4546
396	144	91	calc.	[167]	368	105	7775	4153
367	135	95	calc.	[168]	350	103	7585	4122
350	140	101	calc.	[169]	347	103	7548	4106

**Table 3.3:** Summary of piezoelectric coefficients of GaN for Monte Carlo simulation of piezoelectric scattering.

$e_{15}$	$e_{31}$	$e_{33}$	Data	Refs.	$\langle e_L^2 \rangle$	$\langle e_T^2 \rangle$
[C/m <sup>2</sup> ]	[C/m <sup>2</sup> ]	[C/m <sup>2</sup> ]	Data	Refs.	[C <sup>2</sup> /m <sup>4</sup> ]	[C <sup>2</sup> /m <sup>4</sup> ]
-0.30	-0.36	1.00	exp.	[170]	0.103	0.123
-	-0.55	1.12	exp.	[171]	0.175	0.234
-	-0.33	0.65	calc.	[145]	0.061	0.082
-	-0.49	0.73	calc.	[172]	0.118	0.149
-0.22	-0.22	0.43	calc.	[173]	0.027	0.036
-	-0.32	0.63	calc.	[169]	0.058	0.077
-	-0.44	0.86	calc.	[174]	0.109	0.145

point measurements from [175], [176], [177], [178], [179]. The electron mobilities selected for comparison, consider bulk material and are measured using the Hall effect. The discrepancy between the simulation results and the measured data might be attributed to dislocation scattering which is not considered here. This mechanism is considered to be a source of mobility degradation for GaN samples.

Numerous publications on GaN heterostructure devices (see e.g. a summary in [180]) provide inversion layer mobilities which are higher. These values are derived from transit frequency and device dimensions. However, two-dimensional electron gas heterostructures are plagued, among others, by surface scattering effects, and are not considered in this work.

Fig. 3.2 shows the low-field electron mobility as a function of lattice temperature in GaN at  $10^{17} \text{ cm}^{-3}$  concentration. The experimental data are from [179], [181], [182]. Note, that mobility increased over the years because of the improved material quality (reduced dislocation density).

Fig. 3.3 provides the electron drift velocity versus the electric field. We compare our MC result with other simulations [148], [149], [110], [155], [157], [113], and with the available experimental data [183], [184]. The low field data points are in qualitatively good agreement, at higher fields experimental values are significantly lower. Both experiments [183], [184] of electron velocities in bulk GaN, employed pulsed voltage sources. Many devices with etched constrictions were measured and the peak electron drift velocity  $v_{d,\max}$  was typically found to be about  $2.5 \times 10^7 \text{ cm/s}$  at electric fields  $E_{\text{pk}}=180 \text{ kV/cm}$ . The discrepancy in the reported MC results is due to various uncertainties of parameter values and considerations of scattering mechanisms.

While the low-field transport has been profoundly studied, reports on the high-field transport properties are inconsistent. Several groups observe a negative differential mobility (NDM) in their experiments [185], [184], while others do not obtain any saturation below  $200 \text{ kV/cm}$  [186] (Fig. 3.4). MC simulation results are contradictory too: some simulations yield a maximum of the electron velocity at  $140 \text{ kV/cm}$  [187], [109], while according to others the maximum velocity is at  $180 \text{ kV/cm}$  [148], [111]. Those again are in a disagreement with the NDM as observed in experiments at over  $320 \text{ kV/cm}$  [185].

### 3.2.3 Hole Transport

Modeling the hole transport in GaN is hindered by the lack of high quality  $p$ -type material. Several dopants such as Mg, Zn, Cd, and Be [188], [189], [190], [191] have been investigated. Of all those dopants Mg is known to have the lowest ionization energy [192]. The first  $p$ -type conduction in magnesium-doped GaN grown by MOCVD was realized by Amano *et al.* [188]. The as-grown high-resistivity GaN:Mg is converted into  $p$ -conductive material by hydrogen depassivation [193]. Due to the high activation energy of Mg of 150 to 250 meV [194], [192] only a few percent are active at room temperature. The highest reported efficiency is around 10% [195]. In order to reach a useful hole concentration of  $10^{17}$ – $10^{18} \text{ cm}^{-3}$  a Mg doping as high as  $2 \times 10^{19}$ – $10^{20} \text{ cm}^{-3}$  is needed [196]. However, such high doping concentrations lead to a deterioration of the hole transport properties (Fig. 3.5). Kozodoy *et al.* [197] suggest that at very high doping levels the degree of compensation and self-compensation [198] increases, which suppresses the hole mobility. On the other hand the hole concentration is extremely dependent on the temperature as demonstrated in [199].

One way of improving the performance is by using a  $\delta$ -doping as suggested by Nakamari *et*

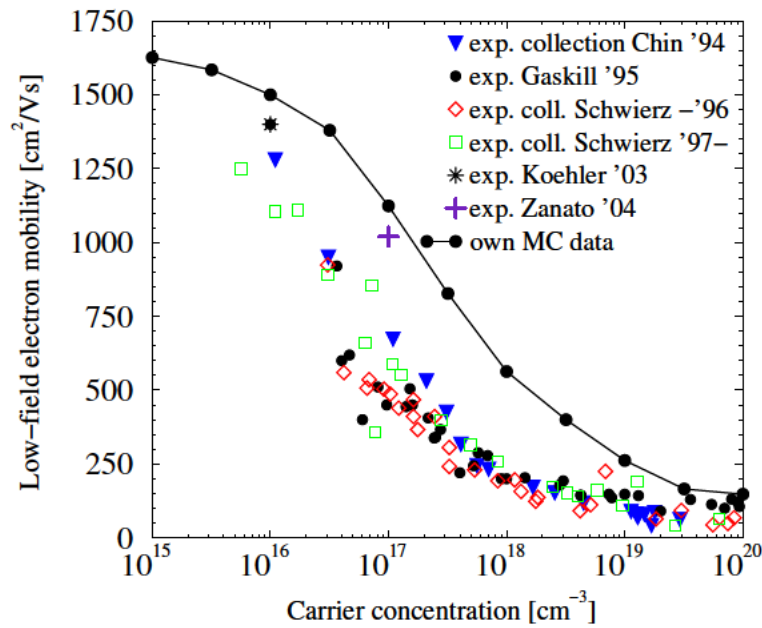


**Figure 3.1:** Low-field electron mobility as a function of carrier concentration in GaN: Comparison of the MC simulation results and experimental data.

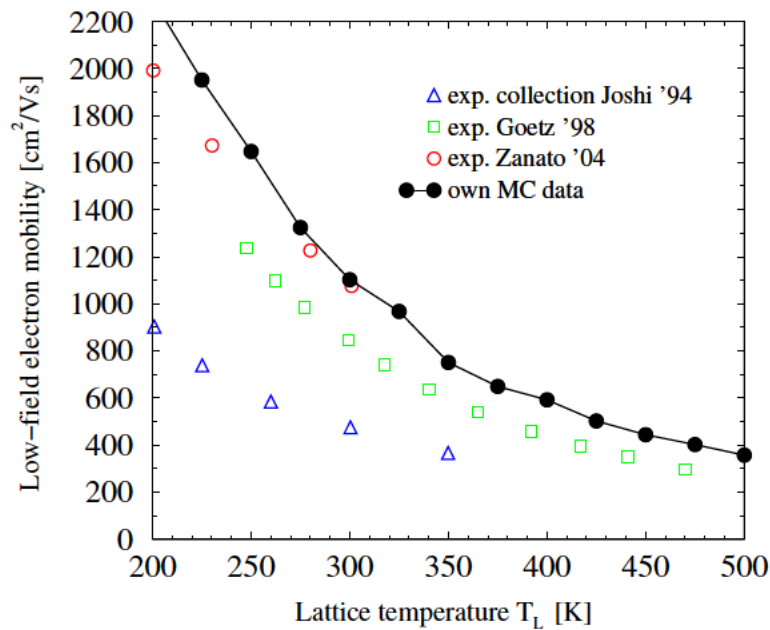


**Figure 3.2:** Low-field electron mobility as a function of lattice temperature in GaN at carrier concentration of  $10^{17} \text{ cm}^{-3}$ .

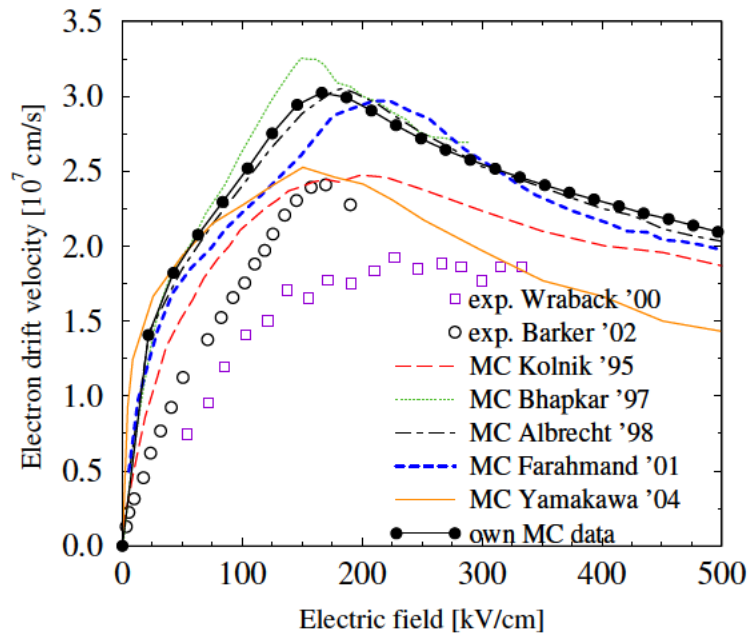


**Figure 3.3:** Electron drift velocity versus electric field in wurtzite GaN: Comparison of MC simulation results and experimental data I.

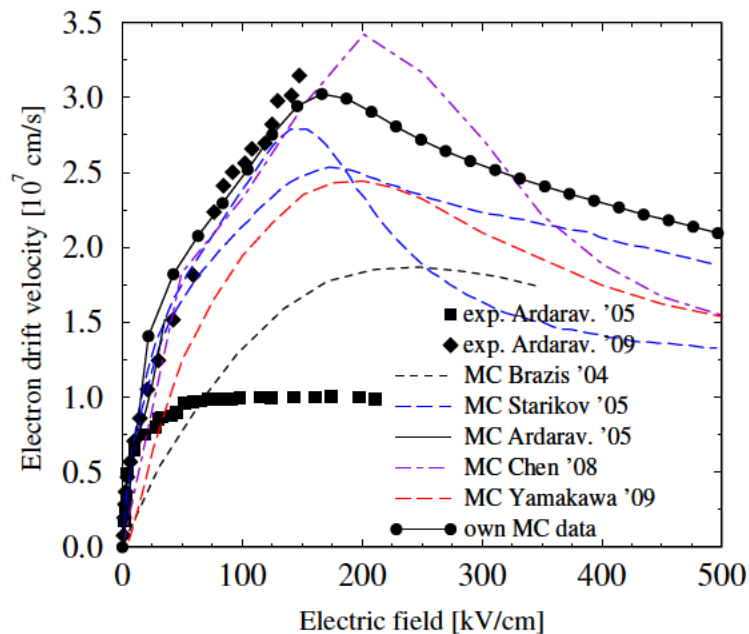


**Figure 3.4:** Electron drift velocity versus electric field in wurtzite GaN: Comparison of MC simulation results and experimental data II.

*al.* [200]. The dislocation density is significantly reduced, and a higher conductivity is achieved in both the lateral and vertical directions. The latter is an issue for Mg-doped heterostructures, where the super-lattice introduces also potential barriers in vertical direction. Such an approach was used by several groups [201], [202], [203], [204]. The variation of the valence band energy caused by the modulation of chemical composition leads to a reduction of the acceptor activation energy. The polarization fields increase the band bending, and the hole concentration rises in addition [202]. The acceptors in the  $\text{Al}_x\text{Ga}_{1-x}\text{N}$  are energetically closer to the valence band edge and are therefore ionized easier [205].

Another problem, which bipolar GaN-based devices face, is the high resistivity of the p-type ohmic contacts. They are sometimes referred to as closer to leaky *Schottky* contacts in their characteristics [84]. Introduction of InGaN/AlGaIn super-lattices greatly improves the contact sheet resistance [206], due to the large oscillations of the valence band.

A parameter also crucial for the modeling of hole transport is the effective hole mass. Estimation of the hole effective masses and their anisotropy was the subject of numerous studies (a comprehensive review is found in [207], [208], [209], [210]). Values ranging from  $0.3m_0$  [211] to  $2.2m_0$  [212] are reported. Kasic *et al.* [208] suggest that the effective hole mass depends on the hole concentration:  $1.0m_0$  for  $p=5\times 10^{16}\text{ cm}^{-3}$ , and  $1.4m_0$  for  $p=8\times 10^{17}\text{ cm}^{-3}$  [213]. In this work a value of  $1.4m_0$  is assumed as reported in [208], lower than the one used in [199] ( $1.6m_0$ ), and slightly higher than the one recommended by Vurgaftman *et al.* ( $1.0m_0$ ) [209].

Fig. 3.7 shows the hole drift velocity as a function of the electric field as calculated by two groups. Rodrigues *et al.* [214] use a rather high hole mass ( $2.0m_0$ ) and a doping concentration of  $10^{18}\text{ cm}^{-3}$ . The calculation of Chen *et al.* [159] relies on a standard ensemble Monte Carlo approach and accounts for various scattering effects including impact ionization. Again the hole velocity is limited by the high density of states of the heavy band ( $1.8m_0$ ).

### 3.3 Indium Nitride

#### 3.3.1 Material Properties

In recent years Indium Nitride (InN) has attracted much attention due to the considerable advancement in the growth of high quality crystals. Furthermore, several new works on the material properties proposed a bandgap of  $\approx 0.7\text{ eV}$  [215], [216], [217] instead of  $\approx 1.9\text{ eV}$  [4]. Here a Monte Carlo approach is used to investigate the electron transport, considering two band structures [218], [219]. The calculations include the three lowest valleys of the conduction band (depending on the chosen band structure, see Table 3.4) and account for non-parabolicity effects. Several stochastic mechanisms such as acoustic phonon, polar optical phonon, inter-valley phonon, Coulomb, and piezoelectric scattering are considered and their impact is assessed [8]. The parameter values for the acoustic deformation potential (ADP  $\Xi=7.1\text{ eV}$ ), polar-optical phonon scattering ( $\hbar\omega_{\text{LO}}=73\text{ meV}$  or  $89\text{ meV}$ ), inter-valley scattering ( $\hbar\omega_{\text{iv}}=\hbar\omega_{\text{LO}}$ ), mass density ( $\rho=6.81\text{ g/cm}^3$ ), and static and high-frequency dielectric constants ( $\epsilon_s=15.3$  and  $\epsilon_\infty=8.4$ ) are adopted from [219], [221]. In addition, the influence of another set of dielectric constants ( $\epsilon_s=11.0$  and  $\epsilon_\infty=6.7$ ) recently proposed in [222] in conjunction with the narrow bandgap and lower effective mass is studied.

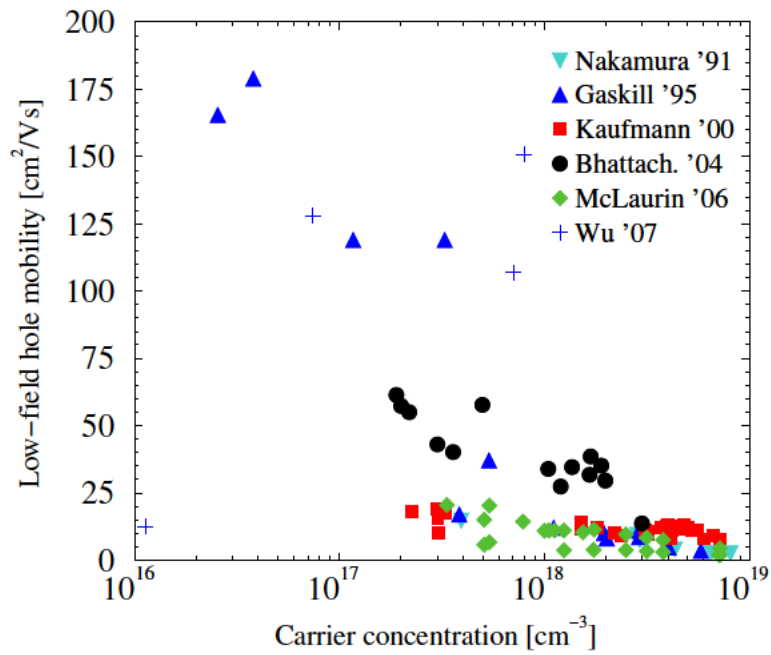


Figure 3.5: Low-field hole mobility as a function of carrier concentration in GaN.

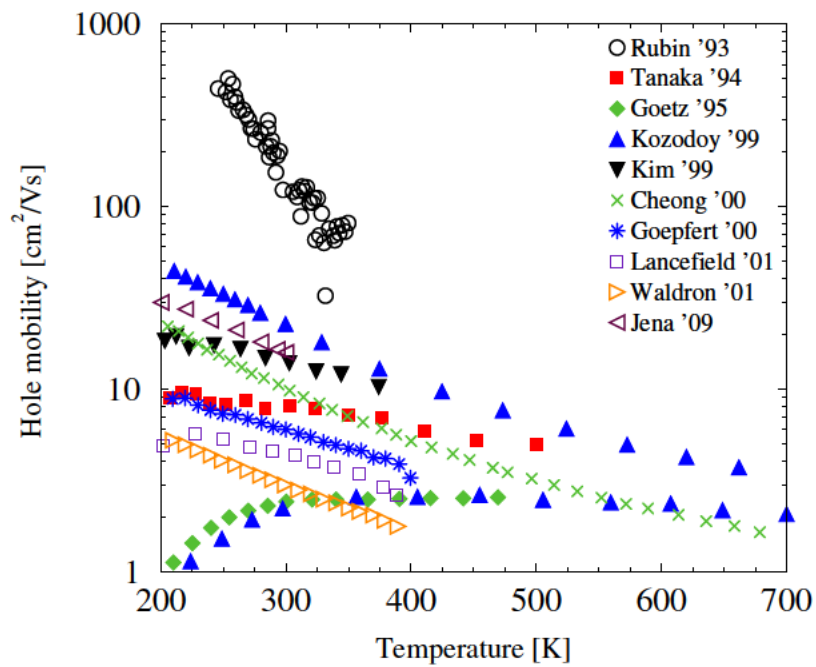
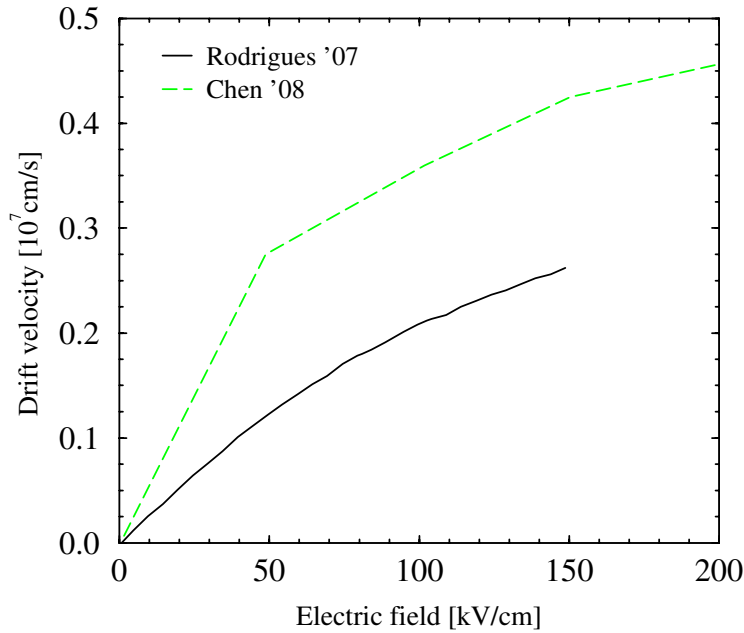


Figure 3.6: Low-field hole mobility as a function of lattice temperature.



**Figure 3.7:** Hole drift velocity versus electric field.

An accurate piezoelectric scattering model, which accounts for non-parabolicity and wurtzite crystal structure, is also employed [223]. Table 3.5 summarizes experimental values for the elastic constants ( $c_{11}$ ,  $c_{12}$ , and  $c_{44}$ ) of wurtzite InN. From these the corresponding longitudinal and transversal elastic constants ( $c_L$  and  $c_T$ ) and sound velocities ( $v_{sl}$  and  $v_{st}$ ) are calculated. Table 3.6 gives theoretical values of the piezoelectric coefficients  $e_{31}$  and  $e_{33}$  available in the literature and the calculated corresponding  $\langle e_L^2 \rangle$  and  $\langle e_T^2 \rangle$  ( $e_{15}=e_{31}$  is assumed). Choosing the set of elastic constants from [168] and piezoelectric coefficients from [224] results in a coupling coefficient  $K_{av}=0.24$ .

### 3.3.2 Electron Transport

Simulations with two different setups are conducted: one with a bandgap of 1.89 eV (effective mass  $0.11m_0$  in the  $\Gamma_1$  valley [218]), and one with a bandgap of 0.69 eV (effective mass of  $0.04m_0$  [219]), as summarized in Table 3.4. Results for electron mobility as a function of lattice temperature, free carrier concentration, and electric field are obtained.

As a particular example, Fig. 3.8 shows the low-field electron mobility in hexagonal InN as a function of free carrier concentration. Results from other groups [176], [222], [231] and various experiments [231], [232], [233], [234] are also included. Assessing the classical band structure model ( $\mathcal{E}_g=1.89$  eV), we achieve an electron mobility of  $\approx 4000$  cm<sup>2</sup>/Vs, which is in good agreement with the theoretical results of other groups using a similar setup [176]. Considering the newly calculated band structure model ( $\mathcal{E}_g=0.69$  eV), a maximum mobility of  $\approx 10000$  cm<sup>2</sup>/Vs is achieved. The corresponding scattering rates are illustrated in Fig. 3.9. The increased mobility can be explained with the lower effective electron mass. Polyakov *et al.* [221] calculated a theoretical limit as high as 14000 cm<sup>2</sup>/Vs, however their simulation does not account for piezo-



**Table 3.4:** Summary of material parameters of wurtzite InN for MC simulation.

Bandgap energy			Electron mass			Non-parabolicity			Scattering models			Ref.
$\Gamma_1$	A	$\Gamma_2$	$m_{\Gamma_1}$	$m_A$	$m_{\Gamma_2}$	$\alpha_{\Gamma_1}$	$\alpha_A$	$\alpha_{\Gamma_2}$	$\hbar\omega_{LO}$	$\epsilon_s$	$\epsilon_\infty$	
[eV]	[eV]	[eV]	[ $m_0$ ]	[ $m_0$ ]	[ $m_0$ ]	[1/eV]	[1/eV]	[1/eV]	[meV]	[-]	[-]	
1.89	4.09	4.49	0.11	0.4	0.6	0.419	0.088	0.036	-	-	-	[218]
1.89	-	-	0.11	-	-	-	-	-	89	15.3	8.4	[176]
1.89	4.09	4.49	0.11	0.4	0.6	0.419	0.88	0.036	89	15.3	8.4	[225]
1.89	-	-	0.11	-	-	0.419	-	-	89	15.3	8.4	[226]
0.8	3.0	3.4	0.042	1.0	1.0	0.419	-	-	89	15.3	8.4	[227]
<b>1.89</b>	4.09	4.49	0.11	0.4	0.6	0.419	0.88	0.036	89	15.3	8.4	
$\Gamma_1$	$\Gamma_2$	M-L	$m_{\Gamma_1}$	$m_{\Gamma_2}$	$m_{ML}$	$\alpha_{\Gamma_1}$	$\alpha_{\Gamma_2}$	$\alpha_{ML}$	$\hbar\omega_{LO}$	$\epsilon_s$	$\epsilon_\infty$	
[eV]	[eV]	[eV]	[ $m_0$ ]	[ $m_0$ ]	[ $m_0$ ]	[1/eV]	[1/eV]	[1/eV]	[meV]	[-]	[-]	
0.69	2.47	3.399	0.04	0.25	1	1.413	0	0	73	15.3	8.4	[221]
0.7	-	-	0.07	-	-	-	-	-	-	9.3	6.7	[228]
<b>0.69</b>	2.47	3.399	0.04	0.25	1	1.413	0	0	75/89	11.0	6.7	

**Table 3.5:** Summary of elastic constants of InN and the resulting longitudinal and transverse elastic constants and sound velocities.

$c_{11}$	$c_{12}$	$c_{44}$	$c_L$	$c_T$	$\nu_{sl}$	$\nu_{st}$	Ref.
[GPa]	[GPa]	[GPa]	[GPa]	[GPa]	[m/s]	[m/s]	
-	-	-	265	44	6240	2550	[176]
223	115	48	218	50	5660	2720	[168]
190	104	10	163	23	4901	1845	[229]
271	124	46	248	57	6046	2893	[167]
258	113	53	242	61	5966	2987	[230]

electric scattering which is the dominant mobility limitation factor at low concentrations (see Fig. 3.9). Fig. 3.10 shows the mobility as a function of concentration for various values of the polar-optical phonon scattering coefficient and the high-frequency dielectric constant. Choosing the lower value results in a much higher maximum mobility, while the dependence on the

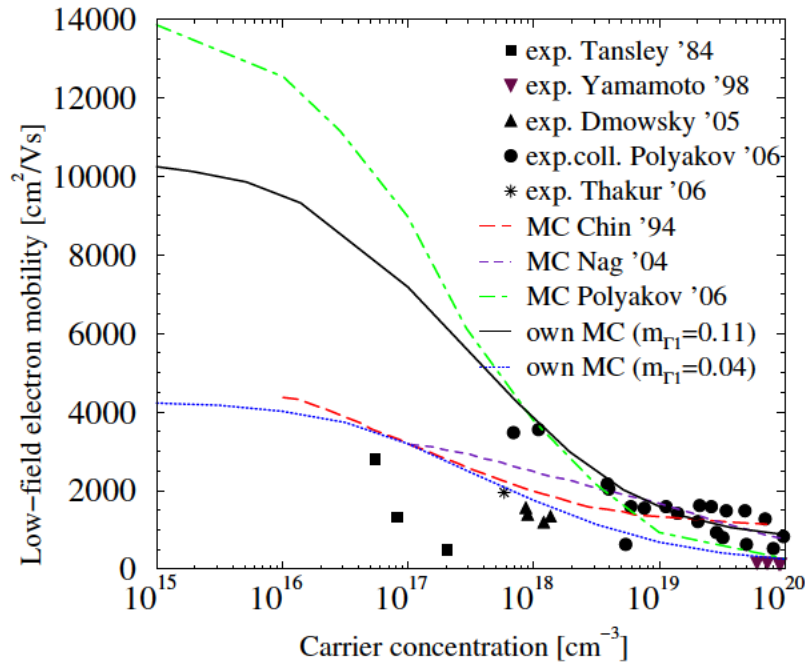


**Figure 3.8:** Low-field electron mobility as a function of carrier concentration in InN: Comparison of the MC simulation results and experimental data.

scattering coefficient is lower.

Fig. 3.11 shows the electron drift velocity versus electric field at  $10^{17} \text{ cm}^{-3}$  carrier concentration. Our MC simulation results differ compared to simulation data from other groups [221], [225], [229], [235] either due to piezoelectric scattering at lower fields or, at high fields, due to the choice of parameters for the permittivity and polar optical phonon energy ( $\hbar\omega_{\text{LO}}$ ). Fig. 3.12 shows our simulation results obtained with  $m_{\Gamma_1}=0.04m_0$  and with different values of the permittivity and phonon energy. The values  $\epsilon_{\infty}=6.7$  and  $\epsilon_s=11.0$  proposed in [222] lead to lower electron velocities. Fig. 3.13 confirms that first the polar optical phonon scattering and then the acoustic deformation potential and inter-valley phonon scattering rates increase with higher electric field, and are therefore decisive for the NDM effects.

**Table 3.6:** Summary of piezoelectric coefficients of InN for MC simulation of piezoelectric scattering.

$e_{31}$	$e_{33}$	$\langle e_L^2 \rangle$	$\langle e_T^2 \rangle$	Ref.
[C/m <sup>2</sup> ]	[C/m <sup>2</sup> ]	[C <sup>2</sup> /m <sup>4</sup> ]	[C <sup>2</sup> /m <sup>4</sup> ]	
-0.57	0.97	0.17	0.72	[224]
-0.11	0.81-1.09	0.13	0.16-0.58	[174]

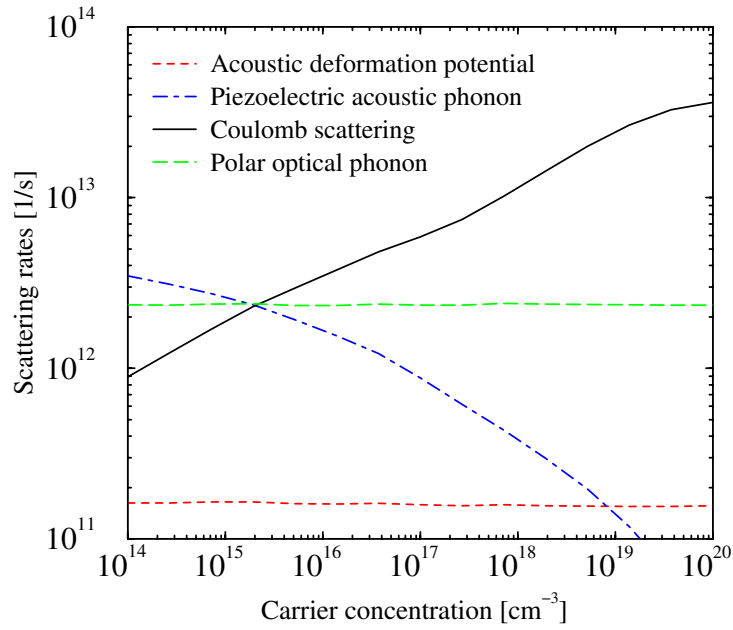


**Figure 3.9:** Illustration of the scattering rates in our simulation for wurtzite InN as a function of carrier concentration at 300 K.

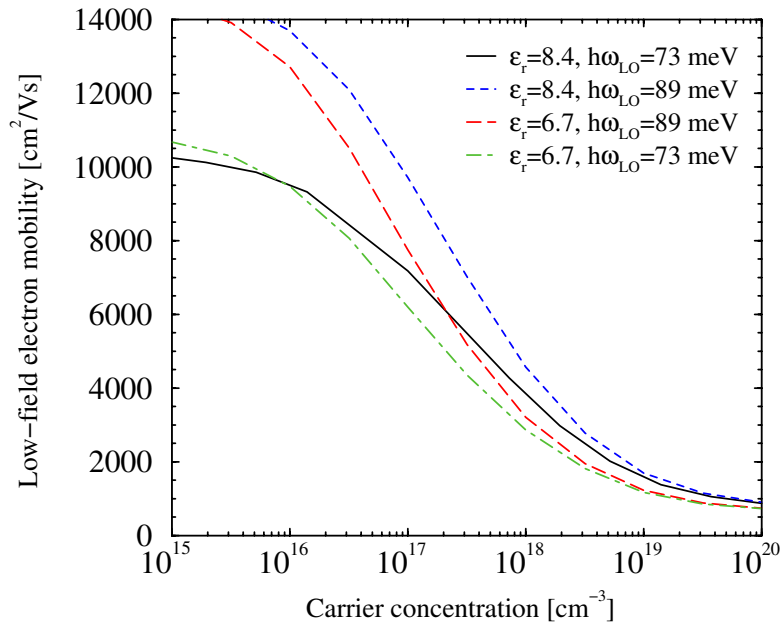


**Figure 3.10:** Low-field electron mobility as a function of carrier concentration in InN: Comparison of the MC simulation results with different setups.

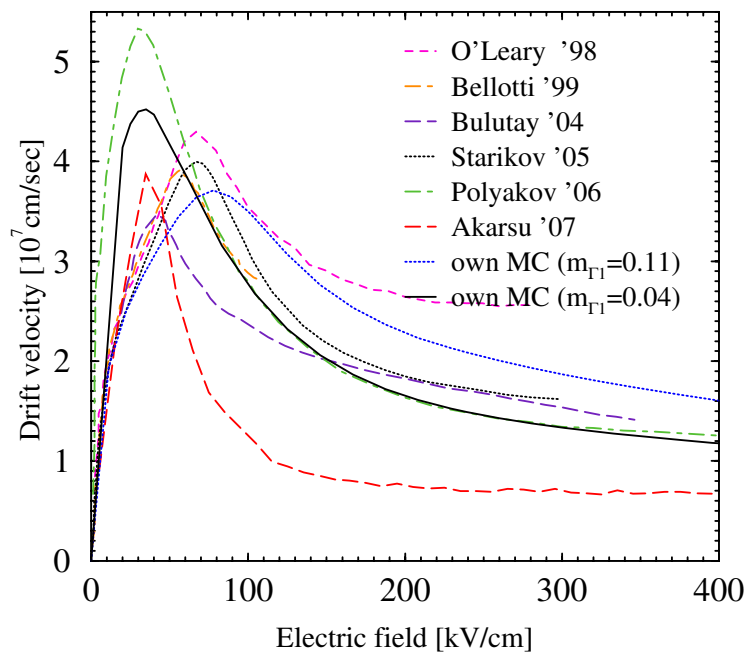


**Figure 3.11:** Drift velocity versus electric field in wurtzite InN: Comparison of MC simulation results.

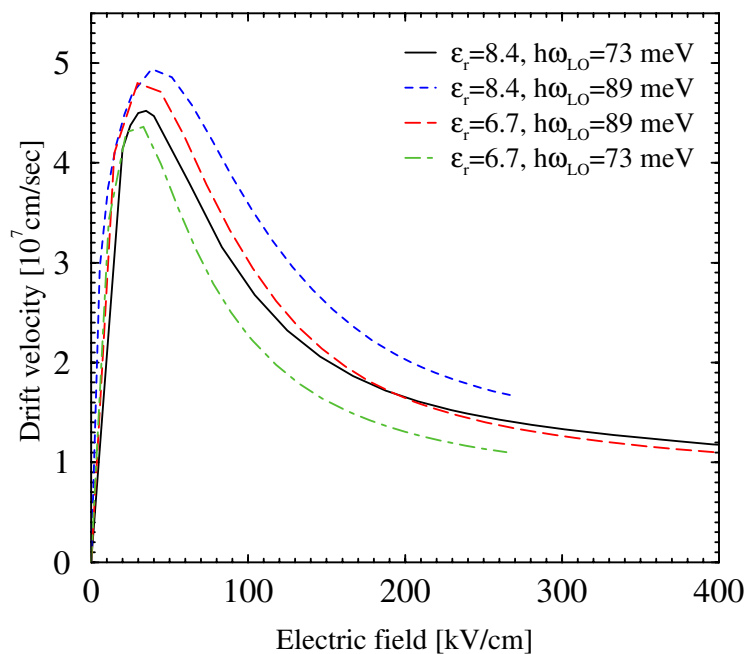


**Figure 3.12:** Drift velocity versus electric field in wurtzite InN: MC simulation results with different parameter setups.

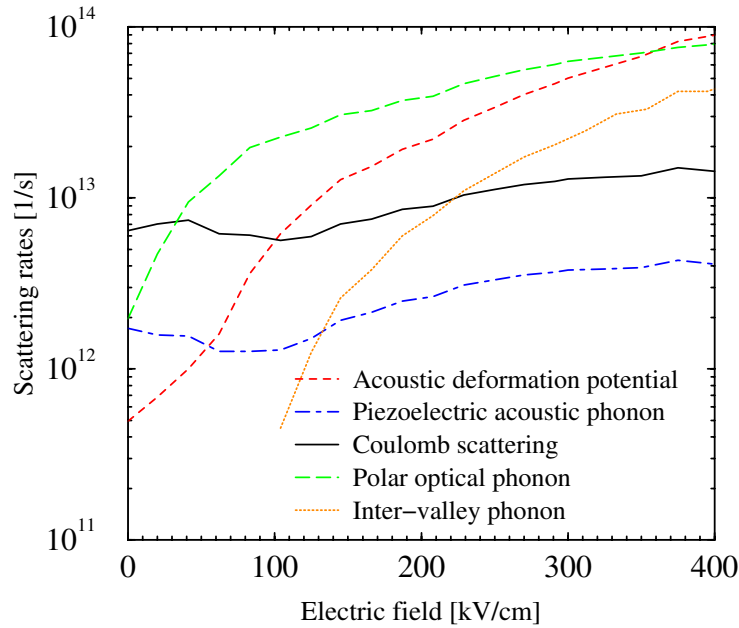


**Figure 3.13:** Illustration of the scattering rates in our simulation for wurtzite InN as a function of electric field.

### 3.3.3 Hole Transport

As in GaN, p-type conductivity in InN has proven to be difficult to achieve. Even though the valence band edge lies 1.6 eV below the Fermi level stabilization energy [236], the low position of the conduction band edge makes efficient p-type doping very difficult. Another issue is the pinning of the surface Fermi level above the conduction band edge, due to native donor defects, which leads to a n-type accumulation layer at the surface [237], [238]. Any study of p-type bulk material has to isolate the effects of this accumulation layer. This was achieved by Jones *et al.*, who provided the first indirect evidence of a net concentration of acceptors, but who were however unable to verify the presence of free holes [239]. Later works were not yet able to demonstrate net p-type conductivity [240], but an activation energy for the Mg acceptor of about 61 meV was extracted by photoluminescence measurements [241]. Using the same value for the activation energy Wang *et al.* [242] calculated a hole mobility in the range of 17–36 cm<sup>2</sup>/Vs for a hole concentration of about  $(1.4\text{--}3.0) \times 10^{18}$  cm<sup>-3</sup>. However, they used a suggested effective hole mass value ( $0.42m_0$ ) [243], which was not experimentally confirmed. The same value was adopted by Fujiwara *et al.* [244], who reported mobilities of 25–70 cm<sup>2</sup>/Vs. Recent works agree [245], that free holes can be detected only for moderate Mg contents. Most of the evidences of electrical conductance related to free electrons are yet to be confirmed.

## 3.4 Aluminum Nitride

Table 3.8 summarizes the experimental and theoretical values of the elastic constants  $c_{11}$ ,  $c_{12}$ , and  $c_{44}$ , available for wurtzite AlN in the literature. From these the corresponding  $c_L$ ,  $c_T$ ,  $v_{sl}$ , and  $v_{st}$  are calculated. The experimental values from [165] are adopted in the MC simulation.

**Table 3.7:** Summary of material parameters of wurtzite AlN for Monte Carlo simulation.

Bandgap energy			Electron mass			Non-parabolicity			Scattering models					Ref.	
$\Gamma_1$	U	$\Gamma_3$	$m_{\Gamma_1}$	$m_U$	$m_{\Gamma_3}$	$\alpha_{\Gamma_1}$	$\alpha_U$	$\alpha_{\Gamma_3}$	ADP	$\hbar\omega_{ij}$	$\hbar\omega_{LO}$	$\rho$	$\epsilon_r$	$\epsilon_\infty$	
[eV]	[eV]	[eV]	[ $m_0$ ]	[ $m_0$ ]	[ $m_0$ ]	[1/eV]	[1/eV]	[1/eV]	[eV]	[meV]	[meV]	[g/cm <sup>2</sup> ]	[-]	[-]	
6.20	6.90	-	0.48	1.0	-	0.044	0	-	9.5	99.2	99.2	3.23	8.5	4.77	[246]
5.84	7.00	8.29	0.326	0.384	0.473	0.29	-	-	9.5	75.8	110.3	3.23	8.5	4.46	[155]
6.00	7.05	8.49	0.26	0.495	0.55	0.207	0.035	0.023	-	76.1	110.7	-	-	4.68	[247]
6.20	6.90	8.20	0.33	0.40	0.50	0.044	0	0	9.5	99.2	99.2	3.23	8.5	4.77	

Table 3.9 summarizes the experimental and theoretical values of the piezoelectric coefficients  $e_{15}$ ,  $e_{31}$ , and  $e_{33}$ .

Fig. 3.14 compares the MC simulation result for AlN against others from [253], [246], [254]. The simulation results are in good agreement with [253], [246], since similar MC parameters are used as shown in Table 3.7. The difference visible at high fields can be explained by different effective electron masses used in the higher valleys. The simulation of [254] differs at low fields, since it ignores some mechanisms, e.g. ionized-impurity scattering.

**Table 3.8:** Summary of elastic constants of AlN and the resulting longitudinal and transverse elastic constants and sound velocities.

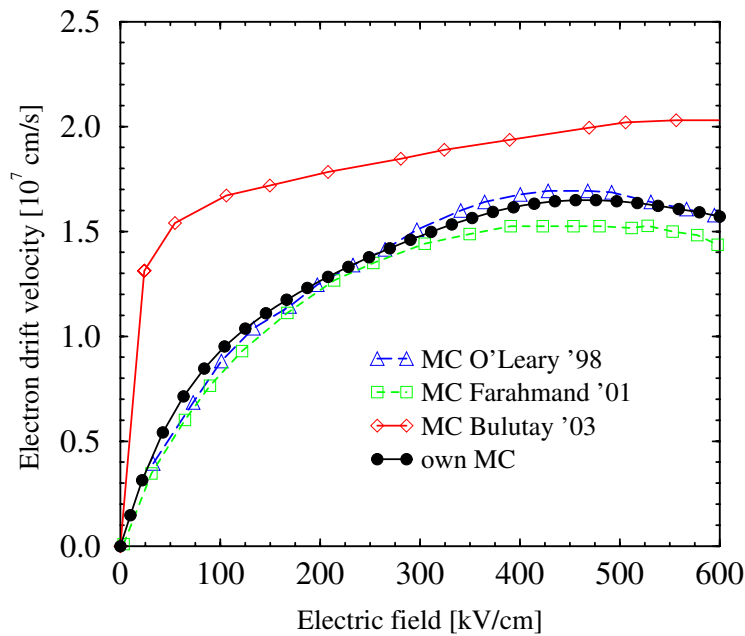
$c_{11}$	$c_{12}$	$c_{44}$	Data	Refs.	$c_L$	$c_T$	$v_{sl}$	$v_{st}$
[GPa]	[GPa]	[GPa]			[GPa]	[GPa]	[m/s]	[m/s]
345	125	118	exp.	[248]	351	115	10430	5962
411	149	125	exp.	[249]	406	127	11214	6280
410	140	120	exp.	[165]	398	126	11100	6246
380	114	109	calc.	[250]	361	119	10569	6060
464	149	128	calc.	[251]	440	140	11677	6579
424	103	138	calc.	[166]	406	147	11211	6746
398	140	96	calc.	[167]	372	109	10726	5814
396	137	116	calc.	[168]	385	121	10920	6131
398	142	127	calc.	[169]	397	127	11089	6280

**Table 3.9:** Summary of piezoelectric coefficients of AlN for Monte Carlo simulation of piezoelectric scattering.

$e_{15}$	$e_{31}$	$e_{33}$	Data	Refs.	$\langle e_{\perp}^2 \rangle$	$\langle e_{\parallel}^2 \rangle$
[C/m <sup>2</sup> ]	[C/m <sup>2</sup> ]	[C/m <sup>2</sup> ]	Data	Refs.	[C <sup>2</sup> /m <sup>4</sup> ]	[C <sup>2</sup> /m <sup>4</sup> ]
-0.48	-0.58	1.55	exp.	[248]	0.251	0.304
-	-0.60	1.50	exp.	[171]	0.260	0.334
-0.29	-0.58	1.39	exp.	[252]	0.102	0.230
-	-0.60	1.46	calc.	[172]	0.251	0.326
-	-0.38	1.29	calc.	[169]	0.169	0.187
-	-0.64	1.80	calc.	[174]	0.349	0.429

### 3.5 Ternary Alloys

Transport simulation of III-V ternaries (and especially AlGaIn) have always suffered under the empirical nature of the alloy scattering models. As reported by Chin *et al.* [255] the alloy scattering is the most important scattering mechanism to consider in the ternary nitrides, as it is the only one to exhibit a "bowing" behavior with changing composition. While the other

**Figure 3.14:** Drift velocity versus electric field in wurtzite AlN: Comparison of MC simulation results.

material properties [256] used in this approach are well known, the alloy scattering potential is still debated.

**AlGaN** The alloy scattering potential was determined based on the Philips' electronegativity theory [255]. The calculations showed, that alloy scattering is extremely pronounced in InAlN and InGaN (especially at low temperatures around 77 K), while it is mostly insignificant in AlGaN. Further works neglected it [257], [154], however some explored the extreme cases [155] and observed that it can become dominant for the largest predicted values of the alloy scattering potential. A convenient way to calculate the latter was chosen in [247], where a value equal to half of the AlN/GaN conduction band energy offset was used. A self-consistent approach to calculate the alloy scattering rate by fitting it to a semi-empirical energy-dependent expression was proposed in [258] and yielded good agreement with low temperature measurements. Also some experimental results from indirect measurements are already available [259].

**InGaN** A value of 0.6–0.65 eV for the alloy scattering potential was calculated by [255] for InGaN. [260] used a slightly lower value of 0.55 eV, while [228] choose the InN/GaN conduction band energy offset as the potential.

**InAlN** The calculation of [255] yielded a value of 0.6 eV for the alloy scattering potential, while [228] used the InN/AlN conduction band energy offset.



---

# Physical Models

---

**M**ODELS which account for the specific physics in a given semiconductor device are crucial for device modeling. This chapter starts with a discussion of the carrier transport models used, and their boundary conditions, and finally introduces lattice, thermal, and transport properties of the relevant materials. The latter also includes a discussion on polarization effects characteristic to III-N semiconductors and essential to HEMT structures.

### 4.1 Semiconductor Equations

The *Boltzmann* transport equation (BTE) provides the fundament for the semiclassical description of carrier transport in semiconductor devices. As a numerical solution is prohibitive due to the extraordinary high computational expenses, several approximations to derive simpler solutions exist. Those differ widely in their computational demand and physical accuracy. This work focuses on the drift-diffusion (DD) transport model and the hydrodynamic (HD) transport model. The former is a simple model, well established today in TCAD tools, while the latter is a higher-order model capable of describing non-local effects. Several other approaches also exist, like the Monte Carlo approach [261] or the method of spherical harmonics [262] for instance, however those are beyond the scope of this engineering-oriented work.

The basic semiconductor equations include *Poisson's* equation, the two current continuity equations and the two current relation equations. The first three are shared by both the DD and HD transport models, however the current relations have different formulations for each model.

#### 4.1.1 Maxwell's Equations

The basic equations solved in a device simulator can be derived from Maxwell's equations. The four partial differential equations relate the electric field ( $\mathbf{E}$ ), the displacement field ( $\mathbf{D}$ ), the magnetic field ( $\mathbf{H}$ ), and the induction field ( $\mathbf{B}$ ) vectors to the current density ( $\mathbf{J}$ ) and the

electric charge density ( $\rho$ ):

$$\nabla \times \mathbf{H} = \mathbf{J} + \frac{\partial \mathbf{D}}{\partial t} \quad (4.1)$$

$$\nabla \times \mathbf{E} = -\frac{\partial \mathbf{B}}{\partial t} \quad (4.2)$$

$$\nabla \cdot \mathbf{D} = \rho \quad (4.3)$$

$$\nabla \cdot \mathbf{B} = 0. \quad (4.4)$$

### 4.1.2 Poisson Equation

The *Gauß's* law for magnetism (4.4) is satisfied by introduction of the vector potential  $\mathbf{A}$  as:

$$\mathbf{B} = \nabla \times \mathbf{A} \quad (4.5)$$

Inserting (4.5) into (4.2) yields

$$\mathbf{E} = -\frac{\partial \mathbf{A}}{\partial t} - \nabla \psi. \quad (4.6)$$

Substituting this into the relation of the electric displacement and the electric field

$$\mathbf{D} = \epsilon \cdot \mathbf{E} \quad (4.7)$$

results into

$$\nabla \cdot \left( \epsilon \cdot \frac{\partial \mathbf{A}}{\partial t} \right) + \nabla \cdot (\epsilon \cdot \nabla \psi) = -\rho. \quad (4.8)$$

The permittivity is considered to be homogenous, therefore the first term in (4.8) is zero due to the definition of  $\mathbf{A}$  (4.5), so the conventional form of the *Poisson* equation is obtained:

$$\nabla \cdot (\epsilon \cdot \nabla \psi) = -\rho. \quad (4.9)$$

The space charge density  $\rho$  can be expressed as the product of the elementary charge  $q$  and the sum of the electron  $n$  and hole  $p$  concentrations and the net concentration of ionized dopants  $C_{\text{net}}$ :

$$\rho = q \cdot (n - p - C_{\text{net}}). \quad (4.10)$$

Substituting (4.10) into (4.9) gives:

$$\nabla \cdot (\epsilon \cdot \nabla \psi) = q \cdot (n - p - C_{\text{net}}). \quad (4.11)$$

### 4.1.3 Continuity Equations

In order to obtain the continuity equations from the first *Maxwell* equation (4.1) the current density  $\mathbf{J}$  has to be split in an electron and hole component  $\mathbf{J}_n$  and  $\mathbf{J}_p$ . Assuming the net concentration of ionized dopants  $C_{\text{net}}$  is time-invariant the following equation is obtained:

$$\nabla \cdot (\mathbf{J}_n + \mathbf{J}_p) + q \cdot \frac{\partial}{\partial t}(p - n) = 0. \quad (4.12)$$

(4.12) can be expressed in two different ways with the help of the quantity  $R$ :

$$\nabla \cdot \mathbf{J}_n - q \cdot \frac{\partial n}{\partial t} = q \cdot R, \quad (4.13)$$

$$\nabla \cdot \mathbf{J}_p + q \cdot \frac{\partial p}{\partial t} = -q \cdot R. \quad (4.14)$$

This formulation gives  $R$  the meaning of the net generation or recombination of electrons and holes. As such, it can be modeled for the respective recombination/generation mechanisms, thereby (4.13) and (4.14) can be considered as two equations.

#### 4.1.4 The Drift-Diffusion Transport Model

The drift-diffusion transport model is the simplest macroscopic transport model based on the solution of the semi-classical *Boltzmann's* transport equation. Together with higher-order macroscopic transport models it is only valid in device operation modes, where quantum effects are negligible. In order to account for such effects several quantum mechanical models were developed. Those, however are beyond the scope of this work and a detailed discussion can be found e.g. in [263].

There are two methods to derive the DD transport model from the BTE: by the method of the moments [264] and from basic principles of irreversible thermodynamics [265]. In the former the BTE is multiplied by a set of weight functions and integrated over the momentum space. The DD transport model takes only the first two moments into account. However, specific to the moments method, each equation of a given moment contains also the next higher moment. Thus, the equation system is under-defined. In order to address this problem (the so called *closure problem*), the carriers are assumed to be in thermal equilibrium with the lattice ( $T_n = T_p = T_L$ ). This yields:

$$\mathbf{J}_n = qn\mu_n \mathbf{E} + k_B \mu_n \nabla (nT_L) \quad (4.15)$$

for electrons, where  $\mu_n$  is the electron mobility and  $k_B$  is the Boltzmann constant. From now on the equivalent equations for holes are omitted as they can be easily derived from those for electrons.

The DD transport model was the de-facto standard model for semiconductor device simulations for many years due to its excellent convergence behavior and relatively low computational cost. However, its major drawback is that it cannot account for non-local effects such as e.g. velocity overshoot and real-space transfer.

#### 4.1.5 The Hydrodynamic Transport Model

The hydrodynamic transport model is again obtained from the BTE by the moment methods, however it accounts for the first three moments instead of only two as the DD transport model.

The resulting equations are:

$$\mathbf{J}_n = qn\mu_n\mathbf{E} + k_B\mu_n\nabla(T_n n), \quad (4.16)$$

$$\nabla \cdot \mathbf{S}_n = \mathbf{E}\mathbf{J}_n - \frac{3k_B}{2} \left( \frac{\partial n T_n}{\partial t} + R T_n + n \frac{T_n - T_L}{\tau_{\epsilon,n}} \right), \quad (4.17)$$

$$\mathbf{S}_n = -\frac{5k_B T_n}{2q} \mathbf{J} + \mathbf{Q}_n, \quad (4.18)$$

for electrons, where  $\mathbf{S}_n$  is the energy heat flux,  $T_n$  is the electron temperature,  $\mathbf{Q}_n$  is the heat flow, and  $\tau_{\epsilon,n}$  is the energy relaxation time of the electrons. The model is closed by using *Fourier's law* for the heat term  $\mathbf{Q}_n$ :

$$\mathbf{Q}_n = -\kappa_n \nabla T_n \quad (4.19)$$

where  $\kappa_n$  is the thermal conductivity. The latter is calculated by the *Wiedemann-Franz law*, proportional to the mobility  $\mu_n$  and carrier temperature  $T_n$ :

$$\kappa_n = \left( \frac{5}{2} + c_n \right) \frac{k_B^2}{q} \mu_n n T_n \quad (4.20)$$

The factor  $c_n$  ( $c_p$  for holes, respectively) is set to zero so that both terms of (4.18) have the same factor and any inconsistency can be avoided. The model obtained is actually an energy transport model as the moment equations were derived under the assumption that the average kinetic energy of the carriers is negligible in comparison to their thermal energy:

$$\frac{m_n v_n^2}{2} \ll \frac{3k_B T_n}{2} \quad (4.21)$$

However, since in literature the terms *energy transport* and *hydrodynamic transport* are often used interchangeably, the name *hydrodynamic transport* is further retained.

#### 4.1.6 The Lattice Heat Flow Equation

Self-heating effects are accounted for by including the lattice heat flow equation

$$\nabla \cdot (\kappa_L \nabla T_L) = \rho_L c_L \frac{\partial T_L}{\partial t} + H \quad (4.22)$$

in the system of partial differential equations.  $\rho_L$  and  $c_L$  are the mass density and the specific heat, respectively. The heat generation term  $H$  depends on the transport model used.

Due to the assumption that the carrier temperature does not deviate from the lattice temperature in the DD model, the energy relaxation times are zero and the heat generation reads:

$$H = E J_n + E J_p + R \mathcal{E}_g. \quad (4.23)$$

The last term in (4.23) gives the recombination heat transferred to the lattice and is proportional to the net recombination  $R$  and the band gap energy  $\mathcal{E}_g$ .

In the HD transport model, the heat generation is obtained by substituting the local energy balance equations (here only for electrons):

$$E^2 \mu = \frac{3k_B(T_n - T_L)}{2q\tau_\epsilon} \quad (4.24)$$

in the DD heat generation term (4.23). The resulting expression reads:

$$H = \frac{3k_B}{2} \left( n \frac{T_n - T_L}{\tau_{\epsilon,n}} + p \frac{T_p - T_L}{\tau_{\epsilon,p}} \right) + R\mathcal{E}_g. \quad (4.25)$$

This solution is obtained from the stationary energy flux balance and the carrier continuity equations (4.13), (4.14). The first term approximates the energy relaxation of the scattering terms of the *Boltzmann* equation [266].

An alternative global self-heating model also exists [267]. By calculating a spatially constant lattice temperature it delivers similar results to the standard model, at greatly reduced computational expenses.

#### 4.1.7 Insulator Equations

In insulating materials only the *Poisson* equation (4.11) and the lattice heat flow equation (4.22) are solved. The carrier continuity equations are not solved because doping and mobile carriers are neglected. This reduces the *Poisson* equation to the *Laplace* equation:

$$\nabla \cdot (\epsilon \nabla \psi) = 0. \quad (4.26)$$

The heat generation term in (4.22) is also neglected:

$$\nabla \cdot (\kappa_L \nabla T_L) = \rho_L c_L \frac{\partial T_L}{\partial t}. \quad (4.27)$$

As a result neither carriers nor current are considered in insulators, however the consideration of charges at semiconductor/insulator interfaces is unaffected.

#### 4.1.8 Boundary Conditions

For the solution of the semiconductor equations a closed domain is required. Boundary conditions for the unknowns in a certain segment must be specified at the boundaries of that segment. Depending on the number of segments (one or two) and the type of the quantity of the unknown (distributed or non-distributed) several model types can be separated [267]. However, in order to illustrate the basic boundary conditions such a differentiation is not needed and therefore not provided here.

##### 4.1.8.1 Artificial Boundaries

The simulation domain usually includes only a single device. In order to separate it from the neighboring devices artificial boundaries, which have no physical origin, are introduced. Through

the *Neumann* boundary conditions a self-contained domain is guaranteed. The fluxes across the boundary are set to zero:

$$\mathbf{n} \cdot \mathbf{E} = 0, \quad \mathbf{n} \cdot \mathbf{J}_{n,p} = 0, \quad \mathbf{n} \cdot \mathbf{S}_{n,p} = 0, \quad \mathbf{n} \cdot \mathbf{S}_L = 0. \quad (4.28)$$

$\mathbf{n}$  is an outward-orientated vector normal to the boundary. (4.28) define the boundary conditions for a semiconductor segment, while for an insulator the first two conditions are sufficient.

#### 4.1.8.2 Semiconductor/Metal

**Ohmic Contact:** Ohmic contacts are defined by *Dirichlet* boundary conditions: the contact potential  $\psi_s$ , the carrier contact concentration  $n_s$  and  $p_s$ , and in the case of a HD simulation the carrier contact temperatures  $T_n$  and  $T_p$  are fixed. The metal quasi-*Fermi* level (which is specified by the contact potential  $\psi_m$ ) is equal to the semiconductor quasi-*Fermi* level. The model assumes charge-neutrality on the boundary. The contact potential at the semiconductor boundary is:

$$\psi_s = \psi_m + \varphi_{bi}, \quad (4.29)$$

where  $\varphi_{bi}$  is the built-in potential:

$$\varphi_{bi} = \frac{k_B T_L}{q} \ln \left( \frac{1}{2C_1} \left( C_{net} + \sqrt{C_{net}^2 + 4C_1 C_2} \right) \right) \quad (4.30)$$

$$= -\frac{k_B T_L}{q} \ln \left( \frac{1}{2C_2} \left( -C_{net} + \sqrt{C_{net}^2 + 4C_1 C_2} \right) \right). \quad (4.31)$$

$C_{net}$  is the net concentration of dopants and other charged defects at the contact boundary. The variables  $C_1$  and  $C_2$  are defined by [268]

$$C_1 = N_C \exp \left( \frac{-\mathcal{E}_c}{k_B T_L} \right) \quad (4.32)$$

$$C_2 = N_V \exp \left( \frac{-\mathcal{E}_v}{k_B T_L} \right) \quad (4.33)$$

where  $N_C$  and  $N_V$  are the effective density of states.

The carrier concentrations in the semiconductor are pinned to the equilibrium carrier concentrations at the contact:

$$n_s = N_C \exp \left( \frac{-\mathcal{E}_c + q\varphi_{bi}}{k_B T_L} \right) \quad (4.34)$$

$$p_s = N_V \exp \left( \frac{\mathcal{E}_v - q\varphi_{bi}}{k_B T_L} \right) \quad (4.35)$$

This model works properly, only if a high doping ( $\geq 10^{18} \text{cm}^{-3}$ ) in the semiconductor is guaranteed.

The carrier temperatures  $T_n$  and  $T_p$  are set equal to the lattice temperature  $T_L$ :

$$T_n = T_L, \quad T_p = T_L. \quad (4.36)$$

**Thermal Interface:** If a contact temperature  $T_C$  is specified, the lattice temperature is calculated using  $T_C$  and a thermal resistance  $R_T$ . The thermal heat flow density  $\mathbf{S}_L$  at the contact boundary reads:

$$\mathbf{n} \cdot \mathbf{S}_L = \frac{T_L - T_C}{R_T}. \quad (4.37)$$

If no thermal resistance is specified, an isothermal boundary condition is assumed and the lattice temperature  $T_L$  is set equal to the contact temperature:

$$T_L = T_C. \quad (4.38)$$

In case of a DD simulation with self-heating an additional thermal energy is accounted for. It is generated, when the carriers transcend the potential difference between the conduction or valence band and the metal quasi-Fermi level. The energy equation reads:

$$\mathbf{J}_n \left( \frac{\mathcal{E}_c}{q} + \varphi_m \right) + \mathbf{J}_p \left( \frac{\mathcal{E}_v}{q} + \varphi_m \right) = \nabla \cdot \mathbf{S}_L. \quad (4.39)$$

The expression  $\nabla \cdot \mathbf{S}_L$  denotes the surface divergence of the thermal heat flux at the boundary considered. In case of a HD simulation with self-heating the thermal heat flow across the boundary is accounted for self-consistently.

**Metal Resistance:** It is possible to include an electric line resistance of the contact  $R_C$  using:

$$\psi_m = V_C - I_C R_C \quad (4.40)$$

with  $V_C$  the applied terminal voltage and  $I_C$  the current through the contact.

**Schottky Contact:** At the *Schottky* contact mixed boundary conditions apply. The contact potential  $\psi_s$ , the carrier contact concentration  $n_s$  and  $p_s$ , and in the case of a HD simulation, the contact carrier temperatures  $T_n$  and  $T_p$  are fixed. The semiconductor contact potential is the difference between the metal quasi-Fermi level and the metal work function difference  $\psi_w$ :

$$\psi_s = \psi_m - \psi_w \quad (4.41)$$

where

$$\psi_w = -\frac{\mathcal{E}_w}{q}. \quad (4.42)$$

The difference between the conduction band energy  $\mathcal{E}_c$  and the metal work function energy gives the work function difference energy  $\mathcal{E}_w$ , which is the so called barrier height of the *Schottky* contact, also denoted as  $\phi_B$ . The applied boundary conditions are:

$$\mathbf{n} \cdot \mathbf{J}_n = -qv_n(n_0 - n_s) \quad (4.43)$$

$$\mathbf{n} \cdot \mathbf{J}_p = qv_p(p_0 - p_s), \quad (4.44)$$

where  $v_n$  and  $v_p$  are the recombination velocities. The carrier concentrations read:

$$n_s = N_C \exp\left(-\frac{\mathcal{E}_c - \mathcal{E}_w}{k_B T_L}\right) \quad (4.45)$$

$$p_s = N_V \exp\left(\frac{\mathcal{E}_v - \mathcal{E}_w}{k_B T_L}\right), \quad (4.46)$$

where  $\mathcal{E}_f$  is the *Fermi* level in the semiconductor. If the values of  $v_n$  and  $v_p$  are set to zero, the current through the *Schottky* contact is suppressed. The *Schottky* contact boundary conditions for the carrier temperatures  $T_n$  and  $T_p$  and for the lattice temperature are similar to those which apply for the Ohmic contact: (4.36) and (4.37) or (4.38).

For the equilibrium situation, the quasi-equilibrium concentrations  $n_0$  and  $p_0$  can be rewritten:

$$n_0 = N_C \exp\left(\frac{-\phi_B}{k_B T_L}\right) \quad (4.47)$$

$$p_0 = N_V \exp\left(\frac{-\phi_B}{k_B T_L}\right). \quad (4.48)$$

The recombination velocities are calculated from:

$$v_n = A^* \frac{T_L^2}{q N_C} \quad (4.49)$$

where  $A^*$  is the *Richardson* constant.

Typical values for the *Schottky* barrier heights of common semiconductor barriers are listed in Table 4.1. Values measured by different methods (*I-V* and *C-V*) for n-GaN/metal differ significantly. This is caused by defects in the surface region, which enhance the tunneling effect and therefore have an impact on the *Richardson* constant [269], [270]. The exact value of the barrier height depends also on orientation, stress, and polarity of the GaN layer [271]. No data is provided for contacts on InN as most metals show ohmic behavior [272]. *Schottky* barrier height varies with annealing temperature: generally it is reduced after annealing.

#### 4.1.8.3 Insulator/Metal

A model similar to the *Schottky* contact model is used to calculate the insulator contact potential. The semiconductor contact potential is the difference of the metal quasi-*Fermi* level and the metal work function difference potential similar to (4.41) and (4.42). The lattice temperature is set equal to the contact temperature (4.38).

#### 4.1.8.4 Semiconductor/Insulator

In the absence of surface charges the normal component of the dielectric displacement and the potential are continuous:

$$\mathbf{n} \cdot \varepsilon_s \mathbf{E}_s - \mathbf{n} \cdot \varepsilon_{\text{ins}} \mathbf{E}_{\text{ins}} = 0, \quad \psi_s = \psi_{\text{ins}}. \quad (4.50)$$



**Table 4.1:** Schottky barrier heights of common contacts.

Materials	$\phi_B$ [eV]	Ref.	Materials	$\phi_B$ [eV]	Ref.
n-GaN/Au	0.87-1.1	[273], [274]	$\text{In}_x\text{Al}_x\text{N}/\text{Pd}$	1.56	[275]
n-GaN/Ni	0.95-1.13	[273]	$\text{In}_{0.17}\text{Al}_{0.83}\text{N}/\text{Ni}$	0.75	[276]
p-GaN/Ni	2.68-2.87	[277]	$\text{p-In}_{0.15}\text{Ga}_{0.85}\text{N}/\text{Ni}$	0.39	[278]
$\text{Al}_{0.11}\text{Ga}_{0.89}\text{N}/\text{Ni}$	0.94-1.24	[279]	$\text{In}_{0.1}\text{Ga}_{0.9}\text{N}/\text{Pt}$	0.62	[270]
$\text{Al}_{0.15}\text{Ga}_{0.85}\text{N}/\text{Ni}$	1.26	[280]	$\text{In}_{0.1}\text{Ga}_{0.9}\text{N}/\text{Ni}$	1.39	[270]
$\text{Al}_{0.23}\text{Ga}_{0.77}\text{N}/\text{Ni}$	1.02-1.30	[279]	$\text{Al}_{0.07}\text{In}_{0.02}\text{GaN}/\text{Ni}$	0.98-0.93	[281]

In the presence of surface charges along the interface, the dielectric displacement obeys the law of *Gauß*:

$$\mathbf{n} \cdot \varepsilon_s \mathbf{E}_s - \mathbf{n} \cdot \varepsilon_{\text{ins}} \mathbf{E}_{\text{ins}} = \sigma_s, \quad (4.51)$$

where  $\sigma_s$  is the interface charge density. This distributed surface charge is introduced to describe the *Fermi* level pinning at the surface due to a high trap density of states.

At the semiconductor/insulator interface the current densities and heat fluxes normal to the interface vanish.

$$\mathbf{n} \cdot \mathbf{J}_{n,p} = 0, \quad \mathbf{n} \cdot \mathbf{S}_{n,p} = 0 \quad (4.52)$$

The lattice temperature at the interface is continuous.

#### 4.1.8.5 Semiconductor/Semiconductor

The calculation of the electrostatic potential at the interfaces between two semiconductor segments is similar to that for semiconductor/insulator interfaces:

$$\mathbf{n} \cdot \varepsilon_{s1} \mathbf{E}_{s1} - \mathbf{n} \cdot \varepsilon_{s2} \mathbf{E}_{s2} = \sigma_s, \quad \psi_{s1} = \psi_{s2} \quad (4.53)$$

The interface charge can take any value including zero. The way to calculate the exact value depending on the materials is discussed in Section 4.5. The subscripts are used to distinguish between the two semiconductor segments on both sides of the interface.

To calculate the carrier concentrations and the carrier temperatures at the interface, three different approaches are considered:

- a model with continuous quasi-*Fermi* level across the interface (CQFL),
- a thermionic emission model,
- a thermionic field emission model.

Each model can be specified for electrons and holes for each semiconductor/semiconductor interface.

In the following  $J_n$  denotes the normal to the interface component of the current density  $\mathbf{J}$ ,  $S_n$  the energy flux density component, and  $\Delta E_\nu$  the difference in the conduction band edges  $\Delta \mathcal{E}_c$ . The effective electron mass is denoted by  $m_i$ . The subscripts denote the semiconductor segment  $i$ . Only the equations for electrons are given, those for holes can be deduced accordingly.

**Continuous Quasi-Fermi Level Model:** *Dirichlet* boundary conditions are applied, when the CQFL is used. The carrier concentrations are determined so that the quasi-Fermi levels remains continuous across the interface [134].

$$n_2 = n_1 \left( \frac{m_2}{m_1} \right)^{3/2} \exp \left( -\frac{\Delta \mathcal{E}_c}{k_B T_{n1}} \right) \quad (4.54)$$

$$T_{n1} = T_{n2} \quad (4.55)$$

$$J_{n2} = J_{n1} \quad (4.56)$$

$$S_{n2} = S_{n2} - \frac{1}{q} \Delta \mathcal{E}_c J_{n2} \quad (4.57)$$

The model is suitable for use at homojunctions. In Chapter 5 it is applied at the interface between segments of the same material but different characteristics (e.g. material quality). However, it is not suitable for heterojunctions, as it ignores the band gap alignment.

**Thermionic Emission and Thermionic Field Emission Model:** To consider the band gap alignment as typical in a heterostructure, the thermionic emission or thermionic field emission interface models must be used.

$$J_{n1} = J_{n2} \quad (4.58)$$

$$J_{n2} = q v_{n2} n_2 - q v_{n1} n_1 \frac{m_{n2}}{m_{n1}} \exp \left( -\frac{\Delta \mathcal{E}_c - \delta \mathcal{E}_c}{k_B T_{n1}} \right) \quad (4.59)$$

$$S_{n2} = S_{n1} - \frac{1}{q} (\Delta \mathcal{E}_c) J_{n2} \quad (4.60)$$

$$S_{n2} = -2k_B \left( T_{n2} v_{n2} n_2 + T_{n1} v_{n1} n_1 \frac{m_{n2}}{m_{n1}} \exp \left( -\frac{\Delta \mathcal{E}_c - \delta \mathcal{E}_c}{k_B T_{n1}} \right) \right) \quad (4.61)$$

(4.58) guarantees the particle conservation at the interface. (4.60) relates the energy and current fluxes on both sides of the interface. The second term corresponds to the conversion of potential energy into kinetic energy, when the electrons descend the step  $\Delta \mathcal{E}_c - \delta \mathcal{E}_c$ . (4.60) describes the thermionic emission across the energy barrier by relating the interface current to the quasi-Fermi level on both sides of the interface [134], [282]. The exponential factor in (4.59) and (4.61) shows that only the fraction of the total electron concentration on Side 1, which is energetically above the barrier, is able to cross the potential step. In both (4.59) and (4.61) the same emission velocities occur:

$$v_{ni}(T_{ni}) = \sqrt{\frac{2k_B T_{ni}}{\pi m_i}} \quad (4.62)$$

Tunneling can be included in this model by assuming that the tunnel effect lowers the barrier  $\Delta\mathcal{E}_c - \delta\mathcal{E}_c$ :

$$\delta\mathcal{E}_c = \begin{cases} qE_{\perp 2}d_{\text{tun}}, & E_{\perp 2} > 0 \\ 0, & E_{\perp 2} \leq 0 \end{cases} \quad (4.63)$$

The barrier lowering  $\delta\mathcal{E}_c$  depends on the electric field orthogonal to the interface  $E_{\perp 2}$  and the effective tunneling length  $d_{\text{tun}}$ . The latter is material dependent: for  $\text{Al}_{0.2}\text{Ga}_{0.8}\text{As}/\text{In}_{0.2}\text{Ga}_{0.8}\text{As}$  it is estimated to 7 nm [283] and for  $\text{Al}_{0.25}\text{Ga}_{0.75}\text{N}/\text{GaN}$  to 3 nm [138].

## 4.2 Lattice and Thermal Properties

The system of differential equations discussed in Section 4.1 contains several physical material parameters. A proper modeling is crucial for a successful device simulation. While some properties are well defined for most of the materials (such as lattice constants and mass density), others (such as thermal conductivity) were subject of numerous studies yielding equivocal results. Therefore, a discussion on the choice of model is required.

### 4.2.1 Permittivity

The dielectric constant of the three materials GaN, InN, and AlN is discussed in Section 3.2, Section 3.3, and Section 3.4, respectively. Here, the range of the reported values is shown in Table 4.2. The values used for the static permittivity for GaN, AlN, and InN are 8.9, 8.5, and 15.3, respectively.

**Table 4.2:** Model parameters for the static permittivity.

	GaN	AlN	InN	References
range	8.5-10.4	8.5	11.0-15.3	[284], [285], [176], [222]
used	8.9	8.5	15.3	

The permittivity of a ternary semiconductor alloy  $A_xB_{1-x}C$  depending on the material composition  $x$  is interpolated by a quadratic function of the permittivities of the basic materials  $\varepsilon_s^{\text{AC}}$  and  $\varepsilon_s^{\text{BC}}$  [286]:

$$\varepsilon_s^{\text{ABC}} = (1-x)\varepsilon_s^{\text{AC}} + x\varepsilon_s^{\text{BC}} \quad (4.64)$$

A linear interpolation is used for the three ternaries [287], [288].

### 4.2.2 Mass Density

The reported value ranges of the mass densities of the three materials are summarized in Table 4.3. For GaN, AlN, and InN values of  $6.15 \text{ g/cm}^3$ ,  $3.23 \text{ g/cm}^3$ , and  $6.81 \text{ g/cm}^3$ , respectively, are adopted. For the alloys a linear interpolation between the basic material values is used:

$$\rho_L^{\text{ABC}} = (1 - x)\rho_L^{\text{AC}} + x\rho_L^{\text{BC}}. \quad (4.65)$$

**Table 4.3:** Model parameters for the mass density [ $\text{g/cm}^3$ ].

Material	Range	Used	References
GaN	6.085–6.15	6.15	[289], [290]
AlN	3.23–3.26	3.23	[176], [291]
InN	6.81	6.81	[176]

### 4.2.3 Thermal Conductivity

The thermal conductivity is modeled by a power law:

$$\kappa(T_L) = \kappa_{300} \cdot \frac{T_L}{300 \text{ K}}^\alpha,$$

where  $\kappa_{300}$  is the value at 300 K. From early experiments  $\kappa_{300}=130 \text{ W/mK}$  for “bulk” GaN [292] was extracted. However, later measurements of epitaxial structures yielded higher values [293], and a strong dependence on the dislocation density was observed [294]. Based on various studies [292], [293], [295], [296], [297], [298] we give two parameter sets in Table 4.4, applicable for different material quality. Fig. 4.1 compares the two model sets with other models and experimental data.

For AlN the variation of the measured values for the thermal conductivity is smaller (Fig. 4.2). We assume  $\kappa_{300}=350 \text{ W/mK}$ , which is close to the value reported in [299]. The parameter  $\alpha$ , which models the decrease with temperature, is calibrated against measured data [299], [300], [301].

As of today no studies of the temperature dependent thermal conductivity of InN are available. Based on [302] a  $\kappa_{300}=176 \text{ W/mK}$  at 300 K is assumed. This is a theoretical estimation, while the measured value was only  $45 \text{ W/mK}$  due to phonon scattering by point-defects and grain-boundaries.

Several expressions exist for the thermal conductivity  $\kappa_{300}^{\text{ABC}}$  of semiconductor alloys. As an example, Adachi *et al.* [303] use one based on Abeles’s complex model [304]. However, an even more straightforward approach is proposed in [305], where a harmonic mean is used to

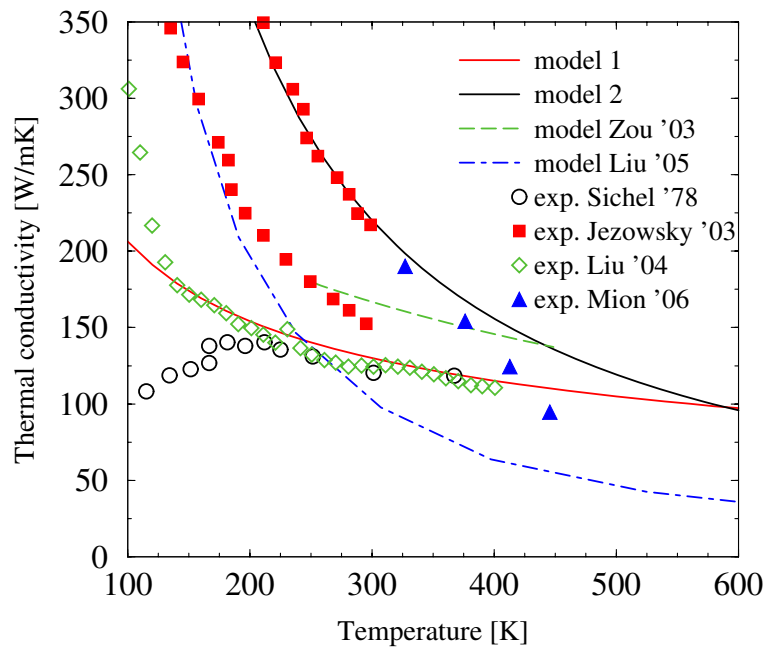


Figure 4.1: GaN thermal conductivity as a function of temperature.

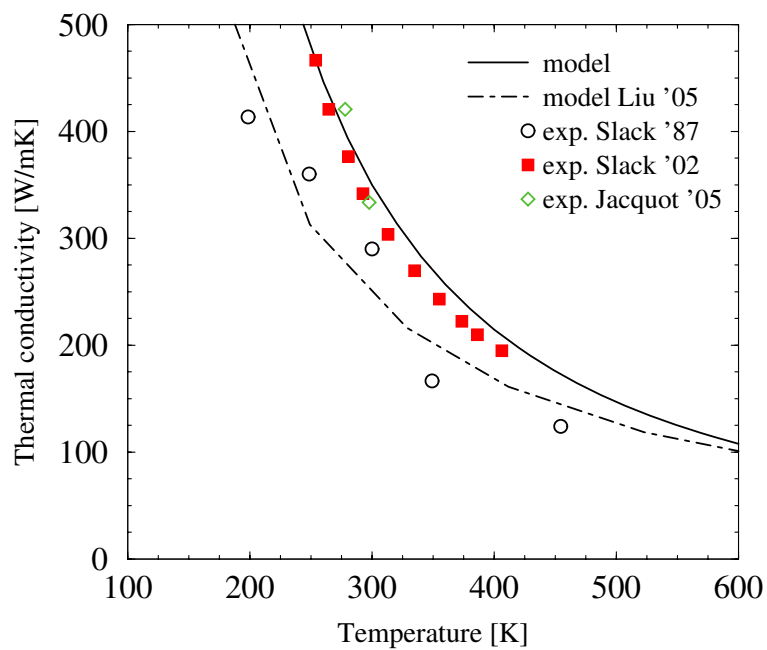


Figure 4.2: AlN thermal conductivity as a function of temperature.

model the conductivity at 300 K, while the exponent  $\alpha^{\text{ABC}}$  is linearly interpolated as there is no experimental data for temperatures other than 300 K yet:

$$\begin{aligned}\kappa_{300}^{\text{ABC}} &= \left( \frac{1-x}{\kappa_{300}^{\text{AC}}} + \frac{x}{\kappa_{300}^{\text{BC}}} + \frac{(1-x)x}{C_\kappa} \right)^{-1}, \\ \alpha^{\text{ABC}} &= (1-x)\alpha^{\text{AC}} + x\alpha^{\text{BC}}\end{aligned}$$

Applying this expressions, a value of 3.1 W/mK is adopted for  $C_\kappa$  of  $\text{Al}_x\text{Ga}_{1-x}\text{N}$ . This results in a fair agreement with the experimental data of Daly *et al.* [306] and Liu *et al.* [298] as depicted in Fig. 4.3 and corresponds to the value used in [303]. For  $\text{In}_x\text{Ga}_{1-x}\text{N}$   $C_\kappa=1.5$  W/mK is adopted, again matching the model in [303] (Fig. 4.4) and the experimental data of Pantha *et al.* [307]. For  $\text{In}_x\text{Al}_{1-x}\text{N}$  a fit to the only available experimental data [308] resulted in an  $C_\kappa=1.2$  W/mK (Fig. 4.5).

#### 4.2.4 Specific Heat

The lattice specific heat  $c_L$  is modeled by the following expression proposed in [305]:

$$c_L(T_L) = c_{L,300} + c_1 \frac{\left(\frac{T_L}{300\text{K}}\right)^\beta - 1}{\left(\frac{T_L}{300\text{K}}\right)^\beta + \frac{c_1}{c_{L,300}}},$$

where  $c_{L,300}$  is the value of the specific heat at 300 K and  $c_1$  and  $\beta$  are fitting parameters. Fig. 4.6 shows a comparison between the calibrated model (values are listed in Table 4.5) and measurements as a function of temperature for GaN. The results both of Kremer *et al.* [309] and Danilchenko *et al.* [310] are from bulk wurtzite GaN while most previous measurements were conducted on polycrystalline powder samples. Our model is calibrated against the model of Danilchenko *et al.*, which is in excellent agreement with their own measurements for the heat capacity in the 0 K–300 K range and also with experimental results given in [309].

The parameter values for AlN are based on the summarized results in [138].

For the heat capacity of InN several works are based on the experimental data provided by Krukowski *et al.* [302]. Their results are shown in Fig. 4.7 together with the models of Leitner

**Table 4.4:** Model parameters for the thermal conductivity.

Material	$\kappa_{300}$ [W/m·K]	$\alpha$
GaN model 1	130	-0.43
GaN model 2	220	-1.2
AlN	350	-1.7
InN	45-176	0

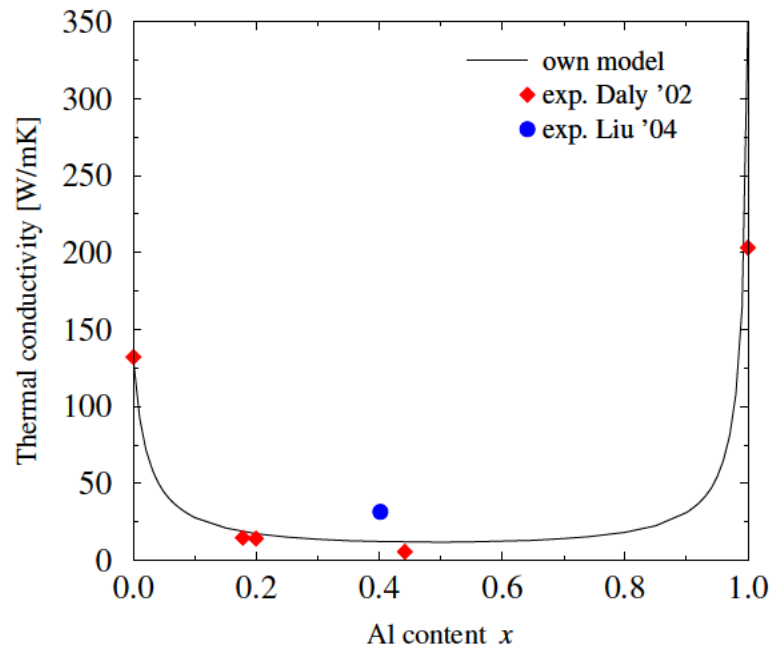


Figure 4.3: AlGaN thermal conductivity as a function of Al content.

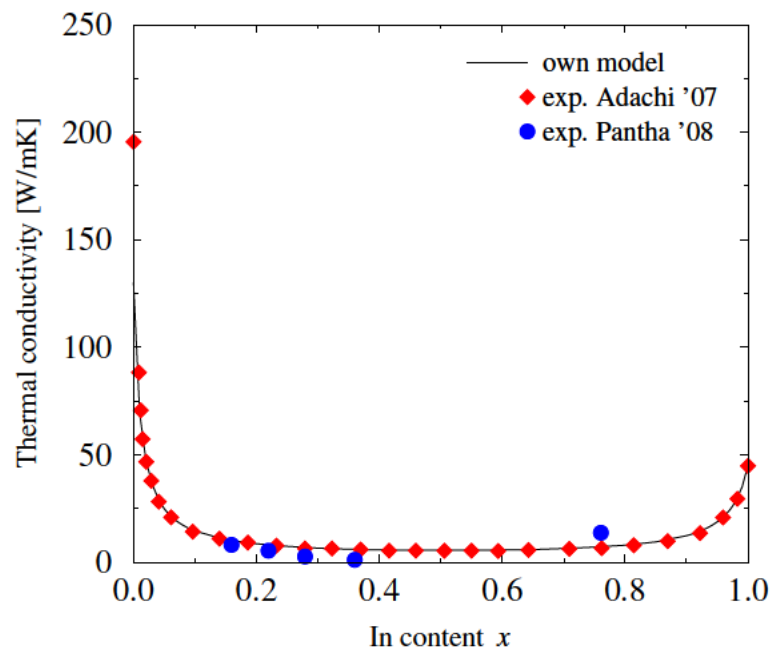
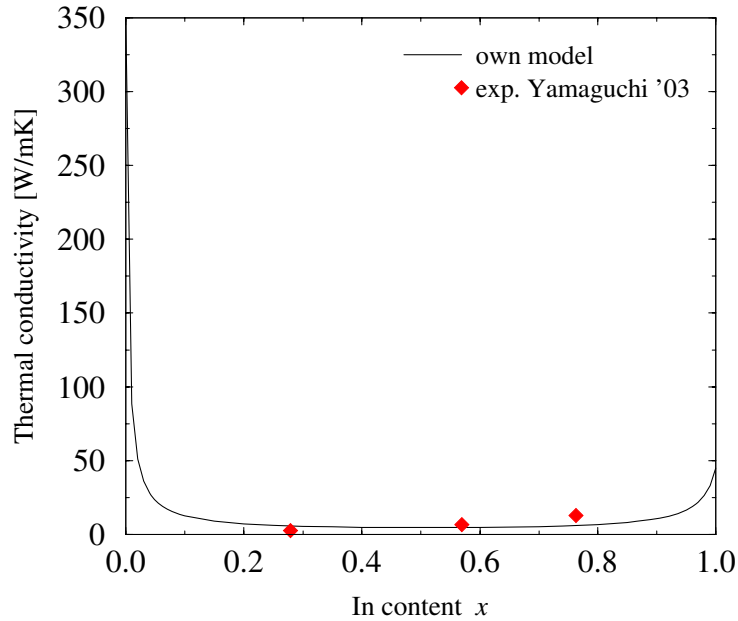


Figure 4.4: InGaN thermal conductivity as a function of In content.



**Figure 4.5:** InAlN thermal conductivity as a function of In content.

*et al.* [311] and Zieborak *et al.* [312], which both provide models based on measurement results. In the present work the model is calibrated against the data in [311].

The specific heat coefficients for alloy materials are expressed by a linear interpolation between the values of the binary materials [305]:

$$c_L^{ABC} = (1 - x)c_L^{AC} + xc_L^{BC}.$$

### 4.3 Band Structure

This section presents a discussion of the models for the band gap energies for both basic materials and their alloys, and also for their temperature dependence. Further, a short overview of the alignment of the band gaps of the different materials is provided.

**Table 4.5:** Parameter values for the specific heat model.

Material	$c_{300}$	$c_1$	$\beta$
	[J/ kg K]	[J/ kg K]	
GaN	431	171	1.75
AlN	748	482	2.29
InN	296	108	1.5



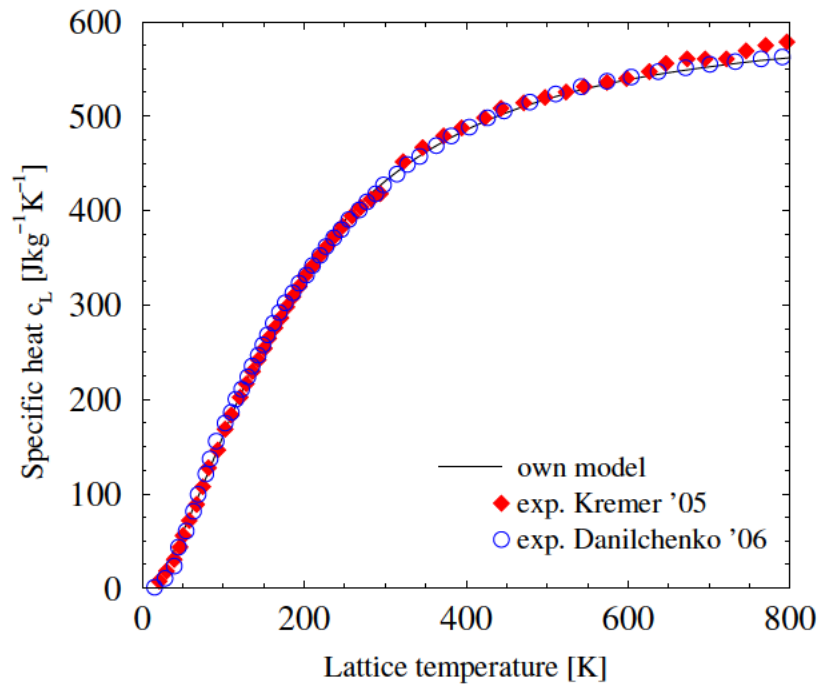


Figure 4.6: GaN specific heat as a function of lattice temperature.

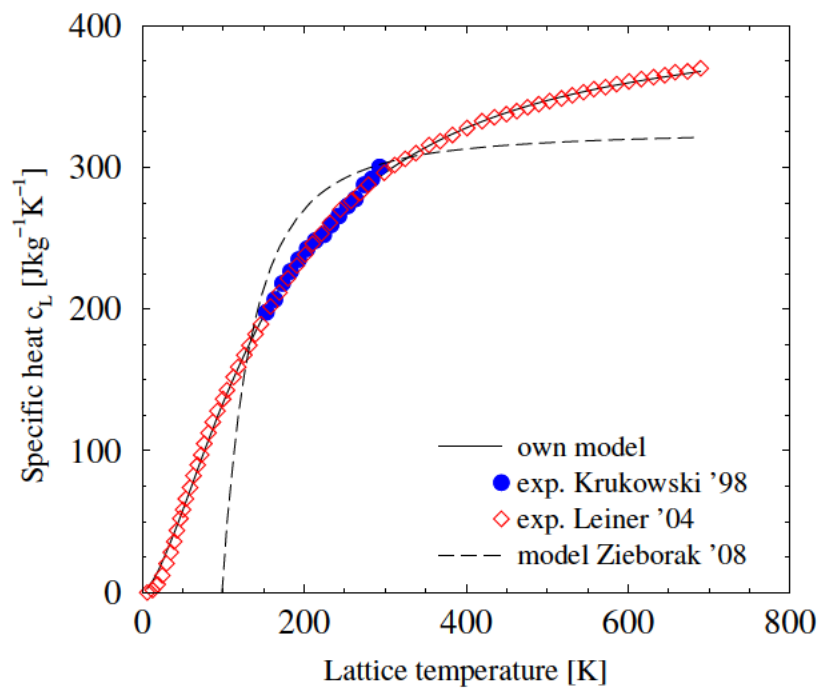


Figure 4.7: InN specific heat as a function of lattice temperature.

### 4.3.1 Band Gap Energy

The *Varshni* formula [313] well describes the temperature dependence of the band gap in nitrides with:

$$\mathcal{E}_g = E_{g,0} - \frac{\alpha_g T_L^2}{\beta_g + T_L}.$$

The values for  $E_{g,0}$  (energy band gap at 0 K),  $\alpha_g$ , and  $\beta_g$  (empirical constants) for GaN, AlN and InN are summarized in Table 4.6. The parameters for GaN are an average of various reported results as summarized in [209], those for AlN are based on the experimental work of Guo *et al.* [314]. For InN the parameters are taken from [315], where three different techniques were used to study the band gap energy and its properties. The results are in agreement with the recently reevaluated band gap energy of InN as discussed in Section 3.3.

The band gap of semiconductor alloys is interpolated by *Vegard's law* [316]:

$$\mathcal{E}_g^{\text{ABC}} = \mathcal{E}_g^{\text{AC}}(1-x) + \mathcal{E}_g^{\text{BC}}x + C_g(1-x)x,$$

with the bowing parameter  $C_g$ . The reported values for  $\text{Al}_x\text{Ga}_{1-x}\text{N}$  of the latter show a large variation ranging from  $-0.8$  eV [317] to  $+1.33$  eV [318]. However, several experiments [319], [320] show a linear variation ( $C_g \approx 0$  eV) which is adopted here.

For InGaN a bowing parameter  $C_g=1.4$  eV in agreement with the work of Walukiewicz *et al.* [315] is well established. It corresponds to the theoretical value given by Caetano *et al.* [321] ( $C_g=1.44$  eV). Other theoretical studies show that a single bowing parameter cannot be used for the whole alloy band gap [322], [323]. While the dependence of the bowing parameter on the composition in the aforementioned works is weak, it still remains to be experimentally verified. Until such studies are available,  $C_g=1.4$  eV and  $C_g=2.1$  eV for unstrained and strained samples, respectively, are adopted [324]

Several works suggest a bowing parameter with a value ranging from 3.0 eV and 6.1 eV [315], [325] for InAlN. Those large disagreements can be attributed to low crystalline quality and high doping levels. Recent calculations and experimental studies showed, however, that the bowing parameter for InAlN is strongly dependent on the material composition [326], [327]. In order to account for this dependence the following expression is proposed in [327]:

$$C_g(x) = \frac{C_{g,1}}{1 + C_{g,2}x}.$$

**Table 4.6:** Summary of band structure model parameters.

Material	$E_{g,0}$ [eV]	$\alpha_g$ [eV/K]	$\beta_g$ [K]
GaN	3.4	$9.09 \times 10^{-4}$	800
AlN	6.2	$18.0 \times 10^{-4}$	1462
InN	0.69	$4.14 \times 10^{-4}$	454

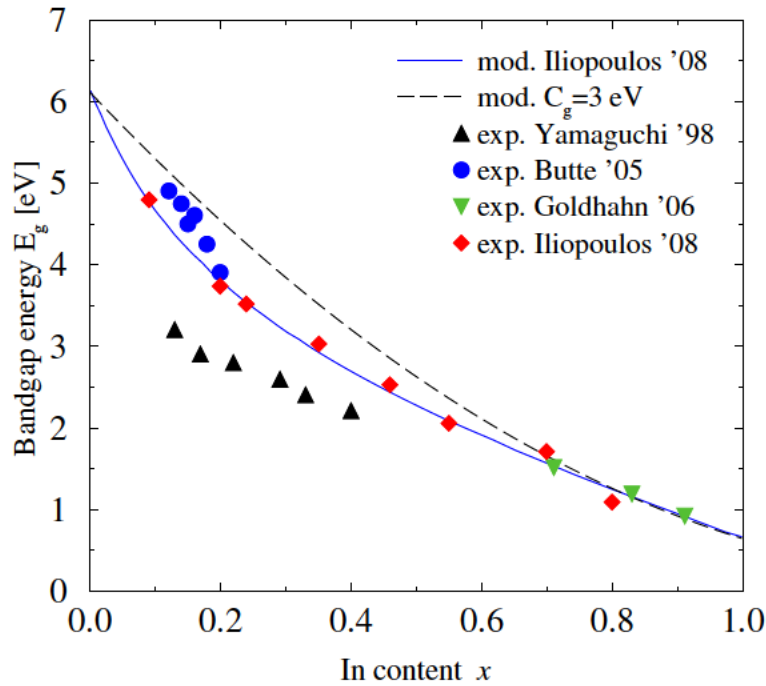


Figure 4.8: Material composition dependence of the band gap of  $\text{In}_x\text{Al}_{1-x}\text{N}$ .

In the same work, the authors propose a value of 15.3 eV and 4.81 eV for  $C_{g,1}$  and  $C_{g,2}$ , respectively. As shown in Fig. 4.8 this model achieves a very good agreement with the experimental data from various other studies [328], [329], [330]. The dependence of the band gap on composition should be attributed to charge transfer effects, related to the large electronegativity differences between III-V atoms [322]. However, as pointed out in [331] Vegard's law is applicable for lattice matched composition ( $\approx 17\%$  as reported in [332]), which is mostly interesting for HEMT applications. For reference the result obtained using a constant  $C_g=3$  eV is depicted, too.

### 4.3.2 Band Gap Energy Offset

An energy offset ( $\mathcal{E}_{\text{off}}$ ) is used to align the valence band of different materials. In this work GaN is chosen as the reference for the III-V materials ( $\mathcal{E}_{\text{off}} = 0$  eV). The energies of the conduction and valence band edges are calculated by

$$\begin{aligned}\mathcal{E}_v &= \mathcal{E}_{\text{off}} \\ \mathcal{E}_c &= \mathcal{E}_v + \mathcal{E}_g\end{aligned}$$

The valence-band-offset of AlN  $\mathcal{E}_{\text{off}}^{\text{AlN}}$  is chosen as 1.12 eV, which is equal to 40% of the total band gap discontinuity as reported by Westmeyer *et al.* [333] obtained from a measurement of the linewidth of the excitonic transition in an  $\text{Al}_{0.18}\text{Ga}_{0.82}\text{N}$  alloy. This value is larger than the previously reported 0.7 eV as in [334] obtained by x-ray photoemission spectroscopy. However,

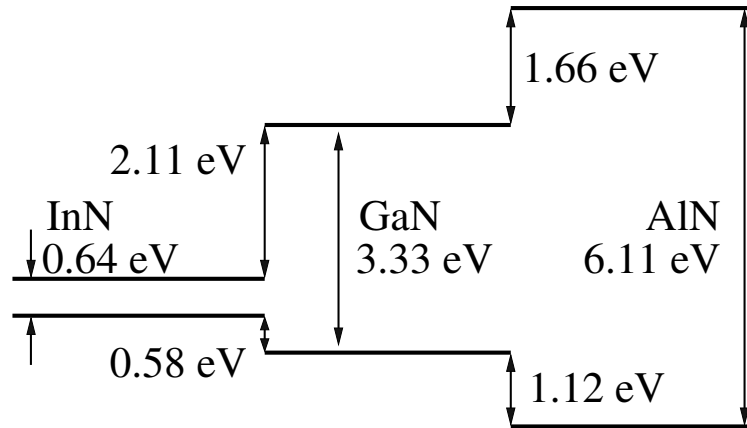


**Figure 4.9:** Band alignment of InN, GaN, and AlN at room temperature.

it is closer to the intrinsic value as it is free from effects introduced by interface defects and inhomogeneities.

The most widely cited value for the valence band offset of InN/GaN is the one reported by Martin *et al.* [334] ( $\mathcal{E}_{\text{off}}^{\text{InN}} = 1.05$  eV). It was however determined over a decade ago, and the recent reevaluation of the band structure have rendered it dated. Recent studies show a valence band offset between 0.58 [335] and 0.62 eV [323]. The band alignment is shown schematically in Fig. 4.9.

For alloys the offset energy is calculated by the following expression [138]:

$$\mathcal{E}_{\text{off}}^{\text{ABC}} = \frac{\mathcal{E}_{\text{off}}^{\text{AC}}(\mathcal{E}_{\text{g}}^{\text{ABC}} - \mathcal{E}_{\text{g}}^{\text{BC}}) - \mathcal{E}_{\text{off}}^{\text{BC}}(\mathcal{E}_{\text{g}}^{\text{ABC}} - \mathcal{E}_{\text{g}}^{\text{AC}})}{\mathcal{E}_{\text{g}}^{\text{AC}} - \mathcal{E}_{\text{g}}^{\text{BC}}},$$

where  $\mathcal{E}_{\text{off}}^{\text{AC}}$  and  $\mathcal{E}_{\text{off}}^{\text{BC}}$  are the offset energies for the binary materials.

As an example, for  $\text{Al}_x\text{Ga}_{1-x}\text{N}$  with  $x=0.22$  the valence-band-offset against GaN is 0.25 eV. Our setup provides a value of 0.225 eV for  $x=0.2$ , which is in a good agreement with the experimentally determined offset of 0.25 eV [336] for the same composition.

## 4.4 Carrier Mobility

Mobility models which account for the specific physics in a given semiconductor material are crucial for device modeling. While for Silicon there exist well established models [337], the III-V material system still poses certain challenges (e.g. negative differential mobility) and nevertheless, is not so well studied (especially concerning InN). Also certain device specific effects such as high electric fields and very strong gradients of electric fields have to be considered for the simulation of HEMTs.

Several groups have proposed various models and model parameter sets for the simulation of GaN-based devices. Farahmand *et al.* [253] provide a low-field model which accounts for temperature and ionized impurity concentrations as well as a high-field model based on Monte Carlo simulation results. Another low-field model, valid in a large temperature and concentration

range is proposed by Mnatsakanov *et al.* [338]. A highly parameterized field-dependent model based on an extensive data pool was developed by Schwierz [175]. Turin *et al.* [339] propose another high-field model which delivers excellent agreement with the results from MC simulations. All those models are suited only for the drift-diffusion transport model. However, the latter is not able to deliver accurate results for sub-micron devices [340], therefore a hydrodynamic transport model is necessary, too.

#### 4.4.1 Low-Field Mobility

**Ionized Impurity Scattering:** The low-field mobility is modeled by an expression similar to that proposed by *Caughey* and *Thomas* [341], [138]:

$$\mu^{\text{LI}} = \mu^{\text{min}} + \frac{\mu^{\text{L}} - \mu^{\text{min}}}{1 + (C_1/C^{\text{ref}})^{\gamma_0}}.$$

$C_1$  denotes the concentration of ionized impurities,  $\mu^{\text{L}}$  is the mobility in undoped material,  $\mu^{\text{min}}$  is the mobility in highly doped material, limited by impurity scattering. The maximum ( $\mu^{\text{L}}$ ) mobility, and minimum ( $\mu^{\text{min}}$ ) mobility, and the parameters describing the mobility decrease with rising impurity concentration ( $C^{\text{ref}}$  and  $\gamma_0$ ) are calibrated against an extensive analysis of available MC simulations results and experimental data.

For GaN our model for electrons assumes the high mobility consistent with the defect-free substrates of the simulated devices (Fig. 4.10). It is calibrated against own Monte Carlo simulation results presented in Section 3.2.2. The values of the parameters for GaN and other materials are given in Table 4.7.

The model for electrons in InN is calibrated against own Monte Carlo (Fig. 4.11) simulation results, too, described in Section 3.3.2. The latter assumes an updated band gap of  $\approx 0.7$  eV and proper electron masses.

While for GaN and InN experimental data exist for the transport properties, for AlN such data are hardly available as the grown AlN films are normally semi-insulating. Most authors therefore rely on MC results [342]. We verified our model against the measurements of *Taniyasu et al.* [343] who achieved a high mobility in Si-doped AlN. They supplemented the experimental data with simulations (Fig. 4.12). The higher maximum mobility used here is in agreement with the value proposed in [253]. It is higher than the measured values, due to our model assumption of dislocation-free conditions.

The hole transport in GaN is plagued by several doping technique issues as discussed in Section 3.2.3. Therefore, it is difficult to give a profound model. Based on the limited experimental data an initial setup is proposed (Fig. 4.13).

Due to the lack of experimental data on the transport properties of holes in InN and AlN, no corresponding parameter setups are given here. Such can be found in [342], however solely based on Monte Carlo simulations.

The low field mobility of alloys is calculated by a harmonic mean:

$$\frac{1}{\mu^{\text{ABC}}} = \frac{1-x}{\mu^{\text{AC}}} + \frac{x}{\mu^{\text{BC}}}.$$

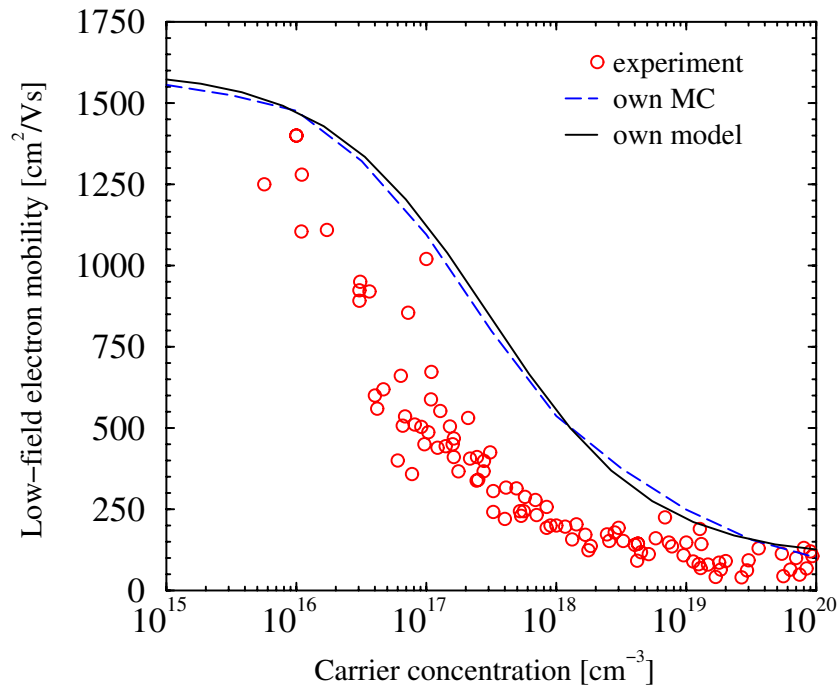


Figure 4.10: Electron mobility versus concentration in GaN.

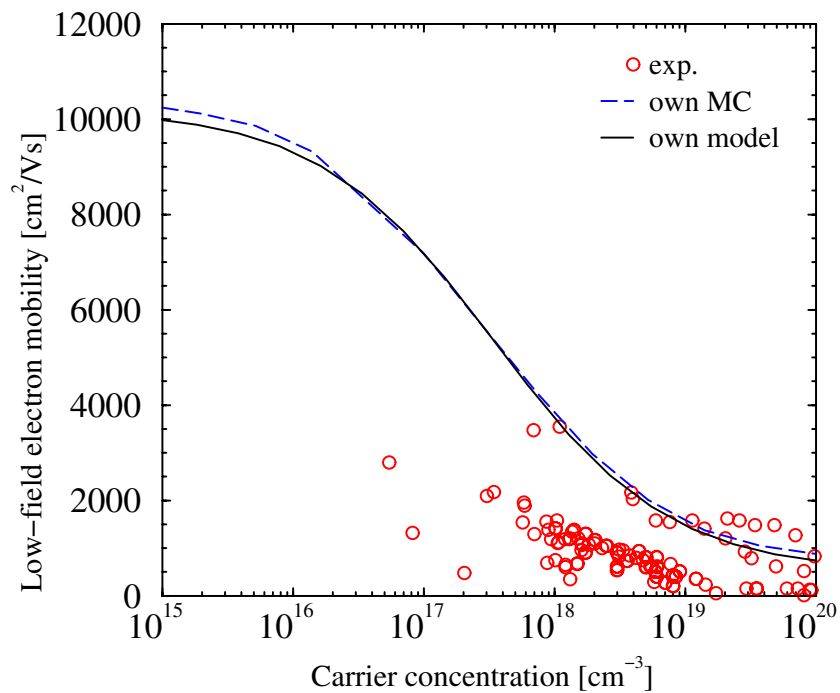


Figure 4.11: Electron mobility versus concentration in InN.

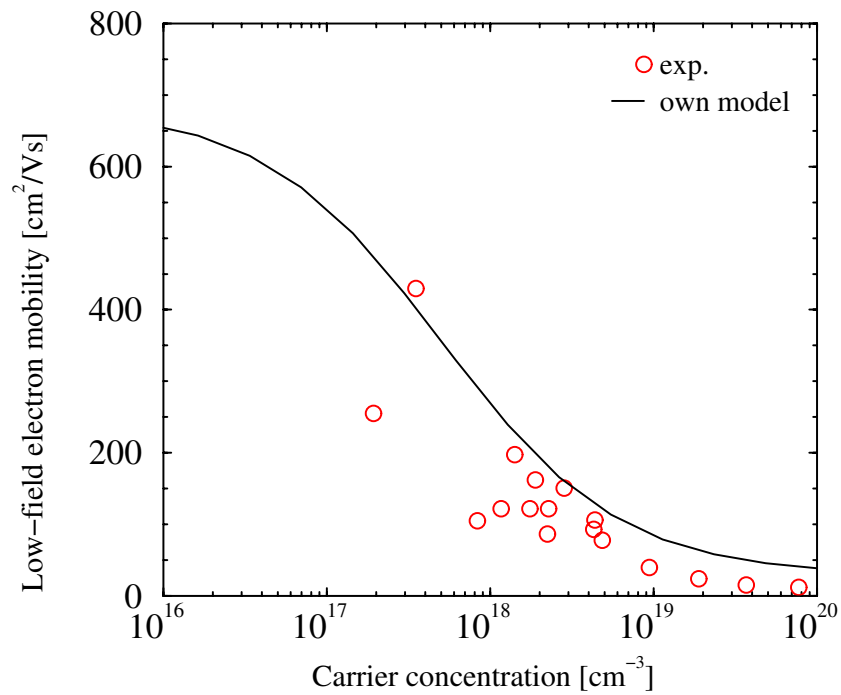


Figure 4.12: Electron mobility versus concentration in AlN.

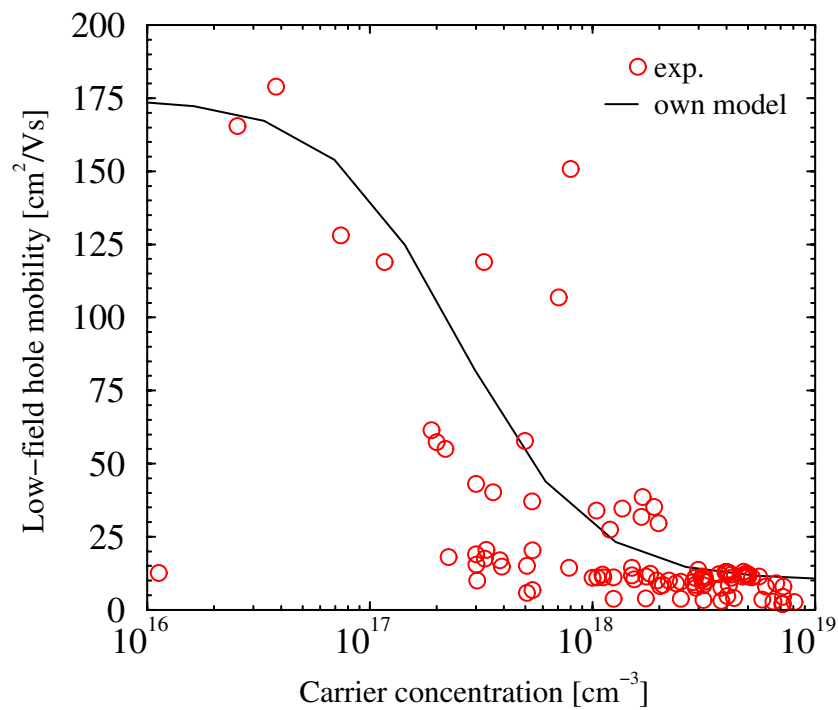


Figure 4.13: Hole mobility versus concentration in GaN.

**Table 4.7:** Parameter values for the low-field mobility.

Material	carrier	$\mu_{300}^L$ [cm <sup>2</sup> /Vs]	$\mu_{300}^{\min}$ [cm <sup>2</sup> /Vs]	$C_{300}^{\text{ref}}$ cm <sup>-3</sup>	$\gamma_0$	$\gamma_1$	$\gamma_2$	$\gamma_3$
GaN	n	1600	100	$3 \times 10^{17}$	0.7	-1.5	-0.2	1.3
	p	175	10	$2.5 \times 10^{17}$	1.5	-3.7	-1.5	1.0
AlN	n	683	29	$5 \times 10^{17}$	0.8	-3.21	1.21	-0.18
InN	n	10200	500	$3.4 \times 10^{17}$	0.65	-3.7	2.39	-0.33

**Temperature Dependence:** In order to model the temperature dependence, the mobilities are parameterized using power laws [15]:

$$\begin{aligned}\mu^L &= \mu_{300}^L \left( \frac{T_L}{300 \text{ K}} \right)^{\gamma_1}, \\ \mu^{\min} &= \mu_{300}^{\min} \left( \frac{T_L}{300 \text{ K}} \right)^{\gamma_2}, \\ C^{\text{ref}} &= C_{300}^{\text{ref}} \left( \frac{T_L}{300 \text{ K}} \right)^{\gamma_3}.\end{aligned}$$

Similar expressions have been also used in [253], [175].

Monte Carlo simulations by other groups [253], [181] and experiments [345], [346] for the electron mobility in bulk GaN as a function of the temperature are shown in Fig. 4.14. Over the years the electron mobilities increase due to the improved quality of the material samples. Models proposed by other groups [175], [338] are also displayed. Fig. 4.15 shows the electron mobility as a function of temperature in the two-dimensional electron gas as experimentally determined by various groups [347], [348], [14], [179], [349], [350]. The mobility exhibits overall higher values especially at high temperatures, while retaining the trend for improved results over time. The parameter values we chose are listed in Table 4.7. The maximum ( $\mu_{300}^L$ ) and minimum mobility ( $\mu_{300}^{\min}$ ) are calibrated against own MC simulations. A decrease of the maximum mobility with temperature ( $\gamma_1 = -1.5$ ), in agreement with the power term of the acoustic phonon mobility expression [110] is assumed. Our MC simulation results and recent experiments from [351] confirmed that the latter is the dominant scattering mechanism at high temperatures. A weak temperature dependence ( $\gamma_2 = -0.2$ ) of the electron mobility at high concentrations is adopted.

Experimental data for the mobility dependence on temperature for InN and AlN is scarce. Therefore, the values from [342] are adopted here.

The hole mobility at different temperatures of GaN is discussed in Section 3.2.3. Based on the experimental data, a value of  $\gamma_1 = -3.7$  is chosen which describes the decay in mobility with higher temperature well.



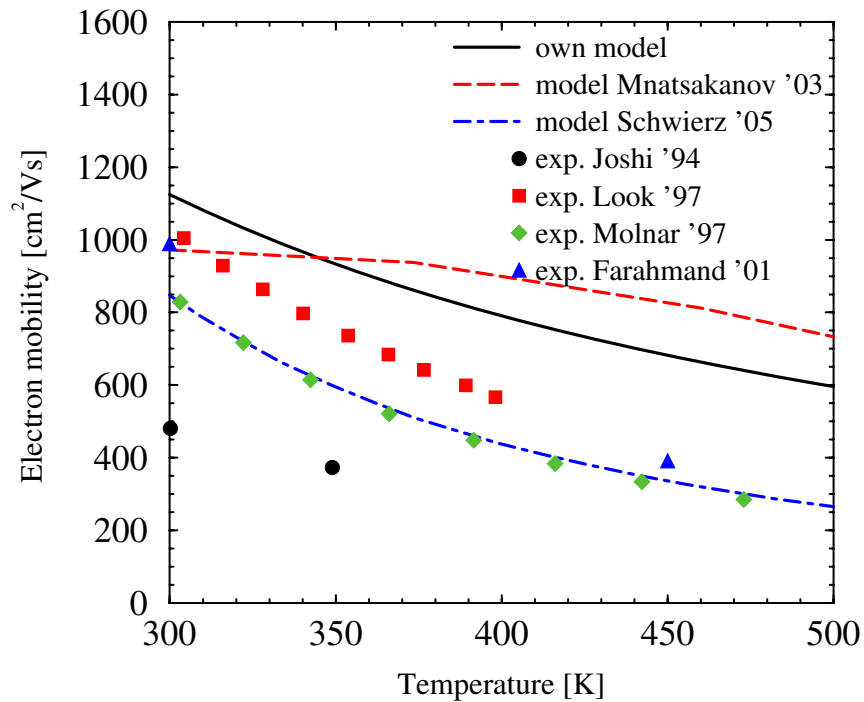


Figure 4.14: Electron mobility versus temperature in bulk GaN.

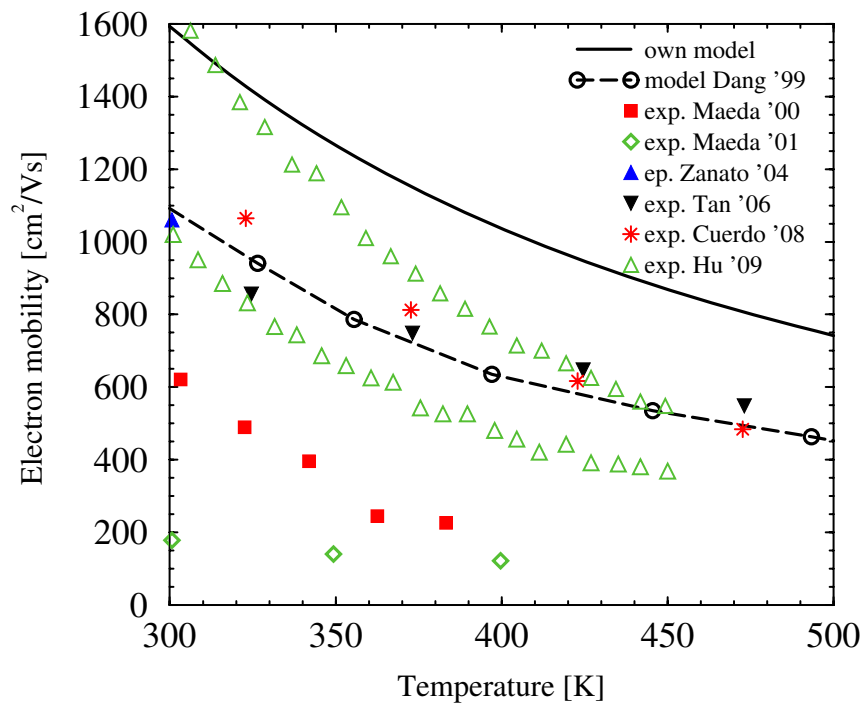


Figure 4.15: Electron mobility versus temperature in 2DEG GaN.

#### 4.4.2 High-Field Mobility for DD Equations

The models proposed for the high-field mobility are based on the mobility expression of the form [352]:

$$\mu^{\text{LIF}}(E) = \frac{\mu^{\text{LI}}}{\xi + \left( (1 - \xi)^\beta + \left( \frac{\mu^{\text{LI}} \cdot E}{v_{\text{sat}}} \right)^\beta \right)^{1/\beta}}. \quad (4.66)$$

$\mu^{\text{LI}}$  is the low-field electron mobility as calculated previously,  $v_{\text{sat}}$  is the electron saturation velocity,  $E$  is the electric field. The same expression was used in [353].

For the DD high-field mobility two different models are available. The first is the convenient model used for Silicon, referred as Model A. The second one is a modified model which can account for negative differential mobility (NDM), referred as Model B. The latter is especially tailored to describe the transport properties of electrons in Nitrides. Further, based on Model B a corresponding HD model can be synthesized.

**Model A:** The basic high-field mobility model has the form:

$$\mu_\nu^{\text{LIF}}(F_\nu) = \frac{\mu_\nu^{\text{LI}}}{\left( 1 + \left( \frac{\mu_\nu^{\text{LI}} \cdot F_\nu}{v_{\text{sat},\nu}} \right)^\beta \right)^{1/\beta}}, \quad \nu = n, p \quad (4.67)$$

where  $F_\nu$  is the driving force, defined as:

$$F_n = \left| \nabla\psi - \frac{1}{n} \nabla \left( \frac{k_B T_L}{q} n \right) \right|,$$

$$F_p = \left| \nabla\psi - \frac{1}{p} \nabla \left( \frac{k_B T_L}{q} p \right) \right|,$$

for electrons and holes, respectively. The saturation velocity  $v_{\text{sat},\nu}$  can be calculated in a separate model, accounting for temperature dependence. The parameter  $\beta$  models the slope of the mobility increase with increasing electric field, respectively driving force. While in the DD model it can be varied, a corresponding HD model can be obtained only for certain values. Therefore, for electrons in all three materials a value of  $\beta=1$  is adopted.

The model is derived from (4.66), with  $\xi=1/2$  and using the driving force  $F$  instead of the electric field  $E$ . It offers excellent convergence behavior and a straight-forward calibration method. However, it cannot account for the velocity decrease at higher electric fields. Yet it offers a reasonable agreement with the experimental data and MC simulation results for electric fields below the maximum velocity for all three materials (Fig. 4.16, Fig. 4.17, and Fig. 4.18) using the parameter setup provided in Table 4.8.

**Model B:** The model is based on the same expression for the mobility (4.66), with  $\beta=1$  and  $\xi=1/2$ . In order to approximate the mobility decay due to intervalley transfer at high fields, two

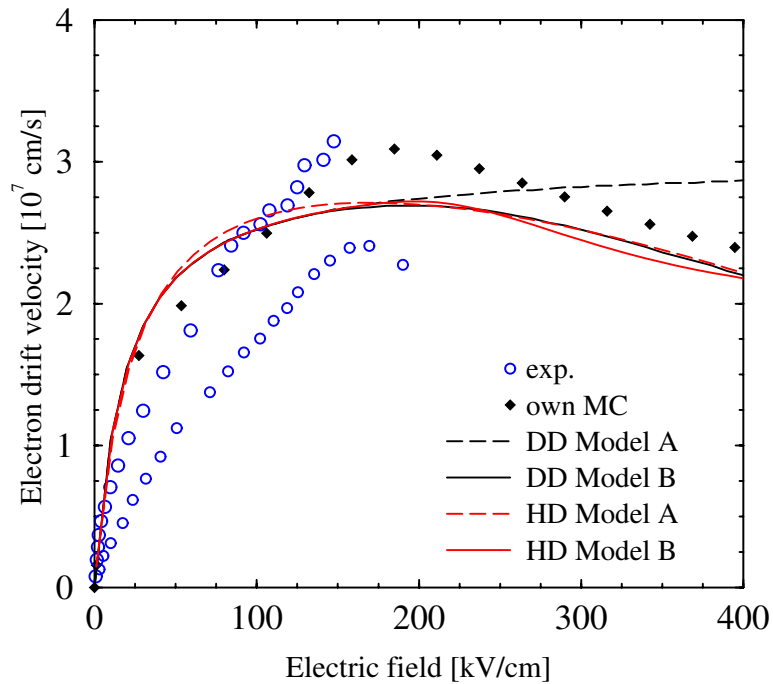


**Figure 4.16:** GaN electron drift velocity versus electric field: simulations with different mobility models compared to MC simulation results and experimental data.

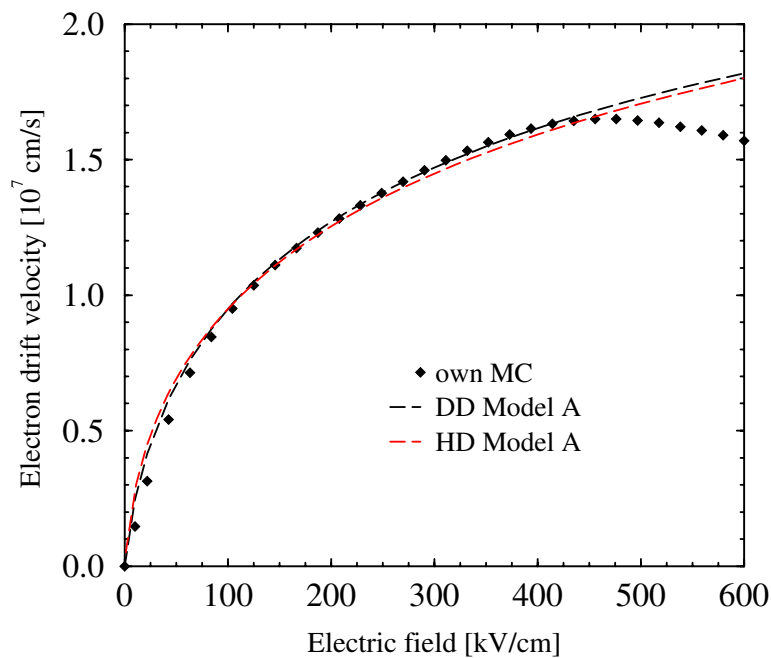


**Figure 4.17:** AlN electron drift velocity versus electric field: simulations with different mobility models compared to MC simulation results.

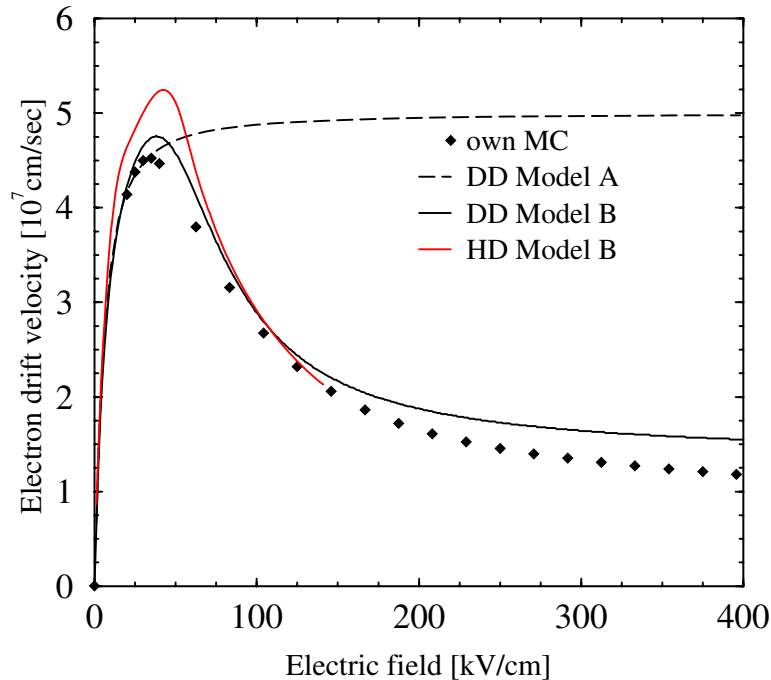
**Table 4.8:** Parameters for DD high-field electron mobility Model A.

	$v_{\text{sat}}$	$\beta$
	[cm/s]	[1]
GaN	$3.0 \times 10^7$	1.0
AlN	$3.7 \times 10^7$	0.45
InN	$5.0 \times 10^7$	1.3

sets of  $\mu$  are used. One describes the mobility  $\mu_{\Gamma}(F)$  in the lower valley and the other one in the higher  $\mu_{\text{U}}(F)$  (while  $\Gamma$  and  $\text{U}$  are the lowest two valleys only in GaN, this notation is retained for the other materials for simplicity):

$$\mu_{\Gamma}(E) = \frac{\mu_{\Gamma}^{\text{LI}}}{1 + \left(\frac{\mu_{\Gamma}^{\text{LI}} E}{v_{\text{sat},\Gamma}}\right)}, \quad (4.68)$$

$$\mu_{\text{U}}(E) = \frac{\mu_{\text{U}}^{\text{LI}}}{1 + \left(\frac{\mu_{\text{U}}^{\text{LI}} E}{v_{\text{sat},\text{U}}}\right)}. \quad (4.69)$$


**Figure 4.18:** InN electron drift velocity versus electric field: simulations with different mobility models compared to MC simulation results.

A weighted mean is built:

$$\mu_n^{\text{LIF}}(E) = \frac{\mu_{\Gamma}(E) + \mu_U(E)P_{\text{DD}}(E)}{1 + P_{\text{DD}}(E)} \quad (4.70)$$

where  $P_{\text{DD}}(E)$  is the valley occupancy [354]:

$$P_{\text{DD}}(E) = 6 A \left( \frac{m_U^*}{m_{\Gamma}^*} \right)^{3/2} \exp \left( - \frac{\Delta E_C}{k_B T_L \left( 1 + \frac{E}{E_0} \right)} \right). \quad (4.71)$$

$m_{\Gamma}^*$  and  $m_U^*$  are the electron masses in the  $\Gamma$  and  $U$  valleys, respectively, and  $\Delta E_C$  is the difference in the conduction bands.

This model allows to set a lower electron mobility and velocity in the higher conduction band. Thus, the characteristic electron velocity decrease of most Nitrides can be described well.

Since all MC simulations and experiments, on which we rely to calibrate the low-field mobility in GaN, were performed at low electric fields, we set  $\mu_{\Gamma} = \mu_{\nu}^{\text{LI}}$  as calculated by the low-field mobility model. Using a down-scaled mobility ( $\mu_U = 0.1 \times \mu_{\nu}^{\text{LI}}$  supported by MC data) and velocity in the higher band results in a decrease of the electron velocity at higher fields. With the parameters listed in Table 4.9, the model delivers an acceptable approximation in comparison to MC simulations, accounting for as much as six bands [355] (Fig. 4.16). Results from different groups vary widely (e.g. peak velocity from  $2.5 \times 10^7$  cm/s to  $3.5 \times 10^7$  cm/s), therefore our goal is not really a perfect agreement with this particular MC simulation. The model (and the corresponding HD model) is a carefully chosen trade-off. On the one hand they provide a velocity-field characteristics close to the one obtained by MC simulation, while on the other hand they maintain low calculation complexity and a good convergence behavior. An extension accounting for three valleys is possible, however, it was ruled out due to the downgraded convergence of the solution process.

For AlN, the model cannot be applied due to the very slow increase of the velocity versus electric field. In order to model the latter properly  $\beta=0.45$  is needed, however, while being straightforward for the DD model, this will increase considerably the complexity of the corresponding HD model. Therefore, no parameter setup is given here for AlN.

Based on the recent MC simulation studies for InN (accounting for the re-evaluated band gap), a parameter setup is extracted (Table 4.9). Due to the value of  $\beta$  close to 1, a good agreement can be achieved (Fig. 4.18) for velocity characteristics below the maximum, while a low value of  $F_0$  accounts for the intervalley transfer at fields starting at 50 kV/cm.

#### 4.4.3 High-Field Mobility for HD Equations

In order to obtain a consistent hydrodynamic mobility expression, the local energy balance equation:

$$E^2 \mu = \frac{3k_B(T_n - T_L)}{2 \cdot q \cdot \tau_e} \quad (4.72)$$

is solved for  $E(T_n)$ , which is then inserted into (4.66). This is performed again with  $\xi=1/2$  for both models, and with  $\beta=2$  for the first model and  $\beta=1$  for the second model, respectively.  $\tau_e$  is the energy relaxation time.

**Table 4.9:** Parameters for DD high-field electron mobility Model B.

	$v_{\text{sat},\Gamma}$	$v_{\text{sat},\text{U}}$	$\mu_{\Gamma}$	$\mu_{\text{U}}$	$\Delta E_{\text{C}}$	$m_{\Gamma}^*/m_0^*$	$m_{\text{U}}^*/m_0^*$	$F_0$
	[cm/s]	[cm/s]	[1]	[1]	[eV]	[1]	[1]	[V/m]
GaN	$3 \times 10^7$	$10^7$	$\mu^{\text{LI}}$	$0.1 \times \mu^{\text{LI}}$	1.4	0.2	0.3	0.26
InN	$6 \times 10^7$	$10^7$	$\mu^{\text{LI}}$	$0.1 \times \mu^{\text{LI}}$	1.78	0.25	0.4	0.035

**Model A:** The expression obtained with the chosen values for  $\xi$  and  $\beta$  is identical with the one proposed by *Hänsch et al.* [356]. In order to account for NDM effects it is modified by introducing two parameters ( $\gamma_4$  and  $\gamma_5$ ) [20]:

$$\mu_n^{\text{LIT}}(T_n) = \frac{\mu (T_n/T_{\text{L}})^{\gamma_4}}{\left(1 + \alpha^{1/\gamma_5} (T_n - T_{\text{L}})^{1/\gamma_5}\right)^{\gamma_5}} \quad (4.73)$$

$$\alpha = \frac{3k_{\text{B}}\mu_n^{\text{LI}}}{2q\tau_{\epsilon}(v_{\text{f}})^2} \quad (4.74)$$

In the standard *Hänsch* model  $v_{\text{f}}$  corresponds to the saturation velocity  $v_{\text{sat}}$  (as in (4.66)). However, due to the powered temperature term  $(T_n/T_{\text{L}})^{\gamma_4}$  in the numerator the velocity is steadily decreasing at high-fields. Hence,  $v_{\text{f}}$  does not describe the saturation velocity as a physical quantity, although it does affect the high-field transport characteristics. The parameter  $\gamma_5$  has a more pronounced effect at low fields, while  $\gamma_4$  influences primarily the high-field mobility, though their impact cannot be isolated to a specific field region. The conventional *Hänsch* model corresponds to the parameter set  $\gamma_4 = 0$ ,  $\gamma_5 = 1$ . However, in order to approximate the simulation and experimental data, a set with  $\gamma_4 = -0.3$  and  $\gamma_5 = 2.4$  is chosen for GaN (Table 4.10). It delivers good agreement with the velocity-field characteristics obtained using the DD Model B (Fig. 4.16). A similar good match with DD Model A can be achieved for AlN, too (Fig. 4.17). Only for InN it is not possible to model the very strong NDM effect.

**Table 4.10:** Parameters for HD high-field electron mobility Model A.

	$\gamma_4$	$\gamma_5$
<i>Hänsch</i>	0.0	1.0
GaN	-0.3	2.4
AlN	0.1	3.3

**Model B:** Inserting (4.72) into (4.66) with  $\xi=1/2$  and  $\beta=2$  gives the following expression for the high-field mobility:

$$\mu_{\Gamma}(T_n) = \frac{2\mu_{\Gamma}^{\text{LI}}}{2 + a_{\Gamma} + \sqrt{a_{\Gamma}(4 + a_{\Gamma})}}, \quad (4.75)$$

$$\mu_{\text{U}}(T_n) = \frac{2\mu_{\text{U}}^{\text{LI}}}{2 + a_{\text{U}} + \sqrt{a_{\text{U}}(4 + a_{\text{U}})}}, \quad (4.76)$$

$$a_{\Gamma} = \frac{3k_{\text{B}}\mu_{\Gamma}^{\text{LI}}(T_n - T_{\text{L}})}{2q\tau_{\Gamma}(v_{\text{f},\Gamma})^2}, \quad (4.77)$$

$$a_{\text{U}} = \frac{3k_{\text{B}}\mu_{\text{U}}^{\text{LI}}(T_n - T_{\text{L}})}{2q\tau_{\text{U}}(v_{\text{f},\text{U}})^2}. \quad (4.78)$$

In order to approximate the intervalley transfer at high fields, two sets of  $\mu_{\text{v}}$  are used as in DD Model B. In this model too,  $v_{\text{f}}$  does not denote the saturation velocity. The weighted mean is built:

$$\mu^{\text{LIT}}(T_n) = \frac{\mu_{\Gamma}(T_n) + \mu_{\text{U}}(T_n)P_{\text{HD}}(T_n)}{1 + P_{\text{HD}}(T_n)}. \quad (4.79)$$

The expression for  $P_{\text{HD}}$  is analogous to that for  $P_{\text{DD}}$ :

$$P_{\text{HD}}(T_n) = 6 \left( \frac{m_{\text{U}}^*}{m_{\Gamma}^*} \right)^{3/2} \exp \left( -\frac{\Delta E_{\text{C}}}{k_{\text{B}}T_n} \right). \quad (4.80)$$

Fig. 4.19 compares the valley occupancy as a function of the electric field as calculated in this model and MC simulation in GaN. The used parameter setup is the same as for DD Model B (Table 4.9). The only additional values needed, are the scaled energy relaxation times listed in Table 4.11 (the base relaxation times  $\tau_{\epsilon,\text{GaN}}$ ,  $\tau_{\epsilon,\text{AlN}}$ , and  $\tau_{\epsilon,\text{InN}}$  are discussed in Section 4.4.4. An excellent agreement between all models is achieved for GaN (Fig. 4.16). For InN the model can describe the abrupt decay in velocity very well (Fig. 4.18), while the maximum velocity value is slightly higher than the one achieved by the DD model (which is possibly due to the high energy relaxation times used).

While the models deliver consistent results, the two approaches expose some differences. HD Model A is close to already established models and offers a straightforward calibration with only two auxiliary parameters (within a narrow value range). HD Model B is more complex, however, it allows for a more flexible calibration. Its parameters are derived from physical quantities.

#### 4.4.4 Energy Relaxation Times

The energy relaxation times are used in the HD mobility models, in the energy balance equations of the hydrodynamic transport model, and in the lattice heat flow equation. They can be either set constant or calculated using the following model depending on the carrier energy:

$$\tau_{\epsilon,n} = \tau_{\epsilon,0} + \tau_{\epsilon,1} \cdot \left( \frac{T_n}{300 \text{ K}} \right) \quad (4.81)$$

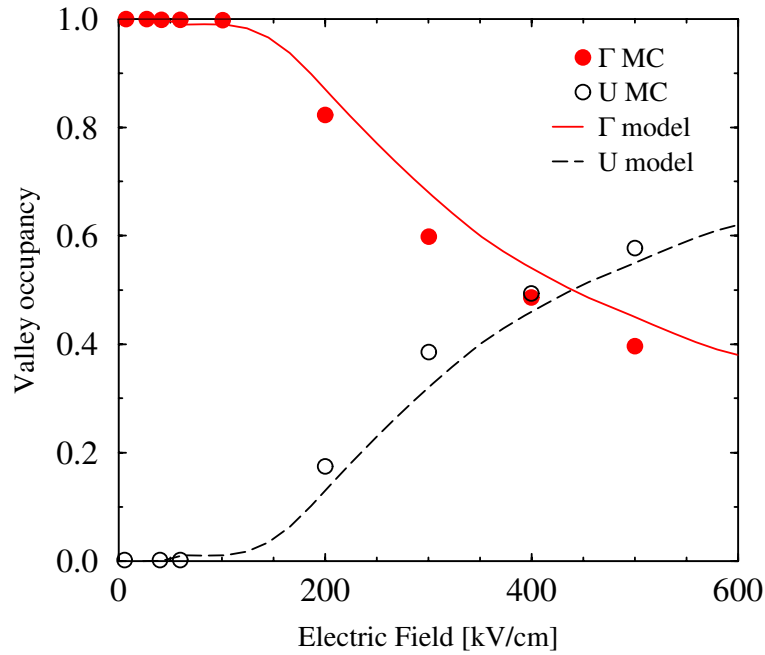


**Figure 4.19:** GaN valley occupancy as a function of the electric field.

**Table 4.11:** Parameters for the energy relaxation times for HD high-field electron mobility Model B [ps].

	$\tau_{\Gamma}$	$\tau_{U}$
GaN	$8.0 \times \tau_{\epsilon, \text{GaN}}$	$\tau_{\epsilon, \text{GaN}}$
InN	$\tau_{\epsilon, \text{InN}}$	$0.1 \times \tau_{\epsilon, \text{InN}}$

For GaN and InN we use the parameter sets as listed in Table 4.12, while for AlN a constant relaxation time of  $\tau_{\epsilon} = 0.1$  ps is assumed. Special care is taken that the relaxation times never reach negative values even at high electric fields (for which Si models indeed yield negative erroneous results).

**Table 4.12:** Parameters for the energy relaxation time model [ps].

	$\tau_{\epsilon,0}$	$\tau_{\epsilon,1}$	$\tau_{\epsilon,2}$
GaN	0.21	0.004	0.0
InN	0.21	0.012	0.0



## 4.5 Spontaneous and Piezoelectric Polarization

A good understanding of the electrical polarization effects at the material interfaces is key to proper device simulation. III-V nitrides are the only III-V materials that show spontaneous polarization  $P_{SP}$ . This has been found to increase from GaN over InN to AlN [172] and it also has a negative sign. The reason is an intrinsic asymmetry of the bonding in the equilibrium wurtzite crystal structure. However, mechanical stress also results in polarization, which is then called piezoelectric polarization  $P_{PZ}$ . It is negative for tensile and positive for compressive strained AlGaIn layers. Therefore, the orientation of the spontaneous and piezoelectric polarization is parallel in case of tensile strain and antiparallel in case of compressive strain. AlGaIn layers grown on GaN buffers are always under tensile strain, thus only this case will be further discussed. As both polarizations have the same direction the total polarization is simply the sum:

$$P = P_{PZ} + P_{SP}.$$

Further, the total polarization of the AlGaIn layer is stronger than that of the underlying relaxed GaN buffer layer. The negative spontaneous polarization of both layers and the negative piezoelectric polarization vector under tensile strain points from the Nitrogen atom towards the nearest Gallium atom along the [0001] axis. Thus, for Ga-faced polarity crystals the total polarization is directed towards the substrate, while for N-faced crystals it is directed towards the surface. It is found that the polarization-induced sheet charge is positive for AlGaIn on top of GaN with Ga-face polarity and GaN on top of AlGaIn with N-face polarity.

In the following the polarization induced charge at an AlGaIn/GaN interface is calculated. Using the provided parameters and the same approach, the polarization for different material interfaces can be determined accordingly.

The spontaneous polarization  $P_{SP}$  at the AlGaIn/GaN interface is calculated by [358]:

$$P_{SP} = P_{SP,AlN} + P_{SP,GaN}(1 - x),$$

The piezoelectric polarization  $P_{PZ}$  is calculated by:

$$P_{PZ} = 2 \cdot \frac{a - a_0}{a_0} \left( e_{31} - e_{33} \cdot \frac{C_{13}}{C_{33}} \right),$$

without taking partial relaxation into account. The parameters  $a$  and  $a_0$  are the lattice constants,  $e_{13}$  and  $e_{33}$  are the piezoelectric coefficients, and  $C_{13}$  and  $C_{33}$  denote the elastic constants. The parameter values for both the spontaneous (Table 4.13) and piezoelectric (Table 4.14) polarization are achieved by the revised calculations of [359].

**Table 4.13:** Spontaneous polarization parameters [C/m<sup>2</sup>].

	GaN	AlN	InN	Refs.
PSP	-0.029	-0.081	-0.032	[172]
PSP	-0.034	-0.090	-0.042	[359]

**Table 4.14:** Piezoelectric polarization parameters.

Material	$a$ [Å]	$a_0$ [Å]	$e_{13}$ [C/m <sup>2</sup> ]	$e_{33}$ [C/m <sup>2</sup> ]	$C_{13}$ [GPa]	$C_{33}$ [GPa]
GaN	3.197	5.210	-0.37	0.67	68	354
AlN	3.108	4.983	-0.62	1.50	94	377
InN	4.580	5.792	-0.45	0.81	70	205

Using the provided method and the listed values, the polarization induced charges for AlGa<sub>x</sub>N/GaN, InAlN/GaN, and InGa<sub>x</sub>N/GaN interfaces are calculated and shown in Fig. 4.20. While using slightly different values than Ambacher *et al.* [358], we still obtain a good agreement with their results. Furthermore, the significantly larger charges at the InAlN/GaN interface must be noted (due to the higher spontaneous polarization in AlN).

The dependence of the spontaneous polarization coefficients for GaN, AlN, and InN on temperature has been measured to be minimal [360], [361]. There are no reports on the temperature dependence of the piezoelectric polarization.

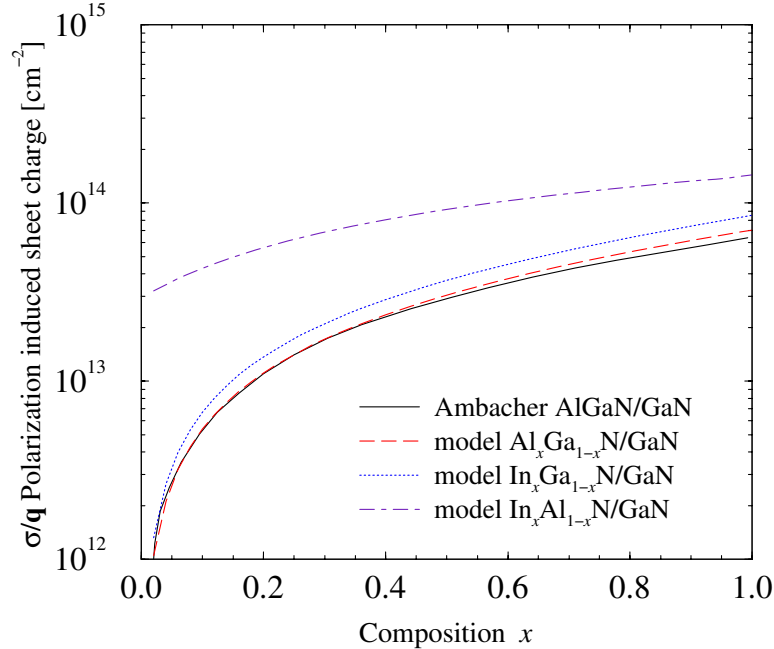


**Figure 4.20:** Piezoelectric and spontaneous polarization-induced charge  $\sigma/q(P_{SP} + P_{PE})$ .

## 4.6 AC Simulation: Equivalent Circuits and Parameter Extraction

The small-signal response of a two-port network (Fig. 4.21) can be described by several equivalent parameter sets. The  $\mathbf{Y}$ -matrix (admittance matrix) gives the relation between input voltages and output currents:

$$\begin{pmatrix} I_1 \\ I_2 \end{pmatrix} = \begin{pmatrix} Y_{11} & Y_{12} \\ Y_{21} & Y_{22} \end{pmatrix} \begin{pmatrix} V_1 \\ V_2 \end{pmatrix} \quad (4.82)$$

with

$$Y_{11} = \left. \frac{I_1}{V_1} \right|_{V_2=0} \quad Y_{12} = \left. \frac{I_1}{V_2} \right|_{V_1=0} \quad (4.83)$$

$$Y_{21} = \left. \frac{I_2}{V_1} \right|_{V_2=0} \quad Y_{22} = \left. \frac{I_2}{V_2} \right|_{V_1=0} . \quad (4.84)$$

Another established relation is the  $\mathbf{Z}$ -matrix (impedance parameters), which links the output voltages to the input currents:

$$\begin{pmatrix} V_1 \\ V_2 \end{pmatrix} = \begin{pmatrix} Z_{11} & Z_{12} \\ Z_{21} & Z_{22} \end{pmatrix} \begin{pmatrix} I_1 \\ I_2 \end{pmatrix} \quad (4.85)$$

with

$$Z_{11} = \left. \frac{V_1}{I_1} \right|_{I_2=0} \quad Z_{12} = \left. \frac{V_1}{I_2} \right|_{I_1=0} \quad (4.86)$$

$$Z_{21} = \left. \frac{V_2}{I_1} \right|_{I_2=0} \quad Z_{22} = \left. \frac{V_2}{I_2} \right|_{I_1=0} . \quad (4.87)$$

However, measurement of those parameter sets requires open or shortcut conditions, which are difficult to achieve at high frequencies. To avoid this problem, matched loads can be used. Thus, the device is embedded into a transmission line with a specific impedance ( $Z_0$ ). For a traveling wave, the inserted network acts as an impedance, different from the characteristic impedance of the line. S-parameters are the complex valued reflexion and transmission coefficients (Fig. 4.22):

$$\begin{pmatrix} b_1 \\ b_2 \end{pmatrix} = \begin{pmatrix} S_{11} & S_{12} \\ S_{21} & S_{22} \end{pmatrix} \begin{pmatrix} a_1 \\ a_2 \end{pmatrix} \quad (4.88)$$



Figure 4.21: Voltages and currents at a two-port network.

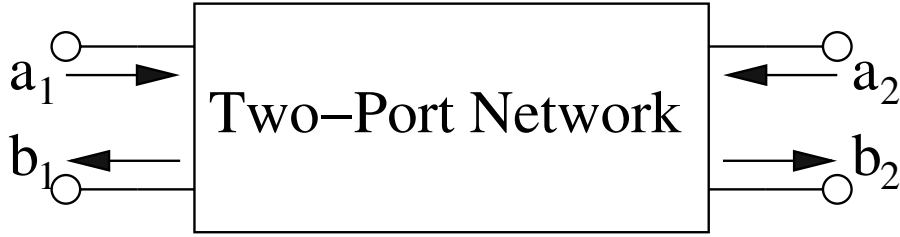


Figure 4.22: Incident and reflected waves at a two-port network.

with

$$S_{11} = \left. \frac{b_1}{a_1} \right|_{a_2=0} \qquad S_{12} = \left. \frac{b_1}{b_2} \right|_{a_1=0} \qquad (4.89)$$

$$S_{21} = \left. \frac{b_2}{a_1} \right|_{a_2=0} \qquad S_{22} = \left. \frac{b_2}{a_2} \right|_{a_1=0} . \qquad (4.90)$$

The power waves can be expressed as a function of the currents, voltages, and the complex reference impedance [362].

In order to obtain important figures of merit for the frequency characteristics of the devices, such as the cut-off frequency and the maximum oscillation frequency, an equivalent circuit is useful. Here, the one used by Dambrine *et al.* [363] for FETs is applied (Fig. 4.23). The expressions to calculate the values of its circuit elements are as following [363], [364]:

$$\omega = 2\pi f \qquad (4.91)$$

$$Y_{GS} = Y_{11} + Y_{12} \qquad (4.92)$$

$$Y_{gm} = Y_{21} - Y_{12} \qquad (4.93)$$

$$Y_{DS} = Y_{22} + Y_{12} \qquad (4.94)$$

$$Y_{GD} = -Y_{12} \qquad (4.95)$$

$$C_{GD} = \frac{-1}{\text{Im}\left(\frac{1}{Y_{GD}}\right)\omega} \qquad (4.96)$$

$$C_{DS} = \frac{\text{Im}(Y_{DS})}{\omega} \qquad (4.97)$$

$$C_{GS} = \frac{-1}{\text{Im}\left(\frac{1}{Y_{GS}}\right)\omega} \qquad (4.98)$$

$$R_{GS} = \text{Re}\left(\frac{1}{Y_{GS}}\right) \qquad (4.99)$$

$$R_{DS} = \frac{1}{\text{Re}(Y_{DS})} \qquad (4.100)$$

$$R_{GS} = \text{Re}\left(\frac{1}{Y_{GD}}\right) \qquad (4.101)$$

$$(4.102)$$

As the cut-off frequency is defined as the frequency at which the gain is unity, based on the

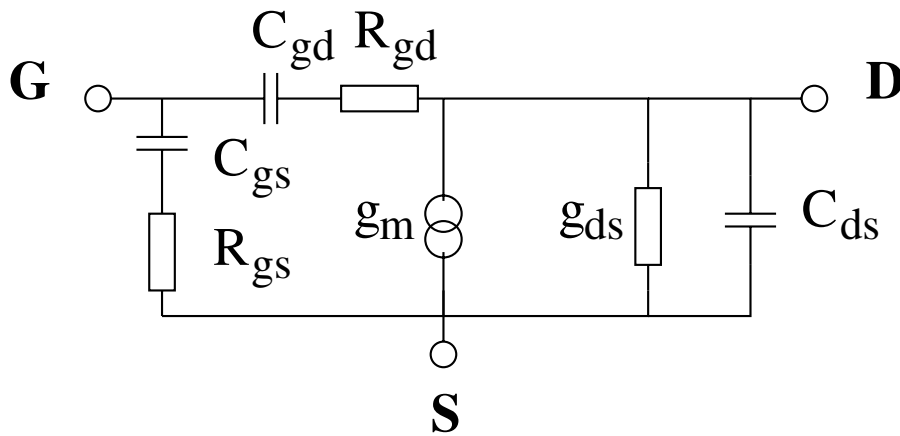


Figure 4.23: Equivalent circuit for a HEMT.

given equivalent circuit the following expression for  $f_t$  can be obtained:

$$f_T = \frac{g_m}{2\pi(C_{GS} + C_{GS})}$$

with

$$g_m = |Y_{gm}(1 + j\omega R_{GS}C_{GS})|.$$

In order to separate eventual errors introduced by the measurement equipment it is helpful to embed the device in a parasitic equivalent circuit, independent of the biasing conditions. Such a parasitic equivalent circuit is shown in Fig. 4.24 [365]. The values for those elements are given in Table 4.15.

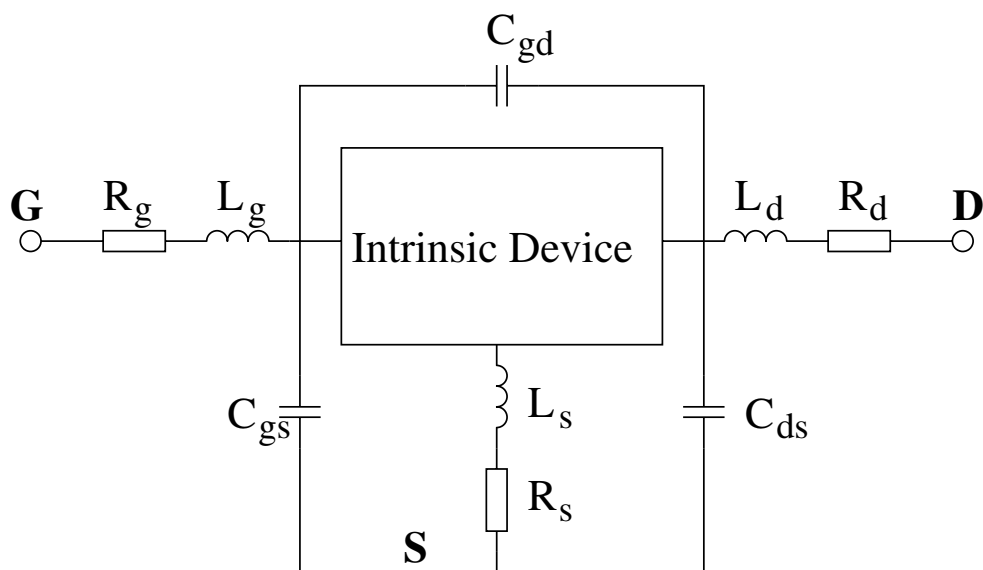


Figure 4.24: Extrinsic parasitic elements.

**Table 4.15:** Applied parasitic elements for GaN HEMT simulation.

Element	$L_s$	$L_g$	$L_d$	$C_{pgs}$	$C_{pgd}$	$C_{pds}$
Unit	[pH]	[pH]	[pH]	[fF]	[fF]	[fF]
Value	1	44	46	18	6	9

## Chapter 5

---

# Simulation Studies

---

VARIOUS hydrodynamic simulation studies of different HEMT structures are presented in this chapter, which can be divided into two main parts: the first part deals with normally-on devices and their characteristics, while the second one focuses on normally-off structures. At the beginning, three different generations of normally-on devices are analyzed by using the models discussed in Chapter 4. Both the *DC* and *AC* characteristics are studied. As several application areas require the devices to operate at elevated temperatures, simulations of AlGaIn/GaN HEMTs at high temperatures are presented, too. The simulator delivers good predictive results for the *DC* and *RF* characteristics of various devices after initial calibration. The temperature dependence of the maximum current and cut-off frequency of submicron devices is further studied.

One of the drawbacks of GaN-based HEMTs is the pronounced decrease of the transconductance  $g_m$  at higher gate bias, due to increasing source-gate and gate-drain resistances. Via simulations it is proved that the electric field distribution and the resulting carrier velocity quasi-saturation are the main source for the transconductance collapse, consequently also for the resistance rise. A shorter source-gate distance leads to a higher  $g_m$  peak value, but a more abrupt collapse at high gate bias. These effects are further discussed with respect to device linearity.

An investigation on the field plate technique in AlGaIn/GaN power HEMTs follows. The critical geometrical variables controlling the field distribution in the channel are determined and optimized for improved device reliability. The results are implemented in the actual design of later device generations.

InAlN/GaN HEMTs have been recently proposed to provide higher polarization charges without the drawback of high strain. Relying on experimental work a simulation study of InAlN HEMTs is conducted. Using the calibrated setup, specific device effects are explored and the *AC* device performance is estimated.

Only a few approaches to obtain normally-off device characteristics exist, as described in Chapter 2. First, the trade-off between high-frequency performance and threshold voltage achieved by a gate recess technique is analyzed. Another approach is a thin InGaIn cap layer, which introduces a polarization field which raises the conduction band of the AlGaIn/GaN interface. Relying on the experimental work of Mizutani *et al.* [18] a simulation study of the proposed

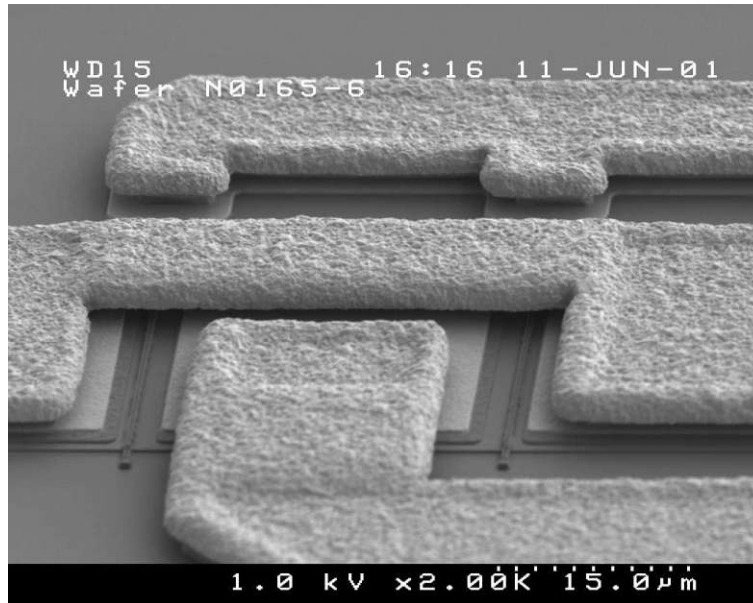


**Figure 5.1:** SEM image of two HEMTs (IAF Freiburg).

devices is conducted. The characteristics of the devices are compared to those of structures featuring the gate recess technique.

All of the presented simulation studies are based on experimental data from real devices. The AlGaIn/GaN structures were produced and measured at the *Fraunhofer-Institute for Solid-State Physics (IAF)*, while the InAlN/GaN structures were fabricated at the *Institute for Solid-State Electronics, TU Wien*.

## 5.1 Depletion-Mode HEMTs

A traditional HEMT structure is conductive at zero gate bias voltage, due to the polarization-induced charge at the barrier/channel interface. Consequently, D-mode transistors are well-studied and have been further developed for several years. The major part of the devices produced currently are therefore normally-off devices.

### 5.1.1 AlGaIn/GaN Devices

All of the measured AlGaIn/GaN devices share some basic properties like identical substrate, layer sequence, and material quality. However, there are differences in the general geometry and AlGaIn layer composition in the particular structures. As an illustration of the device surface geometry a scanning electron microscopy (SEM) image is shown in Fig. 5.1. The top metalization is the gate, the middle one is the source, and the bottom one is the drain. The active transistor area is the shallow channel between the source and drain metalization, with the thin gate electrode running along. In this figure two transistors are shown.



**Table 5.1:** Charge density [ $\text{cm}^{-2}$ ] for three AlGa<sub>x</sub>N/GaN HEMTs.

	Device A	Device B	Device C
channel/barrier	$1.14 \times 10^{13}$	$1.22 \times 10^{13}$	$0.94 \times 10^{13}$
barrier/cap	$-0.4 \times 10^{13}$	$-0.4 \times 10^{13}$	$-0.25 \times 10^{13}$
cap/passivation	$-0.4 \times 10^{13}$	$-0.4 \times 10^{13}$	$-0.4 \times 10^{13}$

### 5.1.1.1 Device Structures

The AlGa<sub>x</sub>N/GaN HEMT technology is based on multi-wafer Metal Oxide Chemical Vapor Deposition (MOCVD) growth on 3-inch semi-insulating SiC substrates. The gate is e-beam defined with different gate lengths ( $L_g=0.25 \mu\text{m}$ ,  $0.5 \mu\text{m}$ , and  $0.6 \mu\text{m}$ ). Device isolation is achieved by mesa isolation. An Al<sub>x</sub>Ga<sub>1-x</sub>N/GaN heterointerface is grown on top of a thick insulating GaN buffer. All layers are unintentionally doped except for the supply layers in some of the devices. A metal diffusion of the metal source and drain contacts reaching into the channel is assumed. The positive charge (introduced by polarization effects) at the channel/barrier interface is compensated by a commensurate negative surface charge at the barrier/cap interface. The charge density values for the three devices are listed in Table 5.1. Using the methodology as described in Section 4.5 theoretical values of  $1.7 \times 10^{13} \text{ cm}^{-2}$  and  $1.2 \times 10^{13} \text{ cm}^{-2}$  for the Al<sub>0.3</sub>Ga<sub>0.7</sub>N/GaN interface and Al<sub>0.22</sub>Ga<sub>0.78</sub>N/GaN interface, respectively, are calculated. However, in real devices several effects such as dislocations and surface states reduce the total sheet charge. Thus, lower values are used in the simulations, adapted in order to achieve a density similar to the one extracted from Hall measurements.

For good control of the sheet carrier concentration in the two-dimensional electron gas (2DEG), the alloy composition and the abruptness of the AlGa<sub>x</sub>N/GaN interface has to be determined. Various methods such as high resolution X-ray diffraction, transmission electron microscopy, and elastic recoil detection have been used [358], [366], [367]. A good estimate of the effective channel thickness of the conducting region is required for the simulator. A nominal value for the thickness of the 2DEG region has been found in the literature to be in the order of 2–3 nm, see e.g. [368], depending on the Al mole fraction in the AlGa<sub>x</sub>N layer. However, the effective thickness of the conducting region may be wider than the 2DEG, albeit with a lower density. For the purpose of calibrating the simulator to produce the same current density as in the measured devices, various effective thicknesses of the defect-free conducting GaN layer were analyzed. A value of 50 nm was used in all simulations throughout this chapter. Self-heating effects are accounted for by using a properly adapted ambient temperature. The barrier height of the Schottky contact to GaN was experimentally determined to be 1.0 eV at room temperature in agreement with experiments by other groups [273].

Devices from three different HEMT generations are measured and simulated: first a device with field-plate structure (Device A), next a device with shield-plate structure (Device B), and last a state of the art device with T-gate only (Device C) [4]. The layer properties are summarized in Table 5.2 and the geometry is shown in Fig. 5.2.

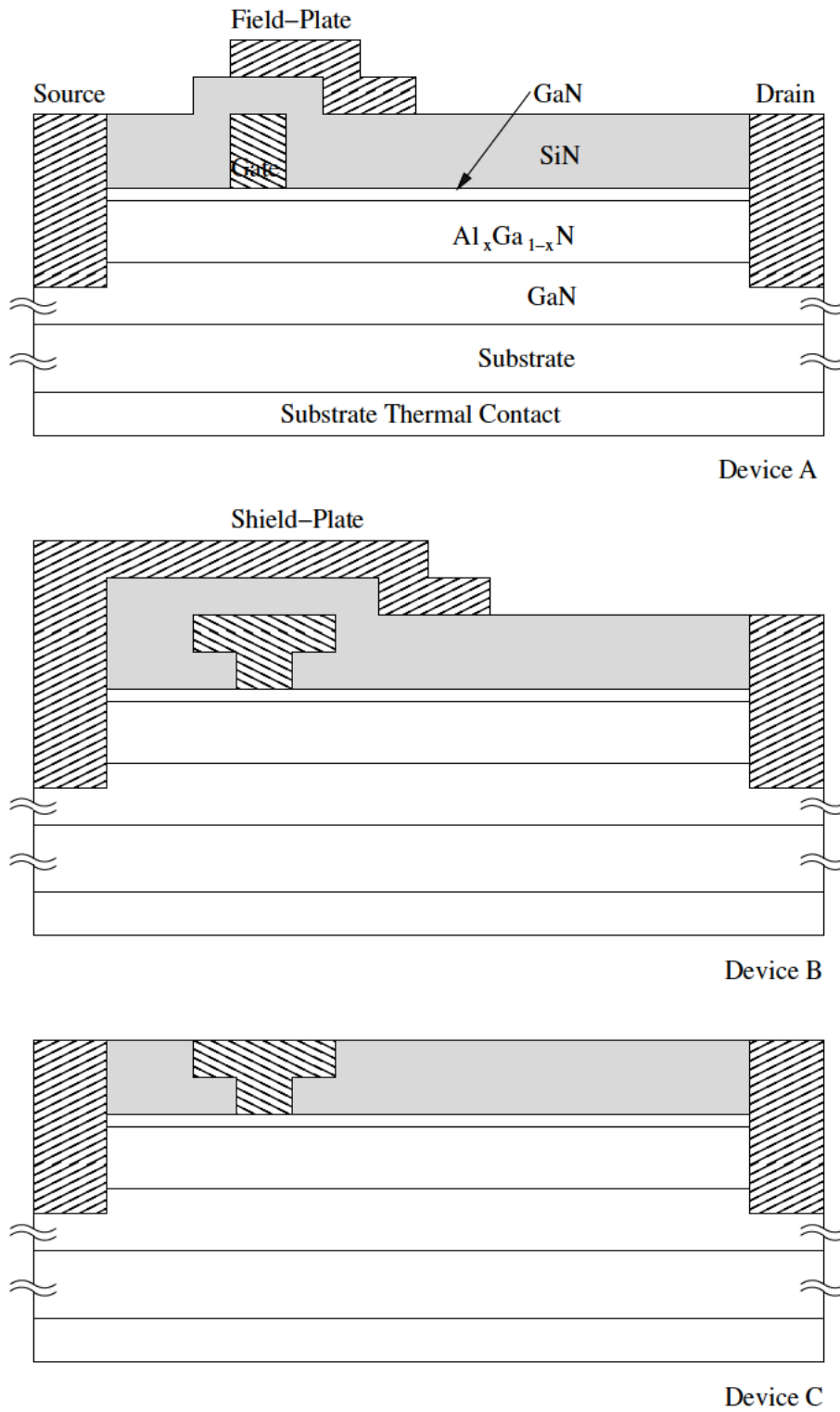


Figure 5.2: Schematic layer structure.

**Table 5.2:** Layer properties for three AlGaIn/GaN HEMTs.

	Device A	Device B	Device C
barrier thickness [nm]	17	17	22
Al composition [%]	30	30	22
$\delta$ doping	yes	yes	no
cap thickness [nm]	5	5	3

Device A has gate length  $L_g = 0.6 \mu\text{m}$ , field-plate extension length  $L_{FP}=0.6 \mu\text{m}$ , and gate width  $100 \mu\text{m}$ . The Al composition in the AlGaIn supply layer is 30%. The latter is  $\delta$ -doped in order to provide additional carriers and to improve access resistance. Contact resistances of  $4 \Omega \text{ mm}$  are assumed.

Device B is a  $L_g = 0.5 \mu\text{m}$  device featuring a source shield-plate. The gate is T-shaped. The Al composition in the barrier layer is 30% with a  $\delta$  doping, too.

The last device has a T-shaped gate with  $L_g = 0.25 \mu\text{m}$  and a gate width  $W_g=2 \times 50 \mu\text{m}$  (taken as  $1 \times 100 \mu\text{m}$  in the simulations). The Al composition in the supply layer is 22%, contact resistance is  $0.2 \Omega \text{ mm}$ .

### 5.1.1.2 Simulation Results

Using the same setup the three generations of AlGaIn/GaN based HEMTs are simulated and the results are compared to experimental data. In the following the results are discussed.

**Device A:** Fig. 5.3 compares the measured transfer characteristics ( $V_{ds} = 12 \text{ V}$ ) with the simulations using the two models described in Section 4.4.3. Both setups provide a good agreement. The minor overestimation of the drain current at high gate voltage is due to either gate leakage or real-space transfer [370]. HD Model B (Section 4.4.3) delivers a slightly higher drain current. The reason is a small difference in the velocity characteristics at very low electric fields ( $<50 \text{ kV/cm}$ ), which, however, are crucial for the steady state transport. Fig. 5.4 shows the output characteristics. Again an overall good agreement is achieved with a pronounced self-heating effect at high gate voltages.

**Device B:** The transfer characteristics is measured at  $V_{ds} = 12 \text{ V}$  but also at  $V_{ds} = 50 \text{ V}$ . Fig. 5.5 compares the experiment with simulations, where the results agree very well. The corresponding output curves are provided in Fig. 5.6.

**Device C:** Fig. 5.7 compares the measured transfer characteristics at  $V_{ds} = 7 \text{ V}$  with simulations. The results achieved with electron mobility Model A match slightly better, however the

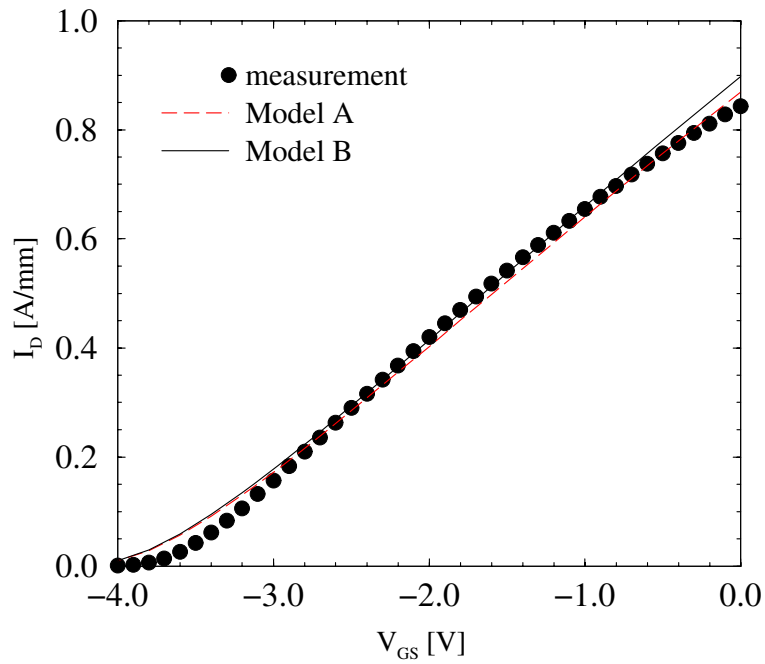


**Figure 5.3:** Comparison of measured and simulated transfer characteristics (Device A).

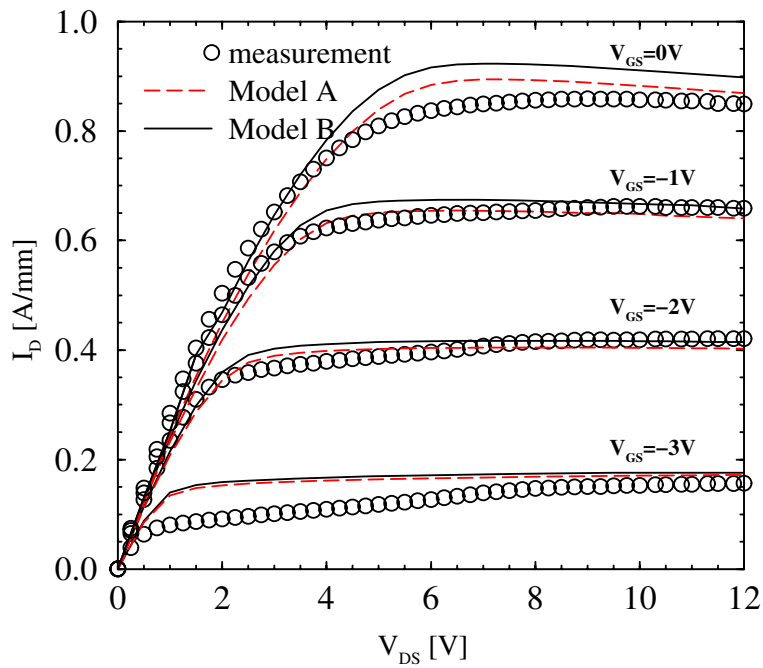


**Figure 5.4:** Comparison of measured and simulated output characteristics (Device A).

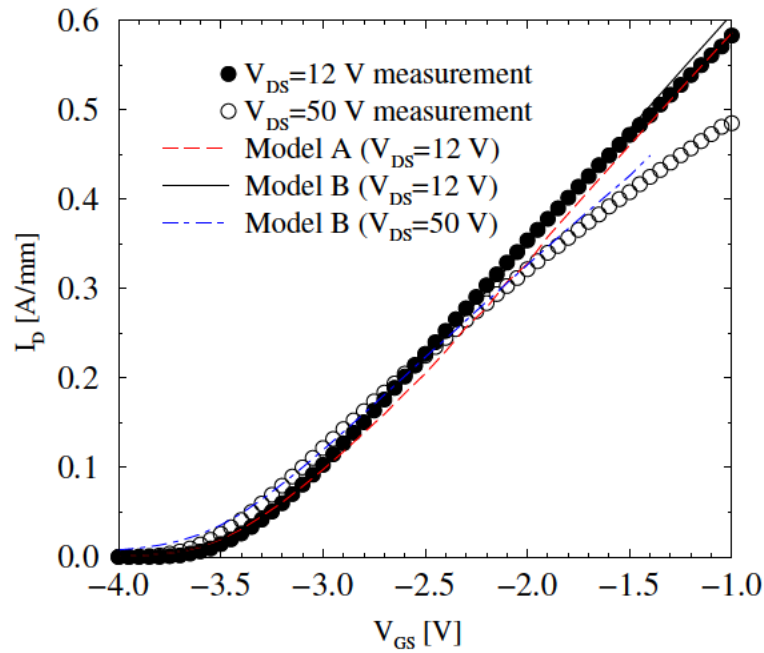


**Figure 5.5:** Comparison of measured and simulated transfer characteristics (Device B).

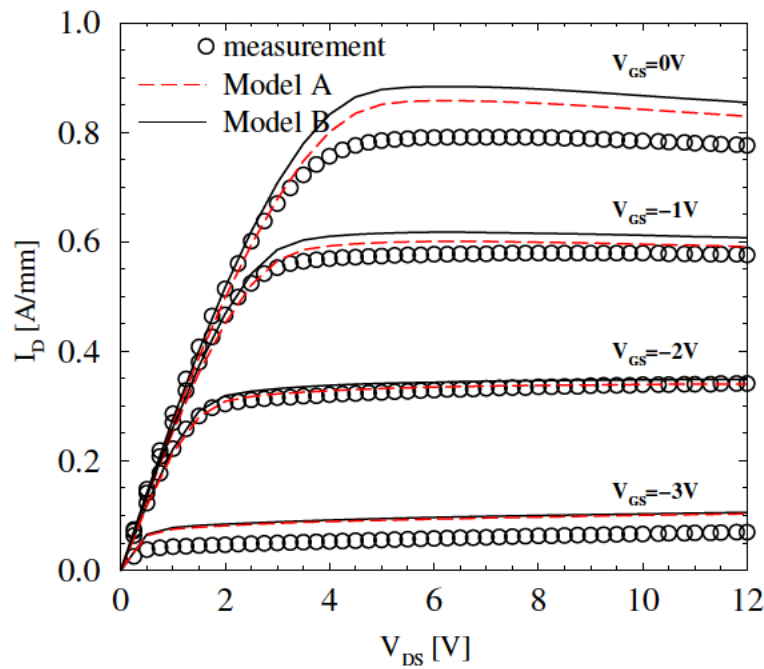


**Figure 5.6:** Comparison of measured and simulated output characteristics (Device B).

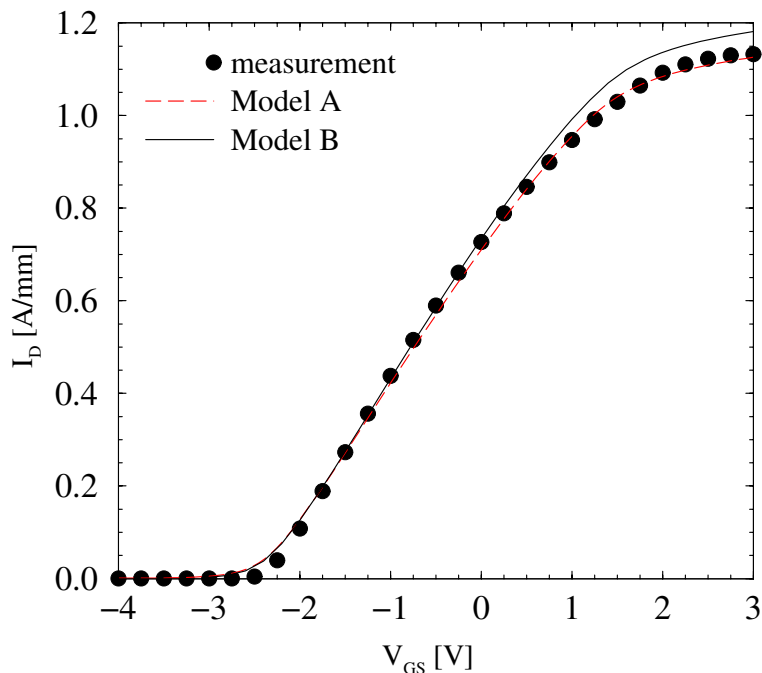


Figure 5.7: Comparison of measured and simulated transfer characteristics (Device C).

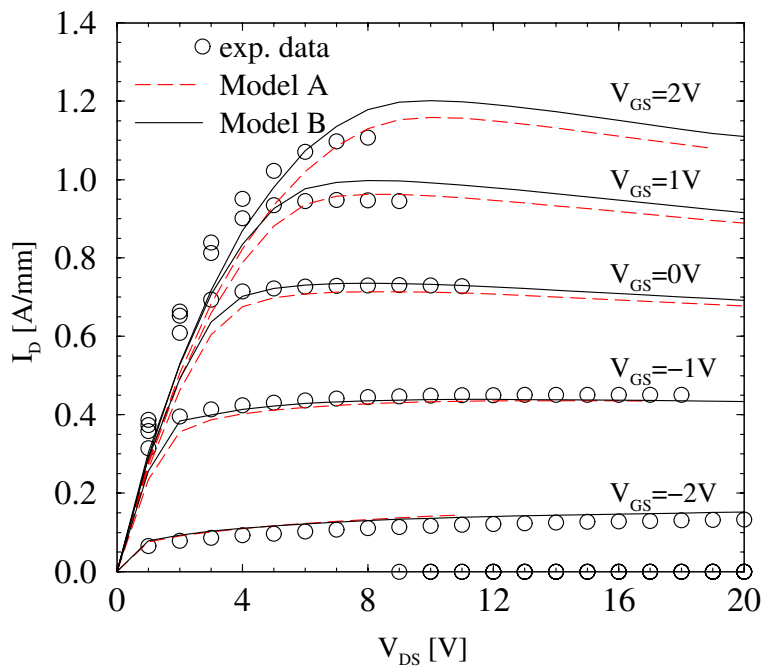


Figure 5.8: Comparison of measured and simulated output characteristics (Device C).

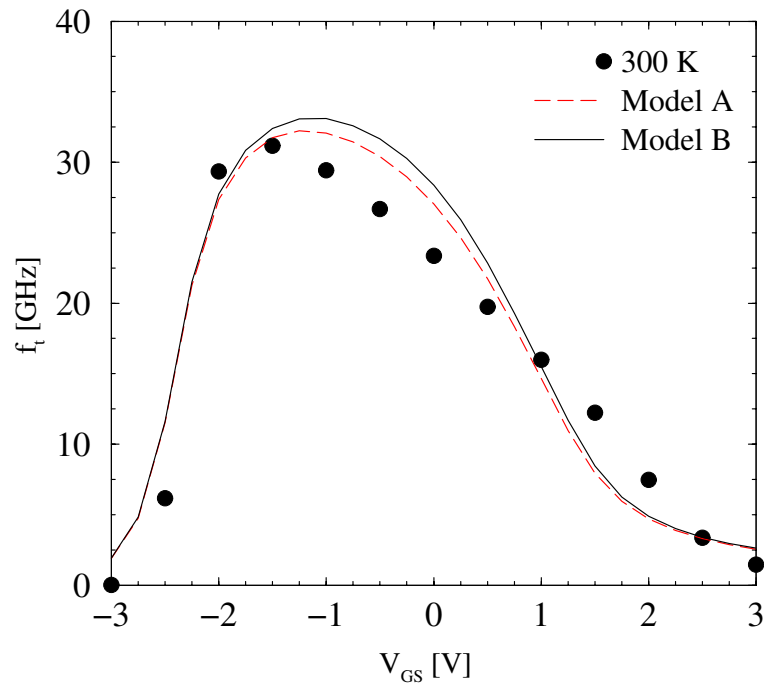


Figure 5.9: Comparison of measured and simulated cut-off frequency (Device C).

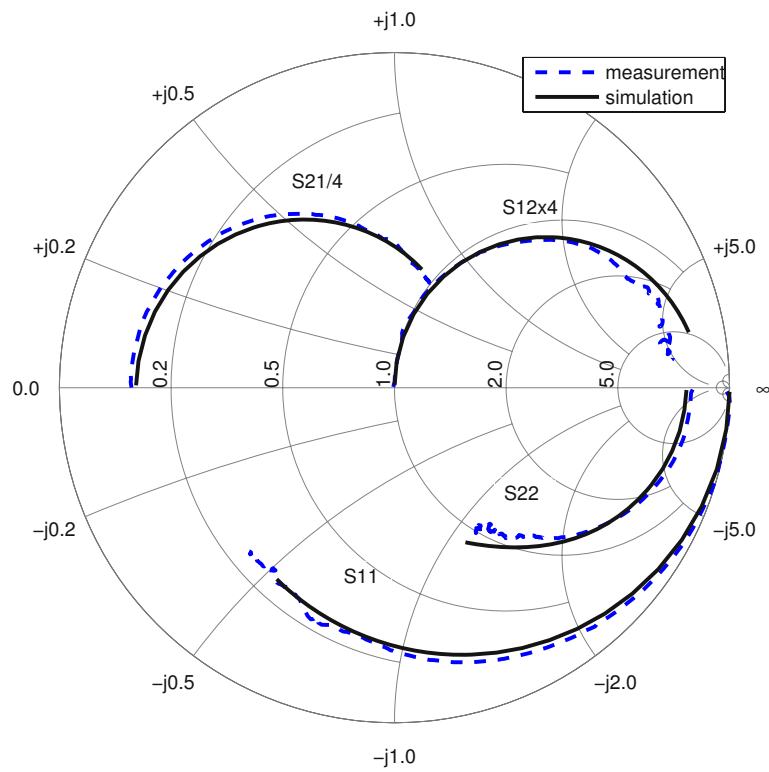
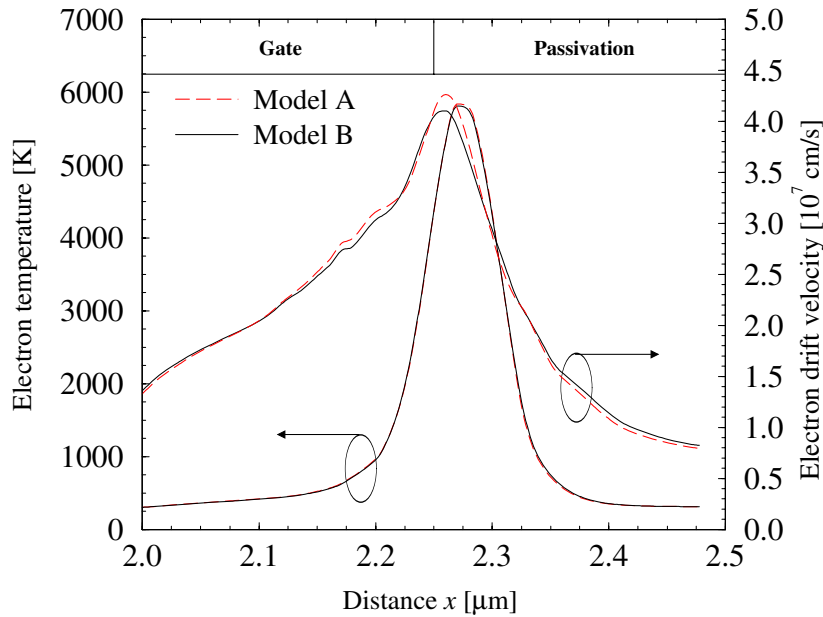


Figure 5.10: Comparison of measured and simulated S-parameters (Device C).



**Figure 5.11:** Simulated electron temperature and velocity along the channel.

model delivers a lower current at low  $V_{DS}$  than measured (Fig. 5.8). One possible reason is a higher electron velocity at lower fields in the real device due to low dislocation scattering effects.

*AC* simulations are performed to compare the calculated and experimental figures of merit e.g. cut-off and maximum frequency. Fig. 5.9 shows the measured and simulated cut-off frequency  $f_t$  (again at  $V_{ds} = 7$  V. In order to account for the parasitics introduced by the measurement equipment, the intrinsic parameters obtained in the simulation are transformed using a standard two-port pad parasitic equivalent circuit. Both models provide a very good agreement with the experiment.

Fig. 5.10 compares the measured and simulated (using Model B) extrinsic S-parameters at  $V_{gs} = -1.5$  V and  $V_{ds} = 7$  V. An excellent agreement is achieved for all parameters in the frequency range 100 MHz–26 GHz.

The electron transport in the channel under the gate is studied at the same bias point. As the electric field reaches its maximum under the drain side of the gate [371], the peak of the electron temperature is also found there (the gate edge is at  $x = 2.25$   $\mu\text{m}$  in Fig. 5.11). Consequently, in the same region a pronounced velocity overshoot is observed. Interestingly, temperature and velocity profiles obtained using both models do not differ significantly.

### 5.1.2 High Temperature Simulations

Several groups have studied the high-temperature *DC* operation of AlGaIn/GaN HEMTs on different substrates (sapphire [372], [373], [374], SiC [373], and Si [374], [350]). *AC* measurements at elevated temperatures, however, are sparse: e.g. the temperature dependence of the cut-off frequency is compared to that of the transconductance by Akita *et al.* [375]. An investigation of



the influence of high temperature on the microwave power performance of AlGaIn/GaN HEMTs is conducted by Arulkumaran *et al.* [376].

The theoretical studies of GaN-based transistors at higher temperature are also rare. There are few analytical models developed [377], [378], [379], however, those are tailored for use in circuit simulation, not for device optimization. To our knowledge there is only one work which focuses solely on high-temperature HEMT device simulation [380], however, it relies on dated experimental data [375] and does not feature *AC* performance.

Based on the temperature dependent material and model parameters as discussed in Chapter 4, the simulator is calibrated with the  $L_g = 0.25 \mu\text{m}$  structure (Device C in the previous section) serving as a calibration device [15]. HD electron mobility Model B is chosen for this study. The already mentioned values for the interface charges (Table 5.1) are retained, as are the other material and model parameters as e.g. the *Schottky* barrier height. However, it should be mentioned that the changes in the barrier height with temperature (in the range under investigation) are found to be negligibly small [381].

Using the same set of models and model parameters a  $L_g = 0.5 \mu\text{m}$  benchmark device is simulated. All other device properties (layer thickness and composition and geometry) are the same. The ambient temperatures at which the devices were measured and are simulated are 300 K, 365 K, and 425 K. For the gate-variation study, two more devices with  $L_g = 0.1 \mu\text{m}$  and  $L_g = 0.15 \mu\text{m}$  are simulated. Also a fourth ambient temperature of 485 K is explored.

### 5.1.2.1 DC Results

Using the values for the polarization-induced interface charges from Table 5.1 a very good agreement between measurement data and simulation results for the transfer characteristics of the calibration device is achieved (Fig. 5.12). Our setup allows for a proper modeling of the drain current also at elevated temperatures. As an example, Fig. 5.13 shows the output characteristics at 425 K. Two curves are shown for  $V_{gs} = 2 \text{ V}$ : without self-heating, which greatly overestimates the current; with self-heating, which delivers a significantly better match, but requires a higher computational effort. While others [382] have observed a significant threshold voltage ( $V_{th}$ ) shift, in our measurements such a shift is almost non-existent. As  $V_{th}$  depends on the carrier density, carrier trap density and the *Schottky* barrier height [383], we can assume that trapping effects in the devices are also temperature-independent in this range (the carrier density change is also negligible).

Fig. 5.14 shows the lattice temperature in the device at  $V_{ds} = 20 \text{ V}$  and  $V_{GS2}$  bias. The area where the lattice is heated from high-energy electrons, is the high-electric field region under the drain side of the gate and the gate-extension.

The same simulations are performed for the benchmark device. Retaining the same interface charge values, a good prediction of the threshold voltage is obtained (Fig. 5.15). Raising the ambient temperature, once again yields a good agreement between simulation results and experimental data, also for the output characteristics (shown at 425 K in Fig. 5.16).

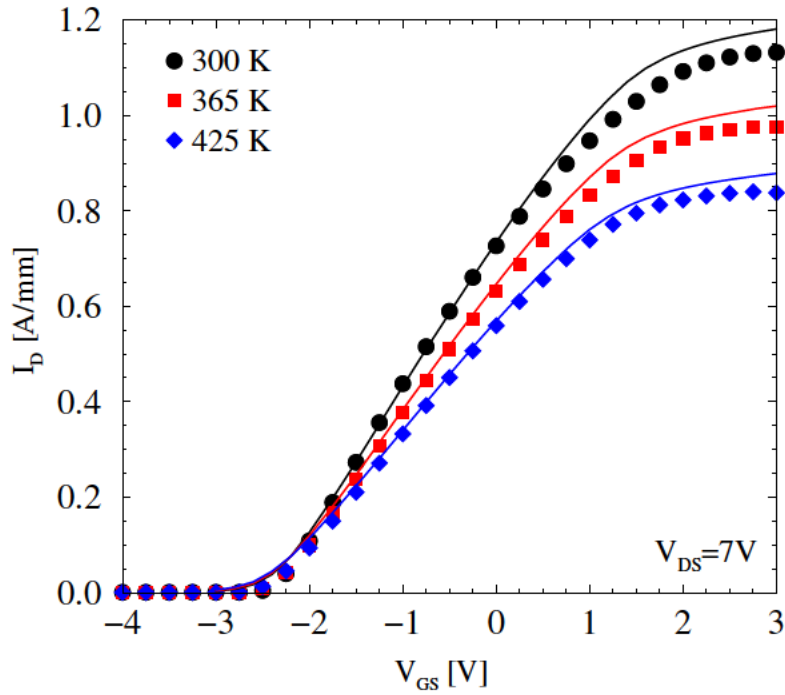


Figure 5.12: Calibrated transfer characteristics (lines) versus experimental data (symbols) for  $L_g = 0.25 \mu\text{m}$  HEMT.

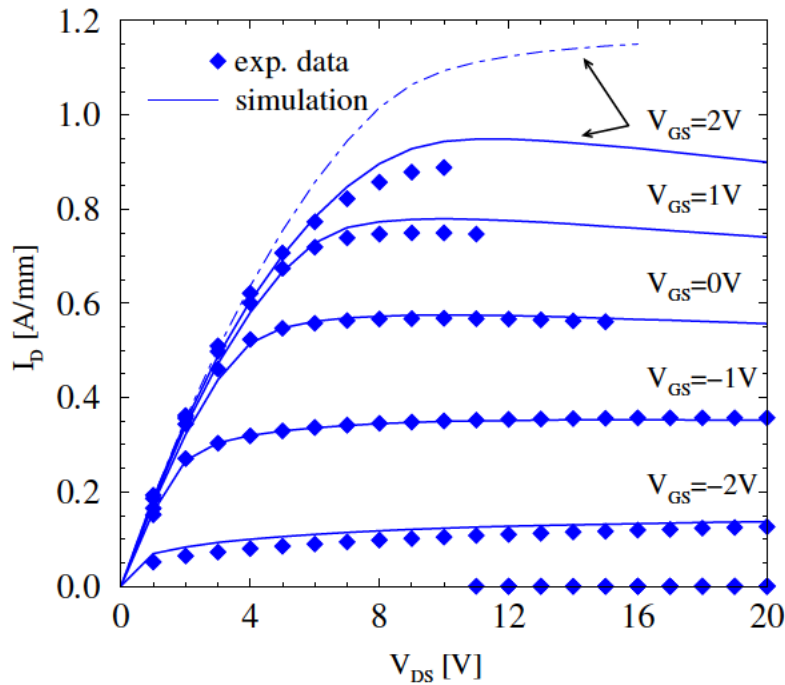


Figure 5.13: Calibrated output characteristics versus experimental (symbols) data for  $L_g = 0.25 \mu\text{m}$  HEMT at 425 K. Dot-dashed lines - without self-heating, solid lines - with self-heating.

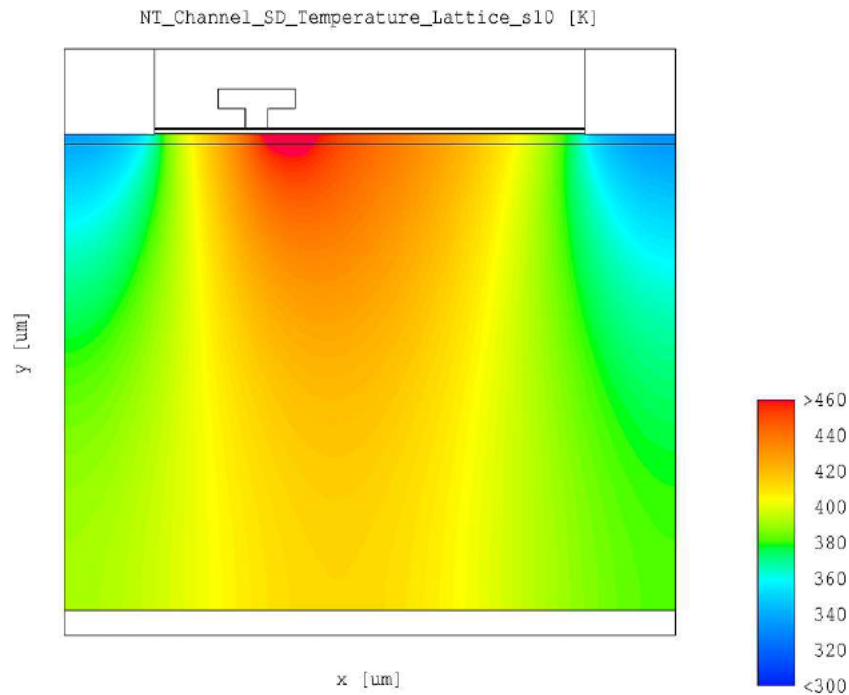


Figure 5.14: Lattice temperature in the calibration device,  $V_{gs} = 2$  V,  $V_{ds} = 20$  V.

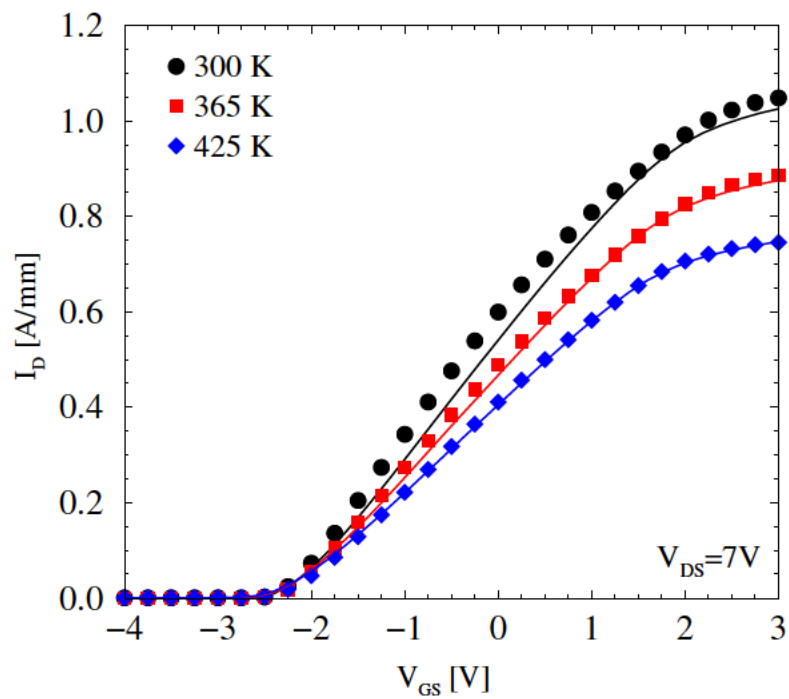


Figure 5.15: Predicted transfer characteristics (lines) compared to measured data (symbols) for  $L_g = 0.5 \mu\text{m}$  HEMT at different temperatures.

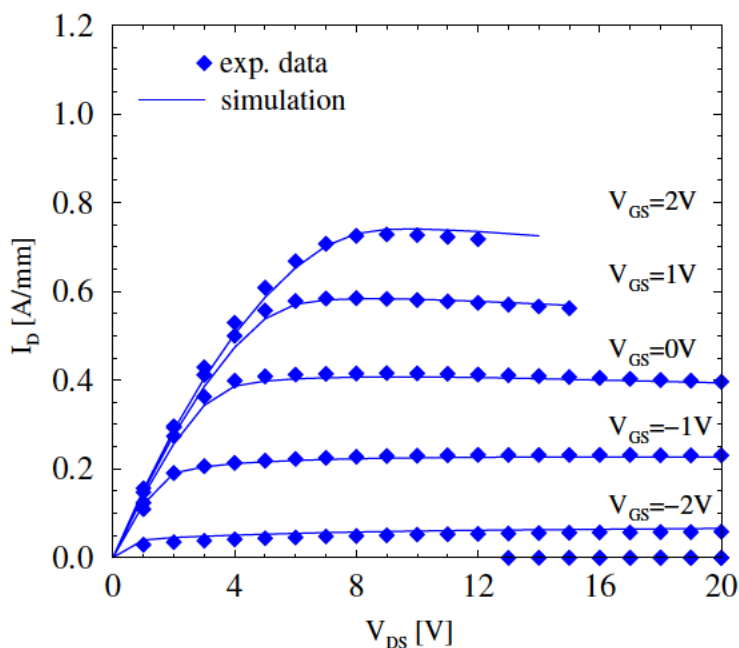


Figure 5.16: Predicted output characteristics versus experimental data for  $L_g = 0.5 \mu\text{m}$  HEMT at 425 K.

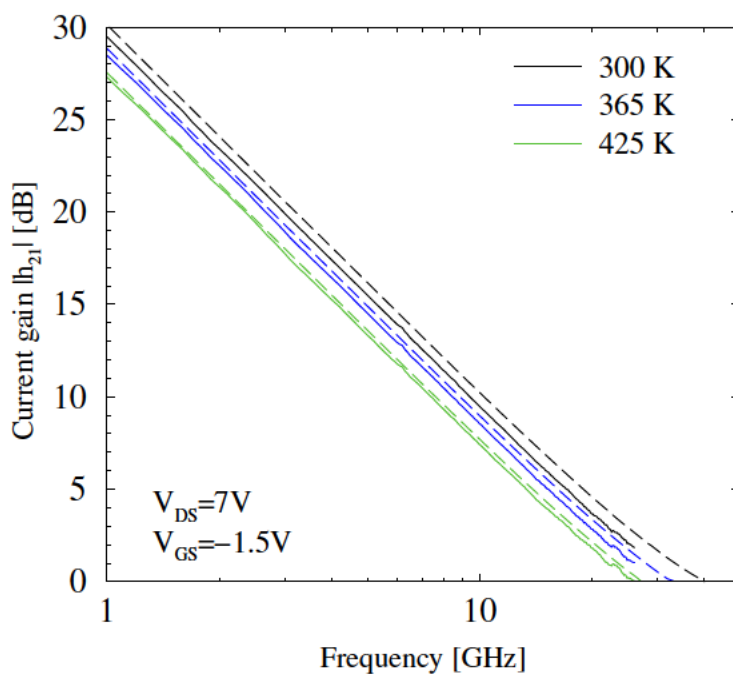
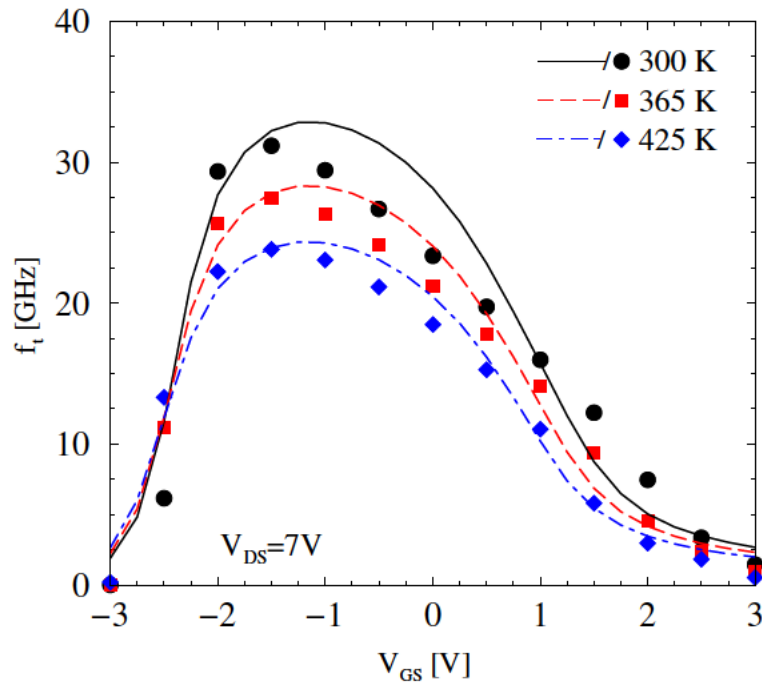


Figure 5.17: Current gain  $|h_{21}|$  for  $L_g = 0.25 \mu\text{m}$  HEMT, experimental data (solid lines) versus simulation (dashed lines).



**Figure 5.18:** Simulated cut-off frequency  $f_t$  (lines) compared to measurements (symbols) for  $L_g = 0.25 \mu\text{m}$  HEMT.

### 5.1.2.2 RF Results

The RF device performance is studied by small-signal AC analysis [365]. Fig. 5.17 shows the current gain  $|h_{21}|$  for the  $0.25 \mu\text{m}$  device for three temperatures. The gain decreases for higher temperatures and the simulation agrees well with the measurements. The calculated cut-off frequency  $f_t$  is compared to the measured one in Fig. 5.18. In order to account for the parasitics introduced by the measurement equipment the intrinsic parameters delivered by the simulation are transformed into extrinsic ones by using a standard two-port pad parasitic equivalent circuit. The values of the circuit elements are listed in Table 4.15. As already mentioned the measured device has two gate fingers of  $50 \mu\text{m}$  width each, which leads to a higher gate capacitance due to three-dimensional parasitic effects, than the simulated single device with  $W_g=100 \mu\text{m}$ .

A very good agreement between measured and simulated S-parameters is achieved at all temperatures both for the calibration device ( $L_g = 0.25 \mu\text{m}$ ) and the benchmark device ( $L_g = 0.5 \mu\text{m}$ ). Fig. 5.19 and Fig. 5.20 compare the simulated and measured intrinsic S-parameters in the range 100 MHz–26 GHz at  $V_{ds} = 7$  V and  $I_D=260$  mA/mm for the  $L_g = 0.25 \mu\text{m}$  HEMT at 300 K and 425 K. Fig. 5.21 and Fig. 5.22 compare predictive simulation results for the  $L_g = 0.5 \mu\text{m}$  device in the same frequency range,  $V_{ds} = 7$  V, and  $I_D=130$  mA/mm at 300 K and 425 K.

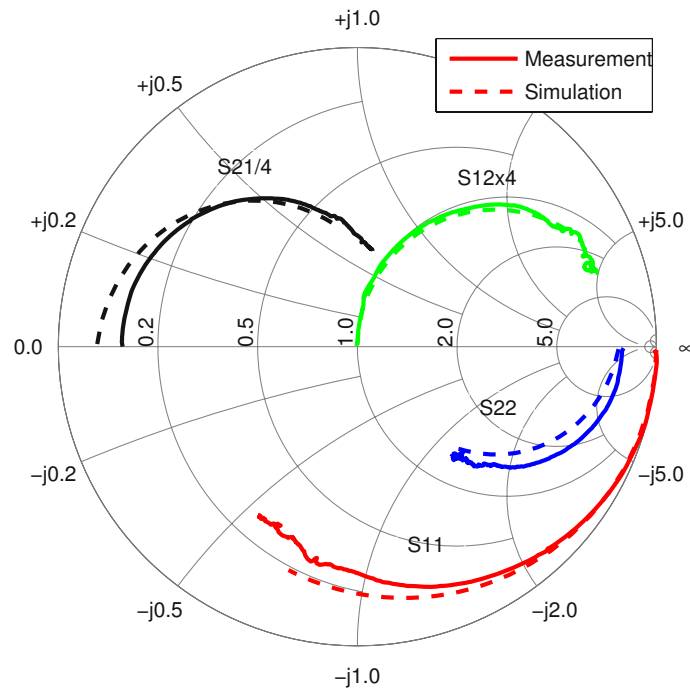


Figure 5.19: S-parameters for the  $L_g = 0.25 \mu\text{m}$  device at 300 K.

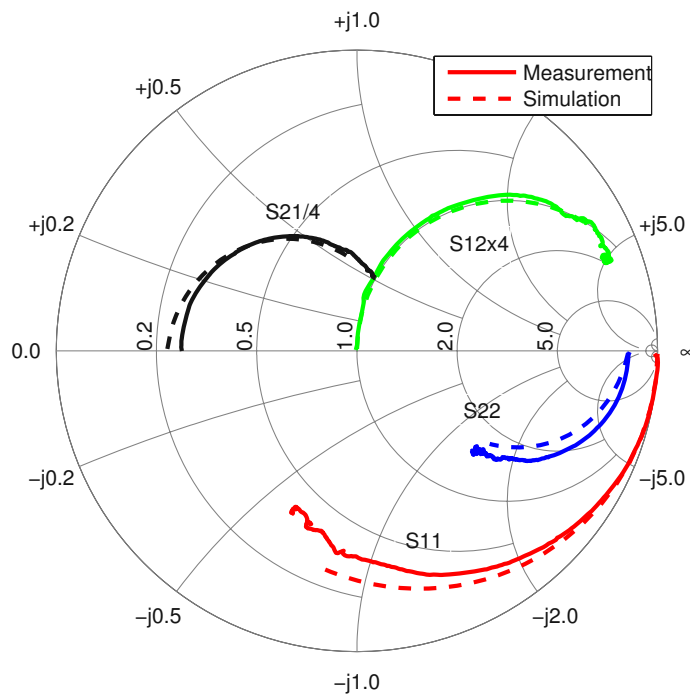


Figure 5.20: S-parameters for the  $L_g = 0.25 \mu\text{m}$  device at 425 K.

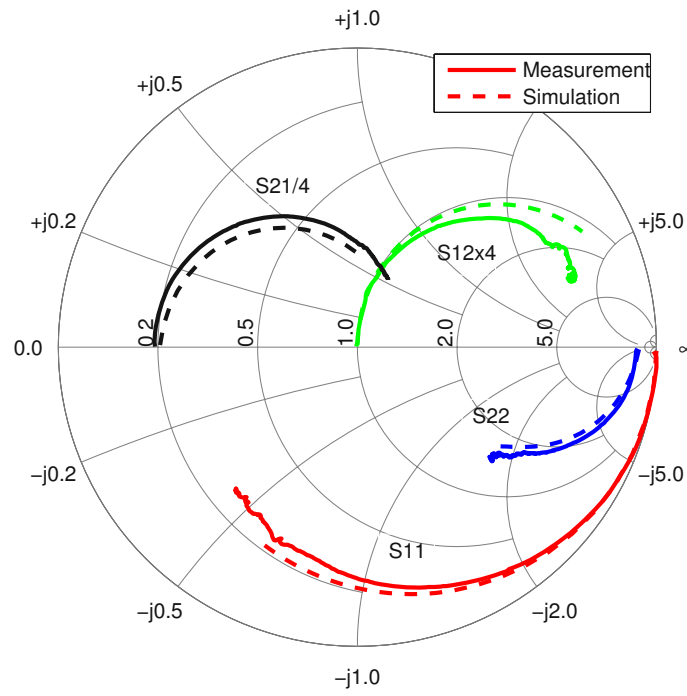


Figure 5.21: S-parameters for the  $L_g = 0.5 \mu\text{m}$  device at 300 K.

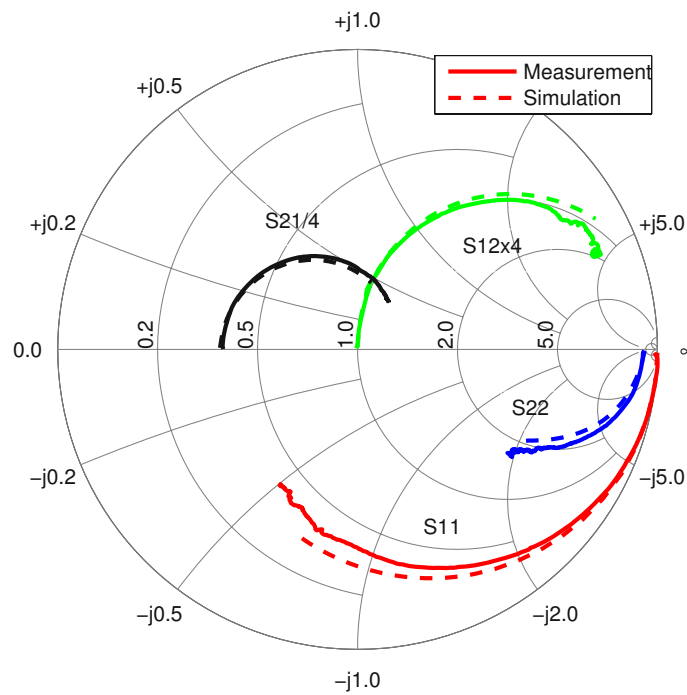
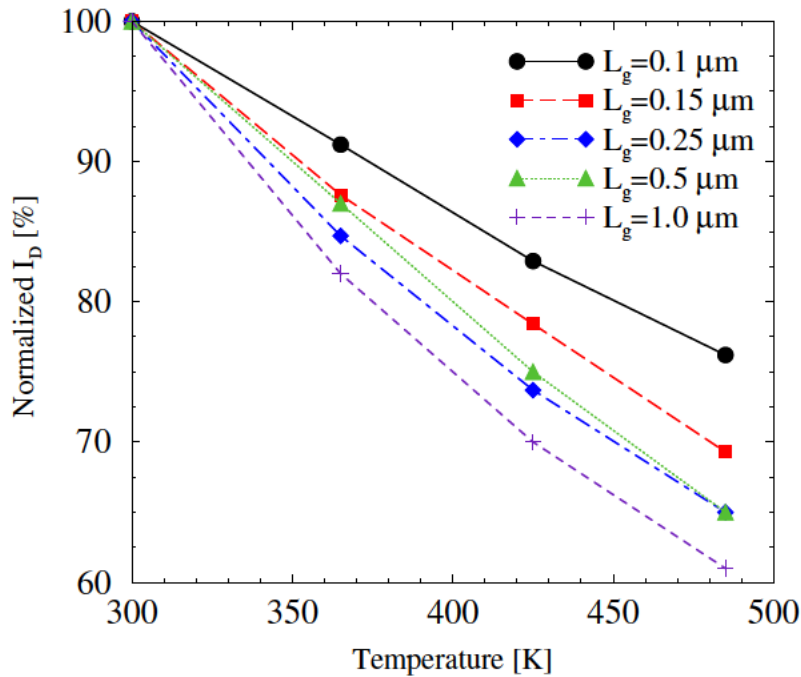


Figure 5.22: S-parameters for the  $L_g = 0.5 \mu\text{m}$  device at 425 K.



**Figure 5.23:** Simulated maximum  $I_D$  ( $V_{ds} = 7$  V) as a function of ambient temperature normalized to 300 K values.

### 5.1.2.3 Gate Length Variation

The geometry of the transistors is pointed out to be an important factor for high-temperature operation. Consequently, several authors have studied the reduction of  $I_D$  with rising temperature for different gate lengths e.g. [350], [349]. There is agreement that for short channel devices ( $L_g < 1 \mu\text{m}$ ) the carriers under the gate travel with saturation velocity. Therefore, the decrease of  $I_D$  is lower, because the decrease of the velocity in the saturation region is also lower. While only submicron devices are studied, the results for  $L_g = 1.0 - 0.25 \mu\text{m}$  structures agree well (Fig. 5.23) with the ones presented by Tan *et al.* [350]. However, for very small gates an even lower temperature dependence is observed. The same effect is more pronounced for the normalized  $f_t$ , where the devices with  $L_g = 1.0 - 0.25 \mu\text{m}$  deliver a similar reduction of  $f_t$  with temperature, while  $f_t$  of the sub-quartermicron devices decreases less (Fig. 5.24). We believe that for such gate length, not only  $L_g$  but also the gate-drain and gate-source distances and the exact geometry gain on importance, as for small gate lengths the parasitic contributions have to be scaled according to typical scaling rules in order to harvest the high-speed performance. In this case the relative contributions of the ohmic elements and thus their temperature dependence are reduced.

### 5.1.3 Transconductance Study

One of the difficulties, which still hampers the wide use of HEMTs, is the very strong dependence of the transconductance on the gate voltage. As the derivatives of the transconductance with respect to the gate voltage are detrimental to intermodulation distortion [384], [19], a profound



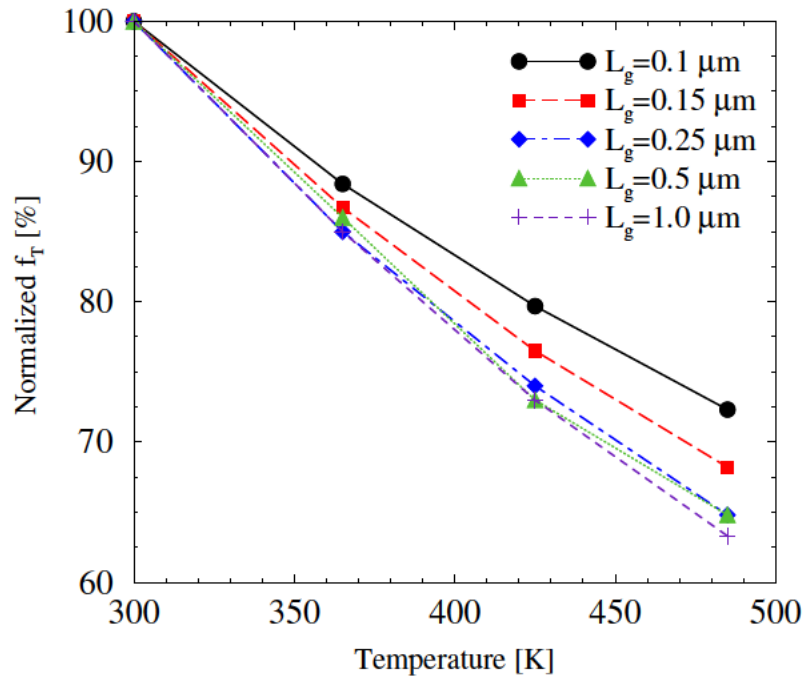


**Figure 5.24:** Simulated maximum  $f_t$  ( $V_{ds} = 7$  V) as a function of ambient temperature normalized to 300 K values.

knowledge of the causes for the transconductance nonlinearity significantly helps the selection of a proper load resistance. The problem has been addressed in numerous works, e.g. [385], [386]. Interface roughness and hot-phonon scattering have been ruled out as possible reasons for the strong dependence of the transconductance on gate voltage. While real space transfer effects are relevant in GaAs-based pHEMTs [370], the lack of a significant leakage current in the studied structures counts against it. Recently, the decrease of transconductance has been attributed to the strong nonlinearity of the source-gate resistance. This has been shown in a couple of studies relying on experimental measurements combined with simulations [385], [386], which employ specially tailored carrier velocity – electric field characteristics. Here, a good agreement with experimental data is achieved by using electron mobility Model B based on Monte Carlo simulation results. The electron transport in the source-gate and gate regions is studied in a wide range of gate-source voltages and the impact of scaling the source-gate distance  $L_g$  on transistor performance is discussed [19]. It is shown that the transconductance decrease should not be attributed to negative differential mobility effects, which is also reproduced by using a velocity-field characteristics from MC simulation results. Device C is used for the study with  $L_g = 0.25 \mu\text{m}$ , which has been already described in the previous sections.

### 5.1.3.1 Simulation Results

Fig. 5.25 shows the measured and simulated transfer characteristics of the device. Without any changes in the models or model parameters a very good agreement is achieved for the drain current as well as for the transconductance. The simulated transconductance exhibits roughly the same maximum value as the measurement and adequately follows the decrease at higher

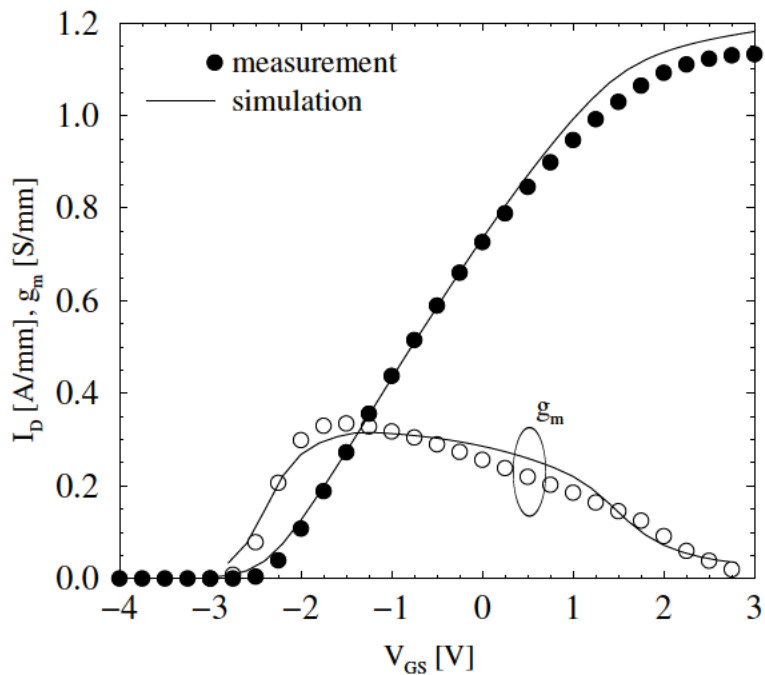


Figure 5.25: Drain current and transconductance at  $V_{ds} = 7$  V: measured data compared to simulation.

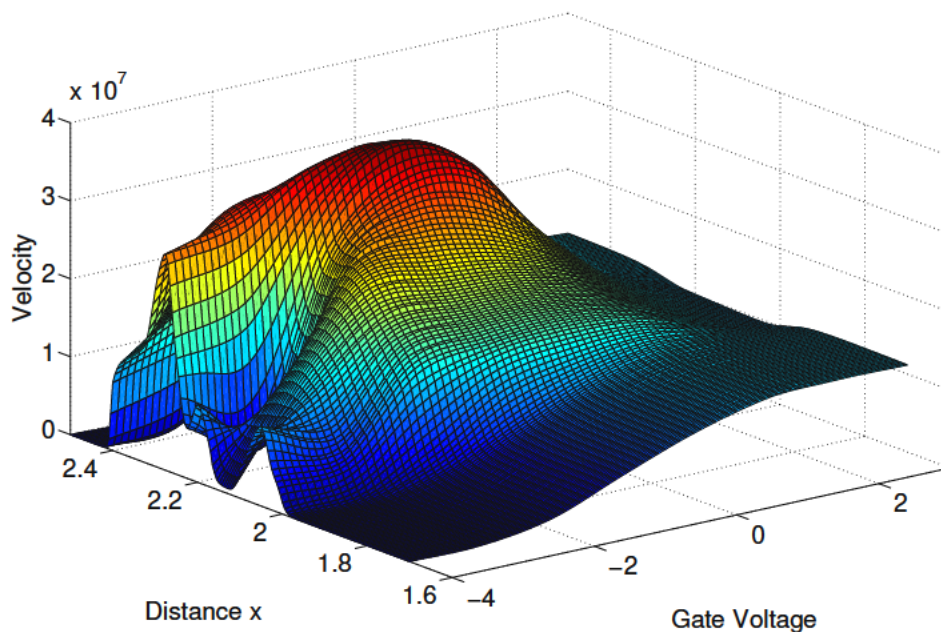


Figure 5.26: Electron velocity along the channel [cm/s].

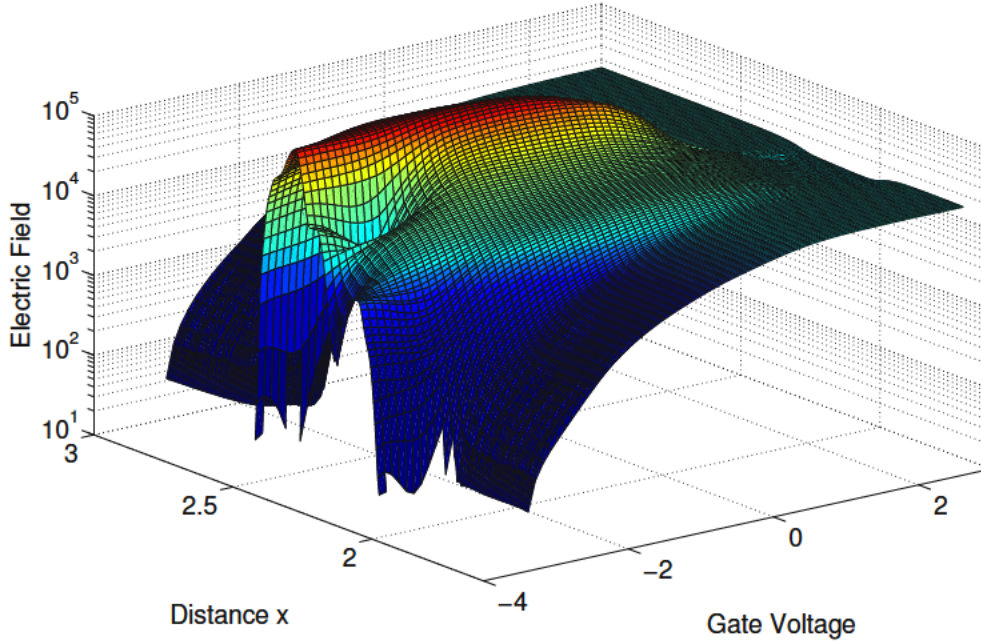


Figure 5.27: Electric field along the channel [V/cm].

gate voltage. In order to gain a better understanding of the carrier transport process in the device, the transconductance can be expressed as:

$$g_m = \frac{\Delta I_D}{\Delta V_{GS}} = \left( \frac{\Delta n}{\Delta V_{GS}} \right) e v + \left( \frac{\Delta v}{\Delta V_{GS}} \right) n e. \quad (5.1)$$

The first term describes the contribution of the change in carrier concentration  $\Delta n$ . The simulations show that it is substantial only under the gate, as in the source-gate and gate-drain areas no variation of the carrier concentration with  $V_{GS}$  is observed. The rapid increase in concentration in the bias range near the maximum transconductance combined with a high electron velocity (Fig. 5.26) indeed results in some contribution of this term to the overall  $g_m$ . However, this contribution is limited to a small area under the gate in a narrow voltage range, therefore for the further studies we focus primarily on the second term (the change in carrier velocity  $\Delta v$ ).

Fig. 5.26 shows the velocity along the channel of the device for  $V_{gs} = -4$  V to  $+3$  V (the gate is located from  $x = 2.0$   $\mu\text{m}$  to  $x = 2.25$   $\mu\text{m}$ ). There are two distinguishable regions: the source-gate region and the effective gate region ( $L_{G,\text{eff}}$ ). The latter exhibits a high velocity up to  $V_{gs} = -1$  V, which then decreases abruptly. This is to be attributed entirely to the electric field profile, which is depicted in Fig. 5.27. The complex form at low  $V_{GS}$  is due to the negative differential velocity at high electric fields, for which the mobility model accounts. As the channel under the gate is entirely depleted at this bias, there is no notable effect on the *DC* characteristics of the device. The flat distribution of the product  $\Delta v n$  (second term in (5.1)) in the gate region as shown in Fig. 5.28 confirms this reasoning.

In the source-gate region a steady increase of the velocity is observed between  $V_{gs} = -3$  V

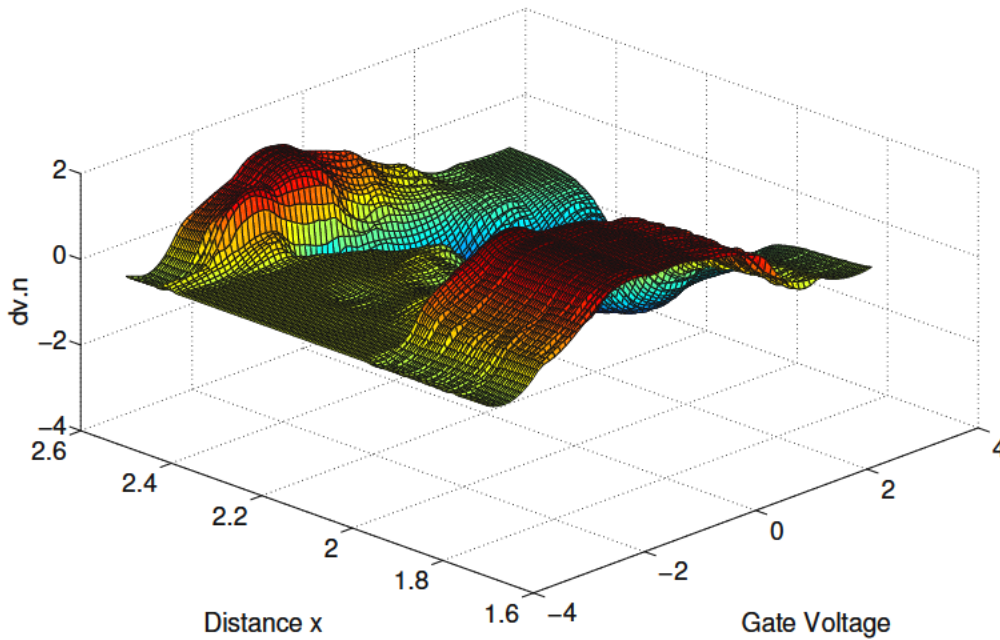


Figure 5.28:  $\Delta v n$  (scaled) along the channel [ $\text{cm}^{-2}\text{s}^{-1}$ ].

and 0 V, which corresponds to the increase in the electric field. Notably, the electron velocity is very low for  $V_{\text{GS}} < -3$  V and almost constant for  $V_{\text{GS}} > 1$  V. The resulting product  $\Delta v n$  shows a distribution which is very similar to the transconductance characteristics. The decrease of the electric field and, consequently, of the electron velocity under the gate at  $V_{\text{GS}} \approx 0$  V produces a significant negative region. Furthermore, the electron mobility in the source-gate region decreases significantly with higher  $V_{\text{GS}}$ , which results in the higher source-gate resistance.

Based on these observations several conclusions are self-evident:

- The electron velocity at low electric fields in the source-gate region has the highest impact on the transconductance.
- The decrease of transconductance is caused by the quasi-saturation of the electron velocity in the source-gate region, due to the reached maximum electric field in this region.
- At very high gate bias the electric field reduces further the velocity under the gate and causes the secondary collapse of the transconductance.

### 5.1.3.2 Source-Gate Distance Scaling

Some authors have pointed out the positive effects of downscaling the source-gate distance ( $L_{\text{SG}}$ ) on the transconductance [386], [388]. Based on the structure described above, four more devices are introduced, which share the same geometry except for the source-gate distance: one

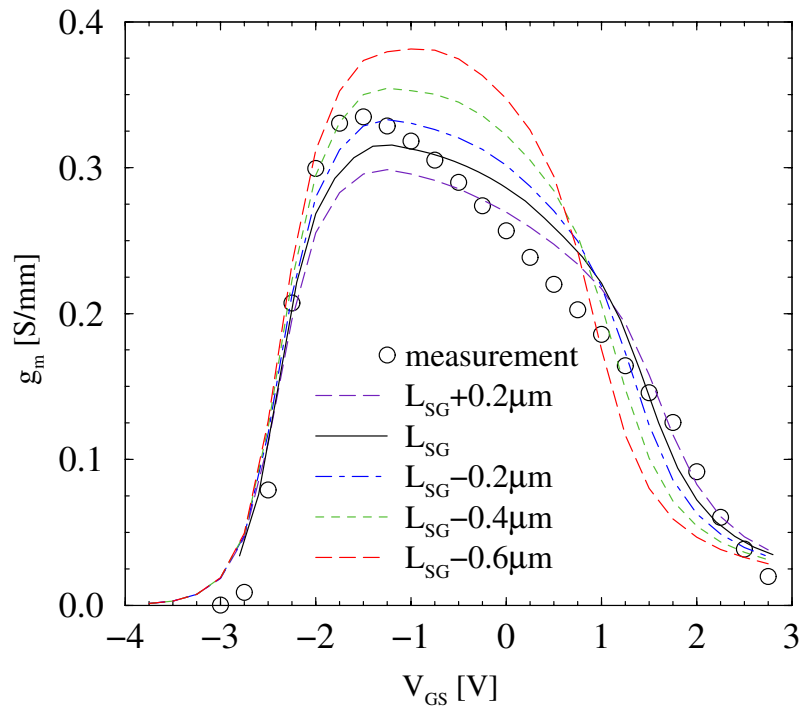


**Figure 5.29:** Transconductance  $g_m$  versus gate voltage  $V_{GS}$  for five devices with different source-gate length ( $V_{ds} = 7$  V).

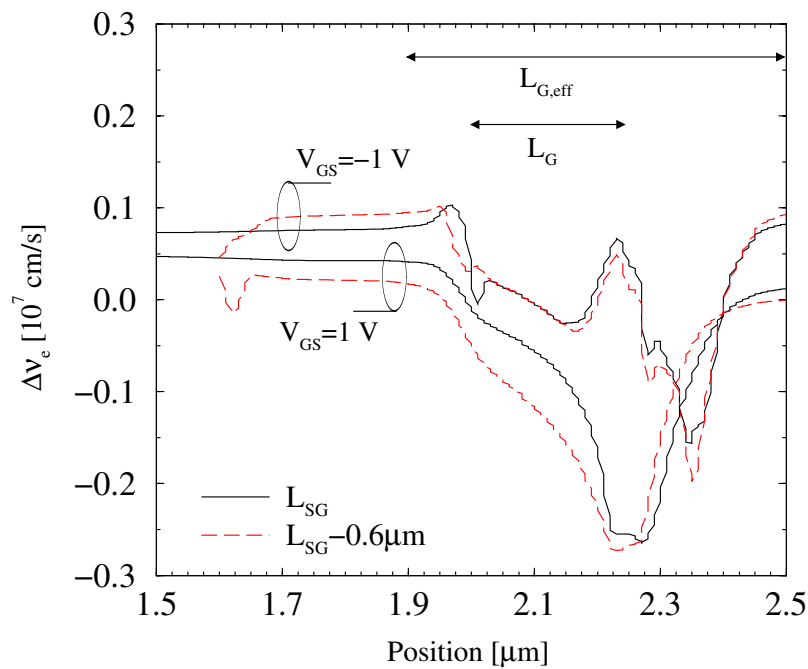


**Figure 5.30:** Change of electron velocity  $\Delta v$  along the channel at  $V_{gs} = -1$  V and 1 V for two devices with different  $L_{SG}$ .

device with a source-gate distance  $0.2 \mu\text{m}$  longer than the nominal value ( $L_{\text{SG}}+0.2 \mu\text{m}$ ), and three devices with source-gate distances  $0.2\text{--}0.6 \mu\text{m}$  shorter than the nominal value ( $L_{\text{SG}} - 0.2/0.4/0.6 \mu\text{m}$ ). In agreement with previous works, decreasing the source-gate distance results in a higher peak transconductance (Fig. 5.29). Also with shorter distance a flatter peak is achieved. These improvements are, however, at the cost of a transconductance collapse at lower  $V_{\text{GS}}$ . In order to find the source of this effect the impact of the carrier velocity and concentration is studied separately as in (5.1).

The simulations show that the change of carrier concentration  $\Delta n/\Delta V_{\text{GS}}$  is roughly equal for devices with shorter  $L_{\text{SG}}$ , thus the different transconductance characteristics are due to the different change of the electron velocity with gate bias  $\Delta v/\Delta V_{\text{GS}}$ . Fig. 5.30 shows the velocity change in the real device (nominal  $L_{\text{SG}}$ ) and a device with a  $L_{\text{SG}}$   $0.6 \mu\text{m}$  shorter for two gate voltages  $V_{\text{gs}} = -1 \text{ V}$  and  $V_{\text{gs}} = 1 \text{ V}$ . The former corresponds to the peak  $g_{\text{m}}$ , in which the transconductance of the shorter device is higher. The reason is the higher  $\Delta v$  in the source-gate region of the smaller device due to the considerably higher electric field. In the second point ( $V_{\text{gs}} = 1 \text{ V}$ )  $\Delta v$  in the shorter device is lower overall, causing the lower  $g_{\text{m}}$ . It must be noted that  $\Delta v$  is lower not only in the source-gate region due to reaching the maximum velocity earlier, but also in the region under the gate. There the electric field decreases more rapidly in the shorter structure, which results in the lower value of  $\Delta v$ .

These results show that the transconductance can be extensively tailored by appropriate scaling of the source-gate distance. However, down-scaling of  $L_{\text{SG}}$  is limited by breakdown effects. Contrary to other studies, here the introduction of a channel implantation or a  $\text{n}^{++}$  cap layer is not supported, as the higher donor concentration deteriorates the electron mobility. Last, it is shown that with a carefully calibrated setup various effects can be successfully explored.

### 5.1.4 Optimization Techniques

A significant improvement of the device performance has been achieved by adopting the field plate technique [68]. With its origins in the context of high-voltage p-n junctions [10] the main purpose of the field plate is to reshape the electric field distribution in the channel and to reduce its peak value on the drain side of the gate edge. The benefit is an increase of the breakdown voltage and a reduced high-field trapping effect. Overall the power density could be increased from  $10 \text{ W/mm}$  [389] to  $40 \text{ W/mm}$  [65]. Although sharing the same principle with FETs/MESFETs the effect of the field plate on HEMTs has to be studied extensively with account of the different transport mechanisms in the later devices.

#### 5.1.4.1 Device Structures

The devices share a similar design with the already simulated structures (especially to Device A, excluding the field plate). The gate is so far e-beam defined with a gate length of  $L_{\text{g}} = 150 \text{ nm}$ ,  $300 \text{ nm}$ , and  $600 \text{ nm}$ . Device isolation is achieved by mesa isolation. Fig. 5.31 gives an example of a typical fully planar AlGaIn/GaN HEMT. An  $\text{Al}_{0.3}\text{Ga}_{0.7}\text{N}/\text{GaN}$  heterointerface is grown on top of a thick insulating GaN buffer. All layers are non-intentionally doped, except the  $\delta$ -doping which is introduced in the AlGaIn supply layer to provide additional carriers and to improve the access resistances. The maximum drain current density is larger than  $900 \text{ mA/mm}$  and the transconductance is larger than  $200 \text{ mS/mm}$  at  $V_{\text{ds}} = 7 \text{ V}$ . The current gain cut-off frequency

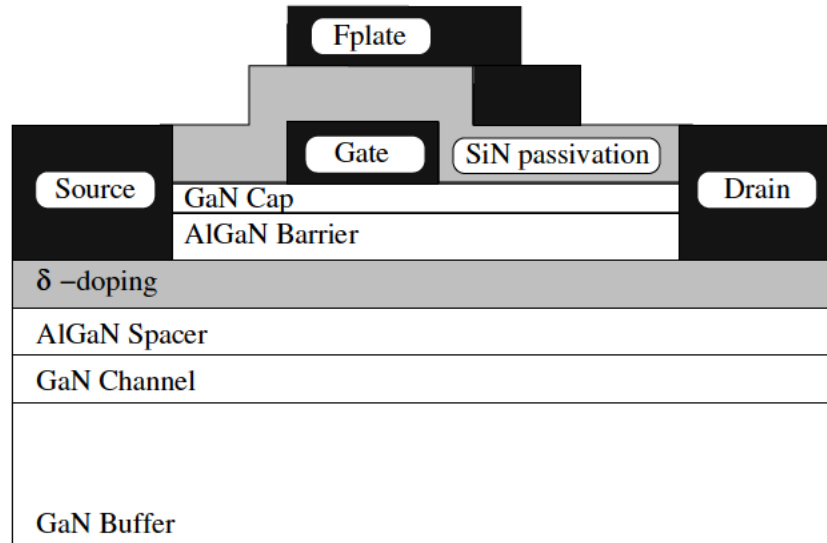


**Figure 5.31:** A schematic layer structure of single heterojunction AlGaIn/GaN HEMTs with field plates.

$f_t$  is well beyond 30 GHz for devices with  $L_g = 300$  nm. The density of the positive charge at the channel/barrier interface is found to be  $\approx 1.1 \times 10^{13} \text{ cm}^{-2}$  (see Fig. 5.32).

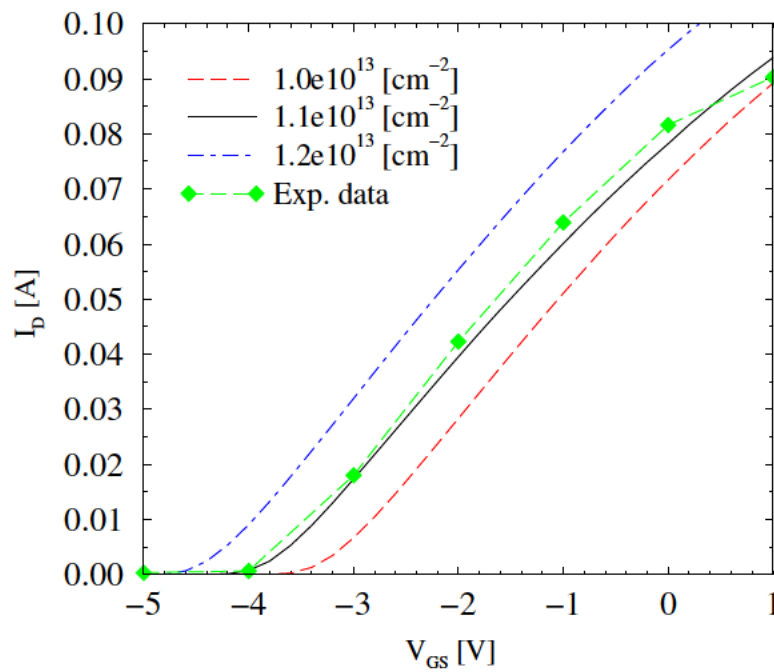


**Figure 5.32:** Transfer characteristics for different polarization charge densities at the AlGaIn/GaN heterojunctions.

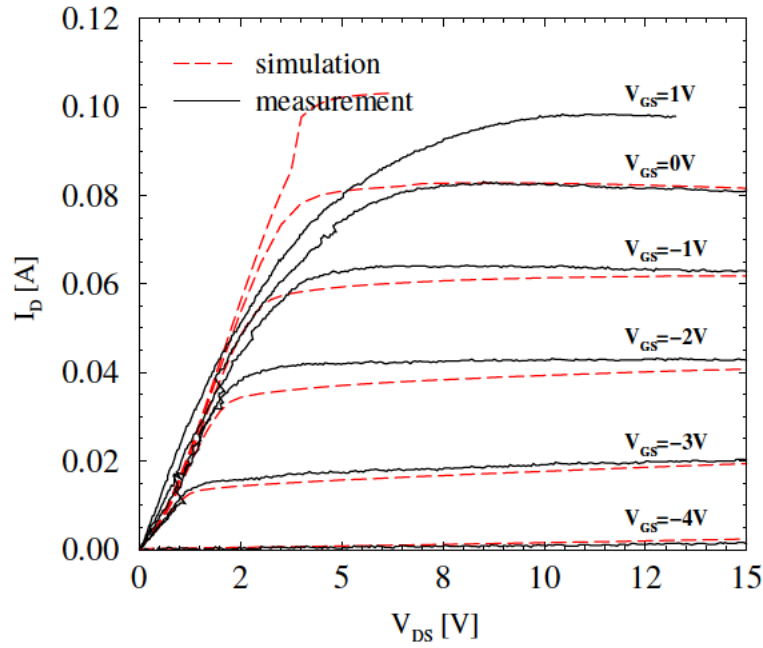


Figure 5.33: Comparison of measured (solid lines) and simulated (dashed lines) output characteristics of  $L_g=L_{FP}=600$  nm HEMTs.

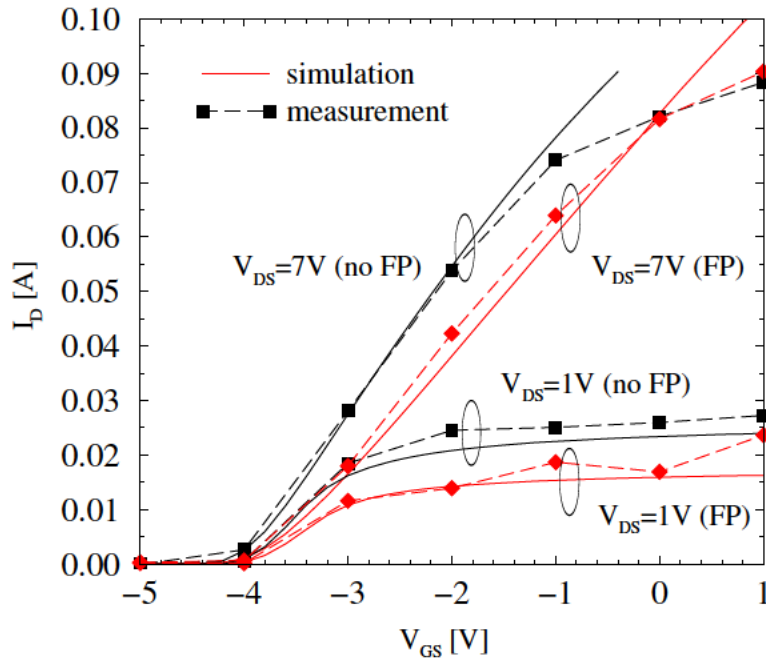
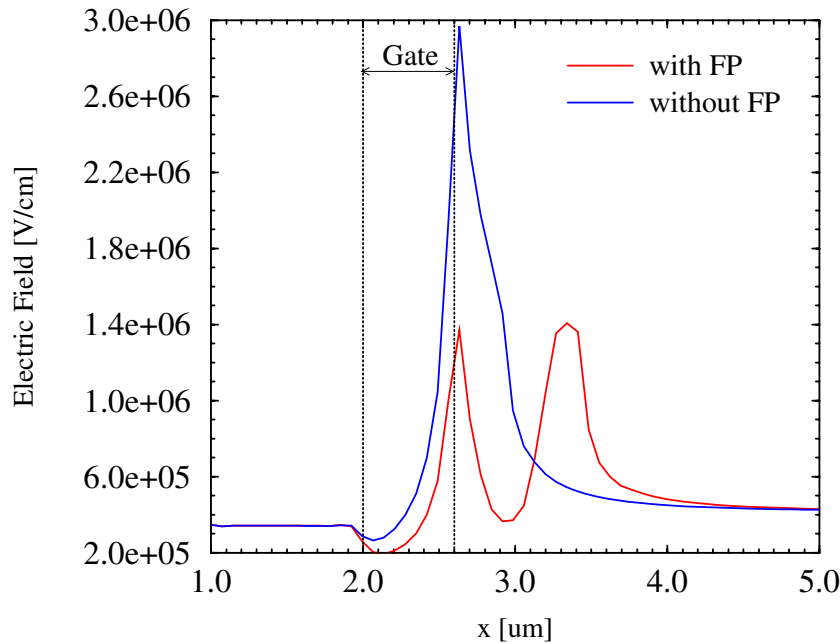


Figure 5.34: Comparison of measured (symbols) and simulated (lines) transfer characteristics of HEMTs with and without field plate.





**Figure 5.35:** Simulated electric field along the channel of  $L_g = 600$  nm HEMTs with and without field plate for  $V_{gs} = 0$  V and  $V_{ds} = 7$  V.

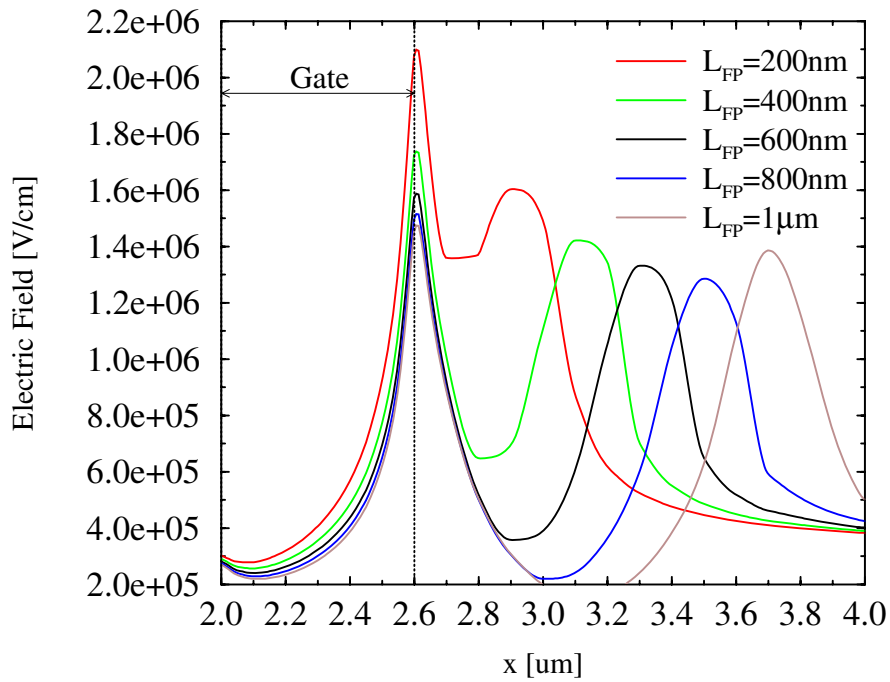
#### 5.1.4.2 Simulation Results

The critical variables associated with the field plate for a given gate length  $L_g$  are the field plate length  $L_{FP}$  and the SiN thickness (see Fig. 5.31). While the gate length is crucial for the transit time, the field plate length is the major factor for the size of the electrical field-resaped region [371]. The nitride thickness controls the onset voltage but has also significant influence on the maximum electric field.

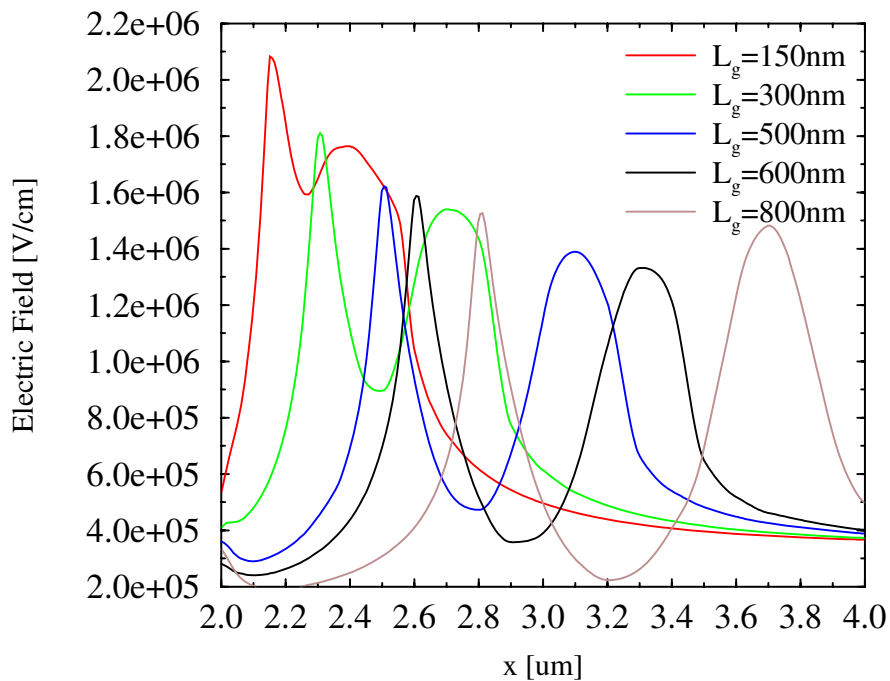
**Calibration and Field Plate Optimization of  $L_g = 600$  nm HEMTs:** AlGaIn/GaN HEMTs with  $L_g = 600$  nm have been used for device analysis and model calibration. Fig. 5.33 shows measured (solid lines) and simulated (dashed lines) output characteristics of  $L_g = 600$  nm HEMTs. Modeling issues remain for  $V_{gs} = 1$  V.

Fig. 5.34 compares measured (symbols) and simulated (lines) transfer characteristics of HEMTs without and with field plate. Very good agreement between simulation and measured electrical data is achieved for both devices. The difference caused by the field plate is better demonstrated by the electrical field distribution in the channel as shown in Fig. 5.35. A 50% reduction of the maximum electric field, located at the drain side of the gate edge, is achieved by the introduction of the field plate. A second peak occurs at the field plate edge.

The choice of an optimum field plate length is made with respect to the desired electrical properties [130]. Here, the aim is the highest reduction of the peak electric fields in the channel for  $V_{GS}=V_{FPS}=-7$  V,  $V_{ds} = 60$  V, thus securing a reliable device operation up to this bias. The optimum field plate length  $L_{FP}=L_g = 600$  nm is found after variation of  $L_{FP}$  in the range 200 nm-800 nm (see Fig. 5.36).



**Figure 5.36:** Simulated electric field along the channel for various field plate lengths  $L_{FP}$  ( $L_g = 600$  nm).



**Figure 5.37:** Simulated electric field along the channel for various gate lengths ( $L_{FP} = L_g$ ).

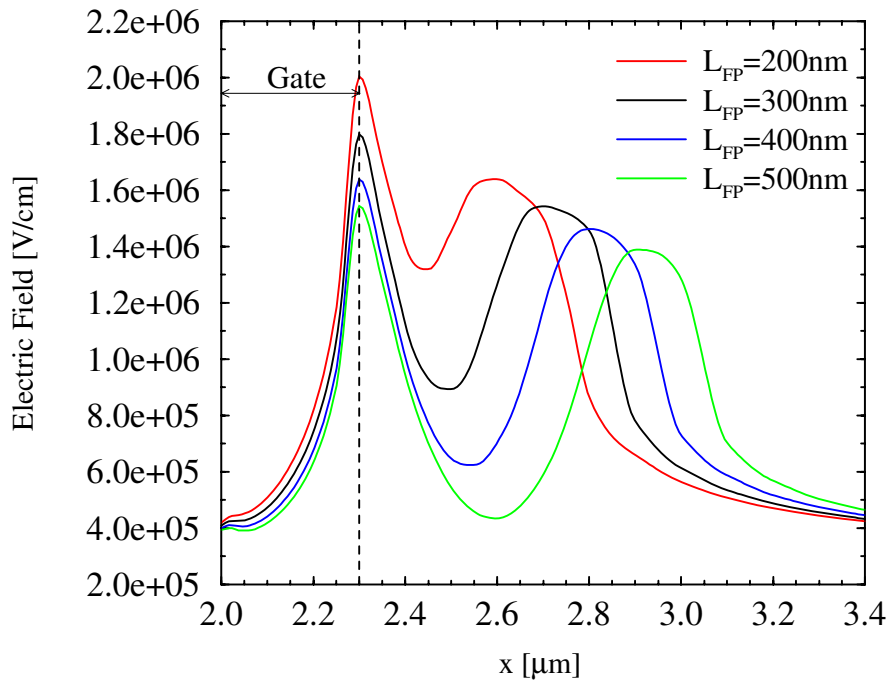


**Figure 5.38:** Simulated electric field along the channel for various field plate lengths  $L_{FP}$  ( $L_g = 300$  nm).

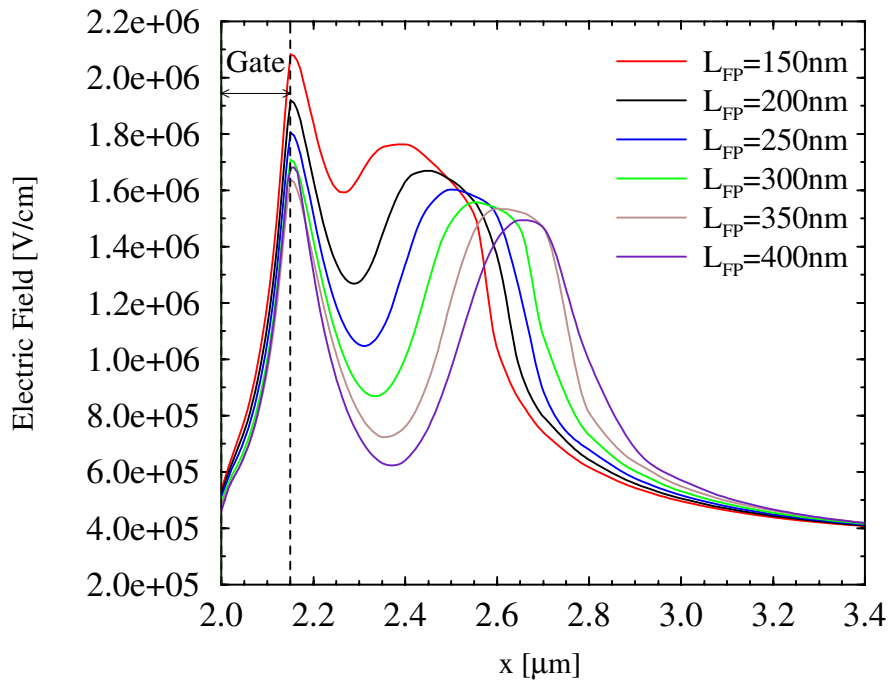


**Figure 5.39:** Simulated electric field along the channel for various field plate lengths  $L_{FP}$  ( $L_g = 150$  nm).

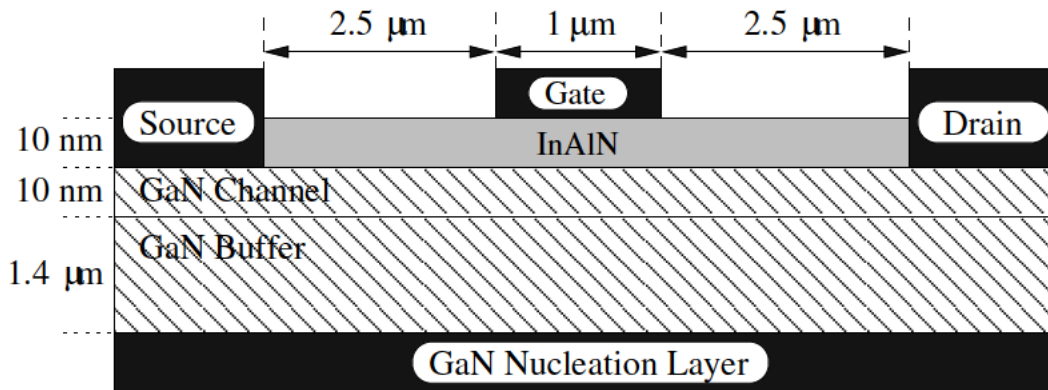


Figure 5.40: Schematic layer structure of the investigated device.

**Field Plate Optimization of Shorter HEMTs:** Fig. 5.37 shows simulation results for HEMTs with shorter gate lengths down to 150 nm. While such devices are economically favored, the simulation results show that for small  $L_g$  the maximum electric field increases by up to 60%, thus requiring a mechanism to compensate the negative impact. The field plate length is kept equal to  $L_g$ . The optimum value for the thickness of the nitride passivation in  $L_g = 600$  nm devices is further preserved.

The next simulations involve devices with  $L_g = 300$  nm (Fig. 5.38). Increasing  $L_{FP}$  is advantageous up to  $L_{FP}=500$  nm regarding the peak electrical field. Fig. 5.39 shows electrical field distribution in the channel of  $L_g = 150$  nm HEMTs.  $L_{FP}$  varies from 100 nm to 400 nm. Compared with the previous simulations a clear improvement for longer field plates is observed. The increase of  $L_{FP}$  from 150 nm to the optimum of about 350 nm helps to decrease the peak electrical field by up to 40%.

### 5.1.5 InAlN/GaN Devices

InAlN/GaN HEMTs have been proposed to provide higher polarization charges without the drawback of high strain [62]. Several groups have demonstrated devices based on InAlN/GaN [390], [391] with maximum current capabilities surpassing those of AlGaIn/GaN structures.

Optimization of the structures has been carried out by using analytical models [62]. In order to fully develop the potential of the device, proper modeling of the materials is required. Based on the material parameters discussed in Chapter 4, a simulation study is conducted. The HEMT structures described in [391] and [392] are used to benchmark the *DC* and *AC* simulation results against measured data. A schematic layer structure of the investigated  $\text{In}_{0.2}\text{Al}_{0.8}\text{N}/\text{GaN}$  device [392] is shown in Fig. 5.40. All layers are non-intentionally doped.

#### 5.1.5.1 Simulation Results

A band gap bowing factor of 3 eV is assumed for InAlN as discussed in Section 4.3.1. This yields a band gap of 4.58 eV for  $\text{In}_{0.2}\text{Al}_{0.8}\text{N}$  at 300 K (Fig. 5.41). The values for the band offsets are  $\Delta E_C=0.66$  eV and  $\Delta E_V=0.59$  eV, corresponding to a 53%/47% setup. The calculated

dielectric permittivity of  $\text{In}_{0.2}\text{Al}_{0.8}\text{N}$  is  $\epsilon_r=9.86$ , which is in a good agreement with the value listed in [392]. The barrier height of the gate *Schottky* contact is 1 eV. The value of the sheet charge density at the  $\text{InAlN}/\text{GaN}$  interface induced by the polarization effects is found to be  $3.3 \times 10^{13} \text{ cm}^{-2}$  from the *DC* characteristics (simulation results for different values are given in Fig. 5.42). A commensurate negative surface charge (as the device is not passivated, a low value of  $10^{13} \text{ cm}^{-2}$  is assumed) at the top of the  $\text{InAlN}$  surface is also considered in the simulation. Simulation results for the transfer characteristics assessing different charge values are shown in Fig. 5.43. Self-heating effects are accounted for by using a thermal resistance of  $R_{\text{th}}=3 \text{ K/W}$  at the substrate thermal contact. Fig. 5.44 compares transfer characteristics without self-heating effects and with different values of  $R_{\text{th}}$ . This value lumps the thermal resistance of the nucleation layer and the sapphire substrate, and possible three-dimensional thermal effects.

The simulation exhibits good agreement with the experimental data under consideration of Ohmic contact resistances  $R_S=R_D=1.3 \text{ } \Omega\text{mm}$ . The simulated output characteristics show a good agreement with the experimental data (Fig. 5.45). By *AC* analysis of the device a cut-off frequency  $f_t \approx 7 \text{ GHz}$  is obtained. This low value can be explained with the conservative design of the device and the low carrier mobility in the channel ( $\mu=230 \text{ cm}^2/\text{Vs}$ ). Downscaled devices are analyzed ( $L_g = 0.5/0.25 \text{ } \mu\text{m}$ ) and the effect of higher quality GaN material on the *AC* performance is studied. In our simulation of a device with  $L_g = 0.25 \text{ } \mu\text{m}$  reported in [391] (carrier mobility  $\mu=530 \text{ cm}^2/\text{Vs}$ )  $f_t=36 \text{ GHz}$  is reached.

## 5.2 Enhancement-Mode HEMTs

The possible approaches to obtain a normally-off device characteristics have been summarized in Section 2.3. Here, two of them are studied: the recessed gate approach and the  $\text{InGaN}$  cap layer approach. For the former experimental data from devices produced at the IAF Freiburg are available, while for the latter, the data were extracted from corresponding publications. The comparison is based on the same  $\text{InGaN}$  cap devices and experimental data provided in [49].

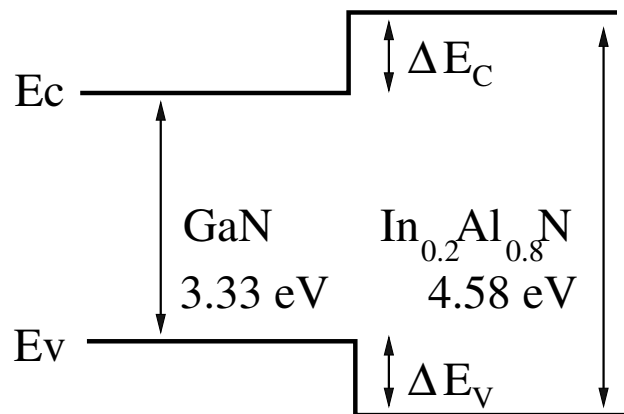


**Figure 5.41:** Band alignment of the heterointerface.

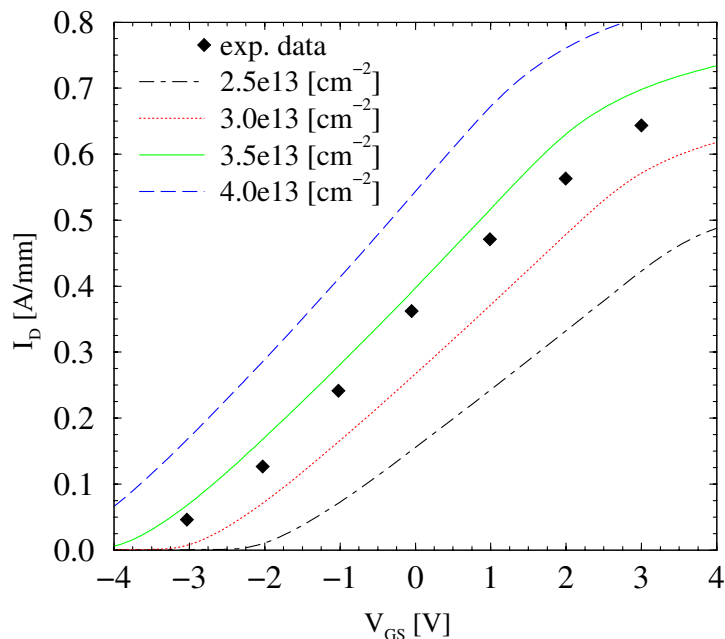


**Figure 5.42:** Transfer characteristics for different values of the polarization charge density at the InAlN/GaN interface and  $-10^{13} \text{ cm}^{-2}$  at the InAlN top surface ( $V_{ds} = 8 \text{ V}$ ).

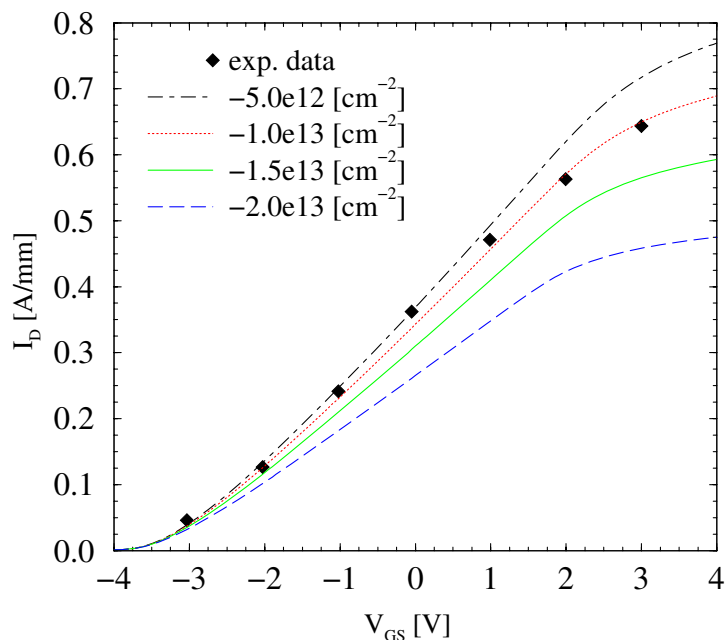


**Figure 5.43:** Transfer characteristics for different values of the total charges (polarization and traps) at the InAlN top surface and  $3.3 \times 10^{13} \text{ cm}^{-2}$  at the InAlN/GaN interface ( $V_{ds} = 8 \text{ V}$ ).

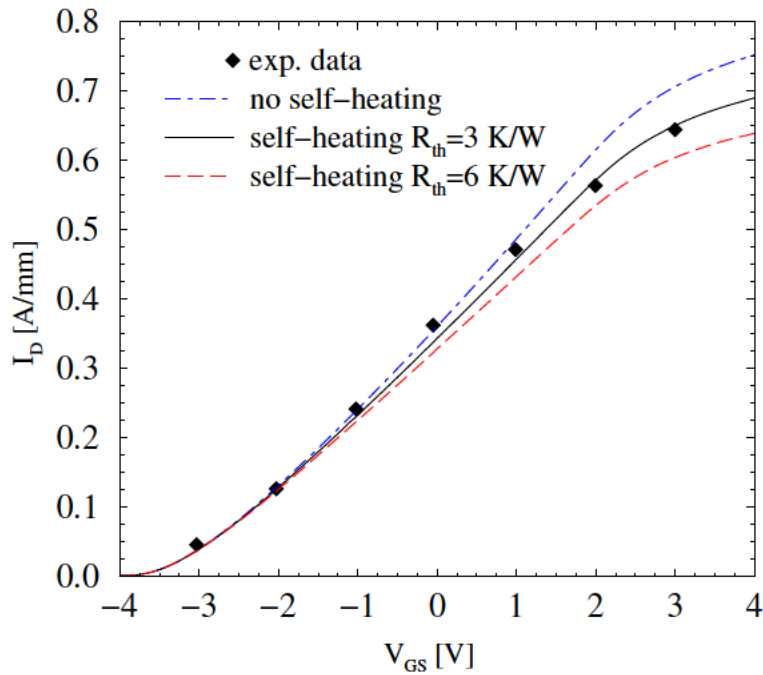


Figure 5.44: Comparison of simulated transfer characteristics for different values of the thermal resistance and experimental data ( $V_{DS} = 8$  V).

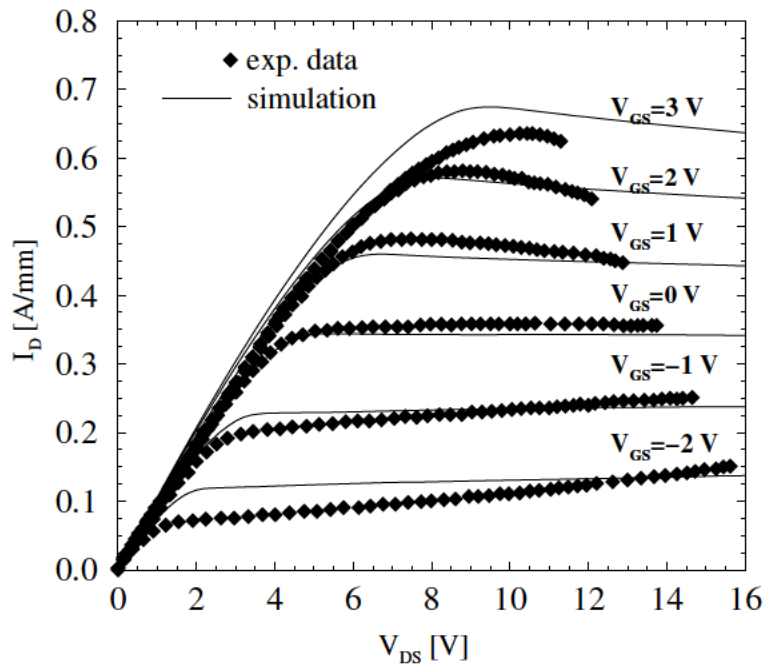


Figure 5.45: Comparison of simulated output characteristics and experimental data.

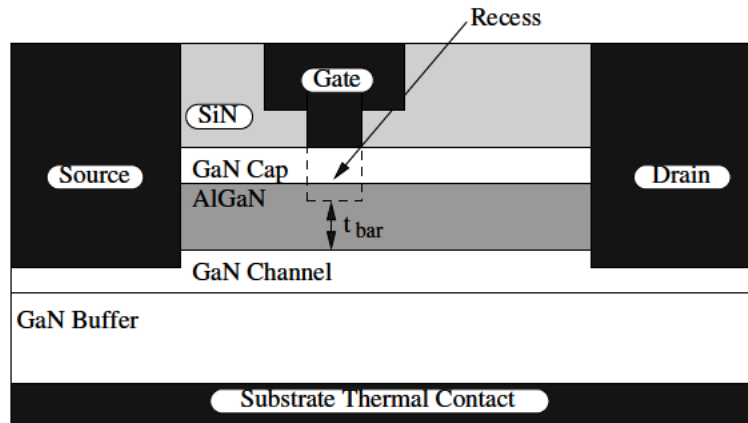


Figure 5.46: Schematic layer structure of the recessed device.

### 5.2.1 Recessed Gate

In order to analyze the trade-off between high-frequency performance and threshold voltage achieved by the gate recess technique [42], results from two-dimensional hydrodynamic simulations supported by experimental data [44] are presented [393].

AlGaN/GaN DHEMT and EHEMT structures with T-gates of 250 nm length share the same layer specification and are processed on the same SiC wafer. The devices consist of GaN buffer, 22 nm thick  $\text{Al}_{0.22}\text{Ga}_{0.78}\text{N}$  ( $\text{Al}_{0.18}\text{Ga}_{0.82}\text{N}$  for the EHEMT device) barrier layer, 3 nm thick GaN cap layer, and SiN passivation (Fig. 5.46). The cap and part of the barrier layer under the gate of the EHEMT are recessed by  $\text{Cl}_2$  plasma etching. A remaining AlGaN barrier thickness  $t_{\text{bar}} \approx 11$  nm is assumed. The Ohmic contacts are assumed to reach the 2DEG in the channel.

The densities of the polarization charges at the channel/barrier interface and at the barrier/cap interface are determined by calibration against the experimental data to be  $9 \times 10^{12} \text{ cm}^{-2}$  and  $-2 \times 10^{12} \text{ cm}^{-2}$ , respectively. Low Ohmic contact resistances of  $0.2 \text{ } \Omega\text{mm}$  are considered [44]. Self-heating effects are accounted with a substrate thermal contact resistance of  $R_{\text{th}} = 5 \text{ K/W}$ . This value lumps the thermal resistance of the nucleation layer and the substrate.

#### 5.2.1.1 Simulation Results

Fig. 5.47 compares the simulated transfer characteristics to experimental data. Both devices are simulated using the same set of models and model parameters, including the interface charge densities. A good agreement is obtained, both for the threshold voltage and the transconductance  $g_m$  (Fig. 5.48). The mismatch between the drain current at high gate voltages is due to the high gate leakage current in the real device, for which the simulation does not account. A possible explanation for the underestimation of the peak  $g_m$  for the recessed device is an overestimation of the sheet resistance under the gate. Simulated output characteristics for both structures are compared to measurements in Fig. 5.49 and Fig. 5.50. The  $RF$  simulations provide slightly higher cut-off frequency  $f_t$  than the experiments for both structures (Fig. 5.51). Note, that both the measured and simulation data show an increase of  $f_t$  and  $f_{\text{max}}$  for the EHEMT structures.



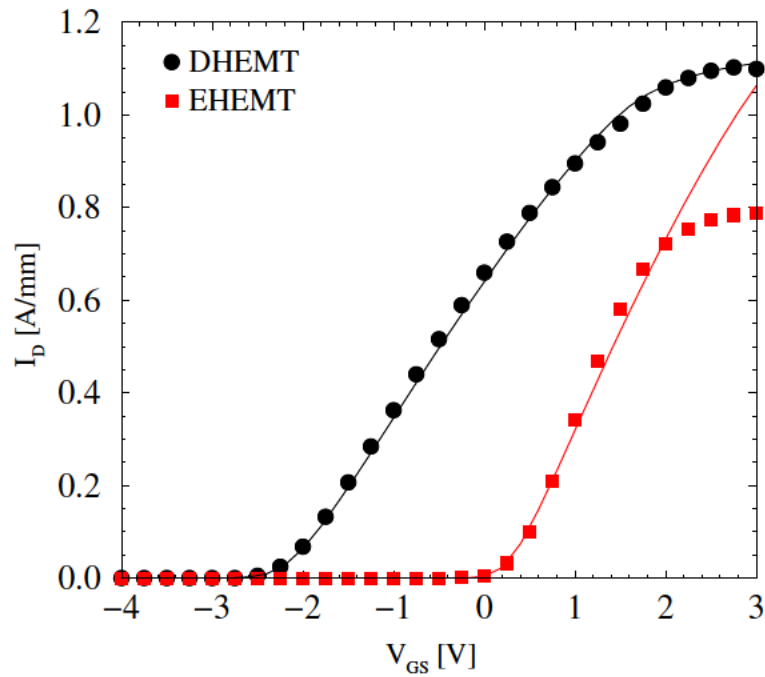


Figure 5.47: Transfer characteristics at  $V_{ds} = 7$  V: lines - simulation, symbols - experimental data.

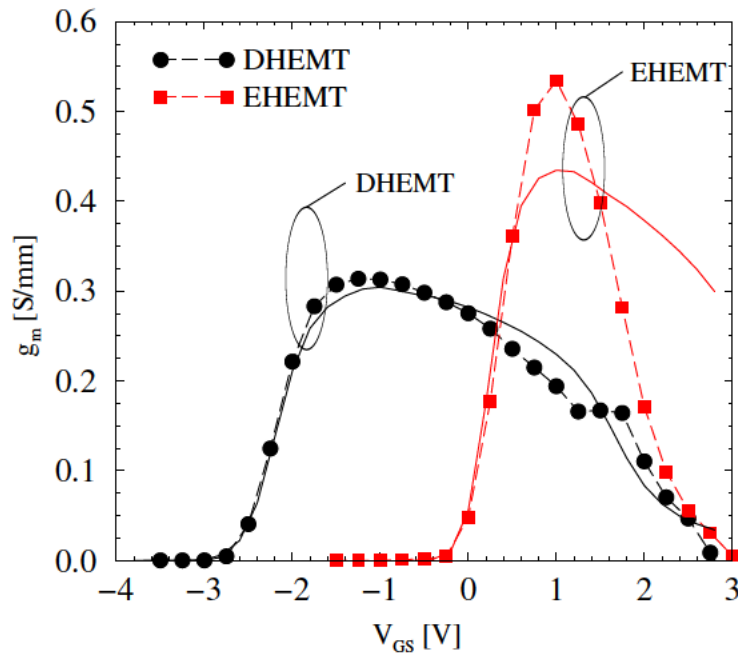


Figure 5.48: Transconductance  $g_m$  at  $V_{ds} = 7$  V: lines - simulation, symbols - experimental data.

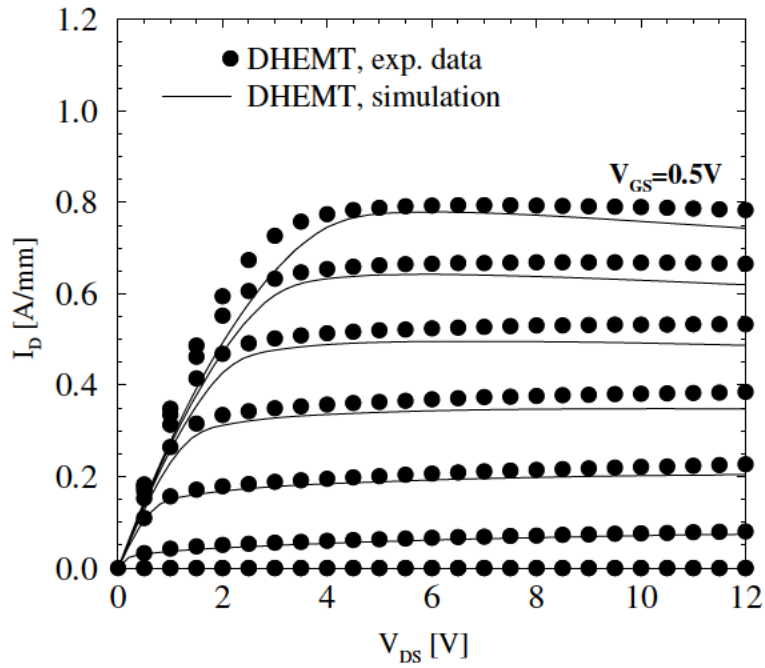


Figure 5.49: Comparison of DHEMT output characteristics,  $V_{GS}$  stepping 0.5 V.

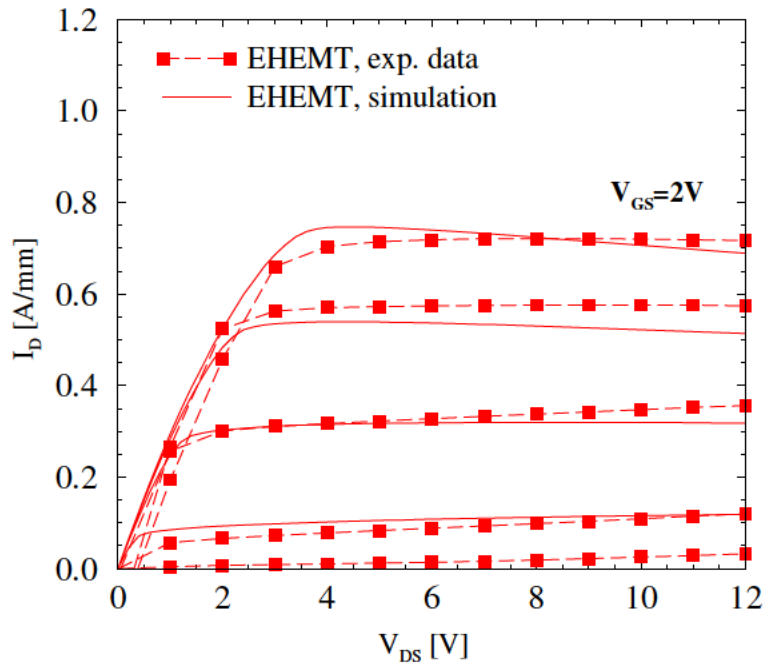
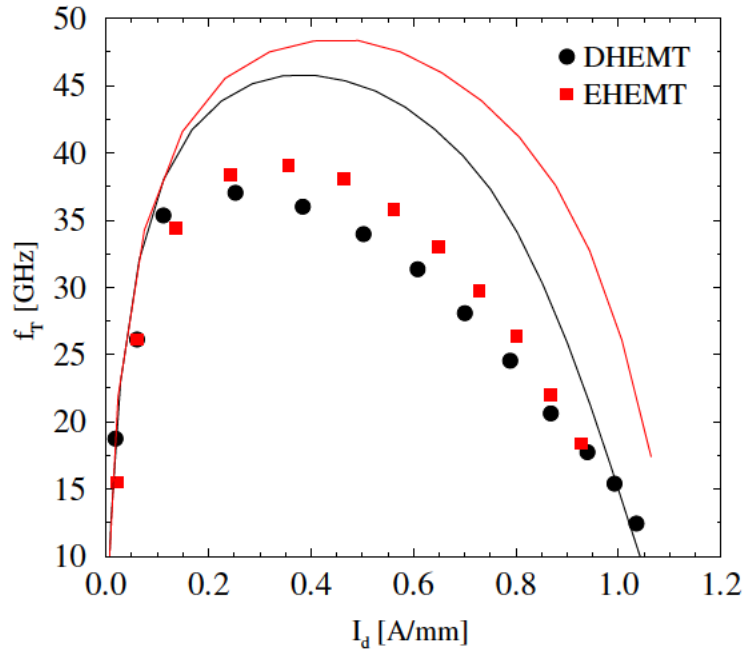


Figure 5.50: Comparison of EHEMT output characteristics,  $V_{GS}$  stepping 0.5 V.



**Figure 5.51:** Comparison of the cut-off frequency  $f_t$ : symbols - simulation, lines - experimental data.

Since the gate capacitance depends on the gate channel distance, several simulations are performed with variable recess depths, which means a variable barrier thickness  $t_{\text{bar}}$  under the gate. As expected a shift in the threshold voltage is observed (Fig. 5.52) and  $g_m$  increases with decreasing  $t_{\text{bar}}$  (Fig. 5.53) due to the lack of charge control for thicker layers. However, the simulated  $f_t$  characteristics do not show any noticeable change (Fig. 5.54). Fig. 5.55 shows the gate source capacitance which increases with decreasing  $t_{\text{bar}}$ . It compensates the increase in  $g_m$ , thereby resulting in a constant  $f_t$ . Thus, the major reason for the rise of  $f_t$  and  $f_{\text{max}}$  of EHEMTs in comparison to DHEMTs (Fig. 5.51) is the absence of barrier/cap negative interface charges under the gate. The exact depth of the recess has less influence on  $f_t$  and  $f_{\text{max}}$ , but has a significant impact on the threshold voltage and the transconductance.

## 5.2.2 InGaN Cap

### 5.2.2.1 Device Structure

The investigated InGaN/AlGaIn/GaN device structure as described in [394] is shown in Fig. 5.56. A 3  $\mu\text{m}$  thick GaN layer is grown on a sapphire substrate. A 20 nm thick  $\text{Al}_{0.25}\text{Ga}_{0.75}\text{N}$  layer is deposited next: the first 5 nm undoped, 10 nm highly-doped ( $2 \times 10^{18} \text{cm}^{-3}$ ) supply layer, and 5 nm undoped material. On-top a 5 nm thick  $\text{In}_{0.2}\text{Ga}_{0.8}\text{N}$  layer is deposited. All layers are non-intentionally doped, except the supply layer. The gate length  $L_g = 1.9 \mu\text{m}$ , source gate distance is 1.5  $\mu\text{m}$ , and gate drain distance is 2.4  $\mu\text{m}$ . Three different HEMT structures are studied: the proposed novel normally-off device (Fig. 5.56), a device with the InGaIn layer removed in the access regions (only the InGaIn film under the gate is left), and a conventional normally-on

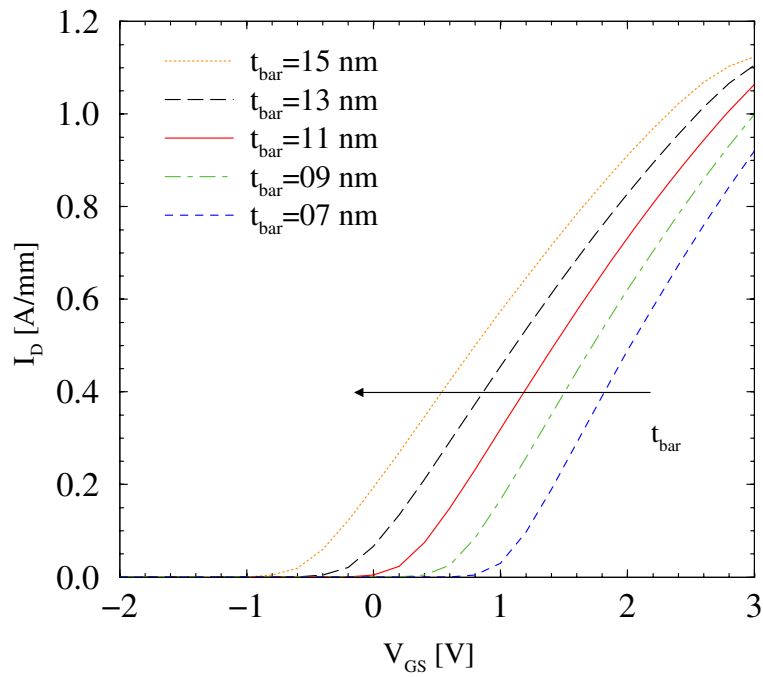


**Figure 5.52:** Simulated transfer characteristics for devices with different barrier thickness  $t_{bar}$  under the gate.

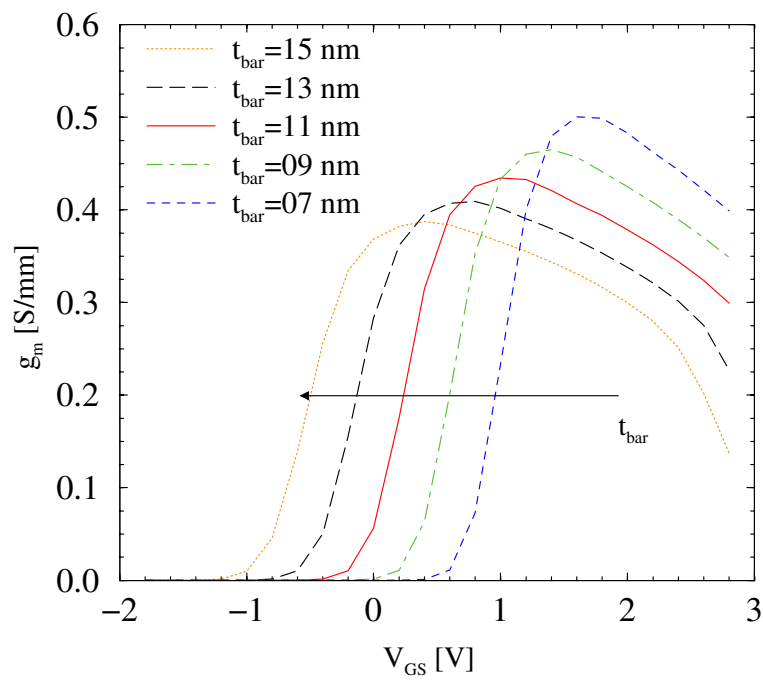


**Figure 5.53:** Simulated transconductance for devices with different barrier thickness  $t_{bar}$  under the gate.

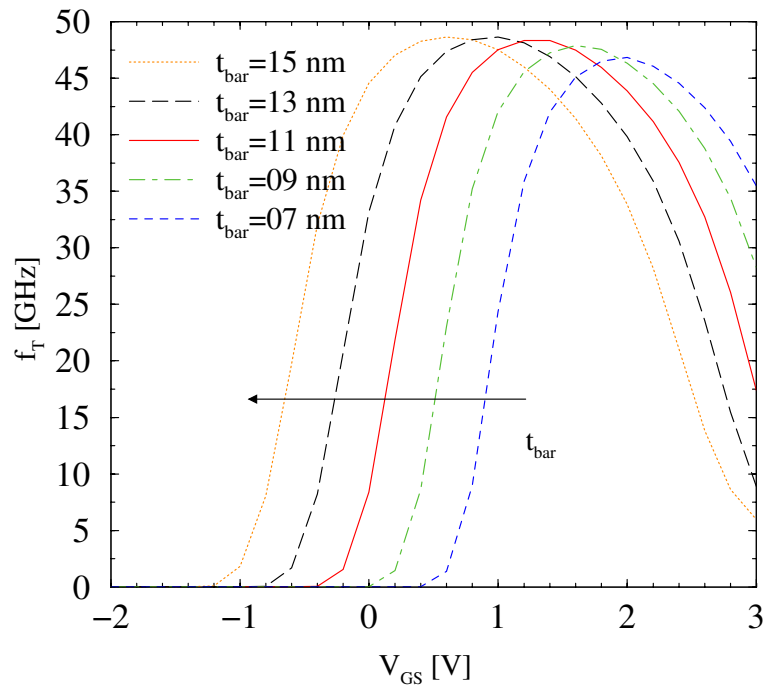


**Figure 5.54:** Simulated cut-off frequency for devices with different barrier thickness  $t_{\text{bar}}$  under the gate.

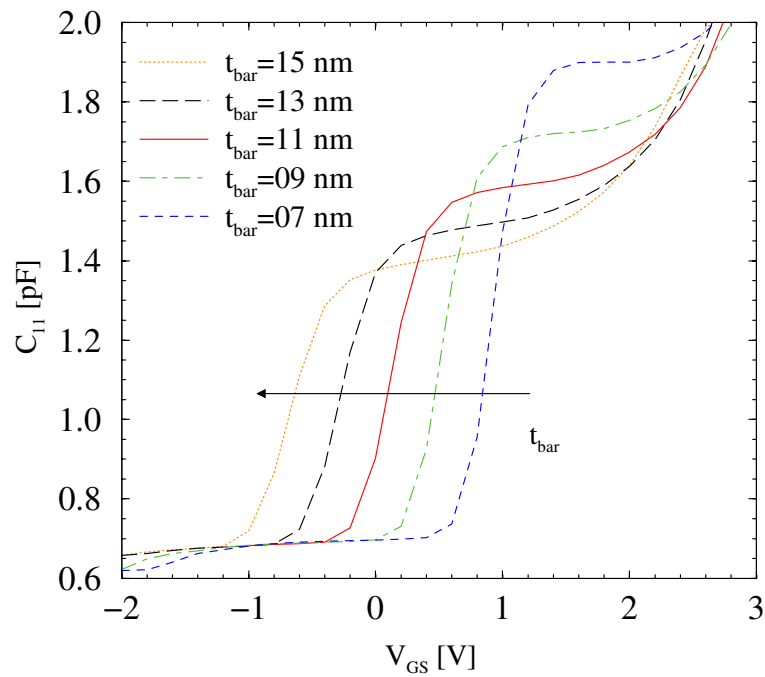


**Figure 5.55:** Simulated gate-source capacitance for devices with different barrier thickness  $t_{\text{bar}}$  under the gate.

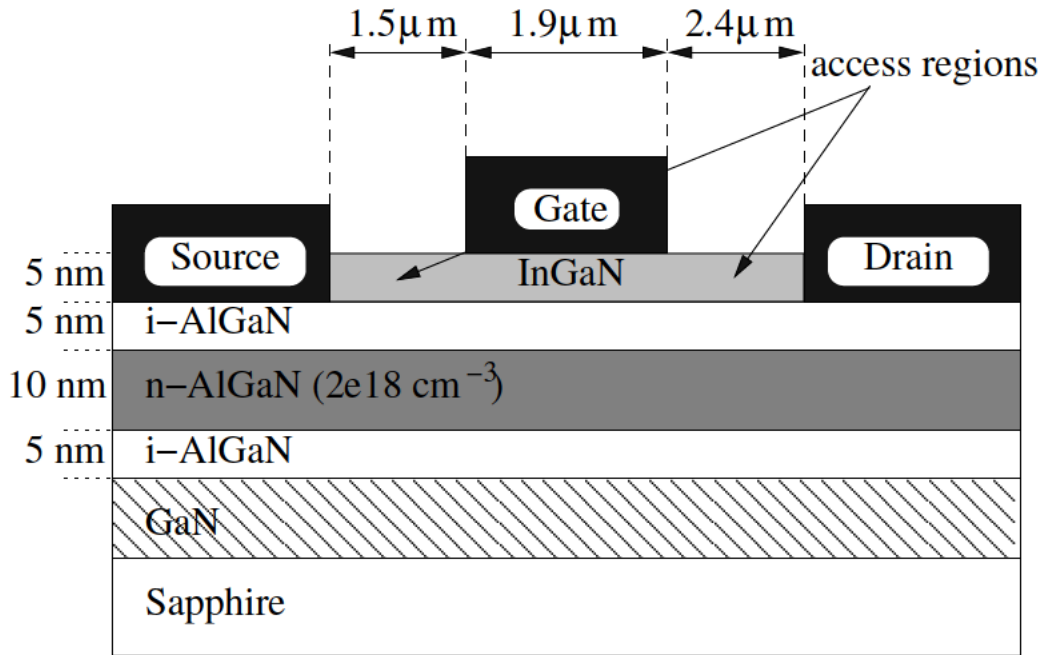


Figure 5.56: Schematic layer structure of the three HEMTs under investigation.

device (as in Fig. 5.56, but without the InGaN layer) [395]. A diffusion of the metal source and drain contacts reaching the highly-doped layer is assumed.

### 5.2.2.2 Simulation Results

The simulation results for the transfer characteristics of the three devices are compared to the measurements of Mizutani *et al.* [394] in Fig. 5.57 for  $V_{ds} = 5 \text{ V}$ . Good overall agreement is achieved. All simulations were conducted using the same parameter setup, except for the work-function energy difference of the gate *Schottky* contact (depending on the underlying material). The values for the interface charge density are summarized in Table 5.3. A positive charge at the channel/supply layer interface is used, a negative charge between the supply layer and the passivation (in the case of D-mode and recessed E-mode), a negative charge between the InGaN cap layer and the AlGaN supply layer (both E-mode devices), and a positive between the InGaN cap layer and the passivation (E-mode non-recessed).

Fig. 5.58 shows the effective conduction band energies of D-mode and E-mode HEMTs at  $V_{gs} = 0 \text{ V}$ ,  $V_{ds} = 5 \text{ V}$  in a vertical cut under the gate metal, as computed by the simulator. The band diagrams are shifted so that both *Fermi* levels are at 0 eV. Indeed, as suggested by Mizutani *et al.*, a 2DEG channel is present in the D-mode device, while the negative piezoelectric charge at the InGaN/AlGaN interface raises the conduction band in the E-mode structure. Thus, the channel is depleted even at  $V_{GS}0$  and the threshold voltage increases to positive values.

Fig. 5.59 compares the simulated *DC*  $g_m$  for the three structures. The drop in the measured  $g_m$  at higher gate bias might be caused by non-idealities in the source and drain ohmic contacts, which are not considered in the simulation. A relatively good agreement between the simulated

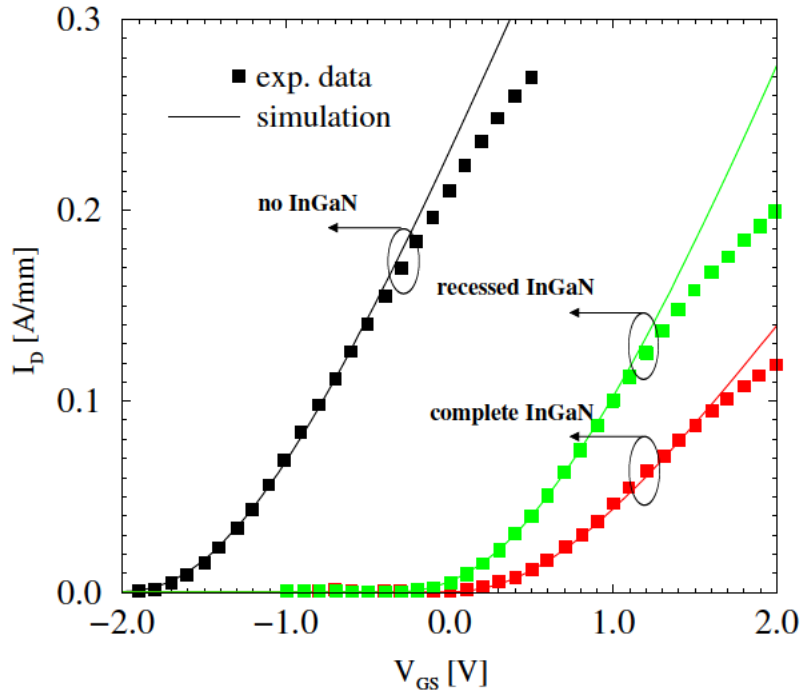


**Figure 5.57:** Comparison of simulated and measured transfer characteristics for the three devices.

and measured output characteristics for a device with InGaN layer is achieved (Fig. 5.60).

Small signal *AC* analysis using the calibrated setup delivers cut-off frequencies of  $f_t=7$  GHz for the device featuring a complete InGaN layer and  $f_t=10$  GHz for the recessed structure, respectively. The simulations suggest that reasonably higher values can be achieved by shorter gate lengths: e.g. peak  $f_t=30$  GHz for  $L_g = 0.8 \mu\text{m}$ .

**Table 5.3:** Summary of values of interface charge density [ $\text{cm}^{-2}$ ] for the three structures.

Interface	D-mode	E-mode	Recessed E-mode
GaN/AlGaIn	$1 \times 10^{13}$	$1 \times 10^{13}$	$1 \times 10^{13}$
AlGaIn/InGaIn	–	$-2.2 \times 10^{13}$	$-2.2 \times 10^{13}$
InGaIn/Passivation	–	$1.4 \times 10^{13}$	–
AlGaIn/Passivation	$-0.6 \times 10^{13}$	–	$-0.6 \times 10^{13}$

### 5.2.3 Comparison Gate Recess versus InGaN Cap Layer

For this comparison the same InGaN cap device is used as described in the previous section. The gate recess structure and its fabrication is reported by Palacios *et al.* [49]. The 11 nm thick GaN channel is grown on-top of a 1 nm thick  $\text{In}_{0.1}\text{Ga}_{0.9}\text{N}$  back-barrier. A 1 nm thick AlN layer between the channel and the 25 nm  $\text{Al}_{0.33}\text{Ga}_{0.67}\text{N}$  is grown in order to improve the electron mobility. After the AlGaIn surface treatment a 12 nm gate recess is performed, resulting in a gate-to-channel distance of 13 nm. The gate length  $L_g$  is 160 nm, source-gate distance is  $0.6 \mu\text{m}$ , and gate-drain distance is  $0.9 \mu\text{m}$ .

#### 5.2.3.1 Simulation Results

Fig. 5.61 shows the results for the transfer characteristics of both devices. After the calibration of the sheet charges a good agreement is achieved. The InGaN/GaN device exhibits lower current. However, a higher threshold voltage is achievable without recessing the InGaN cap layer [18]. The threshold voltage of the recess device can be increased, too, (Fig. 5.62) by increasing the recess depth.

Fig. 5.63 compares the *DC* transconductance  $g_m$  for both devices. The decrease in the measured  $g_m$  of the InGaN/AlGaIn/GaN transistor at higher gate bias might be due to non-idealities in the source and drain ohmic contacts, which are not considered in the simulation. As expected, the recessed gate device exhibits a higher  $g_m$  due to the much shorter gate length  $L_g$  and the reduced gate-to-channel separation.

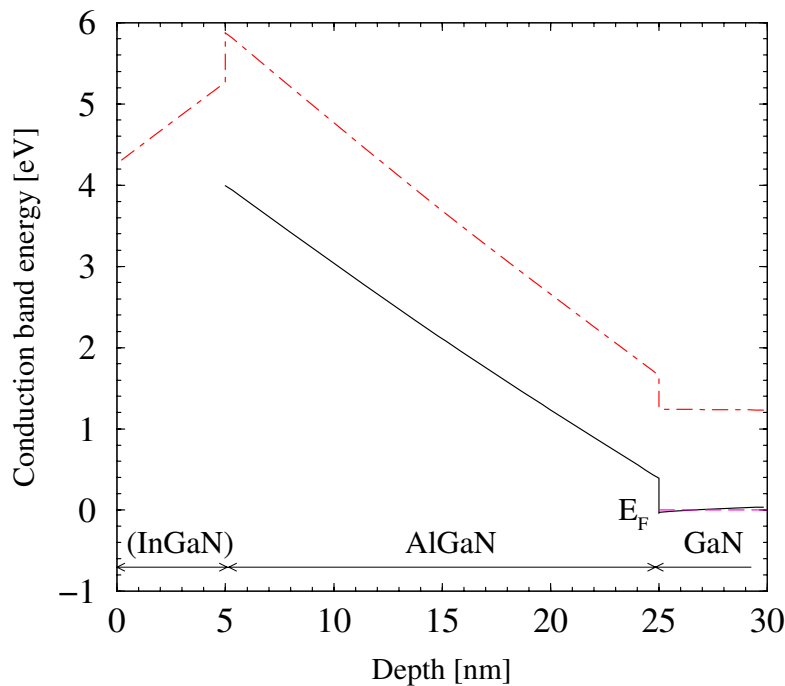


**Figure 5.58:** Energy band diagrams of a HEMT with (dot-dashed line) and without (solid line) InGaN layer.



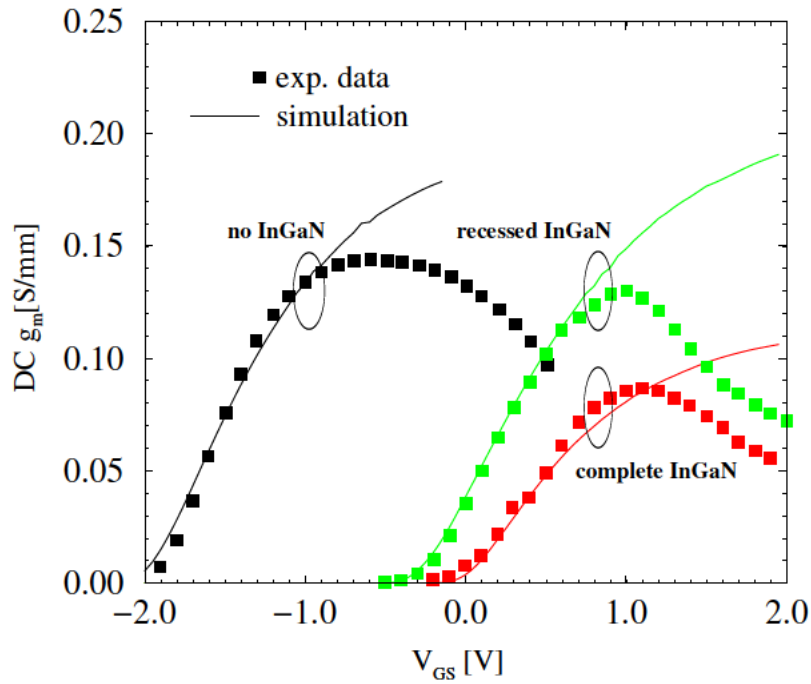


Figure 5.59: Simulated DC  $g_m$  for the three devices.

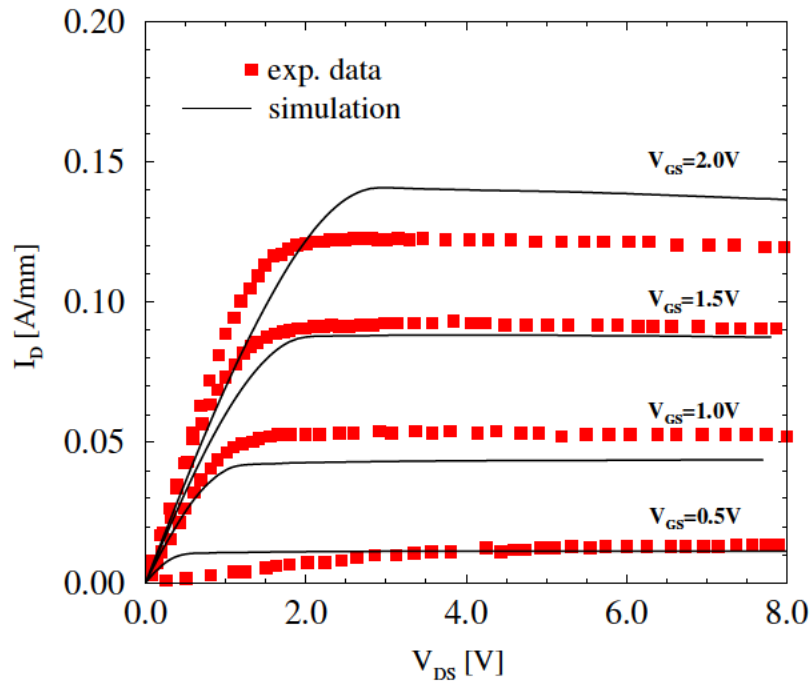
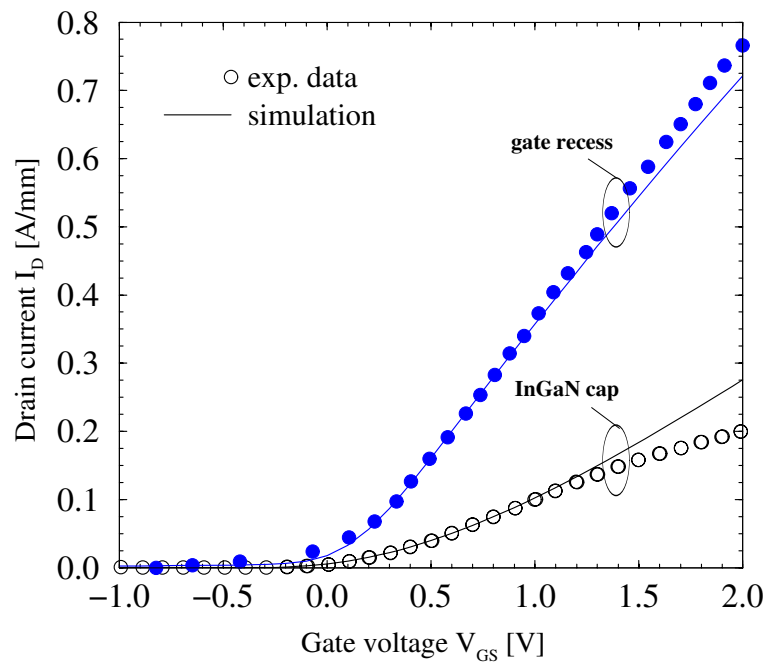
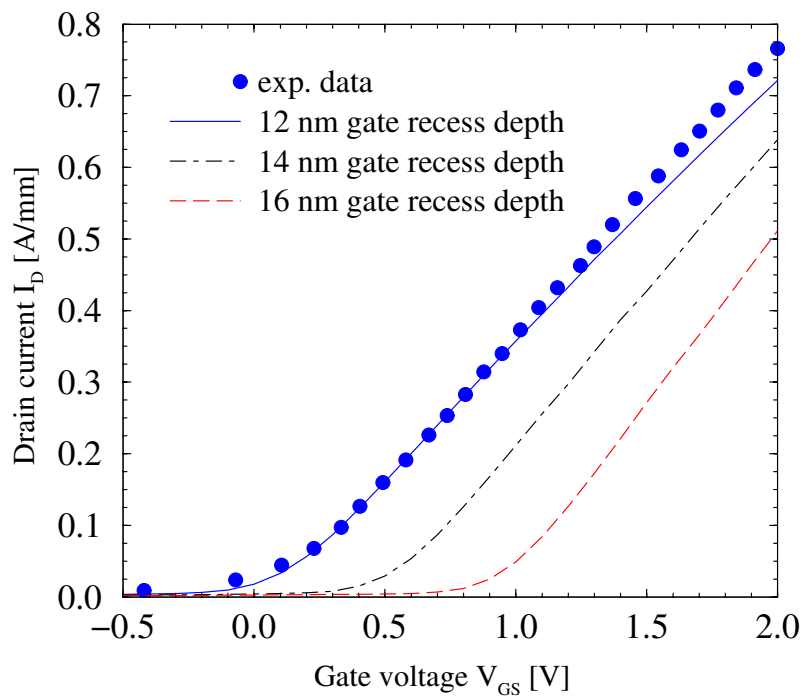


Figure 5.60: Output characteristics of a HEMT with non-recessed InGaN cap layer.



**Figure 5.61:** Comparison of the measured (symbols) and simulated (lines) transfer characteristics at  $V_{ds} = 5$  V.



**Figure 5.62:** Simulated transfer characteristics at  $V_{ds} = 5$  V for HEMTs with different gate recess depths.

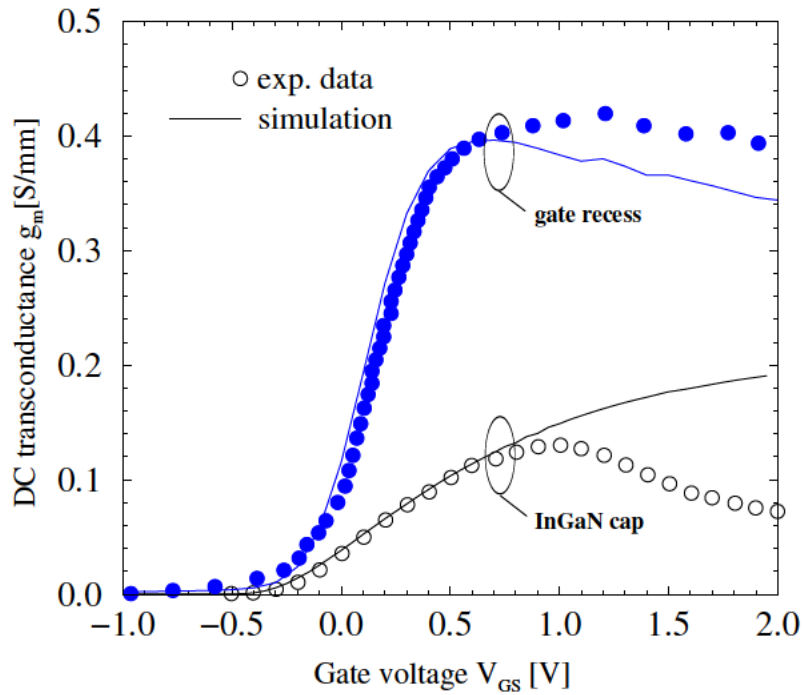


**Figure 5.63:** Comparison of the measured (symbols) and simulated (lines) *DC* transconductance  $g_m$  at  $V_{ds} = 5$  V.

*AC* analysis of the transistors is also performed. The recessed gate structure ( $L_g = 0.16 \mu\text{m}$ ) exhibits a cut-off frequency  $f_t = 85$  GHz, compared to  $f_t = 10$  GHz for the InGaN/AlGaIn/GaN device ( $L_g = 1.9 \mu\text{m}$ ). Note that the product  $f_t \times L_g = 19$  GHz $\cdot\mu\text{m}$  is higher than 14.4 GHz $\cdot\mu\text{m}$  of the recessed-gate device. The simulation of an InGaIn cap structure with  $L_g = 0.8 \mu\text{m}$  shows that  $f_t = 30$  GHz can be achieved, which even gives  $f_t \times L_g = 24$  GHz $\mu\text{m}$ .

Die approbierte gedruckte Originalversion dieser Dissertation ist an der TU Wien Bibliothek verfügbar.  
The approved original version of this doctoral thesis is available in print at TU Wien Bibliothek.



---

# Conclusion and Outlook

---

THE objective of this work was to specify a profound simulation setup for the investigation of GaN-based heterostructure devices and subsequently to study a number of structures. Available material properties (both experimental and theoretical) were summarized with special emphasis on electron transport characteristics. For the latter Monte Carlo simulations were performed while accounting for recent findings (e.g. InN band structure). Based on this extensive compilation and with respect to device peculiarities new models for the electron mobility were developed and calibrated. All other model and material parameters were reexamined and reevaluated according to the current state of knowledge. Relying on this setup several generations of AlGaIn/GaN HEMTs were simulated and excellent predictive results were achieved for both the *DC* and *AC* characteristics. An optimization study of the gate geometry was performed, which had major influence on the design of subsequent transistor generations. Further investigations included high temperature performance and down-scaling phenomena as well as transconductance collapse. Two different approaches towards realizing normally-off operation were examined supported by experimental data and compared: the recessed gate technique and the InGaIn cap layer technique. InAlIn/GaN structures were also simulated in order to estimate the advantages against common AlGaIn/GaN devices.

All those studies showed that the simulation setup describes adequately numerous devices produced by different processes and featuring several material setups and geometries. The simulations proved to allow valuable insights into device physics. This knowledge can be broadened by gate leakage studies which require a modified *Schottky* contact model accounting for tunneling effects from the channel.

Another possible direction for future work is the addition of proper treatment of quaternary alloys to the simulator. Devices with an InAlGaIn barrier have been proposed recently, as the barrier layer can be grown lattice-matched to GaN and offers superb sheet charge density. The simulation of such structures requires models for quaternary alloys to be developed and calibrated.

HEMT performance is still confined by surface traps. This phenomenon is manifested mainly by drain source current collapse or current lag in pulsed mode. The investigation of this effect will require transient simulations and some additional time-variant sheet charge at the surface.

## CHAPTER 6. CONCLUSION AND OUTLOOK

---

Last but not least the presented setup allows the simulation of heterostructure bipolar transistors with some minor model expansion for hole transport. Such simulation studies can answer, whether the reduced device performance is due to intrinsic problems or flawed Ohmic contacts.

Those exciting new investigations will help to further advance Nitride device technology. While they can (and most probably will) offer excellent challenges (either due to the required additional models or through reduced computational stability), this work can serve as a basis for those focused studies.

---

# Bibliography

---

- [1] R. Ross, S. Svensson, and P. Lugli, *Pseudomorphic HEMT Technology and Applications*. Dordrecht-Boston-London: Kluwer Academic Publisher, 1996.
- [2] T. Mimura, “The Early History of the High Electron Mobility Transistor (HEMT),” *IEEE Trans.Microwave Theory and Techniques*, vol. 50, no. 3, pp. 780–782, 2002.
- [3] T. Mimura, S. Hiyamizu, T. Fujii, and K. Nanbu, “A New Field-Effect Transistor with Selectively Doped GaAs/n-Al<sub>x</sub>Ga<sub>1-x</sub>As Heterojunctions,” *Jpn.J.Appl.Phys.*, vol. 19, no. 5, pp. L225–L227, 1980.
- [4] T. Mimura, K. Joshin, S. Hiyamizu, K. Hikosaka, and M. Abe, “High Electron Mobility Transistor Logic,” *Jpn.J.Appl.Phys.*, vol. 20, no. 8, pp. L598–L600, 1981.
- [5] J. Orton, *The Story of Semiconductors*. Oxford: Oxford University Press, 2004.
- [6] C. Weisbuch and B. Vinter, *Quantum Semiconductor Structures*. San Diego: Academic Press, 1991.
- [7] K. Duh, C. Chao, P. Ho, A. Tessmer, J. Liu, Y. Kao, M. Smith, and M. Ballingall, “W-Band InGaAs HEMT Low Noise Amplifiers,” *IEEE Intl. Microwave Symp. Dig.*, vol. 1, pp. 595–598, 1990.
- [8] M. Khan, A. Bhattarai, J. Kuznia, and D. Olson, “High Electron Mobility Transistor Based on a GaN-Al<sub>x</sub>Ga<sub>1-x</sub>N Heterojunction,” *Appl.Phys.Lett.*, vol. 63, no. 9, pp. 1214–1215, 1993.
- [9] S. Mohammad and H. Morkoc, “Base Transit Time of GaN/InGaN Heterojunction Bipolar Transistors,” *J.Appl.Phys.*, vol. 78, no. 6, pp. 4200–4205, 1995.
- [10] F. Conti and M. Conti, “Surface Breakdown in Silicon Planar Diodes Equipped with Field Plate,” *Solid-State Electron.*, vol. 15, no. 1, pp. 93–105, 1972.
- [11] R. Thompson, T. Prunty, V. Kaper, and J. Shealy, “Performance of the AlGa<sub>N</sub> HEMT Structure With a Gate Extension,” *IEEE Trans.Electron Devices*, vol. 51, no. 2, pp. 292–295, 2004.

## BIBLIOGRAPHY

---

- [12] K. Makiyama, T. Ohki, M. Kanamura, K. Imanishi, N. Hara, and T. Kikkawa, “High- $f_{\max}$  GaN HEMT with High Breakdown Voltage over 100 V for Millimeter-Wave Applications,” *Phys.stat.sol.(a)*, vol. 204, no. 6, pp. 2054–2058, 2007.
- [13] L. Shen, S. Heikman, B. Moran, R. Coffie, N. Zhang, D. Buttari, I. Smorchkova, S. Keller, S. DenBaars, and U. Mishra, “AlGaN/AlN/GaN High-Power Microwave HEMT,” *IEEE Electron Device Lett.*, vol. 22, no. 10, pp. 457–459, 2001.
- [14] N. Maeda, T. Saito, K. Tsubaki, T. Nishida, and N. Kobayashi, “Two-Dimensional Electron Gas Transport Properties in AlGaN/GaN Single- and Double-Heterostructure Field Effect Transistors,” *Mat.Sci.Eng.B*, vol. 82, no. 1-3, pp. 232–237, 2001.
- [15] M. Khan, Q. Chen, C. Sun, J. Yang, M. Blasingame, M. Shur, and H. Park, “Enhancement and Depletion Mode GaN/AlGaN Heterostructure Field Effect Transistors,” *Appl.Phys.Lett.*, vol. 68, no. 4, pp. 514–516, 1996.
- [16] Y. Cai, Y. Zhou, K. Chen, and K. Lau, “High-Performance Enhancement-Mode AlGaN/GaN HEMTs Using Fluoride-Based Plasma Treatment,” *IEEE Electron Device Lett.*, vol. 26, no. 7, pp. 435–438, 2005.
- [17] V. Kumar, A. Kuliev, T. Tanaka, Y. Otoki, and I. Adesida, “High Transconductance Enhancement-Mode AlGaN/GaN HEMTs on SiC Substrate,” *Electron.Lett.*, vol. 39, no. 24, pp. 1758–1760, 2003.
- [18] T. Mizutani, M. Ito, S. Kishimoto, and F. Nakamura, “AlGaN/GaN HEMTs With Thin InGaN Cap Layer for Normally Off Operation,” *IEEE Electron Device Lett.*, vol. 28, no. 7, pp. 549–552, 2007.
- [19] R. Quay, *Gallium Nitride Electronics*. Berlin-Heidelberg: Springer, 2008.
- [20] D. Meharry, R. Lander, K. Chu, L. Gunter, and K. Beach, “Multi-Watt Wideband MMICs in GaN and GaAs,” *IEEE Intl. Microwave Symp. Dig.*, pp. 631–634, 2007.
- [21] Y. Lee and Y. Jeong, “A High Efficiency Class-E GaN HEMT Power Amplifier for WCDMA Applications,” *IEEE Microwave and Wireless Comp. Lett.*, vol. 17, no. 8, pp. 622–624, 2007.
- [22] K. Krishnamurthy, J. Martin, B. Landberg, R. Vetury, and M. Poulton, “Wideband 400 W Pulsed Power GaN HEMT Amplifiers,” *IEEE Intl. Microwave Symp. Dig.*, pp. 303–306, 2008.
- [23] N. Lopez, J. Hoversten, M. Poulton, and Z. Popovic, “A 65-W High-Efficiency UHF GaN Power Amplifier,” *IEEE Intl. Microwave Symp. Dig.*, pp. 65–68, 2008.
- [24] S. Hong, Y. Woo, I. Kim, J. Moon, H. Kim, J. Lee, and B. Kim, “High Efficiency GaN HEMT Power Amplifier Optimized for OFDM EER Transmitter,” *IEEE Intl. Microwave Symp. Dig.*, pp. 1247–1250, 2007.
- [25] K. Yamanaka, K. Mori, K. Iyomasa, H. Ohtsuka, H. noto, M. Nakayama, Y. Kamo, and Y. Isota, “C-Band GaN HEMT Power Amplifier with 220W Output Power,” *IEEE Intl. Microwave Symp. Dig.*, pp. 1251–1254, 2007.



- [26] T. Yamamoto, E. Mitani, K. Inoue, M. Nishi, and S. Sano, "A 9.5-10.5 GHz 60W AlGa<sub>N</sub>/Ga<sub>N</sub> HEMT for X-Band High Power Application," *Proc. European Microwave Integr. Circuit Conf.*, pp. 173–175, 2007.
- [27] M. Kao, C. Lee, R. Hajji, P. Saunier, and H. Tserng, "AlGa<sub>N</sub>/Ga<sub>N</sub> HEMTs with PAE of 53% at 35 GHz for HPA and Multi-Function MMIC Applications," *IEEE Intl. Microwave Symp. Dig.*, pp. 627–629, 2007.
- [28] J. Moon, D. Wong, M. Hu, P. Hashimoto, M. Antcliffe, C. McGuire, M. Micovic, and P. Willadson, "55% PAE and High Power Ka-Band Ga<sub>N</sub> HEMTs With Linearized Transconductance via n+ Ga<sub>N</sub> Source Contact Ledge," *IEEE Electron Device Lett.*, vol. 29, no. 8, pp. 834–837, 2008.
- [29] R. Kemerley, H. Wallaca, and M. Yoder, "Impact of Wide Bandgap Microwave Devices on DoD Systems," *Proc. IEEE*, vol. 90, no. 6, pp. 1059–1064, 2002.
- [30] J. Ender, H. Wilden, U. Nickel, R. Klemm, A. Brenner, T. Eibert, and D. Nussler, "Progress in Phased-Array Radar Applications," *European Radar Conference*, pp. 113–117, 2004.
- [31] Y. Mancuso, P. Gremillet, and P. Lacomme, "T/R- Modules Technological and Technical Trends for Phased Array Antennas," *IEEE Intl. Microwave Symp. Dig.*, pp. 614–618, 2005.
- [32] M. Ludwig, C. Buck, F. Coromina, and M. Suess, "Status and Trends for Space-Borne Phased Array Radar," *IEEE Intl. Microwave Symp. Dig.*, pp. 1619–1622, 2005.
- [33] T. Kachi, "Ga<sub>N</sub> Power Devices for Automotive Applications," in *Tech. Dig. IEEE Compound Semiconductor IC Symp.*, pp. 1–4, 2007.
- [34] G. Steinhoff, M. Hermann, W. Schaff, L. Eastman, M. Stutzmann, and M. Eickhoff, "pH Response of Ga<sub>N</sub> Surfaces and its Application for pH-Sensitive Field-Effect Transistors," *Appl. Phys. Lett.*, vol. 83, no. 1, pp. 177–179, 2003.
- [35] B. Kang, F. Ren, B. Gila, C. Abernahty, and S. Pearton, "AlGa<sub>N</sub>/Ga<sub>N</sub>-Based Metal-Oxide-Semiconductor Diode-Based Hydrogen Gas Sensor," *Appl. Phys. Lett.*, vol. 84, no. 7, pp. 1127–1130, 2004.
- [36] G. Mueller, G. Kretz, and J. Schalk, "New Sensors for Automotive and Aerospace Applications," *Phys. stat. sol. (a)*, vol. 185, no. 1, pp. 1–14, 2001.
- [37] Y. Liu, P. Ruden, J. Xie, H. Morkoc, and K. Son, "Effect of Hydrostatic Pressure on the DC Characteristics of AlGa<sub>N</sub>/Ga<sub>N</sub> Heterojunction Field Effect Transistors," *Appl. Phys. Lett.*, vol. 88, pp. 013505–1–013505–3, 2006.
- [38] M. Eickhoff, O. Ambacher, G. Kroetz, and M. Stutzmann, "Piezoresistivity of Al<sub>x</sub>Ga<sub>1-x</sub>N Layers and Al<sub>x</sub>Ga<sub>1-x</sub>N/Ga<sub>N</sub> Heterostructures," *J. Appl. Phys.*, vol. 90, no. 7, pp. 3383–3386, 2001.
- [39] M. Micovic, T. Tsen, M. Hu, P. Hashimoto, P. Willadsen, I. Milosavljevic, A. Schmitz, M. Antcliffe, D. Zhender, J. Moon, W. Wong, and D. Chow, "Ga<sub>N</sub> Enhancement/Depletion-Mode FET Logic for Mixed Signal Applications," *Electron. Lett.*, vol. 41, no. 19, pp. 1081–1083, 2005.

## BIBLIOGRAPHY

---

- [40] A. Endoh, Y. Yamashita, K. Ikeda, M. Higashiwaki, K. Hikosaka, T. Matsui, S. Hiyamizu, and T. Mimura, “Non-Recessed-Gate Enhancement-Mode AlGa<sub>N</sub>/Ga<sub>N</sub> High Electron Mobility Transistors with High RF Performance,” *Jpn.J.Appl.Phys.*, vol. 43, no. 4B, pp. 2255–2258, 2004.
- [41] Y. Liu, T. Egawa, and H. Jiang, “Enhancement-Mode Quaternary AlInGa<sub>N</sub>/Ga<sub>N</sub> HEMT with Non-Recessed-Gate on Sapphire Substrate,” *Electron.Lett.*, vol. 42, no. 15, pp. 884–886, 2006.
- [42] J. Moon, D. Wong, T. Hussain, M. Micovic, P. Deelman, H. Ming, M. Antcliffe, C. Ngo, P. Hashimoto, and L. McCray, “Submicron Enhancement-Mode AlGa<sub>N</sub>/Ga<sub>N</sub> HEMTs,” in *Device Research Conf.Dig.*, pp. 23–24, 2002.
- [43] J. Moon, S. Wu, D. Wong, I. Milosavljevic, A. Conway, P. Hashimoto, M. Hu, M. Antcliffe, and M. Micovic, “Gate-Recessed AlGa<sub>N</sub>-Ga<sub>N</sub> HEMTs for High-Performance Millimeter-Wave Applications,” *IEEE Electron Device Lett.*, vol. 26, no. 6, pp. 348–350, 2005.
- [44] S. Maroldt, C. Haupt, W. Pletschen, S. Mueller, R. Quay, O. Ambacher, C. Schippel, and F. Schwierz, “Gate-Recessed AlGa<sub>N</sub>/Ga<sub>N</sub> Based Enhancement-Mode High Electron Mobility Transistors for High Frequency Operation,” *Jpn.J.Appl.Phys.*, vol. 48, no. 4, p. 04C083(3), 2009.
- [45] H. Okita, K. Kaifu, J. Mita, T. Yamada, Y. Sano, H. Ishikawa, T. Egawa, and T. Jimbo, “High Transconductance AlGa<sub>N</sub>/Ga<sub>N</sub>-HEMT with Recessed Gate on Sapphire Substrate,” *Phys.stat.sol.(a)*, vol. 200, no. 1, pp. 187–190, 2003.
- [46] W. Lanford, T. Tanaka, Y. Otoki, and I. Adesida, “Recessed-Gate Enhancement-Mode Ga<sub>N</sub> HEMT with High Threshold Voltage,” *Electron.Lett.*, vol. 41, no. 7, pp. 449–450, 2005.
- [47] T. Nanjo, N. Miura, T. Oishi, M. Suita, Y. Abe, T. Ozeki, S. Nakatsuka, A. Inoue, T. Ishikawa, Y. Matsuda, H. Ishikawa, and T. Egawa, “Improvement of DC and RF Characteristics of AlGa<sub>N</sub>/Ga<sub>N</sub> High Electron Mobility Transistors by Thermally Annealed Ni/Pt/Au Schottky Gate,” *Jpn.J.Appl.Phys.*, vol. 43, no. 4B, pp. 1952–1929, 2004.
- [48] J. Liu, Y. Zhou, J. Zhu, Y. Cai, K. Lau, and K. J. Chen, “DC and RF Characteristics of AlGa<sub>N</sub>/Ga<sub>N</sub>/InGa<sub>N</sub>/Ga<sub>N</sub> Double-heterojunction HEMTs,” *IEEE Trans.Electron Devices*, vol. 54, no. 1, pp. 2–11, 2007.
- [49] T. Palacios, C. Suh, A. Chakraborty, S. Keller, S. DenBaars, and U. Mishra, “High-Performance E-Mode AlGa<sub>N</sub>/Ga<sub>N</sub> HEMTs,” *IEEE Electron Device Lett.*, vol. 27, no. 6, pp. 428–430, 2006.
- [50] N. Ikeda, K. Kato, J. Li, K. Hataya, and S. Yoshida, “Normally-off Operation Ga<sub>N</sub> HFET Using a Thin AlGa<sub>N</sub> Layer for Low Loss Switching Devices,” *Proc.MRS*, vol. 831, pp. 355–360, 2005.
- [51] Y. Ohmaki, M. Tanimoto, S. Akamatsu, and T. Mukai, “Enhancement-Mode Al-Ga<sub>N</sub>/Al<sub>N</sub>/Ga<sub>N</sub> High Electron Mobility Transistor with Low On-State Resistance and High Breakdown Voltage,” *Jpn.J.Appl.Phys.*, vol. 45, no. 44, pp. L1168–L1170, 2006.

- [52] Y. Cai, Y. Zhou, K. Lau, and K. Chen, "Control of Threshold Voltage of AlGa<sub>N</sub>/Ga<sub>N</sub> HEMTs by Fluoride-Based Plasma Treatment: From Depletion Mode to Enhancement Mode," *IEEE Trans. Electron Devices*, vol. 53, no. 9, pp. 2207–2215, 2006.
- [53] M. Higashiwaki, T. Mimura, and T. Matsui, "Enhancement-Mode AlN/GaN HFETs Using Cat-CVD Si<sub>3</sub>N<sub>4</sub>," *IEEE Trans. Electron Devices*, vol. 54, no. 6, pp. 1566–1570, 2007.
- [54] X. Hu, G. Simin, J. Yang, M. Khan, R. Gaska, and M. Shur, "Enhancement Mode AlGa<sub>N</sub>/Ga<sub>N</sub> HFET with Selectively Grown pn Junction Gate," *Electron. Lett.*, vol. 36, no. 8, pp. 753–754, 2000.
- [55] S. Nakamura, M. Senoh, and T. Mukai, "Highly p-Typed Mg-Doped Ga<sub>N</sub> Films Grown with Ga<sub>N</sub> Buffer Layers," *Jpn. J. Appl. Phys.*, vol. 30, Part 2, no. 10A, pp. L1708–L1711, 1991.
- [56] A. Khan, J. Kuznia, D. Olson, W. Schaff, J. Burn, and M. Shur, "Microwave Performance of a 0.25  $\mu\text{m}$  Gate AlGa<sub>N</sub>/Ga<sub>N</sub> Heterostructure Field Effect Transistor," *Appl. Phys. Lett.*, vol. 65, no. 9, pp. 1121–1123, 1994.
- [57] K. Kasahara, H. Miyamoto, Y. Ando, Y. Okamoto, T. Nakayama, and M. Kuzuhara, "Ka-Band 2.3 W Power AlGa<sub>N</sub>/Ga<sub>N</sub> Heterojunction FET," in *IEDM Tech. Dig.*, pp. 677–680, 2002.
- [58] M. Higashiwaki, T. Mimura, and T. Matsui, *Millimeter-Wave Ga<sub>N</sub> HFET Technology*, vol. 6894. 2008.
- [59] K. Shinohara, I. Milosavljevic, S. Burnham, A. Corrion, P. Hashimoto, D. Wong, M. Hu, C. Butler, A. Schmitz, P. Willadsen, K. Boutros, H. Kazemi, and M. Micovic, "60-nm Ga<sub>N</sub>/AlGa<sub>N</sub> DH-HEMTs with 1.0  $\Omega\cdot\text{mm}$   $R_{\text{on}}$ , 2.0 A/mm  $I_{\text{dmax}}$ , and 153 GHz  $f_{\text{T}}$ ," *Device Research Conf. Dig.*, pp. 167–168, 2009.
- [60] J. Chung, W. Hoke, E. Chumbes, and T. Palacios, "AlGa<sub>N</sub>/Ga<sub>N</sub> HEMT with 300-GHz  $f_{\text{max}}$ ," *IEEE Electron Device Lett.*, vol. 31, no. 3, pp. 195–197, 2010.
- [61] P. Kordos, M. Mikulics, A. Fox, D. Gregusova, K. Cico, J. Carlin, M. Grandjean, J. Novak, and K. Frohlich, "RF Performance of InAlN/GaN HFETs and MOSHFETs with  $f_{\text{T}} \times L_{\text{g}}$  up to 21 GHz $\cdot\mu\text{m}$ ," *IEEE Electron Device Lett.*, vol. 31, no. 3, pp. 180–182, 2010.
- [62] J. Kuzmik, "Power Electronics on InAlN/(In)Ga<sub>N</sub>: Prospect for a Record Performance," *IEEE Electron Device Lett.*, vol. 22, no. 11, pp. 510–513, 2001.
- [63] H. Sun, A. Alt, H. Benedickter, E. Feltin, J. Carlin, M. Gonschorek, N. Grandjean, and C. Bolognesi, "100-nm-Gate (Al,In)N/GaN HEMTs Grown on SiC with  $f_{\text{T}}=144$  GHz," *IEEE Electron Device Lett.*, vol. 31, no. 4, pp. 293–295, 2010.
- [64] Y.-F. Wu, B. Keller, S. Keller, D. Kopolnek, S. Denbaars, and U. Mishra, "Measured Microwave Power Performance of AlGa<sub>N</sub>/Ga<sub>N</sub> MODFET," *IEEE Electron Device Lett.*, vol. 17, no. 9, pp. 455–457, 1996.
- [65] Y.-F. Wu, M. Moore, A. Saxler, T. Wisleder, and P. Parikh, "40-W/mm Double Field-Plated Ga<sub>N</sub> HEMTs," in *Device Research Conf. Dig.*, pp. 151–152, 2006.

## BIBLIOGRAPHY

---

- [66] Y. Wu, S. Wood, R. Smith, S. Sheppard, S. Allen, P. Parikh, and J. Milligan, "An Internally-Matched GaN HEMT Amplifier with 550-Watt Peak Power at 3.5 GHz," in *IEDM Tech.Dig.*, pp. 1–3, 2006.
- [67] Y. Wu, B. Keller, S. Keller, D. Kopolnek, P. Kozodoy, S. Denbaars, and U. Mishra, "Very High Breakdown Voltage and Large Transconductance Realized on GaN Heterojunction Field Effect Transistors," *Appl.Phys.Lett.*, vol. 69, no. 10, pp. 1438–1440, 1996.
- [68] N.-Q. Zhang, S. Keller, G. Parish, S. Heikman, S. DenBaars, and U. Mishra, "High Breakdown GaN HEMT with Overlapping Gate Structure," *IEEE Electron Device Lett.*, vol. 21, no. 9, pp. 421–423, 2000.
- [69] Y. Dora, A. Chakraborty, L. McCarthy, S. Keller, S. DenBaars, and U. Mishra, "High Breakdown Voltage Achieved on AlGaN/GaN HEMTs with Integrated Slant Field Plates," *IEEE Electron Device Lett.*, vol. 27, no. 9, pp. 713–715, 2006.
- [70] T. Egawa, T. Suzue, and S. Selvaraj, "Breakdown Enhancement of AlGaN/GaN HEMTs on 4-in Silicon by Improving the GaN Quality on Thick Buffer Layers," *IEEE Electron Device Lett.*, vol. 30, no. 6, pp. 587–589, 2009.
- [71] Y. Yamashita, A. Endoh, K. Shinohara, K. Hikosaka, T. Matsui, S. Hiyamizu, and T. Mimura, "Pseudomorphic In<sub>0.52</sub>Al<sub>0.48</sub>As/In<sub>0.7</sub>Ga<sub>0.3</sub>As HEMTs with an Ultrahigh  $f_t$  of 562 GHz," *IEEE Electron Device Lett.*, vol. 23, no. 10, pp. 573–575, 2002.
- [72] K. Shinohara, Y. Yamashita, A. Endoh, K. Hikosaka, T. Matsui, T. Mimura, and S. Hiyamizu, "Ultrahigh-Speed Pseudomorphic InGaAs/InAlAs HEMTs with 400-GHz Cutoff Frequency," *IEEE Electron Device Lett.*, vol. 22, no. 11, pp. 507–509, 2001.
- [73] K. Lee, Y. Kim, Y. Hong, and Y. Jeong, "35-nm Zigzag T-Gate In<sub>0.52</sub>Al<sub>0.48</sub>As/In<sub>0.53</sub>Ga<sub>0.47</sub>As Metamorphic GaAs HEMTs With an Ultrahigh  $f_{max}$  of 520 GHz," *IEEE Electron Device Lett.*, vol. 28, no. 8, pp. 672–675, 2007.
- [74] K. Elgaid, H. McLelland, M. Holland, D. Moran, C. Stanley, and I. Thayne, "50-nm T-Gate Metamorphic GaAs HEMTs with  $f_t$  of 440 GHz and Noise Figure of 0.7 dB at 26 GHz," *IEEE Electron Device Lett.*, vol. 26, no. 11, pp. 784–786, 2005.
- [75] K. Su, W. Hsu, C. Lee, T. Wu, Y. Wu, L. Chang, R. Hsiao, J. Chen, and T. Chi, "A Novel Dilute Antimony Channel In<sub>0.2</sub>Ga<sub>0.8</sub>AsSb/GaAs HEMT," *IEEE Electron Device Lett.*, vol. 28, no. 2, pp. 96–99, 2007.
- [76] H. Lin, T. Yang, H. Sharifi, S. Kim, Y. Xuan, T. Shen, S. Mohammadi, and P. Ye, "Enhancement-Mode GaAs Metal-Oxide-Semiconductor High-Electron-Mobility Transistors with Atomic Layer Deposited Al<sub>2</sub>O<sub>3</sub> as Gate Dielectric," *Appl.Phys.Lett.*, vol. 91, no. 21, p. 212101, 2007.
- [77] K. Lee, H. Lin, F. Lee, H. Huang, and Y. Wang, "Improved Microwave and Noise Performance of InAlAs/InGaAs Metamorphic High-Electron-Mobility Transistor with a Liquid Phase Oxidized InGaAs Gate without Gate Recess," *Appl.Phys.Lett.*, vol. 96, no. 20, p. 203506, 2010.

- [78] L. McCarthy, P. Kozodoy, M. Rodwell, S. DenBaars, and U. Mishra, "AlGa<sub>N</sub>/Ga<sub>N</sub> Heterojunction Bipolar Transistor," *IEEE Electron Device Lett.*, vol. 20, no. 6, pp. 277–279, 1999.
- [79] F. Ren, C. Abernathy, J. V. Hove, P. Chow, R. Hickman, J. Klaasen, R. Kopf, H. Cho, K. Jung, J. L. Roche, R. Wilson, J. Han, R. Shul, A. Baca, and S. Pearton, "300°C Ga<sub>N</sub>/AlGa<sub>N</sub> Heterojunction Bipolar Transistor," *MRS Internet J. Nitride Semicond. Res.*, vol. 3, 1998.
- [80] D. Lambert, D. Lin, and R. Dupuis, "Simulation of the Electrical Characteristics of AlGa<sub>N</sub>/Ga<sub>N</sub> Heterojunction Bipolar Transistors," *Solid-State Electron.*, vol. 44, no. 2, pp. 253–257, 2000.
- [81] D. Pulfrey and S. Fathpour, "Performance Predictions for n-p-n Al<sub>x</sub>Ga<sub>1-x</sub>N/Ga<sub>N</sub> HBTs," *IEEE Trans. Electron Devices*, vol. 48, no. 3, pp. 597–602, 2001.
- [82] C. Monier, R. Fan, H. Jung, C. Ping-Chih, R. Shul, L. Kyu-Pil, Z. Anping, A. Baca, and S. Pearton, "Simulation of npn and pnp AlGa<sub>N</sub>/Ga<sub>N</sub> Heterojunction Bipolar Transistors Performances: Limiting Factors and Optimum Design," *IEEE Trans. Electron Devices*, vol. 48, no. 3, pp. 427–432, 2001.
- [83] E. Alekseev and D. Pavlidis, "DC and High-Frequency Performance of AlGa<sub>N</sub>/Ga<sub>N</sub> Heterojunction Bipolar Transistors," *Solid-State Electron.*, vol. 44, no. 2, pp. 245–252, 2000.
- [84] F. Ren, J. Han, R. Hickman, J. V. Hove, P. Chow, J. Klaassen, J. L. Roche, K. Jung, H. Cho, X. Cao, S. Donovan, R. Kopf, R. Wilson, A. Baca, R. Shul, L. Zhang, C. Willison, C. Abernathy, and S. Pearton, "Ga<sub>N</sub>/AlGa<sub>N</sub> HBT Fabrication," *Solid-State Electron.*, vol. 44, no. 2, pp. 239–244, 2000.
- [85] B. Shelton, J. Huang, D. Lambert, T. Zhu, M. Wong, C. Eiting, H. Kwon, M. Feng, and R. Dupuis, "AlGa<sub>N</sub>/Ga<sub>N</sub> Heterojunction Bipolar Transistors Grown by Metal Organic Chemical Vapour Deposition," *Electron. Lett.*, vol. 36, no. 1, pp. 80–81, 2000.
- [86] B. Shelton, D. Lambert, J. Jian, M. Wong, U. Chowdhury, G. Ting, H. Kwon, Z. Liliental-Weber, M. Benarama, M. Feng, and R. Dupuis, "Selective Area Growth and Characterization of AlGa<sub>N</sub>/Ga<sub>N</sub> Heterojunction Bipolar Transistors by Metalorganic Chemical Vapor Deposition," *IEEE Trans. Electron Devices*, vol. 48, no. 3, pp. 490–494, 2001.
- [87] L. McCarthy, I. Smorchkova, X. Huili, P. Kozodoy, P. Fini, J. Limb, D. Pulfrey, J. Speck, M. Rodwell, S. DenBaars, and U. Mishra, "Ga<sub>N</sub> HBT: toward an RF Device," *IEEE Trans. Electron Devices*, vol. 48, no. 3, pp. 543–551, 2001.
- [88] J. Huang, M. Hattendorf, M. Feng, D. Lambert, B. Shelton, M. Wong, U. Chowdhury, T. Zhu, H. Kwon, and R. Dupuis, "Temperature Dependent Common Emitter Current Gain and Collector-Emitter Offset Voltage Study in AlGa<sub>N</sub>/Ga<sub>N</sub> Heterojunction Bipolar Transistors," *IEEE Electron Device Lett.*, vol. 22, no. 4, pp. 157–159, 2001.
- [89] L. McCarthy, I. Smorchkova, P. Fini, M. Rodwell, I. Speck, S. DenBaars, and U. Mishra, "Small Signal RF Performance of AlGa<sub>N</sub>/Ga<sub>N</sub> Heterojunction Bipolar Transistors," *Electron. Lett.*, vol. 38, no. 3, pp. 144–145, 2002.

## BIBLIOGRAPHY

---

- [90] K. Kumakura, T. Makimoto, and N. Kobayashi, “pnp AlGa<sub>N</sub>/Ga<sub>N</sub> Heterojunction Bipolar Transistors Operating at 300°C,” *Phys.stat.sol.(a)*, vol. 194, no. 2, pp. 443–446, 2002.
- [91] H. Xing, P. Chavarkar, S. Keller, S. DenBaars, and U. Mishra, “Very High Voltage Operation (> 330 V) with High Current Gain of AlGa<sub>N</sub>/Ga<sub>N</sub> HBTs,” *IEEE Electron Device Lett.*, vol. 24, no. 3, pp. 141–143, 2003.
- [92] H. Xing, D. Jena, M. Rodwell, and U. Mishra, “Explanation of Anomalously High Current Gain Observed in Ga<sub>N</sub> Based Bipolar Transistors,” *IEEE Electron Device Lett.*, vol. 24, no. 1, pp. 4–6, 2003.
- [93] K. Kumakura, Y. Yamauchi, and T. Makimoto, “High Power Operation of pnp AlGa<sub>N</sub>/Ga<sub>N</sub> Heterojunction Bipolar Transistors,” *Phys.stat.sol.(c)*, vol. 2, no. 7, pp. 2589–2592, 2005.
- [94] K. Kumakura and T. Makimoto, “Carrier Transport Mechanisms of pnp AlGa<sub>N</sub>/Ga<sub>N</sub> Heterojunction Bipolar Transistors,” *Appl.Phys.Lett.*, vol. 92, no. 9, p. 093504(3), 2008.
- [95] K. Hsueh, Y. Hsin, J. Sheu, W. Lai, C. Tun, C. Hsu, and B. Lin, “Effects of Leakage Current and Schottky-Like Ohmic Contact on the Characterization of Al<sub>0.17</sub>Ga<sub>0.83</sub>N/Ga<sub>N</sub> HBTs,” *Solid-State Electron.*, vol. 51, no. 7, pp. 1073–1078, 2007.
- [96] K. Kumakura and T. Makimoto, “High-Temperature Characteristics up to 590°C of a pnp AlGa<sub>N</sub>/Ga<sub>N</sub> Heterojunction Bipolar Transistor,” *Appl.Phys.Lett.*, vol. 94, no. 10, p. 103502(3), 2009.
- [97] T. Makimoto, K. Kumakura, and N. Kobayashi, “High Current Gains Obtained by InGa<sub>N</sub>/Ga<sub>N</sub> Double Heterojunction Bipolar Transistors with p-InGa<sub>N</sub> Base,” *Appl.Phys.Lett.*, vol. 79, no. 3, pp. 380–381, 2001.
- [98] S. Mohammad, A. Salvador, and H. Morkoc, “Emerging Gallium Nitride Based Devices,” *Proc.IEEE*, vol. 83, no. 10, pp. 1306–1355, 1995.
- [99] S. Chiu, A. Anwar, and S. Wu, “Base Transit Time in Abrupt Ga<sub>N</sub>/InGa<sub>N</sub>/Ga<sub>N</sub> HBT’s,” *IEEE Trans.Electron Devices*, vol. 47, no. 4, pp. 662–666, 2000.
- [100] T. Makimoto, K. Kumakura, and N. Kobayashi, “n-AlGa<sub>N</sub>/p-InGa<sub>N</sub>/n-Ga<sub>N</sub> Heterojunction Bipolar Transistors for High Power Operation,” *Phys.stat.sol.(c)*, vol. 0, no. 1, pp. 95–98, 2003.
- [101] T. Makimoto, K. Kumakura, and N. Kobayashi, “High Current Gain (> 2000) of Ga<sub>N</sub>/InGa<sub>N</sub> Double Heterojunction Bipolar Transistors Using Base Regrowth of p-InGa<sub>N</sub>,” *Appl.Phys.Lett.*, vol. 83, no. 5, pp. 1035–1037, 2003.
- [102] T. Makimoto, Y. Yamauchi, and K. Kumakura, “High-Power Characteristics of Ga<sub>N</sub>/InGa<sub>N</sub> Double Heterojunction Bipolar Transistors,” *Appl.Phys.Lett.*, vol. 84, no. 11, pp. 1964–1966, 2004.
- [103] J. Li, D. Keogh, S. Raychaudhuri, A. Conway, D. Qiao, and P. Asbeck, “Analysis of High DC Current Gain Structures for Ga<sub>N</sub>/InGa<sub>N</sub>/Ga<sub>N</sub> HBTs,” *Intl. J. of High Speed Electronics and Systems*, vol. 14, no. 3, pp. 825–830, 2004.

- [104] D. Keogh, P. Asbeck, T. Chung, J. Limb, D. Yoo, J. Ryou, W. Lee, S. Shen, and R. Dupuis, “High Current Gain InGaN/GaN HBTs with 300°C Operating Temperature,” *Electron.Lett.*, vol. 42, no. 11, p. 661(2), 2006.
- [105] T. Chung, D. Keogh, J.-H. Ryou, D. Yoo, J. Limb, W. Lee, S.-C. Shen, P. Asbeck, and R. Dupuis, “High Current Gain Graded GaN/InGaN Heterojunction Bipolar Transistors Grown on Sapphire and SiC Substrates by Metalorganic Chemical Vapor Deposition,” *J.Cryst.Growth*, vol. 298, pp. 852–856, 2007.
- [106] S. Shen, Y. Lee, H. Kim, Y. Zhang, S. Choi, R. Dupuis, and J. Ryou, “Surface Leakage in GaN/InGaN Double Heterojunction Bipolar Transistors,” *IEEE Electron Device Lett.*, vol. 30, no. 11, pp. 1119–1121, 2009.
- [107] A. Nishikawa, K. Kumakura, M. Kasu, and T. Makimoto, “Low-Temperature Characteristics of the Current Gain of GaN/InGaN Double-Heterojunction Bipolar Transistors,” *J.Cryst.Growth*, vol. 311, no. 10, pp. 3000–3002, 2009.
- [108] K. Kumakura, A. Nishikawa, and T. Makimoto, “High Breakdown Field of pnp GaN/InGaN/AlGaN DHBTs with AlGaN Collector,” *Phys.stat.sol.(a)*, vol. 204, no. 6, pp. 2037–2041, 2007.
- [109] K. Brennan, E. Bellotti, M. Farahmand, H.-E. Nilsson, P. Ruden, and Y. Zhang, “Monte Carlo Simulation of Noncubic Symmetry Semiconducting Materials and Devices,” *IEEE Trans.Electron Devices*, vol. 47, no. 10, pp. 1882–1890, 2000.
- [110] J. Albrecht, R. Wang, and P. Ruden, “Electron Transport Characteristics of GaN for High Temperature Device Modeling,” *J.Appl.Phys.*, vol. 83, no. 9, pp. 4777–4781, 1998.
- [111] S. Yamakawa, R. Akis, N. Faralli, M. Saraniti, and S. Goodnick, “Rigid Ion Model of High Field Transport in GaN,” *J.Phys.:Condensed Matter*, vol. 21, no. 17, p. 174206(16), 2009.
- [112] M. Farahmand and K. Brennan, “Comparison between Wurtzite Phase and Zincblende Phase GaN MESFETs Using a Full Band Monte Carlo Simulation,” *IEEE Trans.Electron Devices*, vol. 47, no. 3, pp. 493–497, 2000.
- [113] S. Yamakawa, S. Aboud, M. Saraniti, and S. Goodnick, “Influence of the ElectronPhonon Interaction on Electron Transport in Wurtzite GaN,” *Semicond.Sci.Technol.*, vol. 19, no. 4, pp. S475–S477, 2004.
- [114] F. Sacconi, A. Di Carlo, P. Lugli, and H. Morkoc, “Spontaneous and Piezoelectric Polarization Effects on the Output Characteristics of AlGaIn/GaN Heterojunction Modulation Doped FETs,” *IEEE Trans.Electron Devices*, vol. 48, no. 3, pp. 450–457, 2001.
- [115] T.-H. Yu and K. Brennan, “Theoretical Study of a GaN-AlGaIn High Electron Mobility Transistor Including a Nonlinear Polarization Model,” *IEEE Trans.Electron Devices*, vol. 50, no. 2, pp. 315–323, 2003.
- [116] D. Herbert, M. Uren, B. Hughes, D. Hayes, J. Birbeck, R. Balmer, T. Martin, G. Crow, R. Abram, M. Walmsley, R. Davies, R. Wallis, W. Phillips, and S. Jones, “Monte Carlo Simulations of AlGaIn/GaN Heterojunction Field-Effect Transistors (HFETs),” *J.Phys.:Condensed Matter*, vol. 14, no. 13, pp. 3479–3497, 2002.

## BIBLIOGRAPHY

---

- [117] T. Sadi, R. Kelsall, and N. Pilgrim, “Investigation of Self-Heating Effects in Submicrometer GaN/AlGa<sub>N</sub> HEMTs Using an Electrothermal Monte Carlo Method,” *IEEE Trans. Electron Devices*, vol. 53, no. 12, pp. 2892–2900, 2006.
- [118] J. Mateos, S. Pérez, D. Pardo, and T. González, “High Frequency Noise in GaN HEMTs,” *Noise and Fluctuations: 20th Intl. Conf. on Noise and Fluctuations (ICNF-2009)*, vol. 1129, no. 1, pp. 237–240, 2009.
- [119] Y. Tomita, H. Ikegami, and H. Fujishiro, “Monte Carlo Study of High-Field Electron Transport Characteristics in AlGa<sub>N</sub>/Ga<sub>N</sub> Heterostructure Considering Dislocation Scattering,” *Phys.stat.sol.(c)*, vol. 4, no. 7, pp. 2695–2699, 2007.
- [120] <http://www.tibercad.org>.
- [121] M. Auf der Maur, M. Povolotskyi, F. Sacconi, A. Pecchia, G. Romano, G. Penazzi, and A. Di Carlo, “TiberCAD: Towards Multiscale Simulation of Optoelectronic Devices,” in *Intl. Conf. Numerical Simulation of Optoelectronic Devices*, pp. 43–44, Sept. 2008.
- [122] <http://www.esemi.com>.
- [123] L. Chen, O. Guy, M. Jennings, P. Igit, S. Wilks, and P. Mawby, “Study of a Novel Si/SiC Hetero-Junction MOSFET,” *Solid-State Electron.*, vol. 51, no. 5, pp. 662–666, 2007.
- [124] <http://www.crosslight.com>.
- [125] D. Lin, J. Wu, J. Zheng, and C. Lin, “Optical Characterization of Al<sub>x</sub>Ga<sub>1-x</sub>N/GaN High Electron Mobility Transistor Structures,” *Physica E: Low-dimensional Systems and Nanostructures*, vol. 40, no. 5, pp. 1763–1765, 2008.
- [126] Genius Semiconductor Device Simulator, User’s Guide 2008. <http://www.tcadstudio.com>.
- [127] W. Saito, M. Kuraguchi, Y. Takada, K. Tsuda, I. Omura., and T. Ogura, “Influence of Surface Defect Charge at AlGa<sub>N</sub>-Ga<sub>N</sub>-HEMT upon Schottky Gate Leakage Current and Breakdown Voltage,” *IEEE Trans. Electron Devices*, vol. 52, no. 2, pp. 159–164, 2005.
- [128] N. Braga, R. Mickevicius, R. Gaska, X. Hu, M. S. Shur, M. A. Khan, G. Simin, and J. Yang, “Simulation of Hot Electron and Quantum Effects in AlGa<sub>N</sub>/Ga<sub>N</sub> Heterostructure Field Effect Transistors,” *J. Appl. Phys.*, vol. 95, no. 11, pp. 6409–6413, 2004.
- [129] W. Hu, X. Chen, Z. Quan, C. Xia, W. Lu, and P. Ye, “Self-Heating Simulation of GaN-based Metal-Oxide-Semiconductor High-Electron-Mobility Transistors Including Hot Electron and Quantum Effects,” *J. Appl. Phys.*, vol. 100, no. 7, p. 074501, 2006.
- [130] S. Karmalkar and U. Mishra, “Enhancement of Breakdown Voltage in AlGa<sub>N</sub>/Ga<sub>N</sub> High Mobility Transistors Using a Field Plate,” *IEEE Trans. Electron Devices*, vol. 48, no. 8, pp. 1515–1521, 2001.
- [131] J. Tirado, J. Sanchez-Rojas, and J. Izpura, “Trapping Effects in the Transient Response of AlGa<sub>N</sub>/Ga<sub>N</sub> HEMT Devices,” *IEEE Trans. Electron Devices*, vol. 54, no. 3, pp. 410–417, 2007.



- [132] S. Kumar, A. Agrawal, R. Chaujar, S. Kabra, M. Gupta, and R. Gupta, “Threshold Voltage Model for Small Geometry AlGa<sub>N</sub>/Ga<sub>N</sub> HEMTs Based on Analytical Solution of 3-D Poisson’s Equation,” *Microelectronics Journal*, vol. 38, no. 10-11, pp. 1013–1020, 2007.
- [133] R. Deutschmann, *Entwicklung eines physikalischen HFET – Modells: Parameterextraktion und Verifikation*. Dissertation, Technische Universität Wien, 1995.
- [134] T. Simlinger, *Simulation von Heterostruktur-Feldeffekttransistoren*. Dissertation, Technische Universität Wien, 1996.
- [135] H. Brech, *Optimization of GaAs Based High Electron Mobility Transistors by Numerical Simulations*. Dissertation, Technische Universität Wien, 1998.
- [136] V. Palankovski, *Simulation of Heterojunction Bipolar Transistors*. Dissertation, Technische Universität Wien, 2000.
- [137] R. Quay, *Analysis and Simulation of High Electron Mobility Transistors*. Dissertation, Technische Universität Wien, 2001.
- [138] V. Palankovski and R. Quay, *Analysis and Simulation of Heterostructure Devices*. Wien, New York: Springer, 2004.
- [139] A. Reklaitis and L. Reggiani, “Monte Carlo Study of Hot-Carrier Transport in Bulk Wurtzite Ga<sub>N</sub> and Modeling of a Near-Terahertz Impact Avalanche Transit Time Diode,” *J.Appl.Phys.*, vol. 95, no. 2, pp. 7925–7935, 2004.
- [140] T. Li, R. Joshi, and C. Fazi, “Monte Carlo Evaluations of Degeneracy and Interface Roughness Effects on Electron Transport in AlGa<sub>N</sub>-Ga<sub>N</sub> Heterostructures,” *J.Appl.Phys.*, vol. 88, no. 2, pp. 829–837, 2000.
- [141] G. Kokolakis, J. Gleize, A. Cardo, and P. Lugli, “Exciton Interaction with Piezoelectric and Polar Optical Phonons in Bulk Wurtzite Ga<sub>N</sub>,” *Semicond.Sci.Technol.*, vol. 19, no. 4, pp. 460–462, 2004.
- [142] B. Ridley, *Quantum Processes in Semiconductors*. Oxford University Press, third ed., 1993.
- [143] T. Deguchi, D. Ichiryu, K. Toshikawa, K. Sekiguchi, T. Sota, R. Matsuo, T. Azuhata, M. Yamaguchi, T. Yagi, S. Chichibu, and S. Nakamura, “Structural and Vibrational Properties of Ga<sub>N</sub>,” *J.Appl.Phys.*, vol. 86, no. 4, pp. 1860–1866, 1999.
- [144] V. Palankovski, A. Marchlewski, E. Ungersboeck, and S. Selberherr, “Identification of Transport Parameters for Gallium Nitride Based Semiconductor Devices,” in *Proc. MATHMOD*, pp. 14–1–14–9, 2006.
- [145] M. Littlejohn, J. Hauser, and T. Glisson, “Monte Carlo Calculation of the Velocity-Field Relationship for Gallium Nitride,” *Appl.Phys.Lett.*, vol. 26, no. 11, pp. 625–627, 1975.
- [146] B. Gelmont, K. Kim, and M. Shur, “Monte Carlo Simulation of Electron Transport in Gallium Nitride,” *J.Appl.Phys.*, vol. 74, no. 3, pp. 1818–1821, 1993.

## BIBLIOGRAPHY

---

- [147] N. Mansour, K. Kim, and M. Littlejohn, "Theoretical Study of Electron Transport in Gallium Nitride," *J.Appl.Phys.*, vol. 77, no. 6, pp. 2834–2836, 1995.
- [148] J. Kolnik, I. Oguzman, K. E. Brennan, R. Wang, P. Ruden, and Y. Wang, "Electronic Transport Studies of Bulk Zincblende and Wurtzite Phases of GaN Based on an Ensemble Monte Carlo Calculation Including a Full Zone Band Structure," *J.Appl.Phys.*, vol. 78, no. 2, pp. 1033–1038, 1995.
- [149] U. Bhapkar and M. Shur, "Monte Carlo Calculation of Velocity-Field Characteristics of Wurtzite GaN," *J.Appl.Phys.*, vol. 82, no. 4, pp. 1649–1655, 1997.
- [150] B. Foutz, L. Eastman, U. Bhapkar, and M. Shur, "Comparison of High Field Electron Transport in GaN and GaAs," *Appl.Phys.Lett.*, vol. 70, no. 21, pp. 2849–2851, 1997.
- [151] S. O'Leary, B. Foutz, M. Shur, U. Bhapkar, and L. Eastman, "Electron Transport in Wurtzite Indium Nitride," *J.Appl.Phys.*, vol. 83, no. 2, pp. 826–829, 1998.
- [152] B. Foutz, S. O'Leary, M. Shur, and L. Eastman, "Transient Electron Transport in Wurtzite GaN, InN, and AlN," *J.Appl.Phys.*, vol. 85, no. 11, pp. 7727–7734, 1999.
- [153] J. Cao and X. Lei, "Nonparabolic Multivalley Balance-Equation Approach to Impact Ionization: Application to Wurtzite GaN," *The European Phys. Journal B*, vol. 7, no. 1, pp. 79–83, 1999.
- [154] Y. Ando, W. Contrata, N. Samoto, H. Miyamoto, K. Matsunaga, M. Kuzuhara, K. Kunihiro, K. Kasahara, T. Nakayama, Y. Takahashi, N. Hayama, and Y. Ohno, "Gate Length Scaling for  $\text{Al}_{0.2}\text{Ga}_{0.8}\text{N}/\text{GaN}$  HJFETs: Two-Dimensional Full Band Monte Carlo Simulation Including Polarization Effect," *IEEE Trans.Electron Devices*, vol. 47, no. 10, pp. 1965–1972, 2000.
- [155] M. Farahmand, C. Garetto, E. Bellotti, K. Brennan, M. Goano, E. Ghillino, G. Ghione, J. Albrecht, and P. Ruden, "Monte Carlo Simulation of Electron Transport in the III-Nitride Wurtzite Phase Materials System: Binaries and Ternaries," *IEEE Trans.Electron Devices*, vol. 48, no. 3, pp. 535–542, 2001.
- [156] T.-H. Yu and K. Brennan, "Monte Carlo Calculation of Two-Dimensional Electron Dynamics in GaN-AlGaN Heterostructures," *J.Appl.Phys.*, vol. 91, no. 6, pp. 3730–3737, 2002.
- [157] R. Brazis and R. Raguotis, "Additional Phonon Modes and Close Satellite Valleys Crucial for Electron Transport in Hexagonal Gallium Nitride," *J.Appl.Phys.*, vol. 85, no. 4, pp. 609–611, 2004.
- [158] S. O'Leary, B. Foutz, M. Shur, and L. Eastman, "Steady-State and Transient Electron Transport Within the III-V Nitride Semiconductors, GaN, AlN, and InN: A Review," *Journal of Materials Science: Materials in Electronics*, vol. 17, no. 2, pp. 87–126, 2006.
- [159] S. Chen and G. Wang, "High-Field Properties of Carrier Transport in Bulk Wurtzite GaN: A Monte Carlo Perspective," *J.Appl.Phys.*, vol. 103, no. 2, p. 023703(6), 2008.
- [160] V. Savastenko and A. Sheleg, "Study of the Elastic Properties of Gallium Nitride," *Phys.stat.sol.(a)*, vol. 48, no. 2, pp. 135–144, 1978.

- [161] Y. Takagi, M. Ahart, T. Azuhata, T. Sota, K. Suzuki, and S. Nakamura, “Brillouin Scattering Study in the GaN Epitaxial Layer,” *Physica B*, vol. 219-220, no. 9, pp. 547–549, 1996.
- [162] A. Polian, M. Grimsditch, and I. Gregory, “Elastic Constants of Gallium Nitride,” *J.Appl.Phys.*, vol. 79, no. 6, pp. 3343–3344, 1996.
- [163] R. Schwarz, K. Khachatryan, and E. Weber, “Elastic Moduli of Gallium Nitride,” *Appl.Phys.Lett.*, vol. 70, no. 9, pp. 1122–1124, 1997.
- [164] M. Yamaguchi, T. Yagi, T. Azuhata, T. Sota, K. Suzuki, S. Chichinu, and S. Nakamura, “Brillouin Scattering Study of Gallium Nitride: Elastic Stiffness Constants,” *J.Phys.:Condensed Matter*, vol. 9, no. 1, pp. 241–248, 1997.
- [165] C. Deger, E. Born, H. Angerer, O. Ambacher, M. Stutzmann, J. Hornstein, E. Riha, and G. Fischerauer, “Sound Velocity of  $\text{Al}_x\text{Ga}_{1-x}\text{N}$  Thin Films Obtained by Surface Acoustic-Wave Measurements,” *Appl.Phys.Lett.*, vol. 72, no. 19, pp. 2400–2402, 1998.
- [166] T. Azuhata, T. Sota, and K. Suzuki, “Elastic Constants of III-V Compound Semiconductors: Modification of Keyes’ Relation,” *J.Phys.:Condensed Matter*, vol. 8, no. 18, pp. 3111–3119, 1996.
- [167] K. Kim, W. Lambrecht, and B. Segall, “Elastic Constants and Related Properties of Tetrahedrally Bonded BN, AlN, GaN, and InN,” *Phys.Rev.B*, vol. 53, no. 24, pp. 16310–16326, 1996.
- [168] A. Wright, “Elastic Properties of Zinc-Blende and Wurtzite AlN, GaN, and InN,” *J.Appl.Phys.*, vol. 82, no. 6, pp. 2833–2839, 1997.
- [169] K. Shimada, T. Sota, and K. Suzuki, “First-Principles Study on Electronic and Elastic Properties of BN, AlN and GaN,” *J.Appl.Phys.*, vol. 84, no. 9, pp. 4951–4959, 1998.
- [170] G. O’Clock and M. Duffy, “Acoustic Surface Wave Properties of Epitaxially Grown Aluminum Nitride and Gallium Nitride on Sapphire,” *Appl.Phys.Lett.*, vol. 23, no. 2, pp. 55–56, 1973.
- [171] I. Guy, S. Muensit, and E. Goldys, “Extensional Piezoelectric Coefficients of Gallium Nitride and Aluminium Nitride,” *Appl.Phys.Lett.*, vol. 75, no. 26, pp. 4133–4136, 1999.
- [172] F. Bernardini and V. Fiorentini, “Spontaneous Polarization and Piezoelectric Constants of III-V Nitrides,” *Phys.Rev.B*, vol. 56, no. 16, pp. R10024–R10027, 1997.
- [173] A. Bykhovski, B. Gelmont, and M. Shur, “Elastic Strain Relaxation and Piezoeffect in GaN-AlN, GaN-AlGaN and GaN-InGaN Superlattices,” *J.Appl.Phys.*, vol. 81, no. 9, pp. 6332–6338, 1997.
- [174] A. Zoroddu, F. Bernardi, P. Ruggerone, and V. Fiorentini, “First-principles Prediction of Structure, Energetics, Formation Enthalpy, Elastic Constants, Polarization, and Piezoelectric Constants of AlN, GaN, and InN: Comparison of Local and Gradient-Corrected Density-Functional Theory,” *Phys.Rev.B*, vol. 64, no. 4, p. 45208(6), 2001.

## BIBLIOGRAPHY

---

- [175] F. Schwierz, “An Electron Mobility Model for Wurtzite GaN,” *Solid-State Electron.*, vol. 49, no. 6, pp. 889–895, 2005.
- [176] V. Chin, T. Tansley, and T. Osotchan, “Electron Mobilities in Gallium, Indium, and Aluminum Nitrides,” *J.Appl.Phys.*, vol. 75, no. 11, pp. 7365–7372, 1994.
- [177] D. K. Gaskill, L. Rowland, and K. Doverspike, “Electrical Transport Properties of AlN, GaN and AlGaIn,” *Properties of Group III Nitrides. EMIS Datareviews Series*, vol. 11, pp. 101–116, 1995.
- [178] K. Köhler, S. M. N. Rollbühler, R. Kiefer, R. Quay, and G. Weimann, “Multiwafer Epitaxy of AlGaIn/GaN Heterostructures for Power Applications,” in *Proc. Intl.Symp. Compound Semiconductors*, pp. 235–238, 2003.
- [179] D. Zanato, N. Balkan, G. Hill, and W. Schaff, “Energy and Momentum Relaxation of Electrons in Bulk and 2D GaN,” *Superlattices & Microstructures*, vol. 36, no. 4-6, pp. 455–463, 2004.
- [180] M. Shur and R. Gaska, “Physics of GaN-based Heterostructure Field Effect Transistors,” in *Tech.Dig. IEEE Compound Semiconductor IC Symp.*, pp. 137–140, Oct. 2005.
- [181] R. Joshi, “Temperature-Dependent Electron Mobility in GaN: Effects of Space Charge and Interface Roughness Scattering,” *Appl.Phys.Lett.*, vol. 64, no. 2, pp. 223–225, 1994.
- [182] W. Götz, N. Johnson, C. Chen, H. Liu, C. Kuo, and W. Imler, “Activation Energies of Si Donors in GaN,” *Appl.Phys.Lett.*, vol. 68, no. 22, pp. 3144–3146, 1996.
- [183] M. Wraback, H. Shen, J. Carrano, T. Li, J. Campbell, M. Schurman, and I. Ferguson, “Time-Resolved Electroabsorption Measurement of the Electron Velocity-Field Characteristic in GaN,” *Appl.Phys.Lett.*, vol. 76, no. 9, pp. 1155–1157, 2000.
- [184] J. Barker, R. Akis, D. Ferry, S. Goodnick, T. Thornton, D. Koleske, A. Wickenden, and R. Henry, “High-Field Transport Studies of GaN,” *Physica B*, vol. 314, pp. 39–41, 2002.
- [185] M. Wraback, H. Shen, J. Carrano, C. Collins, J. Campbell, R. Dupuis, M. Schurman, and I. Ferguson, “Time-Resolved Electroabsorption Measurement of the Transient Electron Velocity Overshoot in GaN,” *Appl.Phys.Lett.*, vol. 79, no. 9, pp. 1303–1305, 2001.
- [186] L. Ardaravicius, M. Ramonas, J. Liberis, O. Kiprijanovic, A. Matulionis, J. Xie, M. Wu, J. H. Leach, and H. Morkoc, “Electron Drift Velocity in Lattice-Matched AlInN/AlN/GaN Channel at High Electric Fields,” *J.Appl.Phys.*, vol. 106, no. 7, p. 073708(5), 2009.
- [187] U. Bhapkar and M. Shur, “Monte Carlo Calculation of Velocity-field Characteristics of Wurtzite GaN,” *J.Appl.Phys.*, vol. 82, pp. 1649–1655, 1997.
- [188] H. Amano, M. Kito, K. Hiramatsu, and I. Akasaki, “p-Type Conduction in Mg-Doped GaN Treated with Low-Energy Electron Beam Irradiation (LEEBI),” *Jpn.J.Appl.Phys.*, vol. 28, no. Part 2, No. 12, pp. L2112–L2114, 1989.
- [189] E. Ejder and P. O. Fagerström, “Photoconductivity of Zn-doped GaN,” *J.Phys.Chem. Solids*, vol. 36, no. 4, pp. 289–292, 1975.

- [190] P. Bergman, G. Ying, B. Monemar, and P. O. Holtz, "Time-Resolved Spectroscopy of Zn- and Cd-Doped GaN," *J.Appl.Phys.*, vol. 61, no. 9, pp. 4589–4592, 1987.
- [191] M. Ilegems and R. Dingle, "Luminescence of Be- and Mg-Doped GaN," *J.Appl.Phys.*, vol. 44, no. 9, pp. 4234–4235, 1973.
- [192] S. Strite and H. Morkoç, "GaN, AlN, and InN: A Review," *J.Vac.Sci.Technol.B*, vol. 10, no. 4, pp. 1237–1266, 1992.
- [193] S. Nakamura, N. Iwasa, M. Senoh, and T. Mukai, "Hole Compensation Mechanism of P-Type GaN Films," *Jpn.J.Appl.Phys.*, vol. 31, no. 5A, pp. 1258–1266, 1992.
- [194] I. Akasaki, H. Amano, M. Kito, and K. Hiramatsu, "Photoluminescence of Mg-Doped p-Type GaN and Electroluminescence of GaN p-n Junction LED," *J. of Luminescence*, vol. 48-49, no. 2, pp. 666–670, 1991.
- [195] A. Bhattacharyya, W. Li, J. Cabalu, T. Moustakas, D. Smith, and R. Hergig, "Efficient p-Type Doping of GaN Films by Plasma-Assisted Molecular Beam Epitaxy," *Appl.Phys.Lett.*, vol. 85, no. 21, pp. 4956–4958, 2004.
- [196] D. Green, E. Haus, F. Wu, L. Chen, U. Mishra, and J. Speck, "Polarity Control During Molecular Beam Epitaxy Growth of Mg-Doped GaN," *J.Vac.Sci.Technol.B*, vol. 21, no. 4, pp. 1804–1812, 2003.
- [197] P. Kozodoy, H. Xing, S. DenBaars, U. K. Mishra, A. Saxler, R. Perrin, S. Elhamri, and W. C. Mitchel, "Heavy Doping Effects in Mg-Doped GaN," *J.Appl.Phys.*, vol. 87, no. 4, pp. 1832–1835, 2000.
- [198] U. Kaufmann, P. Schlotter, H. Obloh, K. Köhler, and M. Maier, "Hole Conductivity and Compensation in Epitaxial GaN:Mg Layers," *Phys.Rev.B*, vol. 62, no. 16, pp. 10867–10872, 2000.
- [199] D. Lancefield and H. Eshghi, "Temperature-Dependent Hole Transport in GaN," *J.Phys.:Condensed Matter*, vol. 13, no. 40, pp. 8939–8944, 2001.
- [200] M. L. Nakarmi, K. H. Kim, J. Li, J. Y. Lin, and H. X. Jiang, "Enhanced p-Type Conduction in GaN and AlGa<sub>N</sub> by Mg- $\delta$ -Doping," *Appl.Phys.Lett.*, vol. 82, no. 18, pp. 3041–3043, 2003.
- [201] E. F. Schubert, W. Grieshaber, and I. D. Goepfert, "Enhancement of Deep Acceptor Activation in Semiconductors by Superlattice Doping," *Appl.Phys.Lett.*, vol. 69, no. 24, pp. 3737–3739, 1996.
- [202] P. Kozodoy, M. Hansen, S. P. DenBaars, and U. K. Mishra, "Enhanced Mg Doping Efficiency in Al<sub>0.1</sub>Ga<sub>0.8</sub>N/GaN Superlattices," *Appl.Phys.Lett.*, vol. 74, no. 24, pp. 3681–3683, 1999.
- [203] L. Hsu and W. Walukiewicz, "Theoretical Transport Studies of p-Type GaN/AlGa<sub>N</sub> Modulation-Doped Heterostructures," *Appl.Phys.Lett.*, vol. 74, no. 17, pp. 2405–2407, 1999.

## BIBLIOGRAPHY

---

- [204] E. Waldron, J. Graff, and E. Schubert, “Improved Mobilities and Resistivities in Modulation-Doped p-Type AlGa<sub>N</sub>/Ga<sub>N</sub> Superlattices,” *Appl.Phys.Lett.*, vol. 79, no. 17, pp. 2737–2739, 2001.
- [205] I. D. Goepfert, E. F. Schubert, A. Osinsky, P. E. Norris, and N. N. Faleev, “Experimental and Theoretical Study of Acceptor Activation and Transport Properties in p-Type Al<sub>x</sub>Ga<sub>1-x</sub>N/GaN Superlattices,” *J.Appl.Phys.*, vol. 88, no. 4, pp. 2030–2038, 2000.
- [206] Q. Zheng, Y. Yin, L. Zhu, J. Huang, X. Li, and B. Liu, “Tailoring the Hole Concentration in Superlattices Based on Nitride Alloys,” *Appl.Phys.Lett.*, vol. 94, no. 22, p. 222104(3), 2009.
- [207] K. Kim, W. Lambrecht, B. Segall, and M. van Schilfgaarde, “Effective Masses and Valence-Band Splittings in GaN and AlN,” *Phys.Rev.B*, vol. 56, no. 12, pp. 7363–7375, 1997.
- [208] A. Kasic, M. Schubert, S. Einfeldt, D. Hommel, and T. Tiwald, “Free-Carrier and Phonon Properties of n- and p-Type Hexagonal GaN Films Measured by Infrared Ellipsometry,” *Phys.Rev.B*, vol. 62, no. 11, pp. 7365–7377, 2000.
- [209] I. Vurgaftman, J. R. Meyer, and L. R. Ram-Mohan, “Band Parameters for III–V Compound Semiconductors and Their Alloys,” *J.Appl.Phys.*, vol. 89, no. 11, pp. 5815–5875, 2001.
- [210] B. Santic, “On the Hole Effective Mass and the Free Hole Statistics in Wurtzite GaN,” *Semicond.Sci.Technol.*, vol. 18, no. 4, pp. 219–224, 2003.
- [211] A. Salvador, G. Liu, W. Kim, O. Aktas, A. Botchkarev, and H. Morkoç, “Properties of a Si Doped GaN/AlGa<sub>N</sub> Single Quantum Well,” *Appl.Phys.Lett.*, vol. 67, no. 22, pp. 3322–3324, 1995.
- [212] J. S. Im, A. Moritz, F. Steuber, V. Härle, F. Scholz, and A. Hangleiter, “Radiative Carrier Lifetime, Momentum Matrix Element, and Hole Effective Mass in GaN,” *Appl.Phys.Lett.*, vol. 70, no. 5, pp. 631–633, 1997.
- [213] A. Kasic, M. Schubert, B. Rheinlnder, V. Riede, S. Einfeldt, D. Hommel, B. Kuhn, J. Off, and F. Scholz, “Effective Carrier Mass and Mobility versus Carrier Concentration in p- and n-type α-GaN Determined by Infrared Ellipsometry and Hall Resistivity Measurements,” *Mat.Sci.Eng.B*, vol. 82, no. 1–3, pp. 74–76, 2001.
- [214] C. Rodrigues, A. Vasconcellos, and R. Luzzi, “Nonlinear Hole Transport and Nonequilibrium Thermodynamics in Group III-Nitrides under the Influence of Electric Fields,” *J.Appl.Phys.*, vol. 102, no. 7, p. 073714(7), 2007.
- [215] J. Wu, W. Walukiewicz, W. Shan, K. Yu, J. A. III, E. Haller, H. Lu, and W. Schaff, “Effects of the Narrow Band Gap on the Properties of InN,” *Phys.Rev.B*, vol. 66, no. 20, p. 201403(4), 2002.
- [216] V. Davydov, A. Klochikhin, V. Emtsev, S. Ivanov, V. Vekshin, F. Bechstedt, J. Furthmueller, H. Harima, A. Mudryi, A. Hashimoto, A. Yamamoto, J. Aderhold, J. Graul, and E. Haller, “Band Gap of InN and In-Rich In<sub>x</sub>Ga<sub>1-x</sub>N Alloys (0.36 < x < 1),” *Phys.stat.sol.(b)*, vol. 230, no. 02, pp. R4–R6, 2002.

- [217] T. Matsuoka, H. Okamoto, M. Nakao, H. Harima, , and E. Kurimoto, "Optical Bandgap Energy of Wurtzite InN," *Appl.Phys.Lett.*, vol. 81, no. 7, pp. 1246–1248, 2002.
- [218] W. Lambrecht and B. Segall, *Properties of Group III Nitrides*. INSPEC, London, 1994: EMIS Datareviews Series, 1994.
- [219] D. Fritsch, H. Schmidt, and M. Grundmann, "Band Dispersion Relations of Zinc-Blende and Wurtzite InN," *Phys.Rev.B*, vol. 69, no. 16, p. 165204(5), 2004.
- [220] S. Vitanov and V. Palankovski, "Monte Carlo Study of Electron Transport of InN," in *Springer Proceedings in Physics, Vol. 119*, pp. 97–100, Springer-Verlag, 2008.
- [221] V. Polyakov and F. Schwierz, "Nonparabolicity Effect on Bulk Transport Properties in Wurtzite InN," *J.Appl.Phys.*, vol. 99, no. 11, p. 113705(6), 2006.
- [222] B. Nag, "Electron Mobility in Indium Nitride," *J.Cryst.Growth*, vol. 269, pp. 35–40, 2004.
- [223] S. Vitanov, M. Nedjalkov, and V. Palankovski, "A Monte Carlo Model of Piezoelectric Scattering in GaN," *Lecture Notes in Computer Science*, vol. 4310, pp. 197–204, 2007.
- [224] F. Bernardini, V. Fiorentini, and D. Vanderbilt, "Spontaneous Polarization and Piezoelectric Constants of III-V Nitrides," *Phys.Rev.B*, vol. 56, no. 16, pp. R10024–R10027, 1997.
- [225] S. OLeary, B. Foutz, M. Shur, U. Bhapkar, and L. Eastman, "Electron Transport in Wurtzite Indium Nitride," *J.Appl.Phys.*, vol. 83, no. 02, pp. 826–829, 1998.
- [226] E. Bellotti, B. Doshi, K. Brennan, J. Albrecht, and P. Ruden, "Ensemble Monte Carlo Study of Electron Transport in Wurtzite InN," *J.Appl.Phys.*, vol. 85, no. 2, pp. 916–923, 1999.
- [227] Z. Yarar, "Transport and Mobility Properties of Wurtzite InN and GaN," *Phys.stat.sol.(b)*, vol. 244, no. 10, pp. 3711–3718, 2007.
- [228] L. Hsu, R. Jones, S. Li, K. Yu, and W. Walukiewicz, "Electron Mobility in InN and III-N Alloys," *J.Appl.Phys.*, vol. 102, no. 7, p. 073705(6), 2007.
- [229] A. Sheleg and V. Savastenko, "Izv. Akad. Nauk. SSSR," *Neorg. Mater*, vol. 15, p. 1598, 1979.
- [230] S. Wang and H. Ye, "First-Principles Study on Elastic Properties and Phase Stability of IIIV Compounds," *Phys.stat.sol.(b)*, vol. 240, pp. 45–54, 2003.
- [231] V. Polyakov and F. Schwierz, "Low-Field Electron Mobility in Wurtzite InN," *Appl.Phys.Lett.*, vol. 88, no. 03, p. 032101(3), 2006.
- [232] T. Tansley and C. Foley, "Electron Mobility in Indium Nitride," *Electron.Lett.*, vol. 20, no. 25, pp. 1066–1068, 1984.
- [233] A. Yamamoto, T. Shin-ya, T. Sugiura, and A. Hashimoto, "Characterization of MOVPE-Grown InN Layers on  $\alpha$ -Al<sub>2</sub>O<sub>3</sub> and GaAs Substrates," *J.Cryst.Growth*, vol. 189/190, pp. 461–465, 1998.

## BIBLIOGRAPHY

---

- [234] L. Dmowski, J. Plesiewicz, T. Suski, H. Lu, W. Schaff, M. Kurouchi, Y. Nanishi, L. Konczewicz, V. Cimalla, and O. Ambacher, “Resonant Localized Donor State above the Conduction Band Minimum in InN,” *Appl.Phys.Lett.*, vol. 86, no. 26, p. 262105(3), 2005.
- [235] C. Bulutay and B. Ridley, “Theoretical Assessment of Electronic Transport in InN,” *Superlattices & Microstructures*, vol. 36, pp. 465–471, 2004.
- [236] J. Furthmüller, P. Hahn, F. Fuchs, and F. Bechstedt, “Band Structures and Optical Spectra of InN Polymorphs: Influence of Quasiparticle and Excitonic Effects,” *Phys.Rev.B*, vol. 72, no. 20, p. 205106(14), 2005.
- [237] I. Mahboob, T. Veal, C. McConville, H. Lu, and W. Schaff, “Intrinsic Electron Accumulation at Clean InN Surfaces,” *Phys.Rev.Letters*, vol. 92, no. 3, p. 036804(4), 2004.
- [238] S. Li, K. Yu, J. Wu, R. Jones, W. Walukiewicz, J. Ager, W. Shan, E. Haller, H. Lu, and W. Schaff, “Fermi-Level Stabilization Energy in Group III Nitrides,” *Phys.Rev.B*, vol. 71, no. 16, p. 161201(4), 2005.
- [239] R. Jones, K. Yu, S. Li, W. Walukiewicz, J. Ager, E. Haller, H. Lu, and W. Schaff, “Evidence for p-Type Doping of InN,” *Phys.Rev.Letters*, vol. 96, no. 12, p. 125505(4), 2006.
- [240] P. A. Anderson, C. H. Swartz, D. Carder, R. J. Reeves, S. M. Durbin, S. Chandril, and T. H. Myers, “Buried p-Type Layers in Mg-Doped InN,” *Appl.Phys.Lett.*, vol. 89, no. 18, p. 184104(3), 2006.
- [241] X. Wang, S. Che, Y. Ishitani, and A. Yoshikawa, “Growth and Properties of Mg-Doped In-Polar InN Films,” *Appl.Phys.Lett.*, vol. 90, no. 20, p. 201913(3), 2007.
- [242] X. Wang, S. Che, Y. Ishitani, and A. Yoshikawa, “Hole Mobility in Mg-Doped p-Type InN Films,” *Appl.Phys.Lett.*, vol. 92, no. 13, p. 132108(3), 2008.
- [243] A. Klochikhin, V. Davydov, V. Emtsev, A. Sakharov, V. Kapitonov, B. Andreev, H. Lu, and W. Schaff, “Acceptor States in the Photoluminescence Spectra of n-InN,” *Phys.Rev.B*, vol. 71, no. 19, p. 195207(16), 2005.
- [244] M. Fujiwara, Y. Ishitani, X. Wang, S. Che, and A. Yoshikawa, “Infrared Analysis of Hole Properties of Mg-Doped p-Type InN Films,” *Appl.Phys.Lett.*, vol. 93, no. 23, p. 231903(3), 2008.
- [245] L. Dmowski, M. Baj, T. Suski, J. Przybytek, R. Czernecki, X. Wang, A. Yoshikawa, H. Lu, W. Schaff, D. Muto, and Y. Nanishi, “Search for Free Holes in InN:Mg-Interplay between Surface Layer and Mg-Acceptor Doped Interior,” *J.Appl.Phys.*, vol. 105, no. 12, p. 123713(5), 2009.
- [246] S. O’Leary, B. Foutz, M. Shur, U. Bhapkar, and L. Eastman, “Monte Carlo Simulation of Electron Transport in Wurtzite Aluminum Nitride,” *Solid-State Comm.*, vol. 105, no. 10, pp. 621–626, 1998.
- [247] C. Bulutay, “Electron Initiated Impact Ionization in AlGaN Alloys,” *Semi-cond.Sci.Technol.*, vol. 17, no. 10, pp. L59–L62, 2002.



- [248] K. Tsubouchi and N. Mikoshiba, “Zero-Temperature-Coefficient SAW Devices on AlN Epitaxial Films,” *IEEE Trans.Sonics Ultrason.*, vol. 32, no. 5, pp. 634–644, 1985.
- [249] L. McNeil, M. Grimsditch, and R. French, “Vibrational Spectroscopy of Aluminum Nitride,” *J. American Ceramic Soc.*, vol. 76, no. 5, pp. 1132–1138, 1993.
- [250] R. Kato and J. Jama, “First-Principles Calculation of the Elastic Stiffness Tensor of Aluminium Nitride under High Pressure,” *J.Phys.:Condensed Matter*, vol. 6, no. 38, pp. 7617–7632, 1994.
- [251] E. Ruiz, S. Alvarez, and P. Alemany, “Electronic Structure and Properties of AlN,” *Phys.Rev.B*, vol. 49, no. 11, pp. 7115–7123, 1994.
- [252] G. Bu, D. Ciplys, M. Shur, L. Schowalter, S. Schujman, and R. Gaska, “Electromechanical Coupling Coefficient for Surface Acoustic Waves in Single-Crystal Bulk Aluminium Nitride,” *Appl.Phys.Lett.*, vol. 84, no. 23, pp. 4611–4614, 2004.
- [253] M. Farahmand, C. Garetto, E. Bellotti, K. Brennan, M. Goano, E. Ghillino, G. Ghione, J. Albrecht, and P. Ruden, “Monte Carlo Simulation of Electron Transport in the III-Nitride Wurtzite Phase Materials System: Binaries and Ternaries,” *IEEE Trans.Electron Devices*, vol. 48, no. 3, pp. 535–542, 2001.
- [254] C. Bulutay, B. Ridley, and N. Zakhleniuk, “Electron Momentum and Energy Relaxation Rates in GaN and AlN in the High-Field Transport Regime,” *Phys.Rev.B*, vol. 68, no. 11, p. 115205(7), 2003.
- [255] V. Chin, B. Zhou, T. Tansley, and X. Li, “Alloy-Scattering Dependence of Electron Mobility in the Ternary Gallium, Indium, and Aluminum Nitrides,” *J.Appl.Phys.*, vol. 77, no. 11, pp. 6064–6066, 1995.
- [256] S. Smirnov, *Physical Modeling of Electron Transport in Strained Silicon and Silicon-Germanium*. Dissertation, Technische Universität Wien, 2003.
- [257] B. Ridley, “The Low-Field Electron Mobility in Bulk AlGaN,” *Phys.stat.sol.(a)*, vol. 176, no. 1, pp. 359–362, 1999.
- [258] E. Bellotti, F. Bertazzi, and M. Goano, “Alloy Scattering in AlGaN and InGaN: A Numerical Study,” *J.Appl.Phys.*, vol. 101, no. 12, p. 123706(8), 2007.
- [259] D. Jena, S. Heikman, J. Speck, A. Gossard, U. Mishra, A. Link, and O. Ambacher, “Magnetotransport Properties of a Polarization-Doped Three-Dimensional Electron Slab in Graded AlGaN,” *Phys.Rev.B*, vol. 67, no. 15, p. 153306(4), 2003.
- [260] M. Akarsu, S. Aydogu, and O. Ozbas, “Monte Carlo Calculation of Electron Transport Properties of  $\text{Ga}_x\text{In}_{1-x}\text{N}$ ,” *Phys.stat.sol.(c)*, vol. 4, no. 2, pp. 664–666, 2007.
- [261] C. Jacoboni and L. Reggiani, “The Monte Carlo Method for the Solution of Charge Transport in Semiconductors with Applications to Covalent Materials,” *Rev.Mod.Phys.*, vol. 55, no. 3, pp. 645–705, 1983.
- [262] D. Ventura, A. Gnudi, G. Baccarani, and F. Odeh, “Multidimensional Spherical Harmonics Expansion of Boltzmann Equation for Transport in Semiconductors,” *Appl.Math.Lett.*, vol. 5, no. 3, pp. 85–90, 1992.

## BIBLIOGRAPHY

---

- [263] M. Vasicek, *Advanced Macroscopic Transport Models*. Dissertation, Technische Universität Wien, 2009.
- [264] S. Selberherr, *Analysis and Simulation of Semiconductor Devices*. Wien, New York: Springer, 1984.
- [265] G. Wachutka, “Rigorous Thermodynamic Treatment of Heat Generation and Conduction in Semiconductor Device Modeling,” *IEEE Trans.Computer-Aided Design*, vol. 9, no. 11, pp. 1141–1149, 1990.
- [266] M. Knaipp, *Modellierung von Temperatureinflüssen in Halbleiterbauelementen*. Dissertation, Technische Universität Wien, 1998.
- [267] T. Grasser, *Mixed-Mode Device Simulation*. Dissertation, Technische Universität Wien, 1999.
- [268] C. Fischer, *Bauelementsimulation in einer computergestützten Entwurfsumgebung*. Dissertation, Technische Universität Wien, 1994.
- [269] L. Yu, Q. Liu, Q. Xing, D. Qiao, S. Lau, and J. Redwing, “The Role of the Tunneling Component in the Current–Voltage Characteristics of Metal–GaN Schottky Diodes,” *J.Appl.Phys.*, vol. 84, no. 4, pp. 2099–2104, 1998.
- [270] J. Jang, S. Sohn, D. Kim, and T. Seong, “Formation of Low-Resistance Transparent Ni/Au Ohmic Contacts to a Polarization Field-Induced p-InGaN/GaN Superlattice,” *Semicond.Sci.Technol.*, vol. 21, no. 5, p. 37, 2006.
- [271] Y. Liu, M. Kauser, M. Nathan, P. Ruden, S. Dogan, H. Morkoç, S. Park, and K. Lee, “Effects of Hydrostatic and Uniaxial Stress on the Schottky Barrier Heights of Ga-Polarity and N-Polarity n-GaN,” *Appl.Phys.Lett.*, vol. 84, no. 12, pp. 2112–2114, 2004.
- [272] V. Rangel-Kuoppa, S. Suihkonen, M. Sopanen, and H. Lipsanen, “Metal Contacts on InN: Proposal for Schottky Contact,” *Jpn.J.Appl.Phys.*, vol. 45, no. 1A, pp. 36–39, 2006.
- [273] A. Schmitz, A. Ping, M. Khan, Q. Chen, J. Yang, and I. Adesida, “Schottky Barrier Properties of Various Metals on n-Type GaN,” *Semicond.Sci.Technol.*, vol. 11, no. 10, p. 1464, 1996.
- [274] K. Tracy, P. Hartlieb, S. Einfeldt, R. Davis, E. Hurt, and R. Nemanich, “Electrical and Chemical Characterization of the Schottky Barrier Formed between Clean n-GaN(0001) Surfaces and Pt, Au, and Ag,” *J.Appl.Phys.*, vol. 94, no. 6, pp. 3939–3948, 2003.
- [275] Z. Chen, S. Tan, Y. Sakai, and T. Egawa, “Improved Performance of InAlN-Based Schottky Solar-Blind Photodiodes,” *Appl.Phys.Lett.*, vol. 94, no. 21, p. 213504, 2009.
- [276] E. Arslan, S. Altnadal, S. Özcelik, and E. Ozbay, “Tunneling Current via Dislocations in Schottky Diodes on AlInN/AlN/GaN Heterostructures,” *Semicond.Sci.Technol.*, vol. 24, no. 7, p. 075003, 2009.
- [277] L. Yu, D. Qiao, L. Jia, S. Lau, Y. Qi, and K. Lau, “Study of Schottky Barrier of Ni on p-GaN,” *Appl.Phys.Lett.*, vol. 79, no. 27, pp. 4536–4538, 2001.

- [278] J. Jang, D. Kim, and T. Seong, “Schottky Barrier Characteristics of Pt Contacts to n-Type InGaN,” *J.Appl.Phys.*, vol. 99, no. 7, p. 073704, 2006.
- [279] D. Qiao, L. Yu, S. Lau, J. Redwing, J. Lin, and H. Jiang, “Dependence of Ni/AlGaN Schottky Barrier Height on Al Mole Fraction,” *J.Appl.Phys.*, vol. 87, no. 2, pp. 801–804, 2000.
- [280] L. Yu, D. Qiao, Q. Xing, S. Lau, K. Boutros, and J. Redwing, “Ni and Ti Schottky Barriers on n-AlGaN Grown on SiC Substrates,” *Appl.Phys.Lett.*, vol. 73, no. 2, pp. 238–240, 1998.
- [281] Y. Liu, T. Egawa, H. Jiang, B. Zhang, H. Ishikawa, and M. Hao, “Near-Ideal Schottky Contact on Quaternary AlInGaN Epilayer Lattice-Matched with GaN,” *Appl.Phys.Lett.*, vol. 85, no. 24, pp. 6030–6032, 2004.
- [282] D. Schroeder, *Modelling of Interface Carrier Transport for Device Simulation*. Wien: Springer, 1994.
- [283] T. Simlinger, H. Brech, T. Grave, and S. Selberherr, “Simulation of Submicron Double-Heterojunction High Electron Mobility Transistors with MINIMOS-NT,” *IEEE Trans.Electron Devices*, vol. 44, no. 5, pp. 700–707, 1997.
- [284] S. Davydov, “Estimates of the Spontaneous Polarization and Permittivities of AlN, GaN, InN, and SiC Crystals,” *Phys.Sol.Stat.*, vol. 51, no. 6, pp. 1231–1235, 2009.
- [285] A. Barker and M. Ilegems, “Infrared Lattice Vibrations and Free-Electron Dispersion in GaN,” *Phys.Rev.B*, vol. 7, no. 2, pp. 743–750, 1973.
- [286] S. Adachi, “Material Parameters of  $\text{In}_{1-x}\text{Ga}_x\text{As}_y\text{P}_{1-y}$  and Related Binaries,” *J.Appl.Phys.*, vol. 53, no. 12, pp. 8775–8792, 1982.
- [287] S. Adachi, *Properties of Semiconductor Alloys: Group-IV, III-V and II-VI Semiconductors*. Chichester: Wiley, 2008.
- [288] B. Kang, G. Louche, R. Duran, Y. Gnanou, S. Pearton, and F. Ren, “Gateless AlGaIn/GaN HEMT Response to Block Co-Polymers,” *Solid-State Electron.*, vol. 48, no. 5, pp. 851–854, 2004.
- [289] M. Yamaguchi, T. Yagi, T. Sota, T. Deguchi, K. Shimada, and S. Nakamura, “Brillouin Scattering Study of Bulk GaN,” *J.Appl.Phys.*, vol. 85, no. 12, pp. 8502–8504, 1999.
- [290] M. Levinshtein, S. Rumyantsev, and M. Shur, *Properties of Advanced Semiconductor Materials*. New York-Chichester-Weinheim-Brisbane-Singapore-Toronto: John Wiley & Sons, 2001.
- [291] G. Slack and T. McNelly, “Growth of High Purity AlN Crystals,” *J.Cryst.Growth*, vol. 34, no. 2, 1976.
- [292] E. Sichel and J. Pankove, “Thermal Conductivity of GaN, 25-360 K,” *J.Phys.Chem. Solids*, vol. 38, no. 3, pp. 330–330, 1977.
- [293] C. Mion, J. Muth, E. Preble, and D. Hanser, “Thermal Conductivity, Dislocation Density and GaN Device Design,” *Superlattices & Microstructures*, vol. 40, no. 4-6, pp. 338–342, 2006.

## BIBLIOGRAPHY

---

- [294] D. Florescu, V. Asnin, F. Pollak, A. Jones, J. Ramer, M. Schurman, and I. Ferguson, “Thermal Conductivity of Fully and Partially Coalesced Lateral Epitaxial Overgrown GaN/Sapphire (0001) by Scanning Thermal Microscopy,” *Appl.Phys.Lett.*, vol. 77, no. 10, pp. 1464–1466, 2000.
- [295] J. Zou, D. Kotchetkov, A. Balandin, D. Florescu, and F. Pollak, “Thermal Conductivity of GaN Films: Effects of Impurities and Dislocations,” *J.Appl.Phys.*, vol. 92, no. 5, pp. 2534–2539, 2002.
- [296] W. Liu and A. Balandin, “Thermal Conduction in  $\text{Al}_x\text{Ga}_{1-x}\text{N}$  Alloys and Thin Films,” *J.Appl.Phys.*, vol. 97, no. 7, p. 073710(6), 2005.
- [297] A. Jezowski, B. Danilchenko, M. Bockowski, I. Grzegory, S. Krukowski, T. Suski, and T. Paszkiewicz, “Thermal Conductivity of GaN Crystals in 4.2–300 K range,” *Solid-State Comm.*, vol. 128, no. 2-3, pp. 69–73, 2003.
- [298] W. Liu and A. Balandin, “Temperature Dependence of Thermal Conductivity of  $\text{Al}_x\text{Ga}_{1-x}\text{N}$  Thin Films Measured by the Differential 3 Omega Technique,” *Appl.Phys.Lett.*, vol. 85, no. 22, pp. 5230–5232, 2004.
- [299] A. Jacquot, B. Lenoir, A. Dauscher, P. Verardi, F. Craciun, M. Stolzer, M. Gartner, and M. Dinescu, “Optical and Thermal Characterization of AlN Thin Films Deposited by Pulsed Laser Deposition,” *Applied Surface Science*, vol. 186, no. 1-4, pp. 507–512, 2002.
- [300] G. Slack, R. Tanzilli, R. Pohl, and J. Vandersande, “The Intrinsic Thermal Conductivity of AlN,” *J.Phys.Chem. Solids*, vol. 48, no. 7, pp. 641–647, 1987.
- [301] G. Slack, L. Schowalter, D. Morelli, and J. Freitas, “Some Effects of Oxygen Impurities on AlN and GaN,” *J.Cryst.Growth*, vol. 246, no. 3–4, pp. 287–298, 2002.
- [302] S. Krukowski, A. Witek, J. Adamczyk, J. Jun, M. Bockowski, I. Grzegory, B. Lucznik, G. Nowak, M. Wrblewski, A. Presz, S. Gierlotka, S. Stelmach, B. Palosz, S. Porowski, and P. Zinn, “Thermal Properties of Indium Nitride,” *J.Phys.Chem. Solids*, vol. 59, no. 3, pp. 289–295, 1998.
- [303] S. Adachi, “Lattice Thermal Conductivity of Group-IV and III–V Semiconductor Alloys,” *J.Appl.Phys.*, vol. 102, no. 6, p. 063502, 2007.
- [304] B. Abeles, “Lattice Thermal Conductivity of Disordered Semiconductor Alloys at High Temperatures,” *Phys.Rev.*, vol. 131, no. 5, pp. 1906–1911, 1963.
- [305] V. Palankovski, R. Schultheis, and S. Selberherr, “Simulation of Power Heterojunction Bipolar Transistors on Gallium Arsenide,” *IEEE Trans.Electron Devices*, vol. 48, no. 6, pp. 1264–1269, 2001.
- [306] B. Daly, H. Maris, A. Nurmikko, M. Kuball, and J. Han, “Optical Pump-and-Probe Measurement of the Thermal Conductivity of Nitride Thin Films,” *J.Appl.Phys.*, vol. 92, no. 7, pp. 3820–3824, 2002.
- [307] B. Pantha, R. Dahal, J. Li, J. Lin, H. Jiang, and G. Pomrenke, “Thermoelectric Properties of  $\text{In}_x\text{Ga}_{1-x}\text{N}$  Alloys,” *Appl.Phys.Lett.*, vol. 92, no. 4, p. 042112, 2008.

- [308] S. Yamaguchi, R. Izaki, K. Yamagiwa, K. Taki, Y. Iwamura, and A. Yamamoto, "Thermal Diffusivity and Thermoelectric Figure of Merit of  $\text{Al}_{1-x}\text{In}_x\text{N}$  Prepared by Reactive Radio-Frequency Sputtering," *Appl.Phys.Lett.*, vol. 83, no. 26, pp. 5398–5400, 2003.
- [309] R. Kremer, M. Cardona, E. Schmitt, J. Blumm, S. Estreicher, M. Sanati, M. Bockowski, I. Grzegory, T. Suski, and A. Jezowski, "Heat Capacity of  $\alpha$ -GaN : Isotope Effects," *Phys.Rev.B*, vol. 72, no. 7, p. 075209, 2005.
- [310] B. Danilchenko, T. Paszkiewicz, S. Wolski, A. Jezowski, and T. Plackowski, "Heat Capacity and Phonon Mean Free Path of Wurtzite GaN," *Appl.Phys.Lett.*, vol. 89, no. 6, p. 061901, 2006.
- [311] J. Leitner, P. Marsik, D. Sedmidubsky, and K. Ruzicka, "High Temperature Enthalpy, Heat Capacity and Other Thermodynamic Functions of Solid InN," *J.Phys.Chem. Solids*, vol. 65, no. 6, pp. 1127–1131, 2004.
- [312] I. Zieborak-Tomaszkiewicz, R. Swierzewski, and P. Gierycz, "Heat Capacity of Indium Nitride," *J. Th. Analysis and Calorimetry*, vol. 91, no. 2, pp. 649–653, 2008.
- [313] Y. P. Varshni, "Temperature dependence of the energy gap in semiconductors," *Physica, (Utrecht)*, no. 34, pp. 149–154, 1967.
- [314] Q. Guo and A. Yoshida, "Temperature Dependence of Band Gap Change in InN and AlN," *Jpn.J.Appl.Phys.*, vol. 33, no. 5A, pp. 2453–2456, 1994.
- [315] W. Walukiewicz, S. X. Li, J. Wu, K. M. Yu, J. W. Ager, E. E. Haller, H. Lu, and W. J. Schaff, "Optical Properties and Electronic Structure of InN and In-Rich Group III-Nitride Alloys," *J.Cryst.Growth*, vol. 269, no. 1, pp. 119–127, 2004.
- [316] L. Vegard, "Die Konstitution der Mischkristalle und die Raumfüllung der Atome," *Z. Physik*, no. 5, pp. 17–26, 1921.
- [317] S. Yoshida, S. Misawa, and S. Gonda, "Properties of  $\text{Al}_x\text{Ga}_{1-x}\text{N}$  Films Prepared by Reactive Molecular Beam Epitaxy," *J.Appl.Phys.*, vol. 53, no. 10, pp. 6844–6848, 1982.
- [318] W. Shan, J. Ager, K. Yu, W. Walukiewicz, E. Haller, M. Martin, W. McKinney, and W. Yang, "Dependence of the Fundamental Band Gap of  $\text{Al}_x\text{Ga}_{1-x}\text{N}$  on Alloy Composition and Pressure," *J.Appl.Phys.*, vol. 85, no. 12, pp. 8505–8507, 1999.
- [319] M. Khan, R. Skogman, R. Schulze, and M. Gershenson, "Properties and Ion Implantation of  $\text{Al}_x\text{Ga}_{1-x}\text{N}$  Epitaxial Single Crystal Films Prepared by Low Pressure Metalorganic Chemical Vapor Deposition," *Appl.Phys.Lett.*, vol. 43, no. 5, pp. 492–494, 1983.
- [320] T. Ochalski, B. Gil, P. Lefebvre, N. Grandjean, M. Leroux, J. Massies, S. Nakamura, and H. Morkoç, "Photoreflectance Investigations of the Bowing Parameter in AlGaIn Alloys Lattice-Matched to GaN," *Appl.Phys.Lett.*, vol. 74, no. 22, pp. 3353–3355, 1999.
- [321] C. Caetano, L. Teles, M. Marques, and A. D. P. and L. Ferreira, "Phase Stability, Chemical Bonds, and Gap Bowing of  $\text{In}_x\text{Ga}_{1-x}\text{N}$  Alloys: Comparison between Cubic and Wurtzite Structures," *Phys.Rev.B*, vol. 74, no. 4, p. 045215, 2006.

## BIBLIOGRAPHY

---

- [322] M. Ferhat and F. Bechstedt, “First-Principles Calculations of Gap Bowing in  $\text{In}_x\text{Ga}_{1-x}\text{N}$  and  $\text{In}_x\text{Al}_{1-x}\text{N}$  Alloys: Relation to Structural and Thermodynamic Properties,” *Phys.Rev.B*, vol. 65, no. 7, p. 075213, 2002.
- [323] P. Moses and C. V. de Walle, “Band Bowing and Band Alignment in InGaN Alloys,” *Appl.Phys.Lett.*, vol. 96, no. 2, p. 021908, 2010.
- [324] R. Kudrawiec, M. Siekacz, M. Krysko, G. Cywinski, J. Misiewicz, and C. Skierbiszewski, “Contactless Electroreflectance of InGaN Layers with Indium Content  $\leq 36\%$ : The Surface Band Bending, Band Gap Bowing, and Stokes Shift Issues,” *J.Appl.Phys.*, vol. 106, no. 11, p. 113517, 2009.
- [325] K. Wang, R. Martin, D. Amabile, P. Edwards, S. Hernandez, E. Nogales, K. O’Donnell, K. Lorenz, E. Alves, V. Matias, A. Vantomme, D. Wolverson, and I. Watson, “Optical Energies of AlInN Epilayers,” *J.Appl.Phys.*, vol. 103, no. 7, p. 073510, 2008.
- [326] Z. Dridi, B. Bouhafs, and P. Ruterana, “First-Principles Investigation of Lattice Constants and Bowing Parameters in Wurtzite  $\text{Al}_x\text{Ga}_{1-x}\text{N}$ ,  $\text{In}_x\text{Ga}_{1-x}\text{N}$  and  $\text{In}_x\text{Al}_{1-x}\text{N}$  Alloys,” *Semicond.Sci.Technol.*, vol. 18, no. 9, p. 850, 2003.
- [327] E. Iliopoulos, A. Adikimenakis, C. Giesen, M. Heuken, and A. Georgakilas, “Energy Bandgap Bowing of InAlN Alloys Studied by Spectroscopic Ellipsometry,” *Appl.Phys.Lett.*, vol. 92, no. 19, p. 191907, 2008.
- [328] S. Yamaguchi, M. Kariya, S. Nitta, H. Kato, T. Takeuchi, C. Wetzel, H. Amano, and I. Akasaki, “Structural and Optical Properties of AlInN and AlGaInN on GaN Grown by Metalorganic Vapor Phase Epitaxy,” *J.Cryst.Growth*, vol. 195, no. 1-4, pp. 309–313, 1998.
- [329] R. Butte, E. Feltin, J. Dorsaz, G. Christmann, J.-F. Carlin, N. Grandjean, and M. Illegems, “Recent Progress in the Growth of Highly Reflective Nitride-Based Distributed Bragg Reflectors and Their Use in Microcavities,” *Jpn.J.Appl.Phys.*, vol. 44, no. 10, pp. 7207–7216, 2005.
- [330] R. Goldhahn, P. Schley, A. Winzer, G. Gobsch, V. Cimalla, O. Ambacher, M. Rakel, C. Cobet, N. Esser, H. Lu, and W. Schaff, “Detailed Analysis of the Dielectric Function for Wurtzite InN and In-Rich InAlN Alloys,” *Phys.stat.sol.(a)*, vol. 203, no. 1, pp. 42–49, 2006.
- [331] V. Darakchieva, M. Beckers, M.-Y. Xie, L. Hultman, B. Monemar, J.-F. Carlin, E. Feltin, M. Gonschorek, and N. Grandjean, “Effects of Strain and Composition on the Lattice Parameters and Applicability of Vegard’s Rule in Al-Rich  $\text{Al}_{1-x}\text{In}_x\text{N}$  Films Grown on Sapphire,” *J.Appl.Phys.*, vol. 103, no. 10, p. 103513, 2008.
- [332] K. Lorenz, N. Franco, E. Alves, I. Watson, R. Martin, and K. O’Donnell, “Anomalous Ion Channeling in AlInN/GaN Bilayers: Determination of the Strain State,” *Phys.Rev.Letters*, vol. 97, no. 8, p. 085501, 2006.
- [333] A. Westmeyer, S. Mahajan, K. Bajaj, J. Lin, H. Jiang, D. Koleske, and R. Senger, “Determination of Energy-Band Offsets between GaN and AlN Using Excitonic Luminescence Transition in AlGaIn Alloys,” *J.Appl.Phys.*, vol. 99, no. 1, p. 013705(4), 2006.

- [334] G. Martin, A. Botchkarev, A. Rockett, and H. Morkoç, “Valence-Band Discontinuities of Wurtzite GaN, AlN, and InN Heterojunctions Measured by x-Ray Photoemission Spectroscopy,” *Appl.Phys.Lett.*, vol. 68, no. 18, pp. 2541–2543, 1996.
- [335] P. King, T. Veal, C. Kendrick, L. Bailey, S. Durbin, and C. McConville, “InN/GaN Valence Band Offset: High-Resolution x-Ray Photoemission Spectroscopy Measurements,” *Phys.Rev.B*, vol. 78, no. 3, p. 033308, 2008.
- [336] C. Foxon, S. Novikov, L. Zhao, and I. Harrison, “Isoelectronic Doping of AlGa<sub>N</sub> Alloys with As and Estimates of AlGa<sub>N</sub>/Ga<sub>N</sub> Band Offsets,” *Appl.Phys.Lett.*, vol. 83, no. 6, pp. 1166–1168, 2003.
- [337] S. Selberherr, W. Hänsch, M. Seavey, and J. Slotboom, “The Evolution of the MINIMOS Mobility Model,” *Solid-State Electron.*, vol. 33, no. 11, pp. 1425–1436, 1990.
- [338] T. Mnatsakanov, M. Levinshtein, L. Pomortseva, S. Yurkov, G. Simin, and M. Khan, “Carrier Mobility Model for GaN,” *Solid-State Electron.*, vol. 47, no. 1, pp. 111–115, 2003.
- [339] V. Turin, “A Modified Transferred-Electron High-Field Mobility Model for GaN Devices Simulation,” *Solid-State Electron.*, vol. 49, no. 10, pp. 1678–1682, 2005.
- [340] E. Faraclas and A. Anwar, “AlGa<sub>N</sub>/Ga<sub>N</sub> HEMTs: Experiment and Simulation of DC Characteristics,” *Solid-State Electron.*, vol. 50, no. 6, pp. 1051–1056, 2006.
- [341] D. Caughey and R. Thomas, “Carrier Mobilities in Silicon Empirically Related to Doping and Field,” *Proc.IEEE*, vol. 55, no. 12, pp. 2192–2193, 1967.
- [342] J. Piprek, *Nitride Semiconductor Devices*. Weinheim: Wiley, 2007.
- [343] Y. Taniyasu, M. Kasu, and T. Makimoto, “Increased Electron Mobility in n-Type Si-Doped AlN by Reducing Dislocation Density,” *Appl.Phys.Lett.*, vol. 89, no. 18, p. 182112, 2006.
- [344] S. Vitanov, V. Palankovski, S. Maroldt, and R. Quay, “High-Temperature Modeling of AlGa<sub>N</sub>/Ga<sub>N</sub> HEMTs,” *Solid-State Electron.*, vol. 54, no. 10, pp. 1105–1112.
- [345] D. Look, D. Reynolds, J. Hemsley, J. Szelove, R. Jones, and R. Molnar, “Defect Donor and Acceptor in GaN,” *Phys.Rev.Letters*, vol. 79, no. 12, pp. 2273–2276, 1997.
- [346] R. Molnar, W. Götz, L. Romano, and N. Johnson, “Growth of Gallium Nitride by Hydride Vapor-Phase Epitaxy,” *J.Cryst.Growth*, vol. 178, no. 1-2, pp. 147–156, 1997.
- [347] X. Dang, P. Asbeck, E. Yu, G. Sullivan, M. Chen, B. McDermott, K. Boutros, and J. Redwing, “Measurement of Drift Mobility in AlGa<sub>N</sub>/Ga<sub>N</sub> Heterostructure Field-Effect Transistor,” *Appl.Phys.Lett.*, vol. 74, no. 25, pp. 3890–3892, 1999.
- [348] N. Maeda, T. Saitoh, K. Tsubaki, T. Nishida, and N. Kobayashi, “Two-Dimensional Electron Gas Transport Properties in AlGa<sub>N</sub>/(In)Ga<sub>N</sub>/AlGa<sub>N</sub> Double-Heterostructure Field Effect Transistors,” *MRS Internet J. Nitride Semicond. Res.*, vol. 5S1, no. W4.7, 2000.

## BIBLIOGRAPHY

---

- [349] R. Cuerdo, J. Pedros, A. Navarro, A. Brana, J. Pau, E. Munoz, and F. Calle, “High Temperature Assessment of Nitride-Based Devices,” *J. Mat. Sci.: Materials in Electronics*, vol. 19, no. 2, pp. 189–193, 2008.
- [350] W. Tan, M. Uren, P. Fry, P. Houston, R. Balmer, and T. Martin, “High Temperature Performance of AlGa<sub>N</sub>/Ga<sub>N</sub> HEMTs on Si Substrates,” *Solid-State Electron.*, vol. 50, no. 3, pp. 511–513, 2006.
- [351] D. Donoval, M. Florovic, D. Gregusov, J. Kovc, and P. Kordos, “High-Temperature Performance of AlGa<sub>N</sub>/Ga<sub>N</sub> HFETs and MOSHFETs,” *Microelectron. Reliab.*, vol. 48, no. 10, pp. 1669–1672, 2008.
- [352] T. Grasser, H. Kosina, and S. Selberherr, “Consistent Comparison of Drift-Diffusion and Hydro-Dynamic Device Simulations,” in *Proc. Simulation of Semiconductor Processes and Devices*, pp. 151–154, 1999.
- [353] W. Hänsch and M. Miura-Mattauch, “The Hot-Electron Problem in Small Semiconductor Devices,” *J. Appl. Phys.*, vol. 60, no. 2, pp. 650–656, 1986.
- [354] S. Sze, *Physics of Semiconductor Devices*. New York: Wiley, second ed., 1981.
- [355] J. Albrecht, R. Wang, P. Rudena, M. Farahmand, and K. Brennan, “Electron Transport Characteristics of Ga<sub>N</sub> for High Temperature Device Modeling,” vol. 83, no. 9, pp. 4777–4781, 1998.
- [356] W. Hänsch, M. Orlowski, and W. Weber, “The Hot-Electron Problem in Submicron MOS-FET,” in *Proc. Europ. Solid-State Device Research Conf.*, pp. 597–606, 1988.
- [357] S. Vitinov, V. Palankovski, and S. Selberherr, “Hydrodynamic Models for Ga<sub>N</sub>-Based HEMTs,” in *Proc. Europ. Solid-State Device Research Conference (ESSDERC), Fringe Poster Session*, 2010.
- [358] O. Ambacher, B. Foutz, J. Smart, J. Shealy, N. Weimann, K. Chu, M. Murphy, A. Sierakowski, W. Schaff, L. Eastman, R. Dimitrov, A. Mitchell, and M. Stutzmann, “Two-Dimensional Electron Gases Induced by Spontaneous and Piezoelectric Polarization in Undoped and Doped AlGa<sub>N</sub>/Ga<sub>N</sub> Heterostructures,” *J. Appl. Phys.*, vol. 87, no. 1, pp. 334–344, 2000.
- [359] F. Bernardini, V. Fiorentini, and D. Vanderbilt, “Accurate Calculation of Polarization-Related Quantities in Semiconductors,” *Phys. Rev. B*, vol. 63, no. 19, p. 193201, 2001.
- [360] O. Ambacher, J. Majewski, C. Miskys, A. Link, M. Hermann, M. Eickhoff, M. Stutzmann, F. Bernardini, V. Fiorentini, V. Tilak, B. Schaff, and L. Eastman, “Pyroelectric Properties of Al(In)Ga<sub>N</sub>/Ga<sub>N</sub> Hetero- and Quantum Well Structures,” *J. Phys.: Condensed Matter*, vol. 14, no. 13, pp. 3399–3434, 2002.
- [361] W. Yan, R. Zhang, X. Xiu, Z. Xie, P. Han, R. Jiang, S. Gu, Y. Shi, and Y. Zheng, “Temperature Dependence of the Pyroelectric Coefficient and the Spontaneous Polarization of AlN,” *Appl. Phys. Lett.*, vol. 90, no. 21, p. 212102(3), 2007.
- [362] K. Kurokawa, “Power Waves and the Scattering Matrix,” *IEEE Trans. Microwave Theory and Techniques*, vol. 13, no. 2, pp. 194–202, 1965.



- 
- [363] G. Dambrine, A. Cappy, F. Heliodore, and E. Playez, “A New Method for Determining the FET Small-Signal Equivalent Circuit,” *IEEE Trans.Microwave Theory and Techniques*, vol. 36, no. 7, pp. 1151–1159, 1988.
- [364] M. Berroth and R. Bosch, “High-Frequency Equivalent Circuit of GaAs FETs for Large-Signal Applications,” *IEEE Trans.Microwave Theory and Techniques*, vol. 39, no. 2, pp. 224–229, 1991.
- [365] S. Wagner, *Small-Signal Device and Circuit Simulation*. Dissertation, Technische Universität Wien, 2005.
- [366] D. Jena, I. Smorchkova, A. Gossard, and U. Mishra, “Electron Transport in IIIV Nitride Two-Dimensional Electron Gases,” *Phys.stat.sol.(b)*, vol. 228, no. 2, pp. 617–619, 2001.
- [367] I. Smorchkova, C. Elsass, J. Ibbetson, R. Vetury, B. Heying, P. Fini, E. Haus, S. Den-Baars, J. Speck, and U. Mishra, “Polarization Induced Charge and Electron Mobility in AlGaIn/GaN Heterostructures Grown by Plasma-Assisted Molecular-Beam Epitaxy,” *J.Appl.Phys.*, vol. 86, no. 8, pp. 4520–4526, 1999.
- [368] B. Jogai, “Influence of Surface States on the Two-Dimensional Electron Gas in AlGaIn/GaN Heterojunction Field-Effect Transistors,” *J.Appl.Phys.*, vol. 93, no. 3, pp. 1631–1635, 2003.
- [369] S. Vitinov, V. Palankovski, S. Murad, T. Roedle, R. Quay, and S. Selberherr, “Predictive Simulation of AlGaIn/GaN HEMTs,” in *Tech.Dig. IEEE Compound Semiconductor IC Symp.*, pp. 131–134, 2007.
- [370] R. Quay, K. Hess, R. Reuter, M. Schlechtweg, T. Grave, V. Palankovski, and S. Selberherr, “Nonlinear Electronic Transport and Device Performance of HEMTs,” *IEEE Trans.Electron Devices*, vol. 48, no. 2, pp. 210–217, 2001.
- [371] V. Palankovski, S. Vitinov, and R. Quay, “Field-Plate Optimization of AlGaIn/GaN HEMTs,” in *Tech.Dig. IEEE Compound Semiconductor IC Symp.*, pp. 107–110, 2006.
- [372] I. Daumiller, C. Kirchner, M. Kamp, K. Ebeling, and E. Kohn, “Evaluation of the Temperature Stability of AlGaIn/GaN Heterostructure FETs,” *IEEE Electron Device Lett.*, vol. 20, no. 9, pp. 448–450, 1999.
- [373] S. Arulkumaran, T. Egawa, H. Ishikawa, and T. Jimbo, “High-Temperature Effects of AlGaIn/GaN High-Electron-Mobility Transistors on Sapphire and Semi-Insulating SiC Substrates,” *Appl.Phys.Lett.*, vol. 80, no. 12, pp. 2186–2188, 2002.
- [374] R. Cuerdo, F. Calle, A. Brana, Y. Cordier, M. Azize, N. Baron, S. Chenot, and E. Munoz, “High Temperature Behaviour of GaN HEMT Devices on Si(111) and Sapphire Substrates,” *Phys.stat.sol.(a)*, vol. 5, no. 6, pp. 1971–1973, 2008.
- [375] M. Akita, S. Kishimoto, and T. Mizutani, “High-Frequency Measurements of AlGaIn/GaN HEMTs at High Temperatures,” *IEEE Electron Device Lett.*, vol. 22, no. 8, pp. 376–377, 2001.
-

## BIBLIOGRAPHY

---

- [376] S. Arulkumaran, G. I. Ng, Z. H. Liu, and C. H. Lee, “High Temperature Power Performance of AlGa<sub>N</sub>/Ga<sub>N</sub> High-Electron-Mobility Transistors on High-Resistivity Silicon,” *Appl.Phys.Lett.*, vol. 91, no. 8, p. 083516(3), 2007.
- [377] M. Huque, S. Eliza, T. Rahman, H. Huq, and S. Islam, “Temperature Dependent Analytical Model for Current-Voltage Characteristics of AlGa<sub>N</sub>/Ga<sub>N</sub> Power HEMT,” *Solid-State Electron.*, vol. 53, no. 3, pp. 341–348, 2009.
- [378] H. Huq and S. Islam, “AlGa<sub>N</sub>/Ga<sub>N</sub> Self-Aligned MODFET with Metal Oxide Gate for Millimeter Wave Application,” *Microelectronics Journal*, vol. 37, no. 7, pp. 579–582, 2006.
- [379] Y. Chang, Y. Zhang, Y. Zhang, and K. Tong, “A Thermal Model for Static Current Characteristics of AlGa<sub>N</sub>/Ga<sub>N</sub> High Electron Mobility Transistors Including Self-Heating Effect,” *J.Appl.Phys.*, vol. 99, no. 4, p. 044501(5), 2006.
- [380] Y. Chang, K. Tong, and C. Surya, “Numerical Simulation of Current-Voltage Characteristics of AlGa<sub>N</sub>/Ga<sub>N</sub> HEMTs at High Temperatures,” *Semicond.Sci.Technol.*, vol. 20, no. 2, pp. 188–192, 2005.
- [381] Y. Zhou, D. Wang, C. Ahyi, C. Tin, J. Williams, M. Park, N. Williams, A. Hanser, and E. Preble, “Temperature-Dependent Electrical Characteristics of Bulk Ga<sub>N</sub> Schottky Rectifier,” *J.Appl.Phys.*, vol. 101, no. 2, p. 024506, 2007.
- [382] S. Nuttinck, B. Banerjee, S. Venkataraman, J. Laskar, and M. Harris, “High Temperature Performances of AlGa<sub>N</sub>/Ga<sub>N</sub> Power HFETs,” in *IEEE Intl. Microwave Symp. Dig.*, vol. 1, pp. 221–223, 2003.
- [383] S. Arulkumaran, Z. Liu, G. Ng, W. Cheong, R. Zeng, J. Bu, H. Wang, K. Radhakrishnan, and C. Tan, “Temperature Dependent Microwave Performance of AlGa<sub>N</sub>/Ga<sub>N</sub> High-Electron-Mobility Transistors on High-Resistivity Silicon Substrate,” *Thin Solid Films*, vol. 515, no. 10, pp. 4517–4521, 2007.
- [384] A. Parker and J. Scott, “Intermodulation nulling in GaAs MESFETs,” *Electron.Lett.*, vol. 29, no. 22, pp. 1961–1962, 1993.
- [385] T. Palacios, S. Rajan, A. Chakraborty, S. Heikman, S. Keller, S. DenBaars, and U. Mishra, “Influence of the Dynamic Access Resistance in the  $g_m$  and  $f_T$  Linearity of AlGa<sub>N</sub>/Ga<sub>N</sub> HEMTs,” *IEEE Trans.Electron Devices*, vol. 52, no. 10, pp. 2117–2123, 2005.
- [386] Y. Wu, M. Singh, and J. Singh, “Sources of Transconductance Collapse in III-V Nitrides – Consequences of Velocity–Field Relations and Source/Gate Design,” *IEEE Trans.Electron Devices*, vol. 52, no. 6, pp. 1048–1054, 2005.
- [387] S. Vitanov, V. Palankovski, S. Maroldt, and R. Quay, “Non-Linearity of Transconductance and Source-Gate Resistance of HEMTs,” in *Proc. Europ. Solid-State Device Research Conference (ESSDERC), Fringe Poster Session*, 2010.
- [388] S. Russo and A. D. Carlo, “Influence of the Source-Gate Distance on the AlGa<sub>N</sub>/Ga<sub>N</sub> HEMT Performance,” *IEEE Trans.Electron Devices*, vol. 54, no. 5, pp. 1071–1075, 2007.

- 
- [389] Y. Ando, Y. Okamoto, H. Miyamoto, T. Nakayama, T. Inoue, and M. Kuzuhara, “10-W/mm AlGa<sub>N</sub>-Ga<sub>N</sub> HFET With a Field Modulating Plate,” *IEEE Electron Device Lett.*, vol. 24, no. 5, pp. 289–291, 2003.
- [390] M. Hiroki, H. Yokoyama, N. Watanabe, and T. Kobayashi, “High-Quality InAlN/GaN Heterostructures Grown by Metal-Organic Vapor Phase Epitaxy,” *Superlattices & Microstructures*, vol. 40, no. 4–6, pp. 214–218, 2006.
- [391] F. Medjdoub, N. Sarazin, M. Tordjman, M. Magis, M. Forte-Poisson, M. Knez, E. Delos, C. Gaquiere, S. Delage, and E. Kohn, “Characteristics of Al<sub>2</sub>O<sub>3</sub>/AlInN/GaN MOSHEMT,” *Electron.Lett.*, vol. 43, no. 12, pp. 691–692, 2007.
- [392] J. Kuzmik, A. Kostopoulos, G. Konstantinidis, J. Carlin, A. Georgakilas, and D. Pogany, “InAlN/GaN HEMTs: A First Insight Into Technological Optimization,” *IEEE Trans. Electron Devices*, vol. 53, no. 3, pp. 422–426, 2006.
- [393] S. Maroldt, D. Wiegner, S. Vitinov, V. Palankovski, R. Quay, and O. Ambacher, “Efficient AlGa<sub>N</sub>/Ga<sub>N</sub> Linear and Digital-Switch-Mode Power Amplifiers for Operation at 2 GHz,” *IEICE Trans. Electron.*, vol. E93-C, no. 8, pp. 1238–1244, 2010.
- [394] T. Mizutani, M. Ito, S. Kishimoto, , and F. Nakamura, “AlGa<sub>N</sub>/Ga<sub>N</sub> HEMTs with Thin InGa<sub>N</sub> Cap Layer for Normally Off Operation,” *IEEE Electron Device Lett.*, vol. 28, no. 7, pp. 549–551, 2007.
- [395] S. Vitinov and V. Palankovski, “Normally-Off AlGa<sub>N</sub>/Ga<sub>N</sub> HEMTs with InGa<sub>N</sub> Cap Layer: A Simulation Study,” *Solid-State Electron.*, vol. 52, no. 11, pp. 1791–1795, 2008.



---

## Own Publications

---

- [1] V. Palankovski, S. Vitanov, and R. Quay, "Field-Plate Optimization of AlGa<sub>N</sub>/Ga<sub>N</sub> HEMTs," in *Tech. Dig. IEEE Compound Semiconductor IC Symp.*, (San Antonio), pp. 107–110, Nov. 2006.
- [2] S. Vitanov, V. Palankovski, R. Quay, and E. Langer, "Two-Dimensional Numerical Simulation of AlGa<sub>N</sub>/Ga<sub>N</sub> HEMTs," in *TARGET DAYS - Book of Proceedings*, (Frascati), pp. 81–84, Oct. 2006.
- [3] S. Vitanov, V. Palankovski, S. Murad, T. Roedle, R. Quay, and S. Selberherr, "Hydrodynamic Modeling of AlGa<sub>N</sub>/Ga<sub>N</sub> HEMTs," in *Proc. Intl. Conf. on Simulation of Semiconductor Processes and Devices*, (Vienna), pp. 273–276, Sept. 2007.
- [4] S. Vitanov, V. Palankovski, S. Murad, T. Rdle, R. Quay, and S. Selberherr, "Predictive Simulation of AlGa<sub>N</sub>/Ga<sub>N</sub> HEMTs," in *Tech. Dig. IEEE Compound Semiconductor IC Symp.*, (Portland), pp. 131–134, Oct. 2007.
- [5] S. Vitanov and V. Palankovski, "Normally-Off AlGa<sub>N</sub>/Ga<sub>N</sub> HEMTs with InGa<sub>N</sub> Cap Layer: A Theoretical Study," in *Proc. Intl. Semiconductor Device Research Symp.*, (Maryland), Dec. 2007.
- [6] S. Vitanov, V. Palankovski, R. Quay, and E. Langer, "Modeling of Electron Transport in Ga<sub>N</sub>-Based Materials and Devices," in *AIP Conference Proc.*, vol. 893, pp. 1399–1400, American Institute of Physics, 2007.
- [7] S. Vitanov, M. Nedjalkov, and V. Palankovski, "A Monte Carlo Model of Piezoelectric Scattering in Ga<sub>N</sub>," in *Lecture Notes in Computer Science*, vol. 4310, pp. 197–204, Springer-Verlag, 2007.
- [8] S. Vitanov and V. Palankovski, "Monte Carlo Study of Electron Transport of In<sub>N</sub>," in *Springer Proceedings in Physics*, vol. 119, pp. 97–100, Springer-Verlag, 2008.
- [9] S. Vitanov, V. Palankovski, G. Pozzovivo, J. Kuzmik, and R. Quay, "Systematical Study of InAl<sub>N</sub>/Ga<sub>N</sub> Devices by Numerical Simulation," in *European Workshop on Heterostructure Technology (HETECH) Book of Abstracts*, (Venice), pp. 159–160, Nov. 2008.

- [10] S. Vitanov and V. Palankovski, "Enhancement Mode HEMTs: Evaluation of Two Approaches by Numerical Simulation," in *Junior Scientist Conf. Proc.*, (Vienna), pp. 221–222, Nov. 2008.
- [11] S. Vitanov and V. Palankovski, "Normally-Off AlGaIn/GaN HEMTs with InGaIn cap layer: A simulation study," *Solid-State Electron.*, vol. 52, no. 11, pp. 1791–1795, Nov. 2008.
- [12] S. Vitanov, V. Palankovski, S. Maroldt, and R. Quay, "A Simulation Study of Enhancement-Mode AlGaIn/GaN HEMTs with Recessed Gates," in *European Workshop on Heterostructure Technology (HETECH) Book of Abstracts*, (Guenzburg/Ulm), pp. 109–110, Nov. 2009.
- [13] S. Vitanov, V. Palankovski, S. Maroldt, and R. Quay, "High-Temperature Modeling of AlGaIn/GaN HEMTs," in *Proc.Intl. Semiconductor Device Research Symp.*, (Maryland), Dec. 2009.
- [14] S. Vitanov and V. Palankovski, "Influence of the Gate Recess on the Performance of Enhancement-Mode AlGaIn/GaN HEMTs," in *Annual Journal of Electronics*, (Sozopol), pp. 144–147, Sept. 2009.
- [15] S. Vitanov, V. Palankovski, S. Maroldt, and R. Quay, "High-temperature modeling of AlGaIn/GaN HEMTs," *Solid-State Electron.*, vol. 52, no. 10, pp.1195–1112, 2010.
- [16] S. Maroldt, D. Wiegner, S. Vitanov, V. Palankovski, R. Quay, and O. Ambacher, "Efficient AlGaIn/GaN Linear and Digital-Switch-Mode Power Amplifiers for Operation at 2 GHz," *IEICE Trans.Electron.*, vol. 93, no. 8, pp. 1238–1244, 2010.
- [17] S. Vitanov and V. Palankovski, "High-Temperature Small-Signal Analysis of AlGaIn/GaN HEMTs," in *Junior Scientist Conf. Proc.*, (Vienna), pp. 59–60, Apr. 2010.
- [18] S. Vitanov and V. Palankovski, "Electron Mobility Models for III-Nitrides," in *Annual Journal of Electronics*, (Sozopol), pp. 18–21, Sep. 2010.
- [19] S. Vitanov, V. Palankovski, S. Maroldt, and R. Quay, "Non-Linearity of Transconductance and Source-Gate Resistance of HEMTs," in *Proc. Europ. Solid-State Device Research Conf. (ESSDERC), Fringe Poster Session*, (Sevilla), Sep. 2010.
- [20] S. Vitanov, V. Palankovski, and S. Selberherr, "Hydrodynamic Models for GaN-Based HEMTs," in *Proc. Europ. Solid-State Device Research Conf. (ESSDERC), Fringe Poster Session*, (Sevilla), Sep. 2010.

---

# Curriculum Vitae

---

**January 10<sup>th</sup>, 1981**

Born in Sofia, Bulgaria.

**June 1999**

High school graduation (*Matura*) at the 91. Deutschsprachiges Gymnasium, Sofia.

**October 1999**

Enrolled in Electrical Engineering at the Munich University of Technology, Germany.

**2002-2003**

Praktika and internship at Siemens AG Germany.

**April 2005**

Received the degree of *Diplom-Ingenieur* (M.Sc.) in Electrical Engineering, specializing in Communication Systems from the Munich University of Technology.

**January 2006**

Entered doctoral program at the Institute for Microelectronics, Technische Universität Wien.

